Invasive and non-invasive diagnostics of High Power Impulse Magnetron Sputtering (HiPIMS) discharges

by

Bernd Liebig

The University of Liverpool

Thesis submitted for the degree
of
Doctor of Philosophy

Department of Electrical Engineering and Electronics
Liverpool, March 2013

Declaration

I hereby declare that this thesis is my own work and no further sources of information have been used other than the references cited. Neither this thesis nor any part of it have been submitted to any other university or institution for the application of another degree or qualification.

Liverpool, 09. March 2013

Bernd Liebig

Abstract

HiPIMS discharges operated with a titanium and an aluminium-doped zinc target sputtered with the working gas argon were investigated by means of optical 2d-imaging in combination with Abel-inversion. By using optical bandpass filters, the spatial and temporal evolution of the plasma-induced emission of argon atoms and ions and metal atoms and ions were studied. The discharge ignition was found to be accompanied by an intensity maximum observed remote from the target, followed by an asymmetric intensity profile. During the stage of high discharge current, the intensity distribution indicates strong rarefaction of the working gas, efficient ionisation of the sputtered particles above the target and a wider sputter distribution. The off-time is characterised by an initial drop of the intensity by 4 - 6 orders of magnitude and a transition from electron-impact excitation to excitation by electron-electron-ion recombination. Decay constants in the order of 1 ms and the spatial distribution of the emission suggest the loss of electrons and ions due to ambipolar diffusion across the magnetic field.

Plasma potential measurements by means of emissive probe revealed strongly negative space potentials of up to -300 V and electric fields in the order of 10^4 V m^{-1} during discharge ignition, caused by strong charge separation due to the extended sheath. The plasma potential increases to a stable level of more than -25 V during the second half of the discharge pulse, while the electric field is largely reduced to maximal 1.5×10^3 V m^{-1}. It was found that the space potential is consistently 5 V lower when the substrate is kept floating compared to a grounded substrate, which can be explained by the reduced electron loss rate to the substrate due to the potential barrier. This is confirmed by spatially resolved Langmuir probe measurements, showing a density maximum of 10^{19} m^{-3} in the confined plasma zone, and an increased density in the vicinity of the floating substrate of 1.3×10^{18} m^{-3} compared to 0.8×10^{18} m^{-3} for a grounded substrate. The electron temperature was found to be spatially uniform ranging from 1 eV to 3 eV.

A quasi-continuous transport model for sputtered particles confirmed the high degree of ionisation of the sputtered particles of about 90 % and revealed a return probability for titanium ions to the target of 80 % for Ti^+ and 96 % for Ti^{2+}. Varying the force caused by a modified two-stream instability [1], showed an increasing sideway defletion of ions also increasing the kinetic energy observed for these particles. The spatial distribution of the relative density confirmed efficient ionisation of sputtered particles in the dense

plasma zone adjacent to the target. Average azimuthal velocities of the drifting ion fluid of 3×10^3 m s^{-1} for Ti^+ and 7×10^3 m s^{-1} for Ti^{2+} were obtained.

Acknowledgement

I would like to thank my supervisor Professor James Bradley for his guidance and continued support throughout the entire course of my studies and for allowing me to attend a number of conferences. Professor Nick Braithwaite shall be thanked for his useful comments on the manuscripts published and for his help with the optical 2d-imaging experiments. I would like to thank Professor Peter Kelly for his valuable input and useful discussions.

Dr. Paul Bryant is thanked for his introduction into the Abel-inversion programme written in-house. Dr. Ian C. Smith shall be acknowledged for his assistance in adopting the transport model programme for the use with the University of Liverpool High Throughput Computing system.

Alan Roby from the mechanical workshop is thanked for his gifted hands, as well as Alan Edwards and John Lynch from the electronics workshop for building the HiPIMS power supply and various trouble-shooting issues.

I would also like to thank the members of the research group, namely Nu, Jun-Seok, Panos, Shao-Dong, Michael, Steve, Tobi and Anurag for their valuable input and assistance.

I would like to thank my family and friends who gave me the strength and support to finish this project. Last but not least, I wish to thank my girlfriend Kelly and our daughter Amelie for their unconditional love, their optimism and motivation that enabled me to finish this thesis.

This work was partially funded by EPSRC under reference EP/E003397/1.

List of publications

Research carried out during the course of study has up to date resulted in the following publications:

- P. Poolcharuansin, B. Liebig and J. W. Bradley: *More evidence for azimuthal ion spin in HiPIMS discharges*, Plasma Sources Sci. Technol. 21, 2012, 015001
- B. Liebig, N. St. J. Braithwaite, P. J. Kelly, R. Chistyakov, B. Abraham, J. W. Bradley: *Time-resolved plasma characterisation of modulated pulsed power magnetron sputtering of chromium*, Surface & Coatings Technology 205, 2011, S312-S316
- P. Poolcharuansin, B. Liebig, J. W. Bradley: *Plasma Parameters in a Pre-Ionized HiPIMS Discharge Operating at Low Pressure*, IEEE Transactions on Plasma Science 38(11), 2010, 3007 - 3015
- B. Liebig, N. St. J. Braithwaite, P. J. Kelly, J. W. Bradley: *Spatial and temporal investigation of high power pulsed magnetron discharges by optical 2D-imaging*, Thin Solid Films 519, 2010, 1699 - 1704

Contents

List of Figures

List of Tables

1 Introduction

It has been known for more than a century that ions bombarding a surface can lead to particles been knocked out of this surface and condense on a nearby sample [2]. These early experiments, first reported by Grove had little to do with modern Physical Vapour Deposition (PVD) of thin films, but with improving availability of vacuum equipment, the first commercial application of the sputtering process was patented by Edison in 1902 [3]. Despite this early application, sputtering, in particular DC sputtering, remained a niche application for a long time due to the low deposition rate compared to evaporation processes [4,5]. However, it already shows all the principles. A plasma is created by applying a high voltage to two electrodes placed in a chamber filled with a gas of reduced pressure, usually in the range of a few Torr. Positive ions are extracted from the plasma and accelerated towards the cathode by the electric field present in the sheath adjacent to the cathode. As the ion impinges on the so called target with an energy of several keV, atoms can be released due to a momentum transfer cascade in the target. The sputtered particle then moves to the substrate where it condenses and the film grows. While the basic principles remained largely unchanged over the last decades, significant improvements were made on the deposition rate, the film uniformity and quality. Even though Penning already experimented with magnetically confined plasmas [6] in the 1930's, the first patents on planar magnetron sputtering sources as they are known nowadays were granted to Corbani and Chapin in the 1970's [7, 8]. In their setup, the plasma is confined by a magnetic field produced by permanent magnets close to the target which increases the plasma density in its vicinity and allows for much improved sputtering rates. Further improvements were the introduction of unbalanced magnetrons by Window and Savvides [9], which improved the film quality by allowing a flux of ions to impinge on the substrate and increase the ad-atom mobility. Adding reactive gases such as oxygen and nitrogen greatly enhanced the variety of films coated extending the range of application to non-conductive coatings. This usually causes arcing which was overcome by using sophisticated power supplies with arc handling or by pulsing the target voltage [10–13]. Today, magnetron sputtering is the working horse for the deposition of thin films for various applications, such as semiconductor manufacturing, transparent conductive coatings for displays, magnetic films,

superconductors, absorbers and reflective coatings for solar cells, optical mirrors, as well as hard, wear-resistant, anti-corrosive and decorative coatings [14].

Despite its wide use in industry, research is continuously driven by the ever-growing demands on existing coatings and to apply magnetron sputtering to completely new applications. One drawback of conventional DC magnetron sputtering is the low degree of ionisation of the sputtered flux which limits this technology to mainly coating flat substrates, such as glass or polymers, whereas structured substrates used to be the domain for cathodic vacuum arc deposition [15]. In 1999, a promising technology called High Power Pulsed Magnetron Sputtering (HPPMS) was introduced by Kouznetsov et. al. [16], which has attracted increasing interest from both academics and industry in recent years. This new technology increases the degree of ionisation of the sputtered flux by applying short but intense discharge pulses to the magnetron sputtering source. The superior quality of films [17–21] and the capability of coating structured substrates [16] makes HPPMS a versatile tool for future applications of magnetron sputtering. The advantage of HPPMS or High Power Impulse Magnetron Sputtering (HiPIMS) also comes with a catch. The deposition rate for non-reactive sputtering is usually lower than for a comparable DCMS process [22]. Investigations have also shown that HiPIMS is not only a conventional process with its power quenched into only a fraction of the time, but that it shows a couple of unique features, including strong rarefaction of the working gas [23], sputtering without a working gas due to exceeding the threshold for self-sustained sputtering [24–26], altering the static magnetic field of the magnetron [27], anomalous transport of electrons [1, 28] leading to a significant deflection of ions to the sidewall [29, 30] and the presence of drifting ionisation zones [31–33].

The present work aims to help understand better the complex nature of this pulsed discharge. For this purpose, optical 2d-imaging in combination with Abel-inversion was used to study the spatial and temporal development of HiPIMS discharges. This is to provide an overview over phenomena occurring in such a discharge. The second part of the thesis concentrates on the transport of sputtered particles from the target to the substrate by following the trajectory of test particles moving in the plasma potential distribution, measured by an emissive probe. Ionisation events were calculated from the electron density and temperature obtained from single Langmuir probe measurements. The influence of different substrate configurations, floating or grounded, were studied, as well as the influence of the force caused by a modified two-stream instability [1].

2 Theoretical background

This chapter provides a compilation of principles of plasma physics as well as on magnetron sputtering, including latest development on High Power Impulse Magnetron Sputtering (HiPIMS). The information summarised here is to introduce the theoretical framework of this project. It is not meant to be a complete and detailed description of the subject, which can be found in textbooks such as:

- F. F. Chen "Introduction into Plasma Physics and Controlled Fusion" [34],
- M. A. Lieberman and A. J. Lichtenberg "Principles of Plasma Discharges and Materials Processing" [35],
- I. H. Hutchinson "Principles of Plasma Diagnostics" [36],
- M. Konuma "Plasma Techniques for Film Deposition" [14].

Further information can also be found in references [37–42].

2.1 The plasma state

Plasma is commonly referred to as the fourth state of matter. In the same way one can melt solids or evaporate liquids by supplying heat, one can heat gases further until electrons are stripped of their parent atoms. However, a more precise definition is given by Chen ([34] page 3):

> A plasma is a quasineutral gas of charged and neutral particles which exhibits collective behaviour.

Both positively and negatively charged particles need to be present in equal number to ensure the gas to be quasineutral. Introducing n_+ and n_- as well as q_+ and q_- as the density and charge of positively and negatively charged particles, one can write:

$$\sum_i q_{i+} n_{i+} + \sum_j q_{j-} n_{j-} = 0. \tag{2.1}$$

If only electrons and singly charged positive ions are present in the plasma, the equation simplifies to $n_e = n_i$.

In order to describe the individual species, atoms, ions and electrons, further, one shall consider the velocity as well as the kinetic energy of the particles. As plasmas are defined as "ionised gases" one can readily apply tools well-known from the kinetic theory of gases. Each species, electrons, ions and neutrals, can be described by their velocity distribution function $f(\boldsymbol{v})$. The Maxwellian distribution function is most commonly used:

$$f(\boldsymbol{v}) = n\left(\frac{m}{2\pi k_B T}\right)^{3/2} \exp\left(-\frac{m\boldsymbol{v}^2}{2k_B T}\right), \tag{2.2}$$

where k_B is the Boltzmann constant and m, n and T are the mass, the density and the temperature of the particles, respectively. Using the temperature, one can distinguish between thermal plasmas, i.e. all species are in full thermal equilibrium and can be described by one temperature, and non-thermal or low temperature plasmas. In the latter case, the electron temperature T_e is considerably higher than the temperature of the ions T_i and of the background gas T_g: $T_e >> T_i \geq T_g$. From the distribution function of speed $f(v)$

$$f(v) = \sqrt{\frac{2}{\pi}} n\left(\frac{m}{k_B T}\right)^{3/2} v^2 \exp -\frac{mv^2}{2k_B T} \tag{2.3}$$

one can calculate the particle density n, the flux Γ and the average speed $\langle v \rangle$ as follows:

$$n = \int_0^\infty f(v)dv, \tag{2.4}$$

$$\Gamma = \int_0^\infty v f(v)dv, \tag{2.5}$$

$$\langle v \rangle = \frac{1}{n}\int_0^\infty v f(v)dv. \tag{2.6}$$

Here v is the absolute value of the velocity $|\boldsymbol{v}|$. The average speed is obtained as:

$$\langle v \rangle = \left(\frac{8k_B T}{\pi m}\right)^{1/2}. \tag{2.7}$$

Electrons and ions are also often described by their energy distribution function (EEDF) $f(E) = f(v)/mv$, which has the form:

$$f(E) = \frac{2}{\sqrt{\pi}} n\left(\frac{1}{k_B T}\right)^{3/2} \sqrt{E} \exp -\frac{E}{k_B T}. \tag{2.8}$$

Here, the kinetic energy is used as $E = 1/2mv^2$. The mean energy $\langle E \rangle$can be calculated in analogy to equation 2.6:

$$\langle E \rangle = \frac{1}{n} \int_0^\infty E f(E) dE = \frac{3}{2} k_B T. \tag{2.9}$$

It can be seen, that together with the particle density, the temperature or better the EEDF of a particular species is the most important parameter to obtain. One often uses the temperature, e.g. electron temperature $k_B T_e$, as an expression for the energy of electrons in the unit eV. An electron temperature of 3 eV means an average energy of 4.5 eV. It also implies the presence of a Maxwellian distribution function, which has to be confirmed first. Similar to gases, one can also define a pressure p as:

$$p = n k_B T \tag{2.10}$$

for each species, i.e. there is a pressure not only for the background gas p_g but also for electrons p_e. For a typical electron density of 10^{18} m^{-3} and temperature of 3 eV an electron pressure of 0.5 Pa can be calculated which is of the same order of magnitude as the background gas pressure. Plasmas can be classified by their operating pressure into low pressure, atmospheric pressure or high pressure plasmas. This project will only consider low pressure plasmas.

Until now, the plasma was considered as a gas, described by the kinetic theory of gases, with an equal amount of positive and negative charge, positive ions and electrons, present. In order to better understand the "collective behaviour", one shall follow a thought experiment and disturb the plasma by inserting a probe with potential Φ_0 and observe the different behaviour between a vacuum and a plasma environment. The problem shall be investigated in one dimension x only. The probe position is $x = 0$ and the potential far away from the probe, $x = l$, shall be zero. For both cases, vacuum and plasma, Poisson equation (in one dimension) must be solved:

$$\frac{d^2\Phi}{dx^2} = 0, \tag{2.11}$$

$$\frac{d^2\Phi}{dx^2} = -\frac{e}{\varepsilon_0}(n_i - n_e), \tag{2.12}$$

$$\Phi(x = 0) = \Phi_0, \tag{2.13}$$

$$\Phi(x = l) = 0. \tag{2.14}$$

Here the elementary charge is denoted as e and ε_0 is the permittivity of free space. In the case of vacuum one obtains a linear decrease of the potential with distance:

$$\Phi(x) = -\frac{\Phi_0}{l} x + \Phi_0. \tag{2.15}$$

In the plasma case, the mobile electrons are repelled from negative and attracted towards positive potentials Φ_0, which results in efficient screening of perturbations by external potentials. The potential distribution obeys an exponential law:

$$\Phi(x) = \Phi_0 \exp -\frac{x}{\lambda_d}, \tag{2.16}$$

with the characteristic screening length, the electron Debye length

$$\lambda_d = \sqrt{\frac{\varepsilon_0 k_B T_e}{n_0 e^2}}. \tag{2.17}$$

For plasma properties encountered in the experiments the Debye length is typically between 1 µm and 20 µm. With the Debye length a more accurate definition of quasineutrality of the plasma can be given:

$$\lambda_d << L, \tag{2.18}$$

with L being a characteristic length of the plasma, which is $10-20$ cm in our case. The aforementioned definition allows deviation from absolute equality of the densities n_e and n_i on short scales of length. In other words: Quasineutrality can be broken locally.

The plasma cannot only be perturbed spatially but also temporally. The eigen frequency of the electron system and the ion system is a very important quantity to evaluate, how quickly the species can react to temporal changes of external potentials, electric fields or to determine the temporal resolution of Langmuir probes immersed into the plasma. The electron and ion plasma frequency ω_{pe} and ω_{pi} are given as [35]:

$$\omega_{pe} = \sqrt{\frac{n_e e^2}{m_e \varepsilon_0}}, \tag{2.19}$$

$$\omega_{pi} = \sqrt{\frac{n_i e^2}{m_i \varepsilon_0}}. \tag{2.20}$$

For the plasma investigated in this study, the electron plasma frequency is typically in the range $10^9 \ldots 10^{11}$ s^{-1}, whereas the plasma frequency of the ions is three orders of magnitude lower $10^6 \ldots 10^8$ s^{-1}. Using the plasma frequency, one can formulate another condition that distinguishes plasmas from gases, even when they are ionised. "Collective behaviour" in the case of plasmas means, that interaction between particles is dominated by electromagnetic forces rather than by binary collisions present in gases. If the frequency of collisions between ions and electrons with the neutral background gas is denoted as ν_{in} and ν_{en}, respectively, $\omega_{pi}/\nu_{in} > 1$ and $\omega_{pi}/\nu_{in} > 1$ must hold. These collision frequencies

are typically about 10^5 s^{-1} in this study, which fulfils the plasma criterion.
In summary, a plasma is an ionised gas with the following two conditions [34]:

1. The Debye length is much smaller than the characteristic dimension of the plasma: $\lambda_d << L$.
2. The particle interaction must be dominated by electromagnetic fields and not by collisions: $\omega/\nu > 1$.

The species found in a plasma, namely electrons, positive ions and neutral atoms, can be described by their energy or velocity distribution functions. In the case of Maxwellian distributions a temperature and a pressure can be attributed. The free charge carriers in a plasma rapidly shield perturbations on a characteristic length, the Debye length. They can follow temporal fluctuations in the potential and electric fields up to their eigen frequency, the plasma frequency.

2.2 Particle transport

2.2.1 Motion of a single particle

The motion of a single particle can be described by the equation of motion:

$$m\frac{d}{dt}\boldsymbol{v} = q\left(\boldsymbol{E} + \boldsymbol{v}\times\boldsymbol{B}\right). \tag{2.21}$$

For a vanishing magnetic field, one can directly integrate equation 5.30:

$$\boldsymbol{v} = \frac{q}{m}\int_{t_1}^{t_2}\boldsymbol{E}(\boldsymbol{r},t)dt, \tag{2.22}$$

$$\boldsymbol{r} = \int_{t_1}^{t_2}\boldsymbol{v}(\boldsymbol{r},t)dt. \tag{2.23}$$

In the case of a uniform magnetic field, the solution is a gyration around a guiding centre characterised by the Lamor radius r_c and the cyclotron frequency ω_c:

$$r_c = \frac{mv_\perp}{|q|B}, \tag{2.24}$$

$$\omega_c = \frac{|q|B}{m}. \tag{2.25}$$

with $v_\perp$ being the velocity component perpendicular to the magnetic field. Typical values for electrons and titanium ions during a HiPIMS pulse ($B = 40$ mT) are Lamor radii of 0.2 mm and 15 cm, respectively. The gyration frequency differs by four orders of magnitude, 10^9 s^{-1} for electrons and 10^5 s^{-1} for positive ions. One can see from these values, that electrons are well-confined by the magnetic field, i.e. they are magnetised, whereas hardly any effect on the motion of ions can be observed, i.e. ions are not magnetised.

In most applications, both electric and magnetic fields are present and the motion of the particle gets more complex. However, in a number of cases one can write the complex motion as a superimposition of motions. One example, is the presence of a uniform electric and magnetic field. One can write the velocity $\boldsymbol{v}$ as sum of a constant drift velocity $\boldsymbol{v_e}$ and a velocity $\boldsymbol{v_c}$, yet to be calculated:

$$\boldsymbol{v} = \boldsymbol{v_e} + \boldsymbol{v_c}, \tag{2.26}$$

with the drift velocity perpendicular to $\boldsymbol{E}$ and $\boldsymbol{B}$

$$\boldsymbol{v_e} = \frac{\boldsymbol{E} \times \boldsymbol{B}}{B^2}, \tag{2.27}$$

which is called $E \times B$-drift speed. Equation 5.30 is then written as

$$m\frac{d}{dt}(\boldsymbol{v_e} + \boldsymbol{v_c}) = \frac{q}{m}\left[\boldsymbol{E} + (\boldsymbol{v_e} + \boldsymbol{v_c}) \times \boldsymbol{B}\right]. \tag{2.28}$$

The time derivative $d\boldsymbol{v_e}/dt = \boldsymbol{0}$, as can be seen from the definition of the drift velocity. Analysis of the cross product yields $\boldsymbol{v_e} \times \boldsymbol{B} = -\boldsymbol{E}$ and the equation of motion simplifies to:

$$\frac{d}{dt}\boldsymbol{v_c} = \frac{q}{m}\boldsymbol{v_c} \times \boldsymbol{B}, \tag{2.29}$$

The superimposed motion, is a gyration around a guiding centre, which drifts with a constant speed, the $E \times B$-drift speed, perpendicular to both the electric and the magnetic field. This is plausible, because during each gyration cycle particles are accelerated and decelerated by the electric field. This alters the Lamor radius and a net motion perpendicular to the electric field is observed. It is worth noting, that this drift, does neither depend on particle mass nor on its charge, i.e. positive ions and electrons drift together and no net current due to charge separation is observed. However, the actual effect is limited to electrons, as they are magnetised. The drift of the guiding centre for positive ions hardly has any influence due to their huge Lamor radius. $E \times B$-drift speeds in magnetrons are typically in the order of $10^4 \ldots 10^5$ ms^{-1}.

In general, any force $\boldsymbol{F}$ can cause a drift perpendicular to the force and to the magnetic field:

$$\boldsymbol{v_d} = \frac{1}{q}\frac{\boldsymbol{F}\times\boldsymbol{B}}{B^2}. \tag{2.30}$$

One example is the gravitational drift with $\boldsymbol{F} = m\boldsymbol{g}$. In this case, a net drift current is observed as $v_d \propto m/q$ which leads to opposite directions of ion and electron drift. The magnitude of the gravitational drift is usually very low and this drift can be neglected in magnetron sputtering discharges.

Additional drift speeds arise from curved and inhomogeneous magnetic and electric fields, as well as from time-varying fields. The derivation of the drift speeds can be found in most textbooks, such as reference [34]. Here, the results for the actual drift speeds shall only be summarised. Inhomogeneous magnetic fields lead to a drift $\boldsymbol{v_b}$ caused by the magnetic field gradient and the centrifugal force in the case of curved magnetic field lines:

$$\boldsymbol{v_b} = \frac{m}{q}\frac{\boldsymbol{R_c}\times\boldsymbol{B}}{R_c^2 B^2}\left(v_{||}^2 + \frac{1}{2}v_{\perp}^2\right), \tag{2.31}$$

with $v_{||}$ and $v_{\perp}$ being the velocity components parallel and perpendicular to the magnetic field, respectively. The curvature radius of the magnetic field lines $\boldsymbol{R_c}$ can be calculated by:

$$\frac{\nabla B}{B} = -\frac{\boldsymbol{R_c}}{R_c^2}. \tag{2.32}$$

Non-uniform electric fields give rise to a correction term $\boldsymbol{v_L}$ added to the $E\times B$-drift speed, which is known as the finite Lamor radius effect. If the electric field varies within one gyration cycle, i.e. on the scale of the Lamor radius, the correction term reads:

$$\boldsymbol{v_L} = \frac{1}{4}r_c^2\nabla^2\frac{\boldsymbol{E}\times\boldsymbol{B}}{B^2}. \tag{2.33}$$

This effect is usually quite small, because the speed depends on the Lamor radius squared and the electric field does not very much on the sub-millimetre scale.

The electric and magnetic fields cannot only vary spatially but also temporally. If the electric field changes with time, the drift speed is called polarisation drift $\boldsymbol{v_p}$:

$$\boldsymbol{v_p} = \pm\frac{1}{\omega_c B}\frac{d\boldsymbol{E}}{dt}. \tag{2.34}$$

In contrast to the drift speeds discussed before, the polarisation drift is directed along the electric field lines and not perpendicular to it like the $E\times B$-drift. It is also much higher for higher mass particles due to the mass dependence of the gyration frequency.

Finally, a temporal variation of the magnetic field does not lead to a drift, as such, but to an increase or decrease of kinetic energy of the particle with the magnetic field. A change of the magnetic field does not alter the kinetic energy of the particle directly. However, the Maxwell equation $\nabla \times \boldsymbol{E} = -d\boldsymbol{B}/dt$ shows that an electric field is induced due to the time dependant magnetic induction. No equation for a drift speed can be given, but it can be shown that the magnetic moment μ_{mag}, defined as ratio of kinetic energy and magnetic induction

$$\mu_{mag} = \frac{1/2mv_{\perp}^2}{B} \tag{2.35}$$

is an invariant of motion:

$$\partial \mu_{mag} = 0. \tag{2.36}$$

An increase of the magnetic field causes the velocity component perpendicular to the magnetic field to increase. And so does the Lamor radius increase. A decrease of the magnetic field will decrease the kinetic energy and the Lamor radius. The reason for this can be found from the aforementioned Maxwell equation. If the magnetic field is in z-direction, the problem reveals a cylinder symmetry. Maxwell equation then gives electric fields in radial and azimuthal direction, changing both the velocity and the (Lamor) radius.

An additional drift speed originates from the pressure gradient term in the fluid motion equation, i. e. a pressure gradient causes a particle motion in order to equalise the pressure. One can assign a force $\boldsymbol{F}_{\nabla p}$ to this term:

$$\boldsymbol{F}_{\nabla p} = -\frac{\nabla p}{n}. \tag{2.37}$$

The drift caused by this force is called diamagnetic drift $\boldsymbol{v}_{dia}$:

$$\boldsymbol{v}_{dia} = -\frac{\nabla p \times \boldsymbol{B}}{qnB^2}. \tag{2.38}$$

In summary, analysing the motion of single particles in the given electric and magnetic fields can lead to a lot of information on the behaviour of the entire species of particles. In magnetrons drift speeds due to the crossed electric and magnetic fields are very important for its performance at lower pressure: The drift motion increases the distance an electron has to travel to the anode, hence increasing the ionisation probability. The most important drifts in magnetrons are the $E \times B$-drift, the magnetic field curvature and gradient drift, as well as the diamagnetic drift, which conveniently add up in magnetron sputtering configurations.

The diamagnetic drift already indicated that not only the motion of a single particle is of interest but that species in plasmas can often be described as a fluid. This approach

is called magneto hydrodynamic (MHD). Reproducing the whole set of fluid equations which have to be solved is beyond the scope of this introduction. However, the collective transport of particles due to electric fields and density gradients described by mobility and diffusion shall be discussed briefly.

2.2.2 Collective transport: Mobility and diffusion

As it is known from Fick's first law

$$\boldsymbol{\Gamma} = -D\nabla n, \tag{2.39}$$

with the particle flux $\boldsymbol{\Gamma}$ and the diffusion constant D, a density gradient gives rise to the diffusion of particles that tries to establish a uniform density distribution. Diffusion of particles, such as electrons, positive ions and atoms, can also be expected for plasmas. However, the situation for electrons and ions is much more complex than the free diffusion described by equation 2.39, because the influence of both the electric and the magnetic field as well as collisions have to be considered. Without the presence of a magnetic field, the fluid equation of motion in equilibrium, i.e. without the acceleration term reads:

$$qn\boldsymbol{E} - \nabla p - mn\nu_c\boldsymbol{u} = \boldsymbol{0}, \tag{2.40}$$

with $\boldsymbol{u}$ the velocity of the fluid element. The collision term is written in its explicit form $mn\nu_c\boldsymbol{u}$, with ν_c being the collision frequency. If the particle temperature is spatially uniform the pressure gradient term can be rewritten as $\nabla p = k_B T \nabla n$. The particle velocity is then described by:

$$\boldsymbol{u} = \frac{q}{m\nu_c}\boldsymbol{E} - \frac{k_B T}{m\nu_c}\frac{\nabla n}{n}. \tag{2.41}$$

The particle flux can then be written as:

$$\boldsymbol{\Gamma} = \pm\mu n\boldsymbol{E} - D\nabla n. \tag{2.42}$$

This equation is somewhat similar to Fick's law. Hence, a diffusion constant is defined as:

$$D = \frac{k_B T}{m\nu_c}. \tag{2.43}$$

The additional term describing the flux due to the electric field is called the mobility term and μ the mobility:

$$\mu = \frac{|q|}{m\nu_c}. \tag{2.44}$$

Due to the much lower mass, electrons exhibit higher mobility and diffusion constants. The diffusion constant and the mobility are linked by the Einstein equation:

$$D = \frac{k_B T}{|q|}\mu. \tag{2.45}$$

For plasmas the quasineutrality condition $n_e = n_i = n$ has to be fulfilled, which requires the electron and ion flux to be equal, $\boldsymbol{\Gamma_e} = \boldsymbol{\Gamma_i}$. One can insert equation 2.42 and solve for the electric field, which yields:

$$\boldsymbol{E} = \frac{D_i - D_e}{\mu_i + \mu_e}\frac{\nabla n}{n}. \tag{2.46}$$

This is the so called ambipolar field, which accelerates positive ions towards regions of low density while impeding the electron motion at the same time. The potential Φ tied to the field is the ambipolar potential. One can use the solution for the electric field in equation 2.42 and obtains for the ion flux:

$$\boldsymbol{\Gamma} = -D_a \nabla n, \tag{2.47}$$

with the ambipolar diffusion constant

$$D_a = \mu_i E - D_i = \frac{\mu_i D_e + \mu_e D_i}{\mu_i + \mu_e}. \tag{2.48}$$

Using Einstein equation and account for the largely higher mobility of the electrons $\mu_e >> \mu_i$ the ambipolar diffusion constant can be written as:

$$D_a \approx D_i \left(1 + \frac{T_e}{T_i}\right). \tag{2.49}$$

One can see, that in the case of low temperature plasmas $T_e >> T_i$ the ambipolar diffusion can be several ten times higher than the diffusion of ions alone, whereas thermal plasmas $T_e \approx T_i$ exhibit diffusion constants which are only twice as large as the ion diffusion.

In the presence of a magnetic field, one has to distinguish between the transport along and across magnetic field lines. The diffusion constant and the mobility along magnetic field lines, $D_{||} = k_B T / m\nu_c$ and $\mu_{||} = |q| / m\nu_c$, remain unchanged, whereas both the diffusion constant and mobility perpendicular to the magnetic field, $D_\perp$ and $\mu_\perp$, can be significantly reduced:

$$\mu_\perp = \frac{\mu_{||}}{1 + (\omega_c/\nu_m)^2}, \tag{2.50}$$

$$D_\perp = \frac{D_{||}}{1 + (\omega_c/\nu_m)^2}. \tag{2.51}$$

One can see, that collisions facilitate the particle transport perpendicular to the magnetic field, whereas they impede the transport along magnetic field lines. The diffusion constant, calculated in this "classic" approach, is proportional to B^{-2}. Ambipolar diffusion, i.e. the diffusion of electrons and positive ions together, is also present when a magnetic field is applied. However, the fluid equations for diffusion lead to non-linear, coupled differential equations, which can only be solved analytically for rather unrealistic conditions, such as diffusion exclusively across magnetic field lines. As the diffusion of electrons is strongly impeded across magnetic field lines, an electric field would be established to support electron diffusion. On the other hand, electrons can easily diffuse along magnetic field lines and a current would flow in order to compensate for the charge gradient and the electric field would be lowered. This short example shall illustrate the feedback mechanism in the case of ambipolar diffusion in the presence of a magnetic field.

It was empirically found, that diffusion almost never obeyed the laws proposed by the "classical diffusion". The diffusion constants were found to be too large, especially for fully ionised plasmas, and the diffusion constant scaled with B^{-1} rather than with B^{-2}. A semi empirical formula was found for the diffusion across magnetic field lines, which is known as Bohm diffusion:

$$D_b = \frac{1}{16}\frac{k_B T_e}{eB}. \tag{2.52}$$

If one compares Bohm diffusion with the classical diffusion, equations 2.43 and 2.51:

$$D_\perp = \frac{1}{\omega_c/\nu_m}\frac{k_B T_e}{eB}, \tag{2.53}$$

one finds ω/ν_m to be constant in the case of Bohm diffusion. The parameter ω_c/ν_m often written with the collision time τ_m instead of the collision frequency ν_m, $\omega_c\tau_m$, is often studied in magnetron sputtering and in particularly in High Power Impulse Magnetron Sputtering to describe the mode of diffusion. Recent investigations on particle diffusion in HiPIMS showed values for $\omega_c\tau_m$ close to 2 indicating diffusion processes even faster than Bohm diffusion [28].

In order to obtain the spatial and temporal evolution of particle densities one has to solve Fick's second law of diffusion:

$$\frac{dn}{dt} = D\nabla^2 n, \tag{2.54}$$

with D being one of the aforementioned diffusion constants which describes the process. The differential equation can be solved by separation of variables in the form:

$$n(\boldsymbol{r},t) = n_0\rho(\boldsymbol{r})\exp -\frac{t}{\tau}, \tag{2.55}$$

with $\rho(\boldsymbol{r})$ being the spatial solution and τ a characteristic time constant, which depends on the diffusion constant and the diffusion length Λ. The diffusion length Λ represents the geometry of the diffusion problem which can be approximated as a cylinder with radius R and length l in this project [35]:

$$\Lambda = \left(\frac{2.405^2}{R^2} + \frac{\pi^2}{l^2} \right)^{-1/2}. \tag{2.56}$$

The time constant τ can be calculated as:

$$\tau = \frac{\Lambda^2}{D}. \tag{2.57}$$

2.2.3 Particle collisions

Collisions can occur between particles of the same or of different species. They lead to a transfer of momentum and energy, elastic collisions, but can also change the charge by ionisation or recombination or the inner energy of particles by excitation of atoms or ions, inelastic collisions. Incident particles with a flux Γ travel through a volume of target particles with density n_t. The change of the flux due to collisions $d\Gamma$ within a distance dx must be proportional to the density of particles, the distance dx and the incident flux itself:

$$d\Gamma = -\sigma n_t \Gamma dx. \tag{2.58}$$

The parameter σ is called cross-section and describes the interaction between the incident and the target particle. The cross-section strongly depends on what kind of particles collide and the type of process, elastic scattering, excitation, ionisation etc. The solution for the particle flux is given by:

$$\Gamma = \Gamma_0 \left(1 - \exp - \frac{x}{\lambda} \right), \tag{2.59}$$

with λ being the mean free path, i.e. the average distance an incident particle can travel before colliding with a target particle. The mean free path is defined as:

$$\lambda = \frac{1}{n_t \sigma}. \tag{2.60}$$

The time τ describes the time the particle with speed v needs to cross the mean free path:

$$\tau = \frac{\lambda}{v}. \tag{2.61}$$

Its inverse $\nu = \tau^{-1}$ is known as the collision frequency. Another useful quantity is the rate coefficient

$$k = \sigma v \tag{2.62}$$

which is the collision frequency per target particle density. In general, the cross-section also depends on the kinetic energy of the incident particle $\sigma = \sigma(E)$. For example, inelastic processes, such as ionisation, exhibit a threshold energy which has to be exceeded before the process can occur. In addition, one has to consider that the incident particles are usually not monoenergetic but exhibit a distinct energy distribution $f(E)$. The rate coefficient is then calculated as the integral over the cross-section weighted by the energy distribution function:

$$k(E_e) = \sqrt{\frac{2}{m_e}} \int_0^\infty \sigma(E) f(E) \sqrt{E} dE, \tag{2.63}$$

with E_e being a parameter representing the energy distribution function, e. g. the mean energy or the temperature.

The most simple model for elastic scattering cross-sections is the collision of two hard spheres, as depicted in figure 2.1. The radii of both spheres are r_i and r_t for the incident and the target particle, respectively. The so called impact parameter b describes the minimum distance between the centre of the target particle and the unperturbed trajectory of the incident particle. If the impact parameter b is smaller than the sum of the particle radii $b < r_i + r_t$ a collision takes place. The cross-section for hard spheres σ_{hs} can then be defined as the area of the circle around the centre of the target particle with radius $r_i + r_t$:

$$\sigma_{hs} = \pi \left(r_i + r_t\right)^2. \tag{2.64}$$

An incident particle with velocity $\boldsymbol{v_i}$ collides with a target particle in rest $\boldsymbol{v_t} = \boldsymbol{0}$. One can divide the incident velocity into a component orientated tangentially to the particle surfaces at the contact point and a radial component:

$$v_{it} = v_i \cos\chi, \tag{2.65}$$

$$v_{ir} = v_i \sin\chi, \tag{2.66}$$

with angle χ being derived from geometric considerations as:

$$\sin\chi = \frac{b}{r_i + r_t}. \tag{2.67}$$

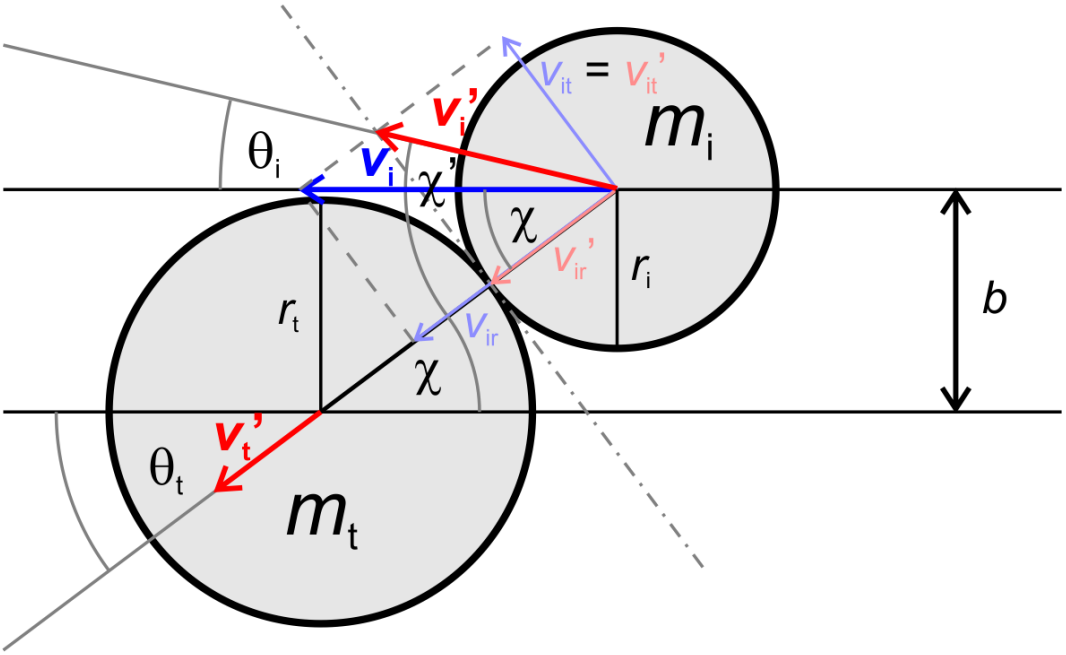

Figure 2.1: Elastic collision process in the hard sphere model. The target particle shall be in rest before the collision.

The radial component can be treated like a head-on collision, momentum and energy conservation apply, while the tangential component does not change at all:

$$v'_{it} = v_{it}, \tag{2.68}$$

$$v'_{ir} = \frac{m_i - m_t}{m_i + m_t} v_{ir}, \tag{2.69}$$

$$v'_i = \sqrt{v'^2_{it} + v'^2_{ir}}. \tag{2.70}$$

The incident particle changes its direction by the scattering angle θ_i in respect to its undisturbed trajectory. It can be calculated as:

$$\theta_i = \chi' - \chi, \tag{2.71}$$

with χ' being the scattering angle in respect to the radial component of the incident particle velocity:

$$\tan\chi' = \frac{m_i + m_t}{m_i - m_t} \tan\chi. \tag{2.72}$$

After the collision, the target particle moves under angle $\theta_t = \chi$ with a speed of:

$$v'_t = \frac{2m_i}{m_i + m_t} v_{ir}. \tag{2.73}$$

The energy transferred from the incident to the target particle ΔE_{trans} can be written as:

$$\frac{\Delta E_{trans}}{E_i} = \frac{4 m_i m_t}{(m_i + m_t)^2} \cos\chi. \tag{2.74}$$

Highest energy transfer is observed if incident and target particle have equal masses. In this case the angle χ' is always 90°. By varying the impact parameter, one can see, that the maximum scattering angle of the incident particle is $\theta_{\mathrm{i}} = 90°$.

2.3 Plasma boundaries and sheath formation

So far, plasmas have only been regarded as a uniform volume with no boundaries. However, when the plasma faces a wall, effects occur in both the plasma and on the surface of the walls. This chapter focusses on the changes in the plasma when it faces a wall with a distinct potential Φ_w. Similarly to the picture of the Debye shielding, a transition layer between bulk plasma and the boundary is present. This transition region is called a sheath and shall be examined under simplified conditions.

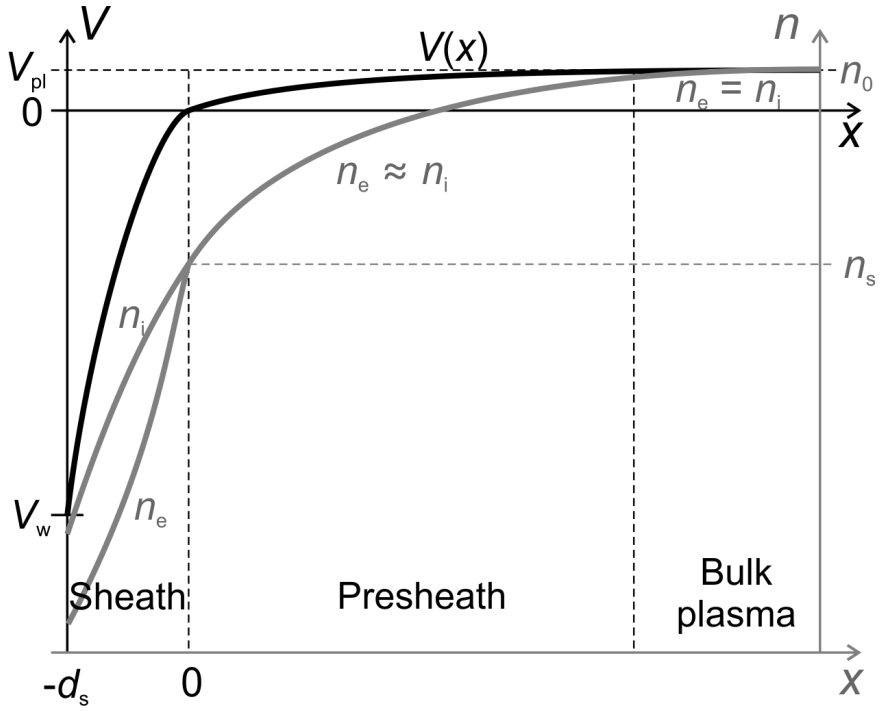

Figure 2.2: Electron density, ion density and potential distribution in front of a negatively biased wall, after [35].

In order to obtain analytical results, one has to make some assumptions:

- The transition region, the sheath, shall be collisionless, i.e. no ionisation or recombination due to particle collision occurs.
- The electron distribution function is Maxwellian and characterised by the temperature T_e.
- The ions are cold, i.e. $T_i = 0$.
- The electron and ion density in the plasma bulk are equal: $n_e = n_i = n_0$.
- The problem shall be reduced to one dimension x.
- The wall potential V_w is negative in respect to the plasma potential in the bulk V_{pl}: $V_w < V_{pl}$.

Figure 2.2 shows the transition from the bulk plasma to the wall for the electron and ion density $n_e(x)$ and $n_i(x)$, as well as for the potential $V(x)$. The edge of the sheath is defined to be $x = 0$, where the potential $V(0) = 0$ and the densities equal $n_e = n_i$. Similarly to the Debye shielding, Poisson equation 2.14 has to be solved. Due to the voltage V_w ions are accelerated towards the wall and the ion density can no longer be regarded as a constant. However, the flux of ions $\Gamma_i(x) = n_i(x)v_i(x)$ has to be constant, because no ions are created or lost while travelling through the sheath. Furthermore, energy is also conserved:

$$\frac{1}{2}m_i v_i^2(x) = \frac{1}{2}m_i v_s^2 - eV(x). \tag{2.75}$$

The ion velocity at the sheath edge is denoted as v_s and inserting equation 2.75 into flux conservation, one can calculate the ion density:

$$n_i(x) = n_{is}\left(1 - \frac{2eV(x)}{m_i v_s}\right)^{-1/2}, \tag{2.76}$$

with n_{is} being the ion density at the sheath edge $x = 0$. An Arrhenius equation can be applied to the electrons:

$$n_e(x) = n_{es}\exp\frac{eV(x)}{k_B T_e}, \tag{2.77}$$

with n_{es} being the electron density at $x = 0$. Poisson equation then reads:

$$\frac{d^2V}{dx^2} = \frac{en_s}{\varepsilon_0}\left[\exp\frac{eV}{k_B T_e} - \left(1 - \frac{2eV}{m_i v_s^2}\right)^{-1/2}\right]. \tag{2.78}$$

The quasineutrality at the sheath edge $n_{es} = n_{is} = n_s$ was used. When equation 2.78 is analysed, it can be found that it only has solutions for sufficient ion velocity at the sheath edge v_s. In particular, the ions have to break the sound barrier at the sheath edge:

$$v_s \geq v_b = \left(\frac{k_B T_e}{m_i}\right)^{-1/2}. \tag{2.79}$$

This criterion for sheath formation is called Bohm criterion and the speed v_b is called Bohm speed. To fulfil the Bohm criterion a potential drop between the bulk plasma and the sheath edge has to exist. This region is called the pre-sheath, in which quasineutrality holds $n_e = n_i$. Using energy conservation the potential drop can be calculated as $\Phi_0 = k_B T_e/2e$ and the plasma density is $n_s \approx 0.61 n_0$.

An important case are electrodes insulated from ground, so-called floating electrodes. Many holders of diagnostic devices or screening plates immersed into the plasma are kept floating, because this minimises the disturbance of the plasma, as no net current is drawn out of the plasma. Hence, the electron and the ion flux towards the electrode have to cancel out, $j_e = j_i$. Because the thermal electron current is significantly higher than the thermal ion current, the electrode is charged to a potential more negative than the plasma space potential. This potential is called floating potential V_{fl}. The electron and ion flux through the sheath are given by:

$$j_e = \frac{1}{4} e n_s \langle v_e \rangle \exp -\frac{e V_{fl}}{k_B T_e}, \tag{2.80}$$

$$j_i = e n_s v_b, \tag{2.81}$$

with $\langle v_e \rangle$ being the electron thermal speed. Solving $j_e = j_i$ for the potential V_{fl}, one can derive the difference between floating and plasma potential [41]:

$$V_{pl} - V_{fl} = \frac{k_B T_e}{2e} \ln \frac{m_i}{2.3 m_e}, \tag{2.82}$$

which is about $5.2 k_B T_e/e$ in the case of argon ions.

Many technological plasmas are electrically driven by high voltages, hence walls with very negative potentials immersed into a plasma are very common. When considering magnetron sputtering, the plasma in front of cathode which also acts as sputtering target is of interest. It has the negative voltage V_t, so $V_w = -V_t$. In this case, $eV_w >> k_B T_e$ and the simple Debye shielding cannot be applied. In a first approximation, one can assume the ion density to be constant in front of the negatively charged wall. The electron density

approaches zero close to the wall. In this special case, the potential distribution has the simple form:

$$V(x) = -\frac{en_s}{\varepsilon_0}\frac{x^2}{2}. \tag{2.83}$$

The sheath width s_m reads:

$$s_m = \left(\frac{2\varepsilon_0 V_t}{en_s}\right)^{-1/2}. \tag{2.84}$$

However, this solution is not consistent, because the ion density in front of the wall is constant, but the acceleration of the ions would lead to an ever increasing ion flux, which would require additional ionisation events to take place in the sheath. The sheath described by Child and Langmuir accounts for this effect and demands the ion current to the wall $j_i = en_i v_i$ to be constant within the sheath. The increase of the ion speed is given by the energy conversation, equation 2.75. The ion current is also given by the Bohm criterion $j_i = en_s v_b$. The self-consistent solution gives a potential distribution:

$$V(x) = -V_t\left(\frac{x}{s_{cl}}\right)^{4/3}, \tag{2.85}$$

with the sheath width

$$s_{cl} = \frac{\sqrt{2}}{3}\frac{\varepsilon_0}{e^2 n_s}\left(\frac{(2eV_t)^3}{k_B T_e}\right)^{1/4}. \tag{2.86}$$

It can now be seen, that a slight dependence on the electron temperature is introduced by fulfilling the ion current that is defined by the Bohm speed. Sheath widths are quite often given in multiples of Debye lengths calculated at the sheath edge λ_{ds}:

$$s_m = \lambda_{ds}\left(\frac{2eV_t}{k_B T_e}\right)^{1/2}, \tag{2.87}$$

$$s_{cl} = \frac{\sqrt{2}}{3}\lambda_{ds}\left(\frac{2eV_t}{k_B T_e}\right)^{3/4}. \tag{2.88}$$

Plasma interaction with its boundaries is still an ongoing topic of research, in particular when considering collisional sheaths or the influence of magnetic fields. A complete analysis is beyond the scope of this introduction and one should refer to textbooks, e. g. reference [35], or papers on sheath formation, for example [43–46].

2.4 Magnetron Sputtering

2.4.1 Basic principles

Energy is needed to create and sustain a plasma. In the stable state it has to compensate for particle loss due to recombination and diffusion by creating ions in a rate equal to the loss rate. This energy can be provided by heat, e.g. focused laser beams or in torches, by radiation, e.g. UV-radiation, and electrically by either applying electrostatic or electromagnetic (RF or microwave) fields. There are certainly more possibilities to provide the required energy, such as chemical or thermonuclear reactions. However, the aforementioned methods are the most commonly-used ones for technological plasmas, which excludes nuclear fusion.

A very simple experimental arrangement is applying a DC high voltage to two opposing electrodes with distance d which are placed in a gas under reduced pressure p, typically around 100 Pa. The breakdown voltage V_b of such an arrangement is given as:

$$V_b = \frac{Bpd}{\ln Apd - \ln\left(\ln\left(1+\gamma_{see}^{-1}\right)\right)}. \tag{2.89}$$

This is the well-known Paschen-law. Two processes of charged particle creation are considered. Firstly, the ionisation of gas atoms in the volume by electron impact is described by two gas-dependent constants A and B. Secondly, ions hitting the cathode can emit electrons. This process is characterised by the secondary electron emission coefficient γ_{see} which depends on the combination of impacting ion and target material. Once the plasma is initiated, the DC voltage, typically above 1 kV, creates a stable discharge, the so called glow discharge. The name is inspired by the characteristic spatially distributed glow phenomena, which are described in detail in most textbooks (e.g. references [14,35,47]). The most important feature for thin film deposition application lies in the cathode dark space, the sheath in front the high voltage electrode which hardly emits light and where most of the applied voltage drops. Hence, the electric field is strong and accelerates positive ions towards the cathode which then impinge with kinetic energies up to the applied voltage equivalent which is well above 1 keV. At such a high impact energy, particles can be knocked out of the cathode. This effect is known as sputtering[1] and is a rather complex momentum transfer process, which is usually described as a sequence of binary collisions between the incident ion and cathode atoms, as well as collisions between cathode atoms.

[1] Sometimes called physical sputtering to distinguish it from chemical sputtering

This can lead to a momentum reversal and one or more surface atoms with sufficient energy can leave the cathode, which is often called target. The efficiency of the sputtering process is quantified by the sputtering yield Y which is the number of particles ejected N_{ej} divided by the number of incident particles N_{inc}:

$$Y = \frac{N_{ej}}{N_{inc}}. \tag{2.90}$$

The sputtering yield strongly depends on the energy and the momentum of the impinging ion. Also the mass ratio of incident ion and the target particles is an important parameter, as it was shown in section 2.2 that most energy is transferred in the case of equal masses. The particle to be ejected from the cathode has to overcome a potential barrier, which is usually expressed by the sublimation energy. More parameters influence the sputtering yield, such as the angle of incidence, the crystal orientation or the smoothness of the surface. A comprehensive description, together with a summary of both experimental results as well as fitting formulae, can be found in reference [48] and will not be presented here. However, we shall give some rules of thumb: The sputtering yield increases with ion energies for energies up to approximately 10 keV, but this increase is less than linear. High sputtering yields can be expected, if the ion and the target atom mass are similar and for target materials with low sublimation energy. Particles ejected from the cathode are not mono-energetic but follow a distribution function $f_s(E)$ which was investigated by Thompson [49] and given in a simplified form by Serikov [50]:

$$f_s(E) = \begin{cases} 2\left(1+\frac{E_s}{\Lambda_e E_i}\right)\frac{E_s E}{(E_s+E)^3}, & E \leq \Lambda_e E_i \\ 0, & E > \Lambda_e E_i, \end{cases} \tag{2.91}$$

Here, the kinetic energy of the incident ion is denoted as E_i, E_s is the surface binding energy of the target material. The parameter Λ_e describes the energy transfer between incident ion and target atoms:

$$\Lambda_e = \frac{m_i m_t}{(m_i+m_t)^2} \tag{2.92}$$

and depends on the masses of the impinging ion m_i and the target atoms m_t. The distribution shows a maximum at half the surface binding energy and a tail towards high energies, which is an important feature of the sputtering process. The mean energy of particles created by sputtering is much higher than for an evaporation process. The angular distribution of sputtered particles is usually described by a cosine law:

$$f_s(E,\theta_s) = f_s(E)\cos\theta_s, \tag{2.93}$$

with θ_s being the angle of ejection in respect to the surface normal. However, a more detailed study by Matsuda et. al. revealed that the angular distribution depends on the energy of the incident ion [51]. For low energies an undercosine function, i.e. increased particle ejection to the sides, was found whereas the sputtered flux is ejected preferably perpendicular to the target surface when the impacting ions have high energies in the range of several keV.

In many cases the sputtering effect is undesirable, as it slowly consumes the cathode. However, the flux of ejected particles can also be used to deposit thin layers of the cathode material on surfaces of work pieces for example, and hence modify its properties. The sputtering rate, i.e. the number of sputtered particles per time, is determined by the ion current to the target, which itself depends on the sheath formed in front of the cathode. Diode sputtering systems are usually operated at pressures of about 10 Pa, with a high voltage $2-3$ kV applied to the cathode, which leads to a target current density in the order of 1 mAcm^{-2}. Deposition rates are typically several 10 nm min^{-1} [4, 5]. A big advantage that many materials, especially metals can readily be sputtered even if they have a high boiling temperature, e.g. tungsten or titanium. However, the downsides of the process significantly limited the use of diode sputtering in industrial applications. The consistently lower deposition rates compared to evaporation is the most striking disadvantage. Due to the high operation pressure a major part of the initially high energy originated from the sputtering process is lost by collisions with the working gas. In addition, almost the entire discharge current (electron current) is drawn by the substrate which also acts as anode. This causes significant substrate heating and hence limits the substrate materials to conductive and heat-resistant materials.

These disadvantages were overcome by applying a magnetic field perpendicular to the electric field, which was already experimented with by Penning [6]. However, the configuration, that is used in modern industrial deposition systems and is well-known as magnetron, was developed in the 1970's. Usually Chapin is credited for the invention of planar magnetron sputtering sources [52]. A schematic diagram of a planar magnetron in the side view is shown in figure 2.3. Permanent magnets are installed behind the cathode. Secondary electrons emitted by ions impinging at the target are accelerated in the sheath where most of the applied voltage, the target voltage V_t, drops. These electrons gyrate along the magnetic field lines and are reflected back into the discharge volume when they come close to the cathode again. At the same time, they perform a drift perpendicular to both the electric and the magnetic field, the $E \times B$-drift. As it was shown in section 2.2.1, several other drifts are usually present, such as the gradient and the curved B-drift as well as

the diamagnetic drift. The electrons can also diffuse across the magnetic field lines, which can classically be described by collisions with the background gas, but is more likely to be governed by Bohm-diffusion [53]. Highest electron densities and temperatures are usually found where the magnetic field is orientated parallel to the cathode [54]. This region is indicated in the figure by the slightly more intense red colour. Most ionisation events take place in this area and the created working gas ions, in most cases argon, are accelerated towards the cathode. The spatial inhomogeneous distribution of ionisation events manifests itself in a radial current density distribution at the target with its maximum where the magnetic field is parallel to the target [55], which leads to a strong target erosion in this area, the so called racetrack. Hence, target utilisation is limited to typically 30 %, as it has to be replaced when it is sputtered through at the thinnest point. Sophisticated engineering, such as carefully arranging the magnetic field to broaden the erosion zone [56], moving the permanent magnets behind the target [57] or rotating a tubular cathode around fixed permanent magnets [58], has led to a dramatic improvement of the target utilisation to up to 90 %.

Atoms that are sputtered from the target are transported towards the substrate where they condensate and form a coating. The transport can either be ballistic for low background pressure and few collisions or it can be dominated by diffusion in the case of frequent collisions. On their way to the substrate, target atoms can also become ionised by electron impact or Penning ionisation. Three main processes govern the film growth at the substrate. Firstly, particles are adsorbed from the gas phase. They can diffuse on the substrate surface and form crystal nuclei which grow to cover the whole substrate. Finally, particles can leave the surface by desorption. The growth process is significantly influenced by the energy and momentum flux from the plasma. The growth process itself is very complex, but simplified structure zone models were developed to help analyse the film growth, structure and properties [59–62]. However, these models can only give advice on how to optimise the deposition process and details have to be worked out for every particular case.

Adding the magnetic field to the diode sputtering arrangement has a number of benefits. Firstly, the electron path to the anode is significantly increased, which shifts the Paschen curve towards lower pressure and lower breakdown voltages [63]. Typically, the target voltage is in the range of a few 100 V and the pressure can be reduced to less than 1 Pa, which increases the mean free path of the sputtered particles, which are now transported ballistically and deposit a higher energy to the film which in turn increases the ad-atom mobility and enhances film growth. The target current density increases by one order of magnitude to several 10 $\mathrm{mA\,cm^{-2}}$ which leads to higher deposition rates of several

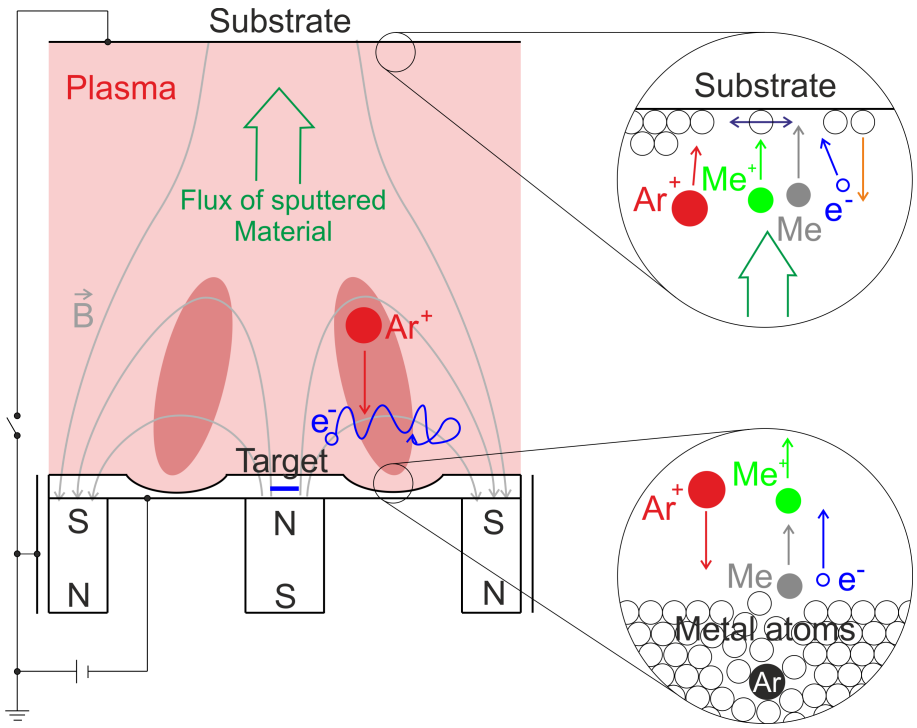

Figure 2.3: Schematic drawing of a planar magnetron sputtering source in the sideview.

100 nm min^{-1} [4]. It is worth noting that the substrate no longer serves as anode which reduces the heat flux caused by the electron current, significantly. This allows a wide range of insulating and heat-sensitive substrate materials, such as polymers, to be coated. Recent development focused on optimising the magnetic field configuration, which led to the introduction of unbalanced magnetrons [64], i.e. the magnetic flux of either the inner or the outer magnetic pole is increased and the magnetic field shows "open" field lines guiding the plasma towards the substrate. An unbalanced magnetron in the now commonly used "type II" arrangement is shown in figure 2.3: The magnetic field of the outer pole is stronger than the field of the inner pole. This increases the ion flux to the target and causes a densification of the growing film.

By introducing reactive gases, such as nitrogen, oxygen or methane, the application of magnetron sputtering could be increased further and allowed compound materials to be deposited with variable stoichiometry, near-bulk density and properties with high deposition rates. However, the introduction of a reactive gas often necessitates sophisticated process control as shown by Berg et. al. [65]. If the compound material is an insulator, problems arise from arcing, an uncontrolled and undesired transition from the abnormal

glow discharge to a vacuum arc, which can cause defects in the film due to macro particle formation typically observed for vacuum arcs. The problem was solved by applying pulsed target voltages as either AC, i.e. sinusoidal waveforms of a selected frequency, [10–12] or pulsed DC, where the negative half-cycle (sputtering process) shows a much more negative target potential than the reverse voltage in the positive half-cycle, [13]. In both cases a positive voltage is applied to eliminate surface charges and prevent the discharge from arcing. Applying a time-dependent target voltage leads to discharge properties which reveal transient effects and even time-averaged plasma properties can differ quite substantially from the continuous case. Further information on reactive sputtering and pulsed magnetron discharges can be found in reference [37].

In summary, magnetron sputtering is a very versatile tool in depositing a variety of coatings, ranging from electronic applications, such as electrodes and capacitors, as well as transparent, conductive coatings (TCO), to absorbers for solar cells, optical mirrors and hard and wear-resistant coatings for cutting and drilling tools. As, in fact, almost any material can be sputtered on almost any substrate, the possibilities for applications are far from fully utilised. The process described here can readily be scaled up allowing deposition processes developed on a laboratory frame to be transferred on to industrial size production. One disadvantage that remains is the generally low degree of ionisation of the sputtered flux which makes it difficult to coat structured or three-dimensional substrates. That is usually claimed to be a speciality for cathodic vacuum arc deposition [15]. Rossnagel and Hopwood used an additional RF discharge to ionise the sputtered flux to overcome this problem [66]. However, RF discharges are not so easily be scaled up to big substrates. An alternative route has therefore been suggested by Kouznetsov [16]: Increasing the power applied to the discharge by about two orders of magnitude to enhance ionisation of the sputtered flux, while reducing the discharge on-time accordingly to avoid damaging the target or the magnetron by overheating them. This technique is called High Power Impulse Magnetron Sputtering (HiPIMS) and will be presented in the next section.

2.4.2 Recent developments in High Power Impulse Magnetron Sputtering

High Power Impulse Magnetron Sputtering (HiPIMS) has recently attracted a lot of attention as it overcomes the generally low degree of ionisation in conventional DC magnetron sputtering. The paper published by Kouznetsov et. al., in which short but high power discharge pulses were used for filling high-aspect ratio trenches [16], is usually regarded

as the origin of the recent development in this field, which has up to date led to a number of review papers on both the underlying physics and the progress in thin film deposition [67–72]. This introduction will therefore only summarise some key developments of HiPIMS research which are discussed in much more detail in the publications cited or in the aforementioned review papers.

HiPIMS discharges are characterised by a low duty cycle $\delta = t_{on}/(t_{on} + t_{off})$, typically less than 10 % and a high instantanous discharge current and power. It is common practice to characterise the discharge by its peak discharge current and peak power normalised by the target surface area. Gudmundsson et. al. define a minimum peak power density of $0.5\,\mathrm{kW\,cm^{-2}}$ for HiPIMS in order to distinguish it from other pulsed magnetron sputtering techniques, such as pulsed DCMS [**?**,73] and Modulated Pulsed Power Magnetron Sputtering [74, 75]. The instantanous power applied to the discharge results in plasma properties well beyond conventional magnetron sputtering. The electron density, for example, was found to easily exceed $10^{18}\,\mathrm{m^{-3}}$ in the bulk of the plasma or even $10^{19}\,\mathrm{m^{-3}}$ in the magnetic trap in the vicinity of the target [76]. This high electron density causes a high degree of ionisation of the sputtered flux, ranging from a few percent for sputtering carbon to more than 90 % for titanium and copper [17, 77–80]. Measurements of the ion energy distribution functions (IEDF) revealed not only a substantial amount of ionised sputtered particles but also the ions to have much higher average energies than argon ions in conventional DCMS [81–83]. Some authors also report on multiply charged ions, however, usually under extreme conditions such as very high instantanous power or low pressure [84, 85]. The flux of ionised sputtered particles is generally considered to be largely beneficial to the film growth as the impinging ions can significantly increase the ad-atom mobility at the substrate and help grow films far away from thermal equilibrium [86, 87].

A number of standard plasma diagnostic techniques, such as Langmuir probes, emissive probes, time and energy-resolved mass spectrometers and optical diagnostics, have been employed to study the temporal development of HiPIMS discharges. The discharge pulse starts with apply a high voltage to the target. The discharge current builds up with a well-defined delay in respect to the target voltage, which is due to the time needed to create ionisation avalanches until full electrical breakdown is achieved [88]. The discharge ignition is also accompanied by strongly negative plasma potentials as well as high axial electric fields [89], which indicates a strongly-expanded sheath. Pajdarova et. al. and Poolcharuansin and Bradley report on two and three distinct electron populations [90, 91]. The majority of electrons with very low energy, electron temperature well below 1 eV, are thought to be remainders from the previous pulse, whereas the super-thermal electrons

with temperatures up to 100 eV originate from the rapidly-expanding sheath by a mechanism not unlike stochastic heating reported for RF discharges [92]. The group of hot electrons with an electron temperature of several eV is thought to be created by electrons originating from ionisation by the super-thermal or beam-like group as well as by secondary electron emission and subsequent energy gain in the cathode sheath after the onset of the sputtering process. Further progressing into the pulse, beam-like electrons cannot be detected anymore and the cold electron group is replaced by hot electrons accompanied by a steady decrease of their electron temperature to about $2-3$ eV. Another transient effect observed by several authors and by applying different diagnostic techniques, is the presence of an ion acoustic wave caused by the rapidly advancing sheath during pulse initialisation [93–95].

The ignition stage of the HiPIMS discharge is followed by a change of the gas composition in front of the target. Hoffman [96] and Rossnagel [97] reported on rarefaction of the working gas in front of the target during magnetron sputtering caused by momentum transfer between the highly-directed sputtered particles and the working gas atoms. This effect is particularly pronounced in HiPIMS due to the enormous discharge current and high sputtering rates associated. Several studies showed the expansion of the sputtered metal vapour into the chamber and the transition from working gas dominated sputtering into a self-sputtering regime [23, 78, 81–83, 95, 98–100]. The further development of the discharge strongly depends on two factors: The power supply and the target material. If the power supply is not capable of sustaining the high voltage at a high level, caused by either a too small capacitor bank or a large target surface area, the plasma will start decaying and transit back into a DC-like stage [95]. If the high voltage can be sustained, usually reported for small laboratory-size magnetrons, the development of the discharge (current) depends on the target material. It was pointed out by Anders et. al. that the sputtering yield changes as the working gas, usually argon, is replaced by the sputtered metal which becomes the dominant ion species impinging on the target [26, 101]. And, secondly, the secondary electron emission from the target, which is the feed of high-energetic electrons that sustain the discharge, strongly alters. In fact, most singly charged metal ions do not carry enough potential energy to cause secondary electron emission. Hence, sputtering most metals show an initial increase of the discharge current up to a maximum and a subsequent transition to a low current stable state which coincides with a conventional DC discharge of similar power [102]. However, if a large fraction of multiply charged ions can be produced, secondary electron emission can be sustained and furthermore, the discharge can be operated in a self-sustained sputtering mode without the presence of a working gas,

as observed for aluminium, silver and copper targets [26, 103]. Sputtering above the self-sputtering runaway shows no decrease of the discharge current but a rather high current plateau or even a continuously increasing discharge current.

In the afterglow a rapid cooling of the electrons and an at least two-fold exponential decay of the electron density extending up to several milliseconds after pulse termination was found [91]. This was confirmed by Hecimovic and Ehiasarian who detected ions of both the working gas and the sputtered metal even several milliseconds after the target voltage was switched off [83, 104]. The ultralong decay times in the millisecond range were attributed to the presence of long-living metastable states of argon [105]. The presence of metastable argon atoms has recently been confirmed by Vitelaru et. al. [100]. However, their influence on the temporal development in the afterglow is still not fully understood. Poucques et. al. showed that the decay of titanium neutrals and ions obeys simple (ambipolar) diffusion [106].

Using HiPIMS for depositing thin films revealed a number of advantages. The high degree of ionisation of the sputtered flux facilitates coating of three-dimensional substrates or filling trenches in semiconductor manufacturing [16,107]. It could also be demonstrated that one can improve film adhesion [17, 18], as well as hardness, wear and corrosion resistance and obtain lower friction coefficients [19, 20]. Better electrical properties were reported by Sittinger et. al. for depositing transparent conductive oxides [21], and by Sarakinos et. al. for the deposition of titanium oxide [108]. Another advantage is the low thermal flux on the substrate compared to pulsed DC magnetron sputtering as reported by West et. al. [109]. In particular, reactive deposition with HiPIMS appears to be a very promising approach because deposition rates higher than for DC magnetron sputtering could be achieved, which was attributed to a narrower hysteresis probably caused by gas rarefaction effects [108, 110]. However, for non-reactive HiPIMS deposition rates were usually found to be up to 70 % lower than in a comparable DCMS process [22]. This particular drawback has attracted somewhat the most interest of researchers, simply due to the fact that deposition rate is one of the key parameters for industrial size application.

A number of explanations have been given on the origin of the deposition rate loss, considering either the sputtering process or the transport of sputtered particles towards the substrate. Emmerlich et. al. pointed out that the sputtering yield increases with incident ion energy less than linear [111]. The higher target voltage in the case of HiPIMS would therefore naturally lead to lower sputtering rates than for a conventional DCMS discharge with the same average power. Alami et. al. argued that the average power is a rather unfortunate parameter for comparing deposition rates, because the higher voltages of HiP-

IMS discharges lead to lower average currents, and hence, lower sputtering rates, if the average power is kept the same as for DCMS [112]. Finally, the ion species sputtering the target has a significant effect, which was analysed by Anders, who found a decrease of the sputtering yield of about 10 % to 15 % when the working gas argon is replaced by ions of the sputtered material with the same incident energy [113]. However, the decrease of the sputtering yield alone cannot explain the sometimes dramatically reduced depostion rates. Thus, the transport of sputtered particles must play a key role. Due to the high electron density [76], sputtered particles are most likely be ionised in the vicinity of the target and can be attracted back to the target by the electric field in the extended magnetic pre-sheath [114]. Konstantinidis et. al. suggested that the low plasma conductivity might inhibit the transport of ionised sputtered particles [115]. Indeed, an additional RF-discharge placed between target and substrate resulted in a faster transport of ions to the substrate [116]. The magnetic field configuration was found to play a key role in the transport of sputtered metal ions. Bohlmark et. al. showed how to improve the deposition rate by guiding the ion flux using a magnetic field created by a coil [117]. Mishra et. al. showed the interdependance of magnetic field strength, plasma potential distribution and its effect on the deposition rate [89].

A phenomenological model was proposed by Christie [118]. This accounts for the influence of the ion species sputtering the target, either working gas or sputtered metal ions. Sputtered particles are then followed through the discharge volume on their way to the substrate. They can get ionised and some of these ions are attracted back to the target where they participate in the sputtering process. Metal ions which overcome the potential barrier towards the substrate have a certain probability to reach the substrate as they can still be scattered out of the discharge volume or got an initial direction from the sputtering process that makes them “miss” the substrate. Sputtered neutral particles can also “miss” the substrate due to scattering or their initial velocity. By varying the influence of the aforementioned processes, one can predict the degree of ionisation of the flux reaching the substrate. Vlcek and Burcalova improved the model and could also determine the return probability of ionised sputtered flux [119].

Lundin et. al. measured the sideway deposition and the energy distribution function of ions leaving the discharge tangentially [29], later confirmed by Poolcharuansin et. al. [30], which is thought to be caused by azimuthal instability waves in the high density region close to the target. This so-called “anomalous” transport was further investigated by measuring the time-varying electric fields in a HiPIMS discharge which gave further evidence on the presence of a two-stream instability, caused by the large relative speed

between drifting electrons and ions at near rest [1]. These instability waves are thought to also be responsible for electron diffusion faster than the semi empirical Bohm-diffusion [28]. More recently, three groups of researchers, Kozyrev et. al. [31], Anders et. al. [32] and Ehiasarian et. al. [33], independently discovered highly localised ionisation zones which move azimuthally over the racetrack area following the electron drift. This finding implies that the transport of particles is influenced by very localised phenomena and it is yet to be analysed if or how the time-averaged description of the particle transport can be used.

2.5 Thesis outline

In this thesis, optical 2d-imaging, emissive and Langmuir probe measurements, as well as Monte Carlo calculations were employed to further investigate the temporal and spatial development of the plasma in a HiPIMS discharge. In the first part, optical 2d-imaging in combination with Abel-inversion is used to give a qualitative overview over phenomena observed in HiPIMS discharges. This investigation covers both the whole on-time of the discharge pulse as well as the development in the afterglow. Using optical bandpass filters, each species, working gas atoms and ions and sputtered metal atoms and ions, can be observed. The non-invasive optical imaging makes use of an extremely sensitive camera which enables the observation of both very fast transient as well as low intensity effects.

In the second part of the thesis, the influence of different substrate and magnetic field configurations on the plasma potential. These results are accompanied by measurements of the electron temperature and density using a single Langmuir probe. The raw data is then fed into a Monte Carlo model in order to analyse the transport of test particles sputtered from the target on their way to the substrate. These calculations have the advantage of saving a significant amount of computational time which would be necessary to model the entire discharge self-consistently. It also allows for varying parameters, such as mean free paths and the azimuthal force caused by the two-stream instability, to investigate their influence independently.

3 Experimental setup

In this chapter, the equipment used in the experiments is summarised. It introduces the features of the vacuum chamber, the magnetron sputtering source and the power supplies used. Target voltage and discharge current are monitored and used for synchronising the plasma diagnostic measurements with the discharge pulse. The specific instruments used for each investigation, e. g. iCCD camera, spectrometer etc., are described in the respective chapters.

3.1 Vacuum chamber

All experiments were carried out in a cylindrical, stainless-steel vessel supplied by *GENCOA Ltd.* with an inner diameter of 388 mm and a length of 600 mm, figure 3.1, which was pumped by a combination of rotary pump, *EDWARDS E2M40* (pumping speed 37 m^3h^{-1}), and turbomolecular pump, *LEYBOLD Vacuum Turbovac 1000* (pumping speed 1150 ls^{-1}). Two pressure gauges installed at position 1, a *BOC Edwards APG100 Active Pirani Gauge* and a *BOC Edwards Active Inverted Magnetron Gauge*, were used to monitor the pressure during pumping to a base pressure in the 10^{-4} Pa range, before pre-conditioning of the chamber was started. The working gas argon was introduced by a mass flow controller *MKS Type 1179A Mass-Flo® Controller* with a full scale of 50 sccm, standard cubic centimetre per minute. The flow rate was set to 30 sccm with an accuracy of ± 1.4 sccm [120]. Adjusting the position of the baffle allowed for adjusting the pumping speed and hence the operating pressure. The working gas pressures, which lay between 0.27 Pa and 1.33 Pa, was measured by a capacitance manometer *MKS Baratron® Type 627* with an accuracy of 0.15 % of the measured value [121].

The *V-Tech™ 150* (*GENCOA Ltd.*) magnetron sputtering source was installed on one of the end flanges as shown in the schematic drawing, figure 3.1. The other end of the chamber could be equipped with either a substrate, an aluminium disc of 200 mm, or was rarely used to insert Langmuir or emissive probes. With the substrate in place the probes were inserted through a DN 250 flange on the side of the vacuum chamber, opposite to

the turbomolecular pump, or occasionally from the top of the chamber. A 400 mm long, cylindrical extension could be installed at this DN 250 flange instead of the custom-made flange carrying feedthroughs for the probes. This extension increases the distance between its end flange and the magnetron discharge, which is useful for optical 2d-imaging, as it reduces the deposition of non-transparent coatings on the glass window installed at the end of the extension. Both the magnetron as well as the substrate can be moved in respect to each other, so varying the distance between magnetron and substrate. However, in most experiments this distance was kept constant at 10 cm and both devices were moved together in order to change the axial position of the probe or to adjust the visible region for optical imaging.

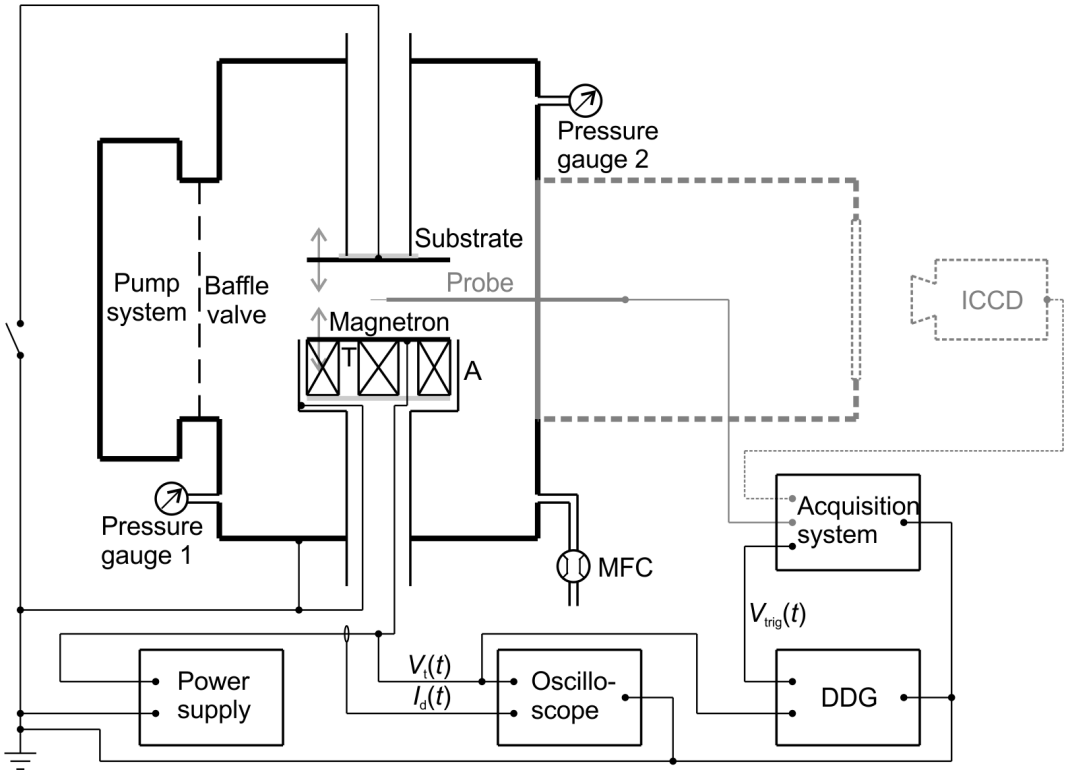

Figure 3.1: Schematic drawing of the experimental setup. The magnetron source was equipped with a 150 mm diameter target (T). The anode cup (A) was kept grounded during all experiments. The working gas argon was introduced through a mass flow controller (MFC) and the pressure monitored by gauges installed at position 1, Pirani and Inverted Magnetron gauge, and position 2, *Baratron®* gauge.

Three power supplies were used for experiments, two of which are HiPIMS power supplies described in section 3.3 and one Pinnacle Plus manufactured by Advanced Energy. The Pinnacle Plus power supply was used to pre-condition the target and vacuum chamber in order to remove contamination such as water vapour. It was operated in DC mode ($P = 200$ W) prior to each HiPIMS experiment for about 10 min.

The target voltage and the discharge current were recorded by a TDS3014 digital phosphor oscilloscope with a 100:1 high voltage P5100 and a TCP202 current probe in combination with a CT4 high transformer connected to it (all manufactured by Tektronix). The accuracy and the temporal resolution of the voltage and the current reading are determined by the combination of the devices used, e. g. high voltage probe and oscilloscope or current probe and transformer and oscilloscope. The accuracy of the target voltage is ± 3.75 % and the accuracy of the discharge current is ± 9 % [122–125]. The temporal resolution, determined by the rise-time of the measured signal, are 5 ns and 28 ns for the voltage and the current measurement, respectively. Most waveforms were recorded using a setting of 20 µs/div, which gave a temporal resolution of 20 ns per digit. Hence, the rise-time of the voltage measurement cannot be recorded in this setting and also the risetime of the current measurement only shifts the measured value by 1 digit, which is negligible in most cases.

Time-resolved measurements need synchronising the actual measurement with the discharge pulse. For this purpose, the target voltage was picked up by a 100:1 buffer probe, built in-house with a voltage rise-time experimentally found comparable to the high voltage probe P5100, and fed into a digital delay generator DG645 manufactured by Stanford Research Systems. The delay generator produces a TTL signal with variable width and delay in respect to the input signal. The TTL signal is then used to trigger the start and the end of the measurement, e. g. with the iCCD camera. The accuracy of the output of the delay generator is 1 ns plus an additional 2 ns rise-time of the TTL flank [126]. The minimum delay time, determined by the accumulated delay of the probes, cables and the generator's internal processing was experimentally measured to be about 100 ns. This was accounted for when setting the delay of the output trigger. For example, a measurement 1 µs after pulse initialisation required the delay time to be set to 900 ns.

3.2 The magnetron sputtering source

The *V-tech™ 150* magnetron is an unbalanced, planar magnetron sputtering source with a cylindrical cross section. It consists of four major parts which are displayed in the

schematic drawing, figure 3.2: A target, permanent magnets arranged in a ring, an anode cup (AC) and a water-cooling system to prevent the sputtering source from overheating. The cylindrical target, diameter 150 mm, thickness 6.3 mm, was clamped onto the water-cooling system by a stainless steel ring (CR), which protrudes the target by about 5 mm. The grounded aluminium ring mounted flush with the clamp ring around the magnetron serves as anode (AC), because it provides the shortest route to ground for electrons scattered out of the confined region in front of the target.

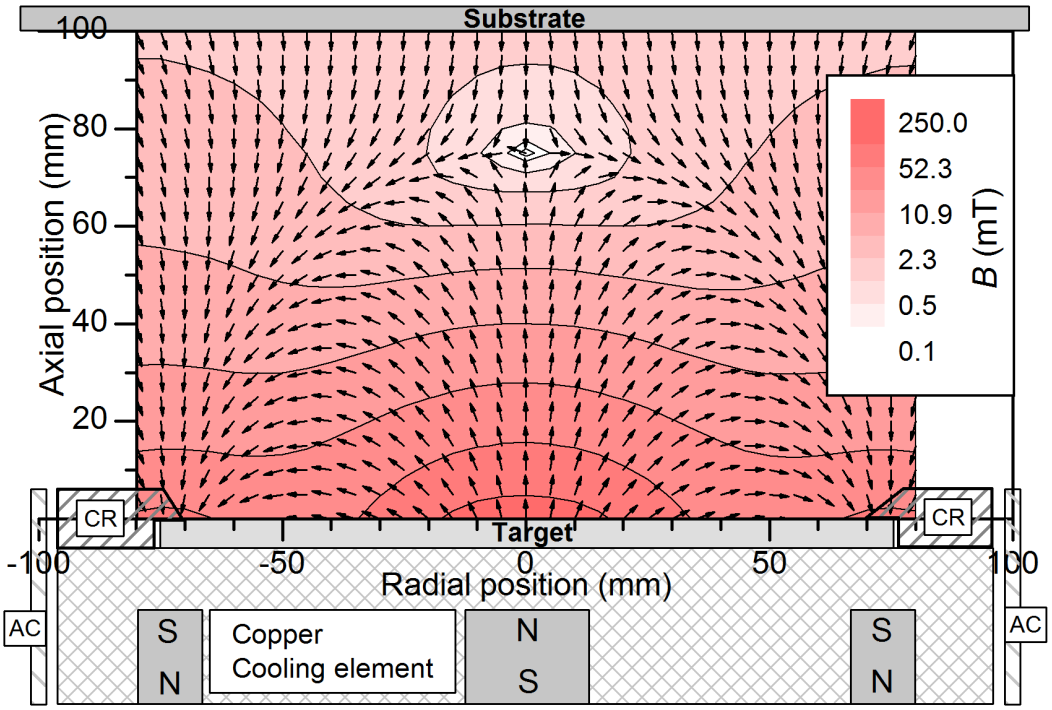

Figure 3.2: Magnetic field of the magnetron in its standard configuration. The axial distance is counted from the target surface and the radial position from the discharge axis, i. e. the axis of symmetry. The target is held in place by a clamp ring (CR). The grounded ring around the magnetron serves as anode (AC).

The magnetic field is produced by permanent ring magnets placed behind the target. It was measured with a hall probe Hirst GM04 with an accuracy of 1 % [127] with a spatial grid of $\Delta = 5$ mm. For this measurement, the clamp ring, the target and a part of the copper cooling element were removed to access positions close to and below the target surface. The absolute value and the direction of this vacuum field measured in a plane perpendicular to the target surface and containing the discharge axis are also shown in

figure 3.2. One can see that the magnetic field is strongest close to the target and decreases with increasing distance from it. The magnetic field is symmetric and forms closed loops in front of the target which confine the electrons and increases the ionisation rate in this region. However, there are quite a few magnetic field lines which do not close in front of the target but extend up to the substrate. This is the so called type II configuration of an unbalanced magnetron [64]. A distinct property of this configuration is a position within the volume where the magnetic field vanishes. This position is called magnetic null and can be found at the discharge axis 75 mm above the target. In order to quantify the balance or unbalance of magnetrons, Powell suggested the use of the parameter G which is defined as the ratio of axial position of the magnetic null z_0 and the target radius R_t [128]:

$$G = \frac{z_0}{R_t}. \tag{3.1}$$

For the setup shown in 3.2 one obtains $G = 1.0$ ($z_0 = 75$ mm, $R_\mathrm{t} = 75$ mm), which would classify the magnetron to be "very unbalanced", the second most unbalanced configuration described in reference [128]. It is worth mentioning, that one can move both the inner and the outer permanent magnet individually by a maximum of 15 mm in respect to the target, hence, the magnetic field can be altered and the parameter G be varied between 1.2 and 0.8 from "very unbalanced" to "extremely unbalanced". The measurements shown in figure 3.2 were made with both magnets placed as close to the target as possible. This configuration shall be called "standard configuration" and is used for all measurements unless explicitly stated otherwise, e. g. all experiments with optical 2d-imaging were carried out in the standard configuration. The total magnetic field measured by the probe is the superimposition of the field of the inner magnet and the outer magnet, in both radial and axial direction. A second magnetic field configuration, named configuration II, with the outer magnet pulled away from the target by 5 mm, which coincides with the spatial grid $\Delta = 5$ mm, was examined and all the measured values stored in a matrix, individually for the radial and the axial component. Each component of the magnetic field can be expressed as the sum of the magnetic field components of the inner and the outer magnet B_i^{in} and B_i^{out}, respectively:

$$\begin{aligned} B_i^I &= B_i^{in} + B_i^{out}, \\ B_i^{II} &= B_i^{in} + B_{i+1}^{out}, \\ i &= 1 \ldots 25, \end{aligned} \tag{3.2}$$

with B_i^I and B_i^{II} being the resulting magnetic field components of the standard, superscript I, and the second configuration, superscript II. This equation accounts for the fact that the

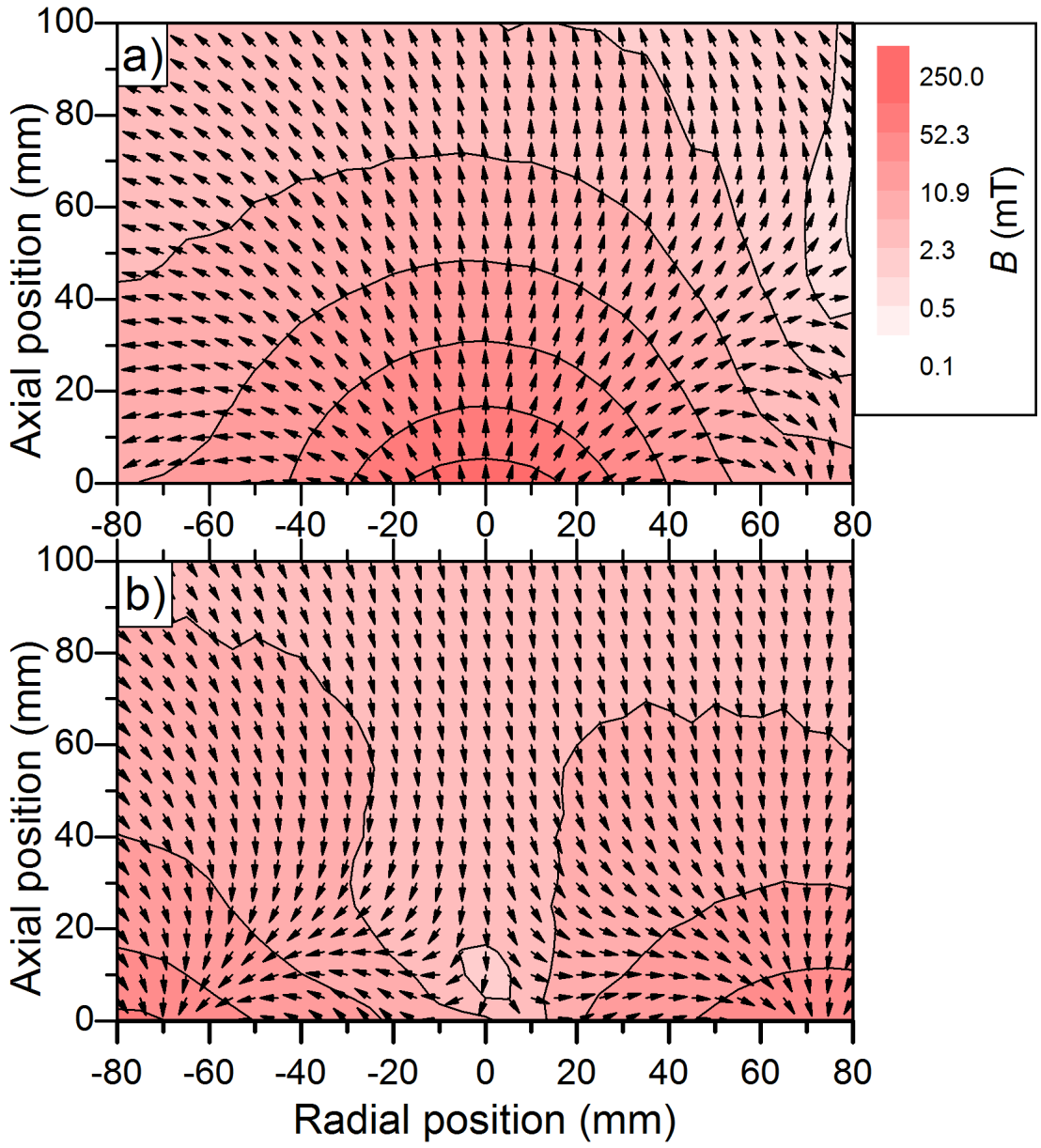

Figure 3.3: Calculated magnetic induction of a) the inner magnet and b) the outer ring magnet.

outer magnet is moved by 5 mm or one step in configuration II. This system of equations is under-determined and one has to make an assumption on the behaviour of the magnetic field component of the outer magnet, which changes very little far away from the target: $B_{26}^{out} = \beta B_{25}^{out}$, with $\beta < 1$. The radial and axial component of the magnetic field of the inner and the outer magnet can be calculated as:

$$\begin{aligned} B_{25}^{out} &= \frac{B_{25}^{I} - B_{25}^{II}}{1-\beta}, \\ B_{i}^{out} &= B_{i}^{I} - B_{i}^{II} + B_{i+1}^{out}, \\ B_{i}^{in} &= B_{i}^{I} - B_{i}^{out}. \end{aligned} \tag{3.3}$$

The magnetic field of both the inner and the outer magnet calculated for $\beta = 0.95$ are displayed in figure 3.3. One can see that the symmetry is slightly disturbed, but that might be caused by relatively large errors in the magnetic field measurements far away from the target. However, it still shows quite clearly the influence of both magnets. For example, the magnetic induction right above the racetrack is caused by the inner and the outer magnet in equal parts.

3.3 HiPIMS power supplies

The biggest difference between HiPIMS and conventional DCMS lies in the power supply. The power is delivered in pulses of length t_{on} and a repetition frequency f. One defines the ratio of the pulse "on"-time to the overall repetition period $1/f$ as duty cycle δ:

$$\delta = t_{on} f. \tag{3.4}$$

As the power delivered to the plasma is often "quenched" into only 1 % duty cycle, one needs a power supply that can store the energy and release it in a short intervall. Even though commercial power supplies are fairly sophisticated devices, the principle of operation is rather simple. The basic setup consists of three major parts: A large capacitor to store the energy, a charging circuit to replenish the capacitor in the discharge "off"-time and a fast high current switch, usually a big MOSFET or IGBT is used. Two different HiPIMS power supplies, a Sinex 3.0 manufactured by Chemfilt Ionsputtering and a power supply built in-house [129, 130], were used for the experiments in this study, with their characteristics summarised in table 3.1. There are two striking differences between the power supplies. The Sinex 3.0 has a rather small capacitor of only 26.8 µF and an inductance L on its output, which limits the rise of the discharge current, if this is not already

done by the plasma impedance. On the other hand, the home-made supply offers a much larger capacity of 640 µF and a limiting resistor $R_{\text{limit}} = 1\ \Omega$ on its output, which limits the current and not the current rise as the Sinex.

Parameter	**Sinex 3.0**	**Home-made power supply**
Average power	max. 10 kW	max. 1.0 kW
Output voltage	max. 2.0 kV	max. 1.2 kV
Output current	max. 3.0 kA	max. 1.5 kA
Frequency	25…600 Hz	20…1000 Hz
Pulse width	20…200 µs	10…500 µs
Capacitor	26.8 µF	640 µF

Table 3.1: Specifications of the HiPIMS power supplies [129, 130].

The discharge can be described by external electrical parameters, such as the target voltage V_t, the discharge current I_d and the average power P_{ave}. The temporal development of the target voltage and the discharge current can directly be recorded using an oscilloscope as described in section 3.1. The instantaneous power delivered to the plasma can be calculated by:

$$P_{in}(t) = V_t(t) I_d(t), \tag{3.5}$$

which can often be done in real-time by the oscilloscopes. HiPIMS discharges are commonly described by the peak power and peak current density, which are the instantaneous peak power and the discharge peak current divided by the target area, 177 cm^2 for the 6 inch magnetron used here. The energy dissipated per pulse E_{pulse} can be obtained by integrating the instantaneous power over the duration of the pulse:

$$E_{pulse} = \int_{pulse} V_t(t) I_d(t) dt, \tag{3.6}$$

which gives the average power when it is multiplied by the repetition frequency:

$$P_{ave} = E_{pulse} f. \tag{3.7}$$

Figure 3.4 shows the temporal development of the target voltage and the discharge current for sputtering a titanium target for both power supplies ($P_{\text{ave}} = 700$ W, $t_{\text{on}} = 100$ µs, $f = 100$ Hz, $p_{\text{Ar}} = 0.53$ Pa and a floating substrate 10 cm above the target). The discharge pulse is initiated by applying a high voltage (about -700 V) to the target, with a rise-

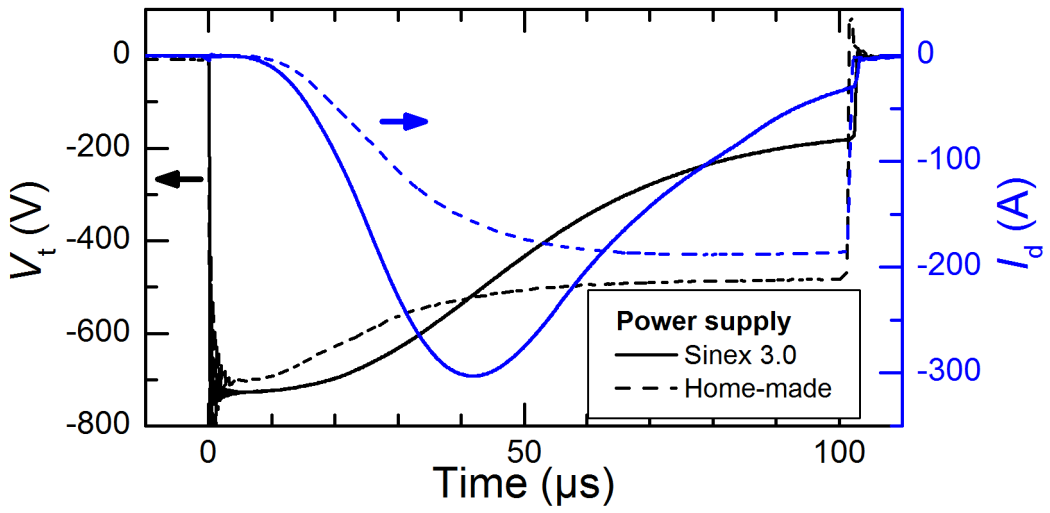

Figure 3.4: Example of target voltage and discharge current waveform of a HiPIMS discharge driven by either a Sinex 3.0 or a home-made power supply. Discharge parameters: $P_{ave} = 700$ W, $t_{on} = 100$ µs, $f = 100$ Hz, $p_{Ar} = 0.53$ Pa, floating substrate 10 cm above the target

time of 200 ns for both supplies. The discharge current starts with a distinct delay after the target voltage was ramped up, the origin of which was found to strongly depend on the target material and applied voltage [88]. As these conditions are the same, except for a difference of about 25 V in the applied voltage, the delay time is almost the same for both devices, 4 µs for the Sinex and 6 µs for the home-made power supply. The further development of the target voltage and the discharge current reflect, the different setups of both devices. For the Sinex, the discharge current quickly increases to a peak of about 300 A 40 µs after pulse initialisation. However, the target voltage already dropped by 25 %, which is due to the small capacitor (26.8 µF). The initial charge 19.5 mC (charging voltage 725 V) decreased by 4.8 mC, obtained from integrating the discharge current up to 40 µs. The discharge current and the target voltage decrease until the pulse is terminated, because the power supply cannot sustain the high voltage level and the discharge develops into a DC-like regime [102]. The home-made power supply starts with almost the same target voltage, which decreases more quickly when the discharge current increases. In this case, the charge lost by the capacitor is negligible (2.3 mC in the first 40 µs) compared to the total charge of 448 mC (640 µF charge with 700 V). Hence, the voltage drop is not caused by the capacitor but by the limiting resistor $R_{limit} = 1\ \Omega$ at the output. This resistor

stabilises the discharge current which slowly increases to 190 A in the second half of the pulse. The faster rise of the discharge current when using the Sinex power supply during the first half of the pulse may occur for two main reasons. Firstly, the magnetic field strength in the racetrack area was probably higher when operating with the Sinex power supply as an old target with a pronounced racetrack was used. The higher magnetic field, 45 mT for a 5 mm deep racetrack compared to 40 mT for no racetrack, confines electrons better because the gyroradius, diffusion and mobility are reduced. This leads to a lower plasma impedance and thus to a higher discharge current at the same applied target voltage. A second difference can be found in the setup of both power supplies. The discharge current causes a voltage drop across limiting resistor of the home-made supply and due transients in the discharge current across the inductance of the Sinex. Observing the target voltage during the first 30 µs in figure 3.4, one can conclude that the target voltage drops more for the home-made power supply. This implies that the limiting impedance is lower for the Sinex than the output resistance of the home-made power supply. The higher target voltage during the initial stage of the discharge allows for higher currents as electrons emitted by the cathode gain higher kinetic energy and subsequently ionise more working gas or sputtered particles, which in turn reduces the plasma impedance.

In summary, both power supplies are capable of creating HiPIMS discharges. The main difference lies in the configuration of the power supply. The Sinex 3.0 is capable of producing a much higher peak power and peak current density, $0.93\,\mathrm{kW\,cm^{-2}}$ and $1.70\,\mathrm{A\,cm^{-2}}$, but at the expense of sustaining these levels for a long time. On the other hand, the home-made power supply delivers somewhat lower peak power and peak current densities, $0.52\,\mathrm{kW\,cm^{-2}}$ and $1.06\,\mathrm{A\,cm^{-2}}$, but it has the advantage of sustaining these levels for a longer time. The instantaneous power does not change by more than 5 % during the second half of the discharge pulse until its termination. One should mention that in both cases the power supply is the limiting factor and not the discharge, which was intensively studied by Anders et. al. [26].

4 Optical 2d-imaging

In optical 2d-imaging the plasma is recorded in snapshots somewhat similar to ordinary photos. By employing optical bandpass filters, one can select light emitted by only one species, which can be investigated both spatially and temporally. If the plasma has cylindrical symmetry one can employ Abel inversion and obtains three-dimensional intensity distributions. This technique has already been applied to pulsed-DC magnetron sputtering by Bradley et. al. [131] and more recently in HiPIMS [132, 133].

4.1 Theoretical background

4.1.1 Corona modell

One property of plasmas is their characteristic glow, called plasma-induced emission (PIE). Atoms, ions and molecules can be excited and relax by emitting photons of a characteristic wavelength. Optical emission spectroscopy utilises this light to study plasma properties. The observed wavelengths typically range between 200 nm and 1000 nm, which covers the entire visible light plus a small part of UV and IR radiation. A basic experimental setup consists of a spectrometer which diffracts the light coupled into it and a detector that measures the intensity. One obtains two quantities; the wavelength and the intensity of the light. The wavelength λ_{21} is determined by the energy difference between the excited $|2\rangle$ and the final state $|1\rangle$ of the electron transition

$$\Delta E_{21} = E_2 - E_1 = hc/\lambda_{21}, \tag{4.1}$$

with h being the Planck constant and c is the speed of light. The energy levels and their difference are characteristic for each species and so is the wavelength. This already gives information on species present in the plasma. Further information is obtained when also the intensity is taken into account. The use of the term intensity is somewhat misleading here, because it does not correspond to the definitions widely used in photometry (power per solid angle). We will understand intensity as the detected counts at the charge couple

device (CCD) normalised by the exposure time. The light emission of the plasma shall be quantified by the line emission coefficient $\varepsilon(\lambda_{21})$ [134]:

$$\varepsilon(\lambda_{21}) = n_2 A_{21} \frac{hc}{4\pi\lambda_{21}}, \tag{4.2}$$

with n_2 being the density of particles in the excited state and A_{21} is the Einstein coefficient for spontaneous emission. One can see, that the measured intensity provides information on the density of the particles in the excited state. This can be quite useful to study emission processes of atoms and molecules, but is not necessarily desired in our case. We want to obtain information on electron density and temperature, as well as on the density of particles in the ground state. Hence, a model is needed to correlate the density of particles in the excited state to the aforementioned desired quantities. Four cases are usually discussed in the literature, e.g. Hutchinson [36]. Firstly, the plasma can be in full thermal equilibrium. All excited states of atoms and ions obey the Boltzmann distribution determined by the plasma temperature $T = T_e = T_i$. The radiation processes, emission and absorption, are also in equilibrium. The observed spectrum is then a continuum and the line emission coefficient $\varepsilon(\lambda, T)$ is that of a black body:

$$\varepsilon(\lambda, T) = \frac{2\pi hc^2}{\lambda^5} \frac{1}{\exp\frac{hc}{\lambda k_B T} - 1}. \tag{4.3}$$

Full thermal equilibrium requires a thermal plasma as it exists inside the sun. The second model still assumes a Boltzmann distribution of all atomic and ionic states but drops the condition of radiative equilibrium. This case is known as Local Thermal Equilibrium (LTE). The spectrum shows lines characteristic for the particles involved. The ratio between the densities of particles in the ground state $|0\rangle$ and in the excited state $|2\rangle$ is given by the Saha equation [36]:

$$\frac{n_e n_2}{n_0} = \frac{g_2}{g_0} \left[\frac{2m_e^3}{h^3} \left(\frac{2\pi k_B T}{m} \right)^{3/2} \right] \exp -\frac{E_{02}}{k_B T}. \tag{4.4}$$

The constants g_0 and g_2 are the statistical weights of the ground and the excited state, respectively. McWhirter published a criterion on when LTE can be applied [135]:

$$n_e >> 10^{19} T^{1/2} E_{02}^3 m^{-3}, \tag{4.5}$$

with the temperature T and the energy difference E_{02} given in eV. For the plasma conditions encountered in the experiments, $n_\mathrm{e} \approx 10^{19}\ \mathrm{m}^{-3}$ and $k_\mathrm{B} T_\mathrm{e} \approx 3$ eV, the energy difference of the atomic or ionic levels must be much less than 1 eV. As this is not the case, LTE cannot be applied.

A model that will be applied in this study is the Corona model, which is widely used for optically thin, i.e. no absorption of emitted light, low temperature plasmas. It makes two crucial assumption on the excitation and the relaxation of the excited state $|2\rangle$. These are shown in figure 4.1. The excited state shall only be created by inelastic electron collision out of the ground state with density n_0. One can write the rate equation:

$$\left.\frac{dn_2}{dt}\right|_{exc} = n_0 n_e k_{02}(T_e). \tag{4.6}$$

This means, that the change of the density of particles in the excited state is proportional to the density of particles in the ground state n_0, the electron density n_e and the rate coefficient k_{02}. The rate coefficient describes how efficient the electron collisions with the ground state particle are. It depends on the electron temperature, if the electrons are Maxwellian, and the cross-section σ_{02} of the collision process. The rate coefficient can be calculated as described by equations 2.63. The relaxation of the excited state into level n_1 shall only be due to spontaneous emission of a photon. Hence, it is described by the Einstein coefficient A_{21}. The rate equation reads:

$$\left.\frac{dn_2}{dt}\right|_{rad} = -n_2 \sum_k A_{2k}. \tag{4.7}$$

The sum over several Einstein coefficients is used to express the fact, that usually more than one way of relaxation is possible, i.e. particles in the same excited state can emit light of different wavelengths. In equilibrium both the excitation and the relaxation rate have to be equal and one can write for the line emission coefficient:

$$\varepsilon(\lambda_{21}) = \frac{hc}{4\pi\lambda_{21}} n_g n_e k_{02}(T_e)\tau_{21}, \tag{4.8}$$

with the branching ratio

$$\tau_{21} = \frac{A_{21}}{\sum_k A_{2k}}. \tag{4.9}$$

The intensity measured by the detector $I(\lambda_{21})$ is related to the emitted intensity $\varepsilon(\lambda_{21})$ by

$$I(\lambda_{21}) = CS(\lambda_{21})\varepsilon(\lambda_{21}). \tag{4.10}$$

The parameters C and $S(\lambda_{21})$ characterise the entire detection system from extraction of the light out of the plasma till the detector. $S(\lambda_{21})$ is the spectral sensitivity and C includes the solid angle of observation, losses due to scattering or absorption in optical fibres, for example. Both parameters can be obtained experimentally by observing spectra of known

spectral (and spatial) intensity distribution. The Corona model can be extended by adding rate coefficients for additional processes that occur at the same time. These processes can be excitation out of metastable states, electron deexcitation or diffusion of the excited particle in or out of the detection volume. In addition, the excited state itself can be a lower state for transition from a level above the excited state considered. Such a process is called excitation via cascades. The rate equations will have to be extended by these processes and the set of differential equations can be solved for particle densities and electron temperature. This more sophisticated model is called Collision-Radiation model (CRM).

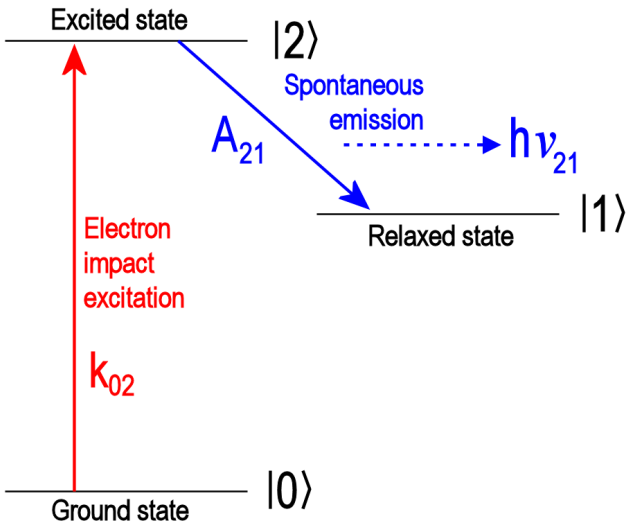

Figure 4.1: Corona model: Excitation by electron impact and relaxation by spontaneous emission.

The two quantities wavelength and intensity measured by optical emission spectroscopy can be used for a variety of applications. The wavelength alone can be used to identify spectral lines and, hence, species present in the plasma. That is particularly useful when organic compounds, such as CH_4, are used as precursors for plasma-enhanced chemical reactions [136]. The temporal development of the intensity can be used for endpoint detection of etching processes [137], for example. In reactive magnetron sputtering optical signals are routinely employed to monitor the deposition process enabling engineers to deposit coatings at high rates and with long time stability of the stoichiometry [138].

More sophisticated techniques use line ratios of two or more spectral lines with wavelength λ_1 and λ_2. In this case, the electron density and the parameter C cancel out, while

the particle densities and rate coefficients remain unknown:

$$\frac{I(\lambda_1)}{I(\lambda_2)} = \frac{n_{01}}{n_{02}} \frac{k_1(T_e)}{k_2(T_e)}. \tag{4.11}$$

The (ratio of) particle densities can be obtained when observing lines that have the same dependence of rate coefficients on the electron temperature, i.e. $k_1(T_e)/k_2(T_e) = const.$ [139–141]. The electron temperature can be calculated from the rate coefficients, if the density ratio n_{01}/n_{02} is known [142, 143]. It should be mentioned, that the electron density cannot be calculated by investigating line ratios. For this purpose, the detection system needs an absolute calibration, i.e. C and $S(\lambda)$ are known, so that the electron density can be calculated from the line emission coefficient according to equation 4.8.

More examples and a more detailed description of applications of optical diagnostics can be found in the literature, e.g. references [14, 35, 36, 135]. These include absorption spectroscopy, as well as laser-assisted techniques, such as laser-induced fluorescence (LIF), Rayleigh, Thompson and Raman scattering.

4.1.2 Abel inversion

Optical emission spectroscopy is a simple to use diagnostic tool, which can quickly provide useful information even with low budget equipment. Using Echelle spectrometers even Doppler broadening becomes applicable to obtain the particle speeds and very fast detectors, such as intensified charge couple devices (iCCD), with a temporal resolution of less than 100 ns makes OES a versatile tool for plasma diagnostics. However, the spatial resolution is somewhat limited by the fact that the measured intensity is integrated over the path along the line of sight. Hence, spatial variation of the emitted intensity along the line of sight is lost.

A way to recover the lost information is to use Abel inversion if the plasma has cylinder symmetry. A schematic drawing of a cylindrically symmetric discharge of radius R is shown in figure 4.2. The intensity detected at a position x_0 is given by integrating the locally emitted intensity $i(x,y)$ along the line of sight:

$$I(x_0) = \int_{-y_0}^{y_0} i(x,y)dy, \tag{4.12}$$

Using the symmetry of the discharge $i(x,y) = i(r)$, the measured intensity reads:

$$I(x_0) = 2\int_{x_0}^{R} \frac{i(r)r}{\sqrt{r^2 - x_0^2}}\mathrm{d}r, \quad 0 \le x_0 \le r \le R, \tag{4.13}$$

with r being the radial coordinate. In the experiments the emitted intensity $I(x_0)$ is measured and the local emittance $i(r)$ is unknown but wanted. Abel's theory shows that the locally emitted intensity can be recalculated as follows [144]:

$$i(r) = -\frac{1}{\pi r}\frac{\mathrm{d}}{\mathrm{d}r}\int_{r}^{R} \frac{I(x)x}{\sqrt{x^2 - r^2}}dx, \quad \text{or} \tag{4.14}$$

$$i(r) = -\frac{1}{\pi}\int_{r}^{R} \frac{I'(x)x}{\sqrt{x^2 - r^2}}dx. \tag{4.15}$$

The programme used for Abel inversion is based on the algorithm suggested by Gueron

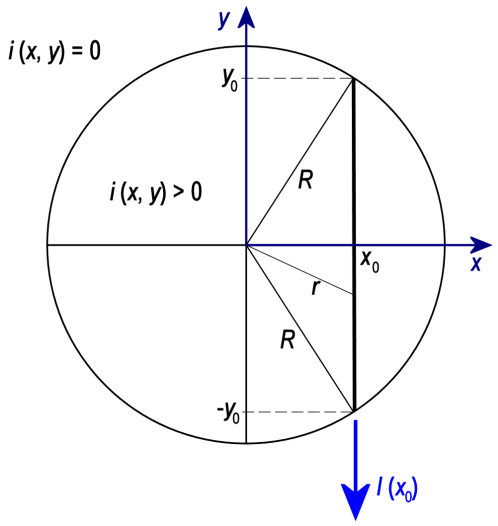

Figure 4.2: Principle of Abel inversion: Light emission of a cross section of a circular magnetron discharge [144].

and Deutsch [145] and was written by **Dr Paul Bryant**. It makes use of a local linear smoothing algorithm before inverting the data.

A number of conditions must be fulfilled to apply Abel inversion and relate the measured data to plasma parameters, such as electron density and temperature (after [146]):

- The emission profile must obey radial symmetry and in particular, the images recorded must be symmetric around the discharge axis.
- The light detected must be parallel.
- Enough data points need to be recorded to enable recalculation.
- The plasma must be optically thin, i. e. no absorption of light on its way to the detector.
- The lifetime of the excited state must be reasonably short to avoid electron impact deexcitation, quenching and prevent the particle from moving away from the place of excitation.
- No reflection of light from chamber walls or any other source.

4.2 Experimental setup

4.2.1 Characterisation of setup

A schematic drawing of the experimental setup is presented in figure 3.1. The HiPIMS discharge was observed through a window made of Kodial 7056 glass using a TV lens Canon V6x16 mounted to an iCCD DH520 manufactured by Andor Ltd. The distance between the lens and the discharge axis was $d_{\text{opt}} = 87$ cm. The detectable wavelength range is limited by the lens, 350 nm lower limit, and by the camera, 850 nm upper limit. A custom-made holder allowed for inserting bandpass filters of various centre wavelengths into the optical path. It was therefore possible to study the temporal and spatial development of each species, argon atoms and ions, as well as metal atoms and ions, individually.

The Andor DH520 is an intensified charge couple device, iCCD, with an array consisting of 1024x256 pixels. During the experiments, it was cooled to $-10\,^{\circ}$C to reduce the background noise. The principle of operation is depicted in figure 4.3 [147]: A photon entering the quartz window impinges on the photocathode made of tungsten which emits a photoelectron. This electron is accelerated by the gate voltage towards the multichannel plate (MCP) which is an arrangement of secondary electron multipliers with a diameter of $6-10\,\mu$m. The electron gain in the multiplier is determined by the voltage, the gain voltage, applied to it. The present model of iCCD allowed to vary the gain voltage by a selector switch on the detector head in arbitrary steps from zero to nine. After the MCP,

the electron is accelerated by a voltage of several kV before it impinges on a fluorescence film where it causes the emission of a photon. This photon is guided by a bunch of optical fibres to the CCD where it is detected.

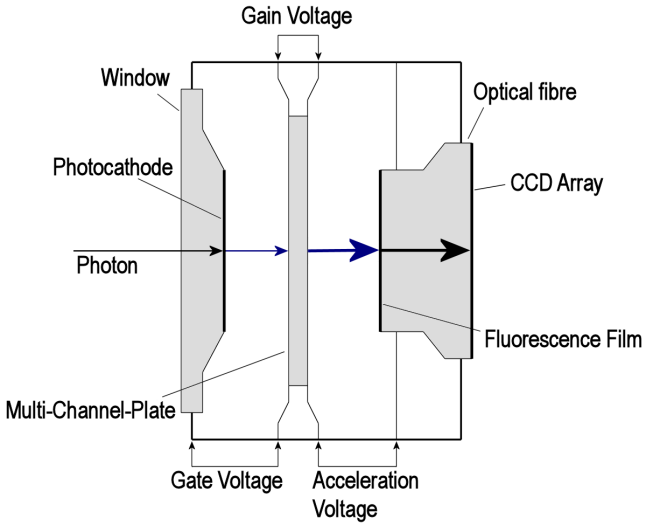

Figure 4.3: Operation principle of an iCCD [147].

The advantage of this setup is the possibility of detecting very low intensities down to single photons. In addition, the gate voltage can be switched very quickly which enables a temporal resolution in the nanosecond range. One defines the gate width t_{gate} as the duration the gate voltage allows electrons to reach the multichannel plate, which coincides with the time the CCD is exposed to light and can measure intensity. The special arrangement of the multichannel plate and the bunch of optical fibres conserve the spatial information of the light which is a unique feature compared to photo multiplier tubes.

In a series of preliminary experiments, the response of each pixel of the iCCD was checked. A detection area was selected that showed little intensity variation when a uniform light source was observed. Neutral density filters were used to check for linear dependence of the measured intensity with the incoming intensity. The angle of divergence was obtained experimentally to be about $\alpha = 6^\circ$, which agrees well with the theoretical value $\alpha = 6.6^\circ$ calculated by using:

$$\tan\alpha = \frac{d_d - d_l}{d_{opt}}, \tag{4.16}$$

with the discharge diameter $d_\mathrm{d} = 16\,\mathrm{cm}$, the diameter of the lens $d_\mathrm{l} = 6\,\mathrm{cm}$ and the distance between the discharge axis and the lens being 87 cm. The discharge is an extended

light source, which means, that some places of light emission are further away than others. When varying the distance between an illuminated sheet of paper, which can be approximated as a Lambert emitter, and the optical system, iCCD and lens, from 70 cm to 100 cm the measured intensity decreased by less than 3 %. The distance dependence of the intensity can therefore be neglected. Finally, the influence of the gain was investigated, which can be adjusted by a selector switch in arbitrary settings from 0 to 9. This means, that no information on the actual gain voltage or on the electron gain in the multichannel plate is available. The same light source as for the distance measurements was used but kept at a fixed distance to the iCCD. The measured intensity was normalised by the intensity measured with gain 0 and is summarised in table 4.1. It can be seen, that the intensity increases exponentially and that adjusting the gain can increase the measured intensities by two orders of magnitude, which helps detecting light with low intensity or transient phenomena with very short gate time. The error given for the normalised intensities represents the deviation of the individual pixels from the average value. As this deviation is generally below 5 %, one can conclude that the individual pixels respond in a very similar way to the gain setting. A comparison to the manufacturer's data is given, too, which agrees up to a gain of 5. For gain 6 and 7, the measured increase of intensity is less than expected from the performance data sheet and gain 8 and 9 showed quite substantial noise, that these settings cannot be used for any measurements [148]. Maybe, the MCP has already started degrading, as the iCCD is already more than 10 years old. The normalised intensities summarised in table 4.1 are used as conversion factors to normalise the intensity.

4.2.2 Optical bandpass filters

Spectra of the HiPIMS discharges were recorded using an optical probe, developed by Swindellis [149], to couple the light out of the plasma and into a Newport MS260i, a spectrometer in Czerny-Turner configuration. Its entrance focal length is 220 mm and it has two gratings installed, 600 mm^{-1} and 2400 mm^{-1}. With the entrance slit set to 50 µm a spectral resolution of 0.34 nm and 0.08 nm could be achieved [150]. Optical filters with a diameter of 50 mm, supplied by L.O.T. Oriel and Melles Griot, were chosen according to the spectral lines observed in both discharges [151–156]. Their properties, as well as the spectral lines and their lifetimes are summarised in table 4.2. Neutrals are indicated by a "I" in brackets after the element symbol, whereas ions are denoted by "II" for singly charged, "III" for doubly charged, etc. One can see that all lifetimes are reasonably short, being in the range of 10 . . . 200 ns, except for the emission of zinc ion

Gain setting	Measured intensity	Manufacturer data
0	1.000 ± 0.016	1.0
1	3.46 ± 0.06	3.48
2	9.38 ± 0.22	9.6
3	21.4 ± 0.6	21.4
4	45.1 ± 1.4	47.66
5	73 ± 4	83.8
6	107 ± 6	138.2
7	141 ± 8	206.4
8	—	7680
9	—	8132

Table 4.1: Influence of the gain setting on the intensity measured by an iCCD Andor DH520 [148].

line Zn(II) at 589.4 nm. The upper level is metastable with a lifetime of 2.2 µs [157]. One has to keep this in mind when analysing the spatial distribution of the intensity, e. g. a zinc ion in the excited state with a velocity of $1000\,\mathrm{m\,s^{-1}}$ can move 2.2 mm before it emits a photon.

In addition to the properties of the filters summarised in table 4.2, spectra were recorded with the objective connected to the spectrometer by an optical fibre. Figure 4.4 shows these spectra with and without using the bandpass filters. The filters reduce the detected intensity by about half depending on the wavelength region, but they also block out light of any undesired wavelength. One should point out, that argon ions could only be investigated when sputtering the aluminium-doped zinc target, because too many spectral lines of titanium atoms and titanium ions were present. Figure 4.4 shows this problem, when using the filter a with central wavelength of 436 nm. Two titanium lines are present within the transmission range of the filter. A similar observation can be made for the filter with a central wavelength of 752 nm. In this case, two Zn(II) lines can be seen in the spectrum. Hence, only the filter with a central wavelength of 811 nm can be used to investigate the spatial and temporal evolution of argon neutrals when sputtering the aluminium-doped zinc target.

Centre Wavelength (nm)	**FWHM (nm)**	**Species**	**Wavelength (nm)**	**Lifetime (ns)**	**Excitation threshold (eV)**
436.58	4.26	Ar(I)	434.517	3400	14.52
		Ar(II)	434.806	8.5	19.49
		Ar(II)	435.220	47	19.31
		Ar(II)	437.075	15	21.49
		Ar(II)	437.133	45	19.26
		Ar(II)	437.595	49	19.97
		Ar(II)	437.967	10	19.64
502.55	10.95	Ti(I)	496.472	139	4.47
		Ti(I)	496.857	112	4.48
		Ti(I)	498.173	15	3.34
		Ti(I)	499.107	17	3.32
		Ti(I)	499.950	19	3.31
		Ti(I)	500.721	20	3.29
		Ti(I)	501.419	199	2.47
		Ti(I)	502.003	88	3.31
		Ti(I)	502.287	72	3.29
		Ti(I)	502.484	76	3.28
		Ti(I)	502.557	23	4.51
		Ti(I)	503.591	—	3.92
		Ti(I)	503.646	25	3.90
		Ti(I)	503.840	26	3.89
		Ti(I)	503.996	257	2.48
		Ti(I)	506.466	264	2.50
		Ti(I)	508.706	71	3.87
591.19	9.53	Zn(II)	589.433	2200	8.11
637.92	10.44	Zn(I)	636.235	21	7.72
752.1	10.6	Ar(I)	750.387	22	13.48
		Ar(I)	751.465	25	13.27
811.63	9.15	Ar(I)	810.369	40	13.15
		Ar(I)	811.531	30	13.08

Table 4.2: Optical bandpass filters and observed spectral lines with lifetime and excitation threshold of the excited state [151–174].

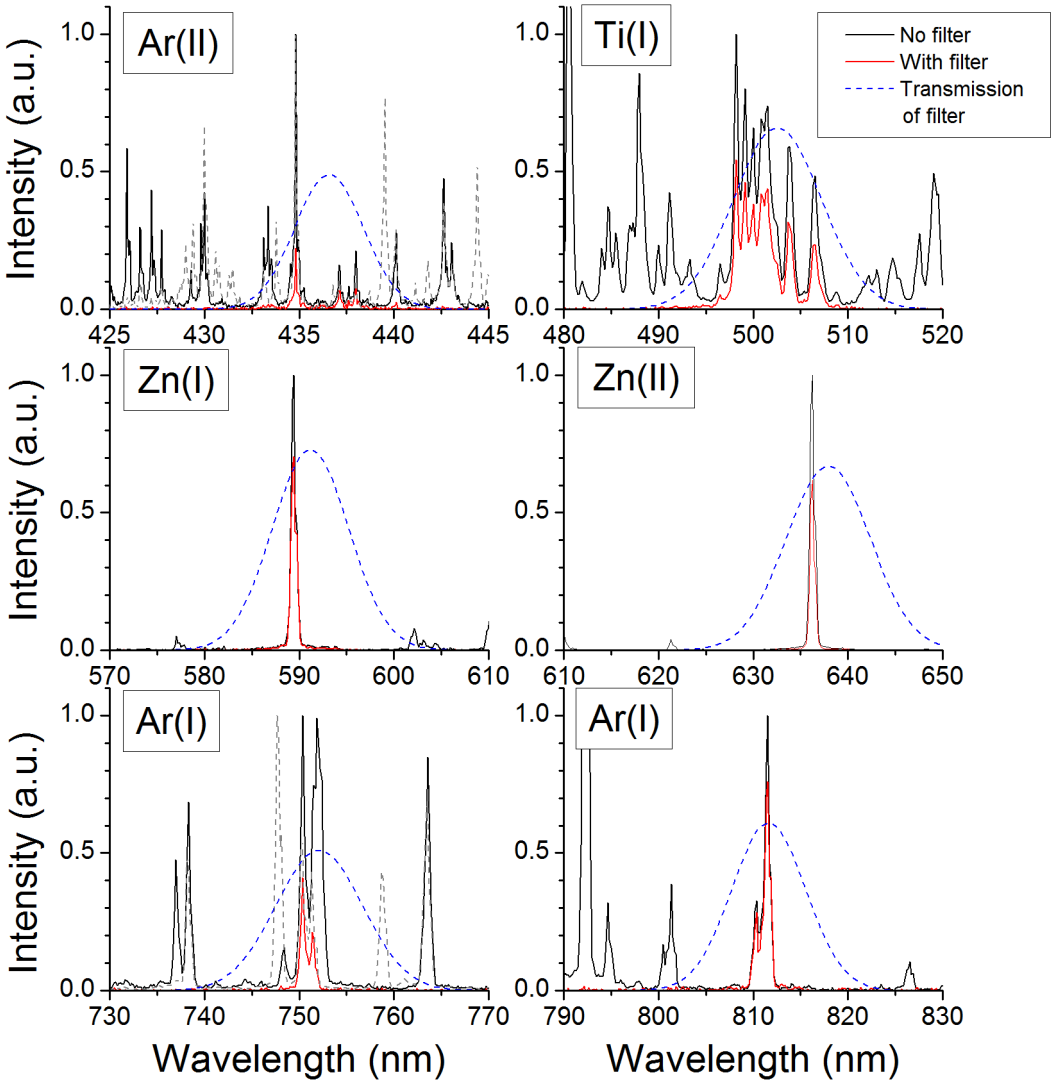

Figure 4.4: Spectra of HiPIMS discharges observed with (red line) and without (black line) optical bandpass filters. The transmission of the filters is shown by the blue dashed line. The dashed grey line represents the spectrum of the discharge that has spectral lines of more than one species present in the transmission range of the filter. For filter 436 nm spectral lines of titanium are present in a range dominated by Ar(II) emission. In the range of the 750 nm Zn(II) lines can be detected besides Ar(I) lines [151–156].

4.2.3 Measuring parameters and analysing procedure

The temporal and spatial evolution of the plasma-induced emission of HiPIMS discharges with either a titanium or an aluminium-doped zinc target was investigated. The discharge parameters and the settings of the iCCD are summarised in table 4.3. It was tried to keep the average power and the energy delivered per pulse the same for all discharges. However, sputtering the Al_5Zn_{95}-target without sudden switch off of the discharge, needed a high target voltage which resulted in an elevated energy per pulse of 8 J. In order to reduce the thermal load and the sputtering rate, the frequency was reduced to 50 Hz. The substrate was always placed 10 cm above the target.

Setting	**Ti target**	**Ti target**	**Al_5Zn_{95} target**
Pressure (Pa)	0.53	1.33	1.33
Argon flow (sccm)	30	30	30
Set voltage (V)	500	500	900
Peak voltage (V)	670	720	965
Peak current density (A cm^{-2})	2.6	3.0	1.3
Peak power density (kW cm^{-2})	1.2	1.3	1.0
Average power (W)	650	650	400
Frequency (Hz)	100	100	50
Pulse width (µs)	100	100	100
Duty cycle (%)	1.0	1.0	0.5
Substrate	Distance 10 cm, floating		
Optical gate width (µs)	varied between 0.1 . . . 100		
iCCD gain	varied between 0 . . . 7		

Table 4.3: Measuring parameters for optical 2d-imaging.

The measuring and analysing procedure was as follows:

1. Calibrate the position, i. e. the discharge coordinate system, by imaging a ruler.
2. Find discharge axis by imaging various species in a DCMS discharge.
3. Record image of the discharge and the background of the iCCD.
4. Subtract the background and normalise the corrected intensity by the gate width, the exposure time and the gain.

5. Apply Abel-inversion, if the image is symmetric around the discharge axis (less than 10 % difference).

6. Display the spatially-resolved data using the calibration of the position and discharge axis and label with the temporal position.

7. Transpose data $I_t(r,z)$ to obtain the temporal development of the intensity $I(t)$ at any position r and z.

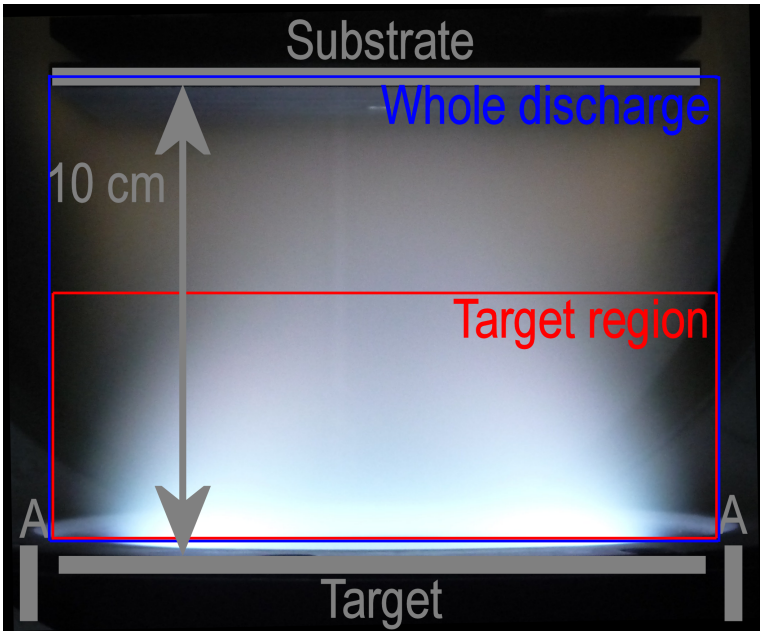

Figure 4.5: Areas of observation for optical 2d-imaging: The Magnetron consists of the target which also serves as cathode, the target holder and the hidden anode cup (A). The substrate is installed in 10 cm distance from the target. Discharge conditions: Titanium target, $f_{\mathrm{Ar}} = 30$ sccm, $p = 0.53$ Pa, P = 500 W (DC).

One final thought before continuing with the actual measurements: Test experiments on DCMS discharges revealed, that imaging the discharge as a whole can lead to an undesired effect at the target and the substrate position. As the camera "looks from above" both the front and the back part of the plasma torus can be seen, separately. The photo in figure 4.5 shows this effect rather nicely at the substrate position. Due to the perspective of the image, one can see the lateral extension of the substrate, which of course causes errors when such an image is Abel-inverted, because the cylindrical symmetry of the discharge is broken in

the plane of observation. This problem was avoided by adjusting the position of the iCCD so that the region of interest lies close or at the optical axis. Two areas of observation, one to observe the discharge close to the target and one to study phenomena effecting the whole discharge volume, were chosen. Both regions are also depicted in figure 4.5.

4.3 Results: DC magnetron sputtering discharge

As a first benchmark, a DCMS discharge equipped with a titanium target, $P = 500\,\mathrm{W}$, $p = 1.33\,\mathrm{Pa}$, $f_{\mathrm{Ar}} = 30\,\mathrm{scmm}$, was observed by means of optical 2d-imaging. The optical bandpass filters with a centre wavelength of 500 nm and 750 nm were employed and the intensity distribution emitted by titanium and argon neutrals were Abel-inverted. Figure 4.6 shows an example of a radial intensity profile measured with filter 750 nm at an axial position of 6 mm. One can see, that the profile is symmetric but exhibits considerable noise. Hence, the first step of Abel-inversion is smoothing the raw data with a local linear algorithm. The resulting, Abel-inverted radial emittance of argon neutrals, dashed red line, features a distinct maximum at a radial position of about 47 mm and a strong intensity decrease towards the discharge axis and the outer edge of the plasma. It is worth noting, that the slight maximum obtained close to the discharge axis is an artefact of Abel-inversion. As one can see from equation 4.15, a singularity occurs at a radial position $r = 0$. In a general rule of thumb, the accuracy of Abel-inversion increases with increasing distance from the discharge axis.

The spatially-resolved emittance of argon and titanium neutrals is displayed in figure 4.7 in comparison to the magnetic field of the magnetron. One can clearly see that the overall maximum of the intensity of both species can be found close to the target at a radial position between 45 mm and 50 mm. The intensity then decreases continuously with increasing distance from the target. At the same time, the radial position of the maximum shifts towards the discharge axis, which can be seen in figure 4.7 (b). To understand this behaviour we concentrate on the emission of argon neutrals, first. The intensity is caused by electron impact excitation of argon atoms and depends on the density of argon neutrals, the electron density and the electron temperature through the rate coefficient (equation 2.63). The argon atoms are considered to be distributed homogeneously throughout the vacuum chamber and the rate coefficient is assumed to be constant, i.e. the electron temperature does not have a spatial variation. In this case the intensity profile of Ar(I) represents the electron density distribution. As the motion of the electrons is influenced by both the elec-

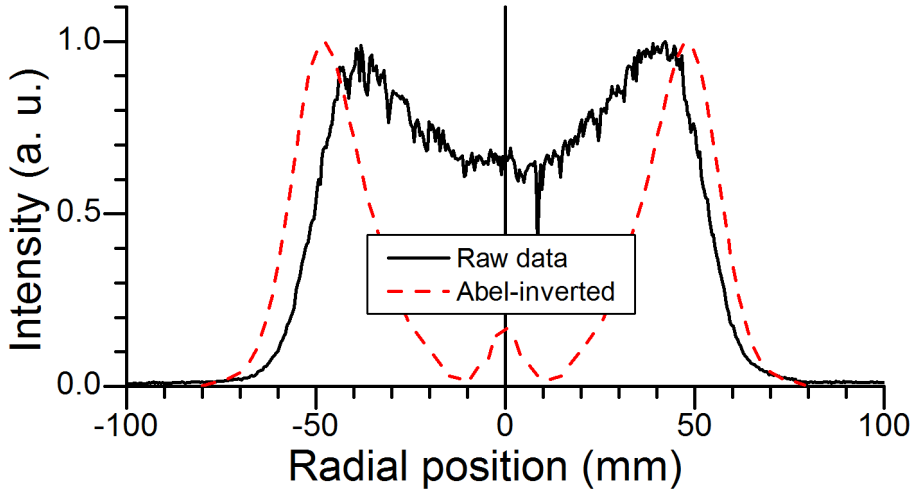

Figure 4.6: Measured intensity (black solid line) and calculated local emittance (red dashed line) of argon neutrals (750 nm) in a DCMS discharge at an axial distance of 6 mm. Discharge conditions: Titanium target, $P = 500$ W, $p = 0.53$ Pa, $f_{\mathrm{Ar}} = 30$ sccm.

tric and the magnetic field, highly energetic secondary electrons ejected from the target have a high residence time at positions where the magnetic field is oriented parallel to the target surface. This causes an increase of the electron density in this region. Consequently, the position of the emission maximum clearly reflects the magnetic field configuration (figure 4.7 (b)). In addition, the electrons emitted by the target surface, initially gyrate along a magnetic field line close to the target surface. A change of this trajectory can only happen during a collision with another particle. A higher density is therefore expected close to the target surface and has already been measured [54], causing the overall intensity maximum to occur close to the target.

The emission of titanium neutrals shows many similarities compared to the argon neutrals emission. The position of the maxima agrees very well with that found for Ar(I) and is caused by the same reasons as previously discussed. Besides this agreement, there is also a striking difference: The intensity of the titanium neutrals emission drops much more rapidly with increasing distance from the target. In contrast to the argon atoms, the titanium atoms are not homogeneously distributed, because they are sputtered from the target and have an anisotropic velocity distribution. The kinetic energy follows the following

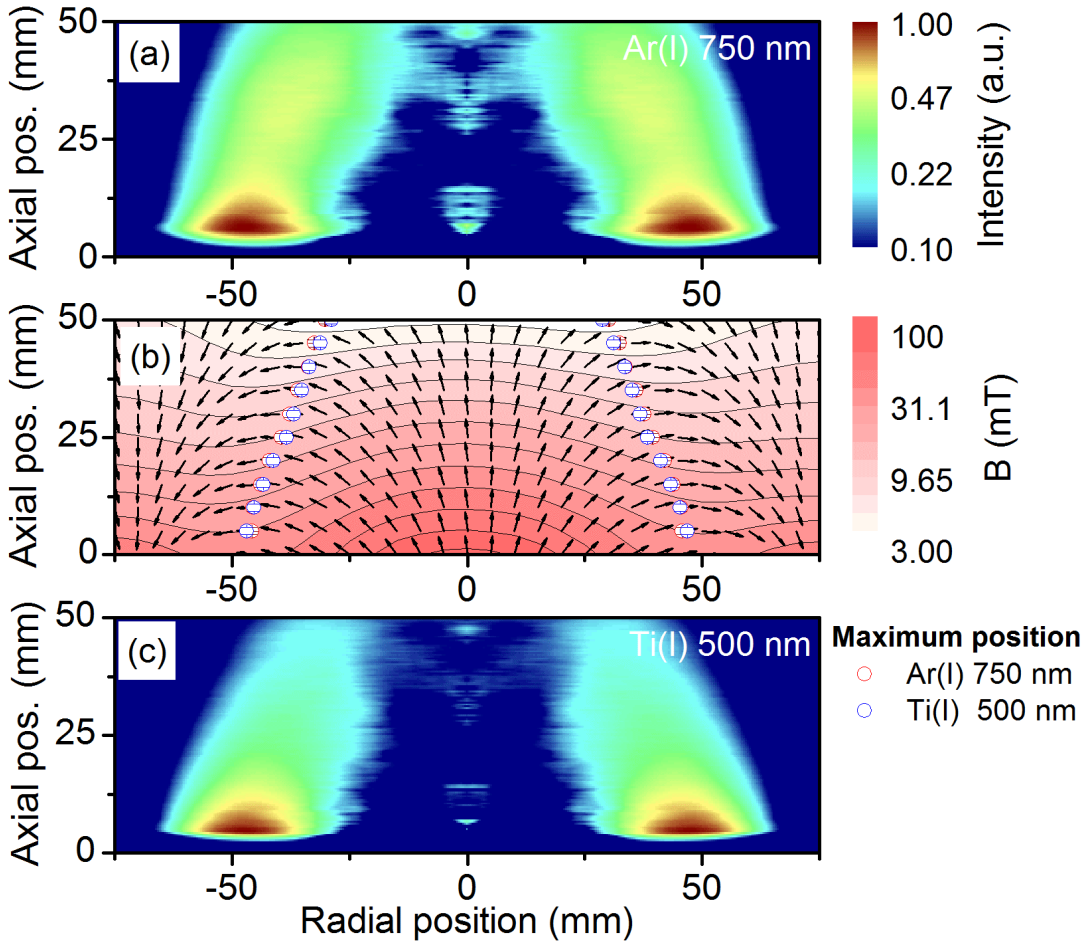

Figure 4.7: Comparison of the argon (filter 750 nm, figure (a)) and titanium (filter 500 nm, figure (c)) neutrals emission with the magnetic field configuration (figure (b)). Discharge parameters: Titanium target, $P = 500$ W, $p = 1.33$ Pa, $f_{\mathrm{Ar}} = 30$ sccm.

distribution $f(E,\alpha)$ also depending on the emission angle α [48, 175]:

$$f(E,\alpha) \propto \frac{E}{(E_t+E)^3}\cos\alpha, \tag{4.17}$$

with E and E_t being the incident energy of the impinging particle and E_t the surface binding energy of the target material. The motion is linear unless a collision with the background gas occurs. This process may be neglected, as the mean free path for collisions with the background gas at a pressure of 0.53 Pa can be calculated to 4.5 cm (see equation 2.60). The superimposition of the electron density (deduced from the Ar(I) emission) with the wide-spread density of the titanium atom density leads to the intensity profile shown in figure 4.7 (c). A further evidence for this explanation can be found when looking at the width of the emission maximum for different axial positions. The FWHM of the emission of both species is quite similar close to the target (axial position 5 mm), (24.06 ± 0.17) mm and (23.72 ± 0.05) mm for Ar(I) and Ti(I), respectively. The difference is much more pronounced 50 mm away from the target, where the FWHM for Ar(I) is (35.6 ± 0.4) mm and (41.6 ± 0.6) mm for Ti(I). As the results presented here agree very well with previous studies of DC magnetron sputtering discharges, it can conclude that the 2D-imaging in combination with the Abel inversion works.d density of the titanium atom density leads to the intensity profile shown in figure 4.7 (c). A further evidence for this explanation can be found when looking at the width of the emission maximum for different axial positions. The FWHM of the emission of both species is quite similar close to the target (axial position 5 mm), (24.06 ± 0.17) mm and (23.72 ± 0.05) mm for Ar(I) and Ti(I), respectively. The difference is much more pronounced 50 mm away from the target, where the FWHM for Ar(I) is (35.6 ± 0.4) mm and (41.6 ± 0.6) mm for Ti(I). As the results presented here agree very well with previous studies of DC magnetron sputtering discharges, it can conclude that the 2D-imaging in combination with the Abel inversion works.

4.4 Results: HiPIMS discharges

The spatial and temporal development of HiPIMS discharges, operated with a titanium target (pressures 0.53 Pa and 1.33 Pa) and an aluminium-doped zinc target (pressure 1.33 Pa) was investigated by recording a series of images of the discharges. Both discharges were sputtered with an energy of 7 J per pulse. However, the repetition frequency had to be reduced to 50 Hz for the Al_5Zn_{95}-target compared to 100 Hz for the Ti target. This leads to an increased duration of the afterglow. The optical bandpass filters summarised in table

4.2 were used to study each species, argon neutrals and ions, as well as metal neutrals and ions, individually. The experiments cover the whole discharge from applying the target voltage until the late afterglow.

4.4.1 Temporal development

For the discharge pulse the gate width of the iCCD was set to 1 µs and images were taken every 5 µs to cover the entire duration of the discharge "on"-time. Finer steps of 1 µs were employed during the transient times, i. e. when the target voltage was applied ("off"-"on" transition) and when the pulse was terminated ("on"-"off" transition). The temporal development of the species investigated extracted from the images 5 mm above the target at the centre of the discharge (no Abel inversion performed) is shown in figure 4.8. For better comparison, the target voltage and the discharge current of both discharges are displayed, as well. Both waveforms show characteristics typical for the operation of HiPIMS discharges with the Sinex power supply as discussed in section 3.3. Due to the longer

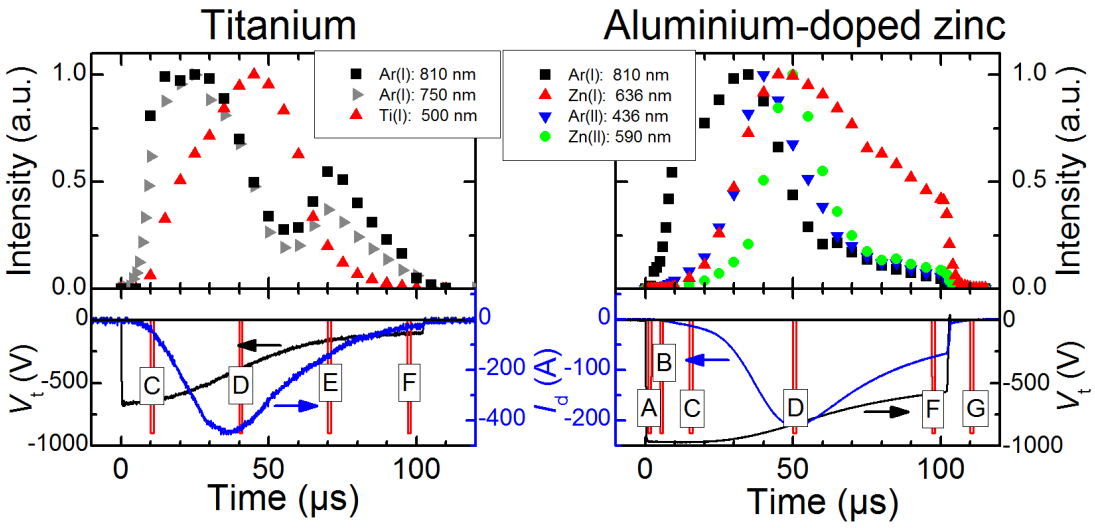

Figure 4.8: Temporal evolution of the intensity of argon neutrals Ar(I) and ions Ar(II), as well as titanium neutrals Ti(I) and zinc neutrals Zn(I) and ions Zn(II). Temporal positions of discharge phenomena are labelled by capital letters A-G for future reference. Sputtering titanium was carried out at a working gas pressure of 0.53 Pa, whereas the Al_5Zn_{95}-target was sputtered at 1.33 Pa. Further discharge parameters are summarised in table 4.3

afterglow, about 20 ms for the Al_5Zn_{95}-target compared to 10 ms for the Ti-target, the electron density left from the previous pulse is lower when sputtering the Al_5Zn_{95}-target. Thus, the discharge current develops more slowly and reveals a longer delay of the current onset. The red curve represents the trigger signal which controls start and end of the measurement. Several of these measuring pulses are shown to label phenomena observed in the discharges. However, only one of them was used at any one time. Hence, the images were recorded in a sequence over several pulses and not as "one shot" high-speed or streak cameras would produce [31, 32].

The discharge is ignited by applying a highly negative voltage to the target. This voltage ramp also serves as zero for the time axis. The pulse initialisation is followed by a sharp increase of the emission of Ar(I) and Ar(II) with a distinct delay. As the dominating excitation mechanism during the discharge "on"-time is electron impact excitation, the rise of the intensity reflects the increase of the electron density and temperature [90, 91]. Argon ion emission observed with filter 436 nm starts rising with a delay of about 10 µs, as the particles in the ground state, i. e. argon ions, have to be produced in sufficient quantity, first. Note, that a two step ionisation and subsequent excitation process is assumed, as the ionisation and excitation in a single step is rather unlikely due to the high electron energy of about 35 eV [158,176]. The intensity of both species increases until it reaches its maximum well before the discharge current peaks. With the electron density still rising [90, 91], the reason must be looked for in the rate coefficient, i. e. electron temperature, and the density of the argon neutrals and ions. The rate coefficient might already be decreasing, because the electron temperature was found to be decreasing [90, 91], which was attributed to the depletion of the energetic tail of the EEDF by inelastic collisions with sputtered metal particles having a low excitation and ionisation threshold (compare table 4.2 and ref. [177]). In addition to the decrease of the rate coefficient, it is also very likely that the working gas in front of the target is rarefied [23, 96]. A lower density of argon atoms results in a lower intensity of the light emitted by this species, as well as in a lower ionisation rate which in turn causes the emission of argon ions to decrease. Looking at the further development of the discharge, one can see a major difference between both discharges. When sputtering the titanium target, the intensity of argon neutrals shows a second maximum 70 µs after pulse initialisation, which coincides with a peak in the electron density reported by Poolcharuansin and Bradley [91]. They explain the additional maximum by the arrival of the ionised sputtered flux at the probe position 100 mm above the target. However, the intensity maximum is shown for a distance of only 5 mm and was observed at the same time throughout the entire discharge. From the target voltage and the discharge current

displayed in figure 4.8 labelled by “E”, one can see that both the voltage and the current have already decreased substantially compared to its peak at 35 µs; from 450 V to 200 V and from 450 A to 150 A, respectively. The sputtering yield of the target, assuming singly charged titanium ions with a kinetic energy equivalent to the target potential, drops from 0.5 to 0.1 [48] and the ion flux to the target by a factor of 3. The sputtering rate is therefore reduced by one order of magnitude, which makes it very likely that argon gas already flows back into the depleted region above the target. The increasing number of argon particles can then also lead to an increased intensity. Another indicator for this assumption is the steep drop of the intensity of light emitted by titanium atoms as seen in figure 4.8 which also suggests a strong reduction in the sputtering rate. In contrast to sputtering titanium, the target voltage and the discharge current are still high until the end of the HiPIMS pulse in the case of sputtering Al_5Zn_{95}, which shows that a sufficient sputtering rate prevents the argon gas from streaming back into the discharge volume. Pulse termination about 102 µs after its initialisation is followed by a rapid reduction of the emitted intensity.

The temporal development of the emission of metal neutrals and ions differs from the development of the intensity emitted by the working gas. Besides a small remnant density left over from the previous discharge pulse, the majority of these particles has to be created by the discharge through sputtering. Hence, the intensity in the first few microseconds is extremely low (but still detectable). It only increases after the onset of sufficient sputtering which is closely related to the onset of the discharge current, which is an ion current to the target causing secondary electron emission and sputtering of the target material. One can see, that the discharge current rises faster for sputtering titanium than for sputtering the aluminium-doped zinc target, and so does the intensity of the titanium neutrals compared to the emission of zinc atoms. The intensity of Ti(I) starts with a delay of 10 µs in respect to the pulse initialisation, whereas the delay of Zn(I) is about 15 µs. One should note, that the emission of argon ions starts slightly earlier in the pulse than Zn(I) which is plausible as the zinc atoms are created by sputtering the target by argon ions at the beginning of the discharge. The further development of the intensity of both metal atom species is strongly related to the discharge current. The emission peaks shortly after the discharge current peak and decreases with decreasing current until the discharge pulse terminates and the intensity drops quickly, as both the sputtering process, as well as creation of energetic electrons is stopped abruptly.

The onset of the intensity of zinc ions, Zn(II) 589.8 nm, is delayed most. For DCMS discharges, Rossnagel and Saenger found that the intensity is proportional to the discharge current power 1.0, 2.0 and 3.0 for argon neutrals, sputtered metal neutrals and metal

ions [178], respectively. This means that the intensity emitted by zinc ions strongly depends on the temporal development of the discharge current. It is extremely low when the discharge current is low at the beginning of the pulse and rises quickly when the current increases towards its peak. In contrast to the considerations for continuous discharges, such as DCMS, further delay of the investigated intensity arises when the discharge is pulsed. The intensity of Zn(II) at [**?**]nm requires three steps, which all contribute to the formative delay of the onset of the emission. Firstly, zinc atoms have to be sputtered from the target, which has, secondly, to be ionised and finally excited. Again, the latter two steps could occur in combination, but require an electron energy of about 17.5 eV [172, 179]. Due to the steps involved, the onset of Zn(II) emission is delayed most, by about 20 µs. The intensity increases quickly until it peaks at 50 µs and decreases much more rapidly than the emission of Zn(I) in the second half of the pulse before it drops dramatically after pulse termination. A similar observation was made by Ehiasarian et. al. for chromium ions [98]. The power supply used in their study shows a similar feature as the Sinex used in these experiments: It cannot sustain a high target voltage throughout the entire HiPIMS pulse due to the high current level and small capacitance of the power supply. Hence, the high degree of ionisation cannot be sustained and the intensity of metal ions, chromium and zinc, decreases. This transition into a DC-like stage was also reported by Lundin et. al. [102] and by means of optical studies by Hala et. al. [95]. Comparing the ionisation threshold of both chromium and zinc, the faster decrease of Zn(II) emission is not surprising, because the threshold is with 9.39 eV higher than for chromium 6.77 eV [179, 180]. Other researchers, such as Alami et. al. [112], observed an almost constant intensity of metal ion emission, while Hala et. al. reported a slight decrease of the intensity as the target voltage and discharge current decreases [95]. It appears, that the temporal development comes down to the power supplies capability of sustaining a high target voltage at a high discharge current.

Finally, it shall be noted, that hardly any difference in the emission of both argon neutral ranges (750 nm and 810 nm) can be observed. This is a very promising result, as it allows to only discuss the images recorded with the filter with a centre wavelength of 810 nm when sputtering the aluminium-doped zinc target. The filter with a central wavelength of 750 nm cannot be used, because of a spectral line emitted by zinc neutrals at 747.8 nm which is well within the wavelength range transmitted by that particular filter (compare figure 4.4).

In order to identify phenomena observed in the HiPIMS discharges, several temporal positions are labelled with capital letters A-G. This labelling partly agrees with the discharge

stages identified by Hala et. al. [95], namely the ignition, followed by a metal-dominated phase which develops into a transient stage and finally, a DC-like phase. The ignition is characterised by an increase of the intensity of argon neutrals and ions. During this stage, three distinct phenomena can be observed during the early ignition (label A), the plasma build-up (label B) and the stabilising stage (label C). The metal-dominated stage is rather short in the present experiments and is mainly limited to the discharge current peak (label D). Label E can only be identified when sputtering the titanium target, because it refers to the second maximum in the intensity of argon atoms. It can probably be described best by the transient phase. The DC-like stage of the discharge can be found just before pulse termination (label F). The development during and shortly after pulse termination is labelled by G and a last temporal position is not labelled in the figure above. The spatial and temporal development of the intensity in the afterglow several 100 µs after pulse termination was also observed and will be discussed separately, label H.

4.4.2 Overview over characteristic temporal positions

After the discussion of the temporal development of the intensity at a selected position of the discharge, the spatial distribution of the plasma-induced emission shall be discussed. An overview over the temporal positions labelled in figure 4.8 is presented for observing the discharge region close to the target, because this area is the most interesting during the pulse "on"-time. Abel inversion was applied to all recorded data to calculate the spatially emitted intensity unless explicitly stated differently. Each image was normalised to its intensity maximum to make the spatial variation of the intensity clearly visible. For the development of the relative intensity one should refer to figure 4.8.

The spatial and temporal development of argon and titanium atoms observed when sputtering the titanium target at an argon pressure of 0.53 Pa shall be presented first, figure 4.9. It was discussed in the previous section, that the HiPIMS discharge starts with the emission of argon neutrals which is displayed for a time 10 µs after pulse initialisation (label C). One can see that the spatial intensity distribution of both spectral ranges (750 nm and 810 nm) look very similar to the DCMS discharge shown in figure 4.7. The influence of the magnetic field can clearly be seen, i. e. the highest intensity can be found where the magnetic field is orientated parallel to the target, where the highest electron density is expected [76]. However, the intensity distribution also reveals a striking difference compared to the DCMS profile: The overall intensity maximum can be found in a region detached from the target and not immediately above it. This intensity maximum was found to travel

away from the target not unlike an ion acoustic wave caused by the rapid motion of the sheath during pulse initialisation [93–95, 131].

During the same time, the sputtering of the titanium target has just started, which is indicated by the onset of the discharge current. The low density of titanium atoms, hence their emission of light, is concentrated close to the source, immediately above the racetrack.

With increasing current I_d, the discharge develops into the metal-dominated regime [95]. One can clearly see, what this means for the plasma-induced emission of Ar(I) and Ti(I) in figure 4.9 label D. The intensity of argon atoms is strongly depleted above the target, which cannot be explained by a decrease of electron density [76] or the rate coefficient, i. e. the electron temperature (compare figure 5.19). Thus, the density of argon atoms must be reduced, which might either be caused by ionisation or gas rarefaction due to the momentum transfer between the sputtered particles and the working gas [96]. The simultaneous reduction of the intensity emitted by the argon ions observed when sputtering the aluminium-doped zinc target (figure 4.8) rules out the first option and only the gas rarefaction remains. This conclusion is supported by Monte Carlo simulations of the particle flow during HiPIMS pulses reported by Kadlec [23]. Following this explanation one would expect a large number of titanium atoms having replaced the working gas in front of the target. However, the emission of Ti(I) observed during this time shows a lack of intensity exactly at the position, where this large amount of titanium particles is supposed to be. Instead, two distinct intensity maxima can be observed which lie closer or further away from the discharge axis then the position of the racetrack. All targets sputtered in HiPIMS mode with the present magnetron showed only one racetrack at a radial position of about 45 mm. This confirms that titanium atoms are preferably sputtered in this region, but they are lost on their way into the detection region, which starts 4.5 mm above the target. This loss is most likely due to ionisation by the extraordinarily high electron density above the target.

It shall be noted that the intensity of the titanium neutrals emission is consistently higher closer to the discharge axis than at the outer edge of the discharge. The reason for this behaviour is not entirely clear, because the intensity depends on the three parameters electron density and temperature, as well as the density of titanium atoms. None of the aforementioned parameters are known for the present discharge, as the Langmuir probe studies shown in figure 5.19 are only carried out for axial distances 10 mm and above from the target. Assuming a symmetric sputtering profile with its centre being the racetrack, it might be possible that the electron density and temperature favour higher ionisation at the outer edge of the discharge, hence, reducing the density of titanium atoms and their emitted

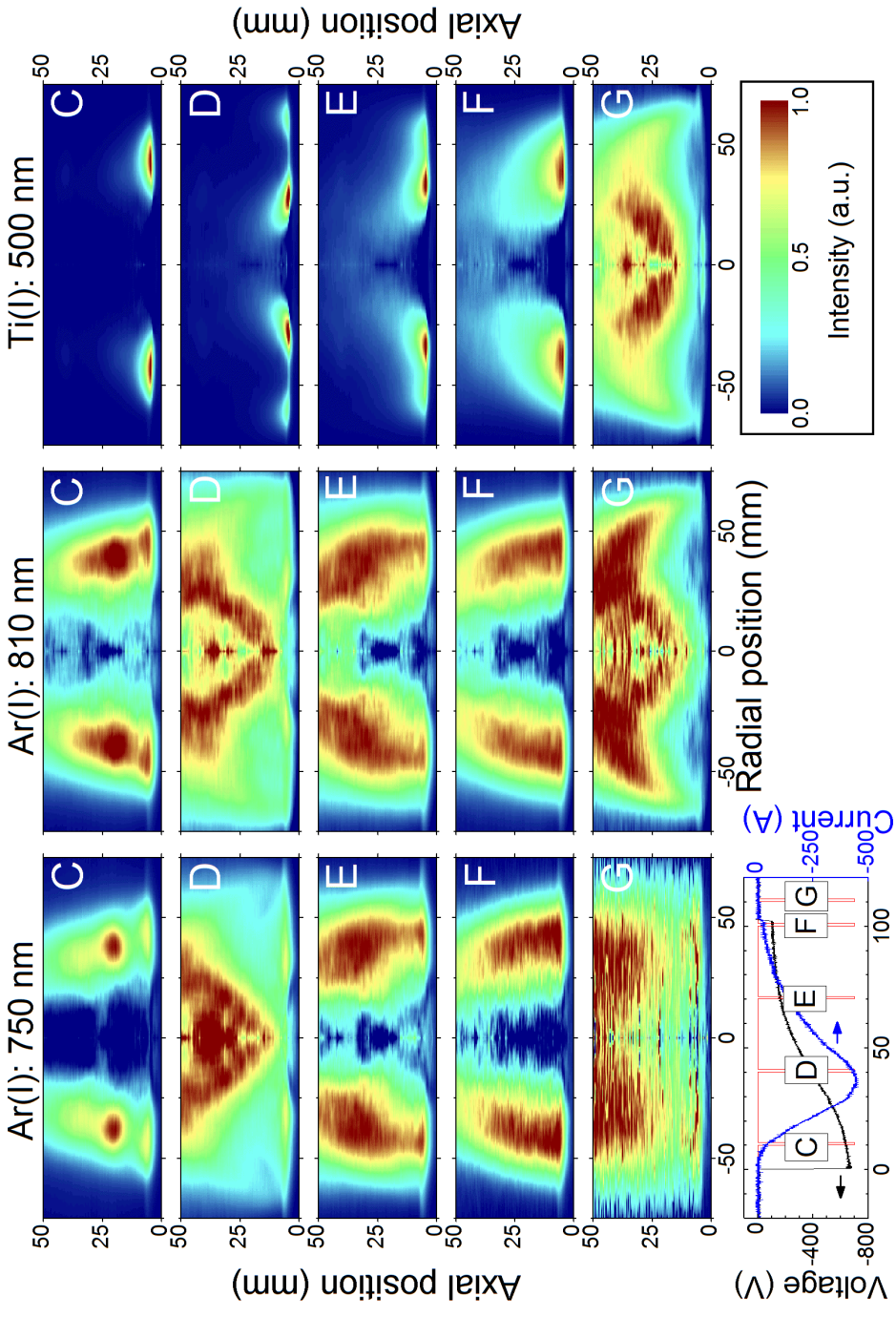

Figure 4.9: Spatially resolved emission profiles when sputtering a titanium target (argon pressure 0.53 Pa) at characteristic temporal positions: C stabilising phase, D discharge peak current, E second intensity maximum, F DC-like stage, G transition into "off"-phase. Discharge parameters are summarised in table 4.3.

intensity in this region. However, the emission of zinc neutrals does not show such a large difference in the intensity of both maxima, compare figure 4.10 D. Further investigation on the spatial distribution of the electron density and temperature and the density of sputtered metal atoms right above the target ($z < 5$ mm) are necessary to clarify the finding.

The metal-dominated stage is followed by a transition into a DC-like stage, which is characterised by a decreasing discharge current and the flow of argon gas back into the discharge volume [95, 102]. Two temporal positions, labelled E and F, were selected to represent this transition. An additional maximum of the intensity emitted by argon atoms was observed 70 µs after pulse initialisation. The spatial distribution of Ar(I) emission shows a DC-like profile, with the only difference that the overall intensity maximum is not found close to the target, because the working gas might still be depleted there. The two intensity maxima of Ti(I) emission move closer together, which indicates less ionisation of titanium atoms in front of the target, probably due to a reduction of the electron density. For the same reason, the intensity extends further into the discharge volume. This trend continues until the end of the discharge pulse (F), where both intensity maxima have merged and only one maximum is observed. As in the DCMS discharge, the intensity of Ti(I) emission extends further away from the target. Comparing the intensity distribution with the profile recorded for DCMS (figure 4.7), one can clearly justify the expression "DC-like state". This is also true for the emission of argon atoms.

After pulse termination, the intensity of all spectral lines decreases rapidly. However, this decay appears to be faster close to the target, as it can be seen in the images labelled with G. The intensity is lowest in an "arch" right above the target. In this region, electrons can be lost most efficiently as the magnetic field lines intersect the target. This means, that electrons are guided along the magnetic field lines towards the target, which is now at ground potential. Electrons with sufficient energy (above the plasma potential equivalent eV_{pl}), can easily be lost in this way. The higher intensity further away from the target might be caused by a "magnetic mirror" effect occurring when electrons move close to the target at high radial positions, where the magnetic field is very strong.

For the first time, one can see a significant difference between the emission of both argon species. The two spectral lines transmitted by the filter with a centre wavelength of 750 nm decays much faster than the intensity observed with filter 810 nm. This can be explained by different excitation mechanisms of the excited states involved, which leads to different decay times [181]. The creation of the upper states of the Ar(I) lines emitted at 750.347 nm and 751.465 nm, $2p_1$ and $2p_5$, respectively, is mainly due to direct or cascade excitation out of the argon ground state and requires an electron energy of at least 13.27 eV [182].

Boffard et. al. showed that especially the $2p_9$ state of argon emitting at 811.531 nm can be efficiently populated by electron impact excitation out of the $1s_5$ metastable state, requiring an electron energy as little as 1.5 eV. It can be concluded, that the intensity recorded with filter 750 nm is much more sensitive to the loss of energetic electrons than the emission observed with filter 810 nm. Vitelaru et. al. have shown recently, that a sufficient density of metastable argon atoms are present in a HiPIMS discharge [100], which further supports this supposition. A similar explanation can be given for the decay of Ti(I) emission. The electron energy necessary to excite the upper state can be as low as 2.5 eV, table 4.2. Hence, the decay is about as slow as for argon neutrals observed with filter 810 nm.

In order to confirm and extend the initial results from observing argon and titanium atoms, an aluminium-doped zinc target was sputtered and the emission of argon and zinc neutrals, as well as their singly charged ions were observed. Due to the higher zinc content (95 at.-% compared to 5 at.-% for Al) and the higher sputtering yield (neglecting effects arising from sputtering compound materials) for zinc, the density of aluminum particles is neglected in all discussions. The spatial intensity distribution is shown in figure 4.10.

Due to the slow increase of the discharge current compared to sputtering the titanium target, two additional phenomena (labelled A and B) were observed. It is worth mentioning, that these phenomena are not caused by the change of the target material but by the slower development of the discharge. This was confirmed by test measurements on a brand-new titanium target, which also showed a slower increase of the discharge current. The pulse initialisation is accompanied by a very low intensity emitted by all species in a region above the racetrack at a distance between 40 mm and 50 mm above the target, labelled A. This maximum is strongly influenced by the magnetic field, i. e. it is found at a radial position where the field is orientated parallel to the target, which leads to the conclusion that this phenomenon is caused by electrons. The presence in the emission of all species is a further indication. Within $1 \ldots 2$ µs the maximum increases in intensity and extends towards the cathode just before the onset of the discharge current can be detected. Shortly after this, the intensity rises and the plasma-induced emission shows an asymmetric profile, so Abel inversion cannot be applied (label B). The complexly-shaped intensity distribution observed shows a lot of similarities between the different species, e. g. maxima are roughly at the same position. It was speculated about localised instabilities of the plasma, or plasmoids, which might be present during this highly transient stage which would decay with time and leave a symmetric discharge as observed until the end of the pulse. Kozyrev et. al., Anders et. al. and Ehiasarian et. al. have recently shown, that localised ionisation zones, so called spokes, are present during sputtering with very

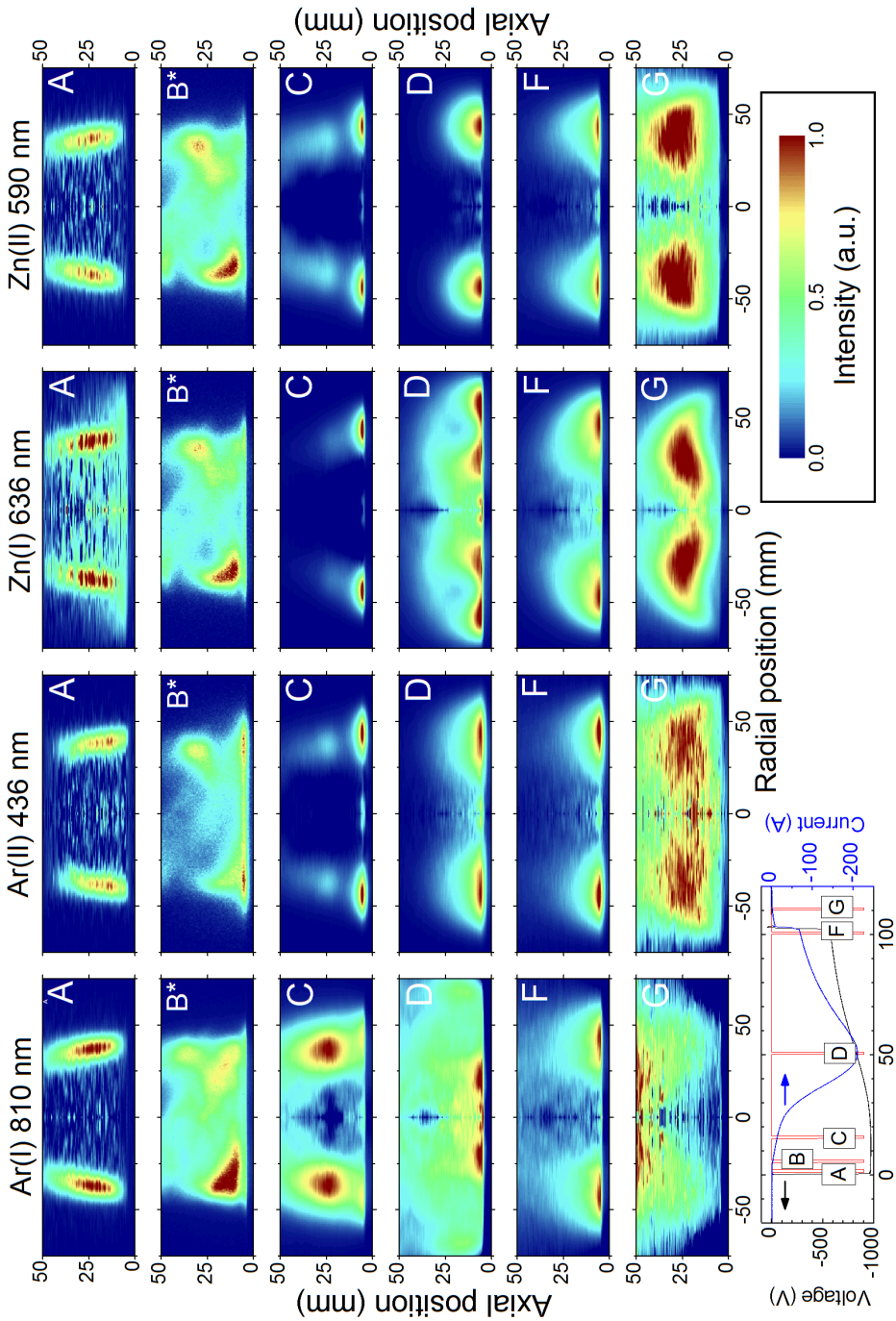

Figure 4.10: Spatially resolved emission profiles when sputtering an aluminium-doped zinc target at characteristic temporal positions: A early ignition, B plasma build-up, C stabilising phase, D discharge peak current, E second intensity maximum, F DC-like stage, G transition into "off"-phase, * not Abel-inverted. Discharge parameters are summarised in table 4.3

high current densities of several $\mathrm{A\,cm^{-2}}$ [31–33]. However, the discharge current during the temporal position B is still very low (< 10 A), which makes the presence of spokes very unlikely. During the later stage of the pulse, a symmetric intensity profile is recorded, as the ionisation zones forming under the condition of high discharge current drift above the racetrack with a speed of several $1000\,\mathrm{m\,s^{-1}}$. Averaging over several discharge pulses smears out the localised nature and a symmetric image is recorded.

The further development of the spatial intensity distribution confirms the findings from the titanium discharge quite well. An intensity maximum travelling away from the target can be observed for all species during time C. However, this phenomenon is superimposed with the asymmetric behaviour of the discharge at the beginning of the pulse.

In the metal-dominated stage D, the intensity of argon neutrals is depleted and the emission of zinc neutrals reveals two distinct maxima, just as it was found for sputtering titanium. The ions, argon and zinc, have their intensity maximum right above the racetrack confirming a high electron density in this region and preferred sputtering of the target at the racetrack position ($r = 45$ mm). Zinc atoms are therefore ejected at this position and directly ionised as one can see from the spatial distribution of Zn(II) emission. The fraction of ionisation of the sputtered flux appears to be lower when sputtering the aluminium-doped zinc target compared to the titanium target, which is plausible because of the higher ionisation threshold of zinc (9.39 eV compared to 6.83 eV for Ti [177, 179]) and the lower discharge current which implies lower electron density above the target. The discharge then evolves into a DC-like stage without an additional maximum in the intensity of argon neutral emission. The images labelled with F show that the spatial distribution of the intensity of all species at the end of the pulse are very similar to the distributions recorded for a DCMS discharge (figure 4.7), with the intensity maximum close to the target and the intensity decreasing with increasing distance from the target.

After pulse termination, the intensity of all spectral lines decreases, most quickly close to the target as discussed for sputtering the titanium target.

4.4.3 Stage A: Discharge ignition

The initialisation of the HiPIMS discharge is accompanied by a distinct phenomenon in the plasma-induced emission. Unlike during the pulse on-time, the intensity is not concentrated close to the target, but emission starts about 50 mm above the target as shown in figure 4.11 for sputtering the aluminium-doped zinc target. One can still see an influence of the magnetic field, because the intensity is highest where the magnetic field is orien-

tated parallel to the target. With progressing time, the intensity extends towards the target, while the measured intensity increases. The speed of the maximum was found to be nearly constant during this process and was calculated to be $(29.3 \pm 0.8)\,\mathrm{km\,s^{-1}}$. The velocity, which is about an order of magnitude higher than the ion acoustic speed, and the spatial distribution of the emission led to the conclusion, that this phenomenon is dominated by the mobile electrons. This assumption is confirmed by the fact, that it could be observed for all species, Ar(I), Ar(II), Zn(I) and Zn(II) in the same way, compare figure 4.10 A.

Transient effects during discharge ignition have already been reported by Bradley et. al. [131] and Welzel et. al. [183] for mid-frequency pulsed DCMS discharges. Optical 2d-imaging showed the emission of Ar(I) remote from the target at the outer edge of the magnetron ($r \approx 65$ mm), where the magnetic field lines of the unbalanced magnetron extend towards the substrate, about 0.4 µs after ramping up the target voltage. On the other hand, studies of the electron density by means of time-resolved Langmuir double probe showed a density maximum at the centre of the discharge, also detached from the target. Both phenomena were related to the acceleration of remnant electrons during pulse initialisation.

The ignition process of HiPIMS discharges is of particular interest, because the onset of the discharge current can have a delay of several 10 µs to 100 µs. This is a significant fraction of the total pulse on-time, during which no sputtering, due to the lack of a discharge current, and hence, no deposition is observed. Yushkov and Anders describe a global model for the ignition of the discharge and find the delay of the discharge current to be proportional to V_t^{-1} [88]. With the present results, it is hoped to study the processes involved more thoroughly from the aspect of particle (electron and ion) motion in the magnetic field of the magnetron. One initial thought was that the position of the intensity maximum represents the sheath width which decreases in thickness during the ignition process. A reduced sheath width would then accelerate the secondary electrons from the cathode faster, ionisation events might take place closer to the target, i. e. at the sheath edge where the maximum of the electron density is found. In addition, ions would travel through the thinner sheath faster and accelerate the process further, which would eventually lead to sufficient gas breakdown and a quick rise of the discharge current. Sheath thickness measurements by observing the cathode dark space were carried out by Gu and Lieberman for DCMS discharges [184], which confirms that measurements like this should be principally possible.

With these preliminary thoughts in mind, a more intense study was conducted using a titanium target instead of aluminium-doped zinc. This has mainly practical reasons;

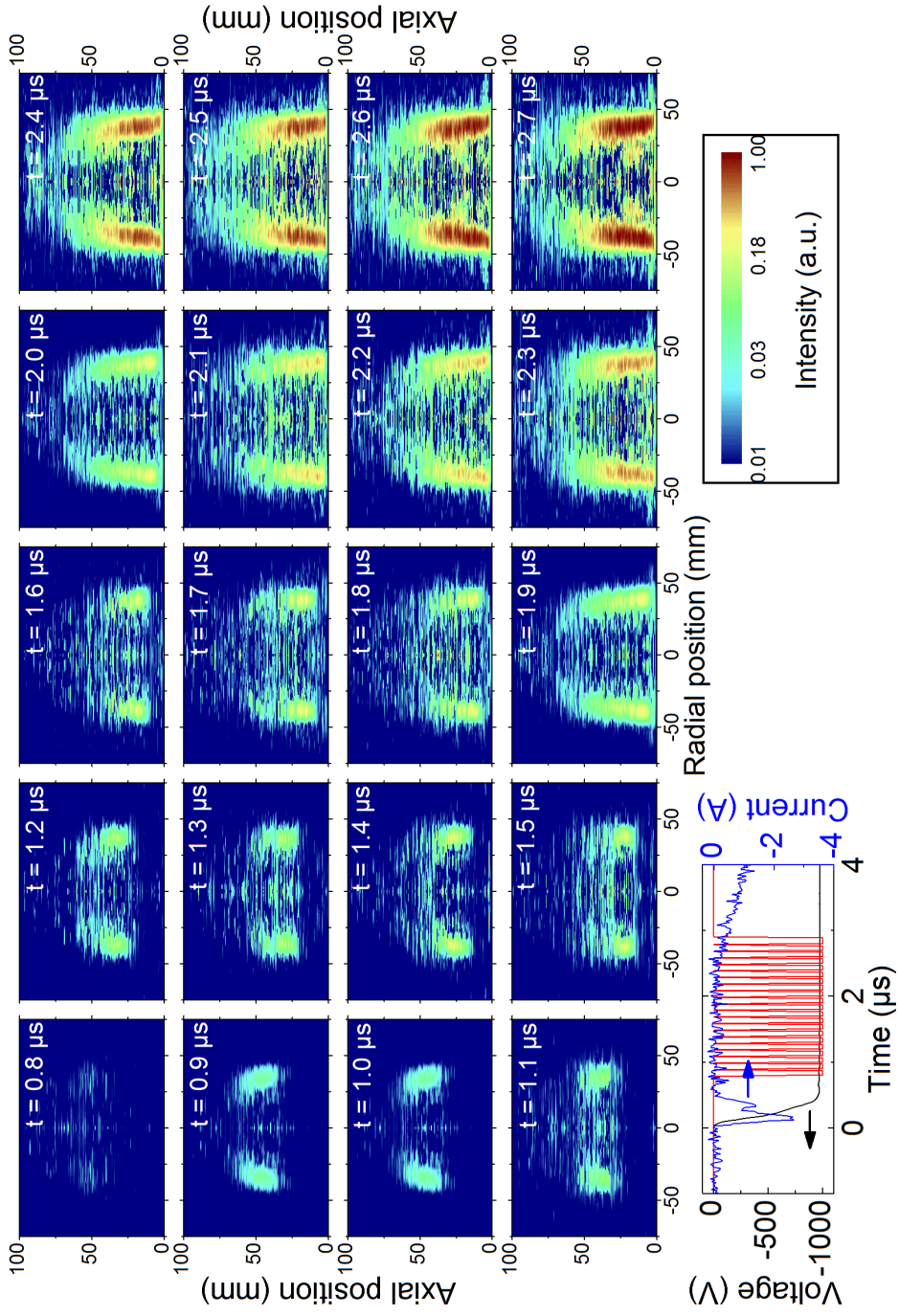

Figure 4.11: Spatially resolved emission profiles of Ar(I) 810 nm during discharge ignition when sputtering an aluminium-doped zinc target. Discharge parameters are summarised in table 4.3

discharge conditioning is much easier for titanium, i. e. much less arcing was observed and the lower sputtering yield allows for longer operation without the influence of a strongly sputtered racetrack. No substrate was used in this study which makes inserting Langmuir and emissive probes easier. The argon gas pressure was kept at 0.53 Pa, the pulse on-time at 100 µs and the energy delivered per pulse was 6.5 J, while the repetition frequency was set to 50 Hz, 75 Hz and 100 Hz. This increases the off-time from 10 ms, to 13.3 ms and 20 ms. This allows for varying the electron density left from the previous pulse, which was measured by a Langmuir probe placed at the centre of the discharge 10 cm above the target, 10 µs before pulse initialisation. The emission of the plasma was observed with the bandpass filter 750 nm, because the excitation mechanisms of both spectral lines are well-known and the density of argon gas can be assumed to be uniform at the beginning of the pulse. Characteristic parameters for all three discharge conditions are summarised in table 4.4. A few words shall be spent on the temporal resolution. The gate width of

	$f = 50$ Hz	$f = 75$ Hz	$f = 100$ Hz
V_t (V)	-750 ± 8	-698 ± 6	-667.9 ± 2.4
n_e (m^{-3})	1.39×10^{14}	1.20×10^{15}	3.28×10^{15}
$k_B T_e$ (eV)	0.2	0.2	0.2
ω_{pi} (s^{-1})	2.46×10^6	7.50×10^6	1.20×10^7
τ_{pi} (µs)	2.6	0.8	0.5
Matrix sheath (mm)	24.4	8.0	4.7
Child-Langmuir sheath (mm)	107	35	20
Position of intensity maximum (mm)	52	27	24
Velocity (km s^{-1})	24.4 ± 0.7	18.7 ± 1.0	19.9 ± 1.4

Table 4.4: Discharge characteristics when investigating the discharge ignition. Langmuir probe measurements were carried out 10 cm above the target at the centre of the discharge.

the iCCD was set to 100 ns and the intensity was measured in steps of also 100 ns. A measurement labelled by $t = 0$ ns describes the interval from 0 ns to 100 ns and so on. The gate width is defined by the TTL signal produced by the delay generator and was monitored by the oscilloscope. The cable between the oscilloscope and the input of the camera had a length of 2.5 m, adding a delay of the signal of 8.3 ns. The optical path between the discharge and the camera is 0.87 m which makes the iCCD detect intensity emitted 2.9 ns

before it is measured. The total delay is therefore 5.4 ns and can be neglected. Further delay arises from signal processing within the camera, which is unknown. The excitation and emission processes in the plasma also give rise to uncertainties. While the excitation process by electron impact is usually considered fast, the relaxation and emission process is described by an exponential law with the transition probability A_{12} or the decay time τ_{12} which is summarised for all transitions in table 4.2. The lifetime of both excited states is 22 ns and 25 ns for the emission of spectral line 750.4 nm and 751.5 nm, respectively. This is probably the most significant contribution to the delay and the stochastic nature of the emission process make it difficult to correct for it. One can only conclude, that the intensity detected in each measuring interval might be created at the end of the previous interval.

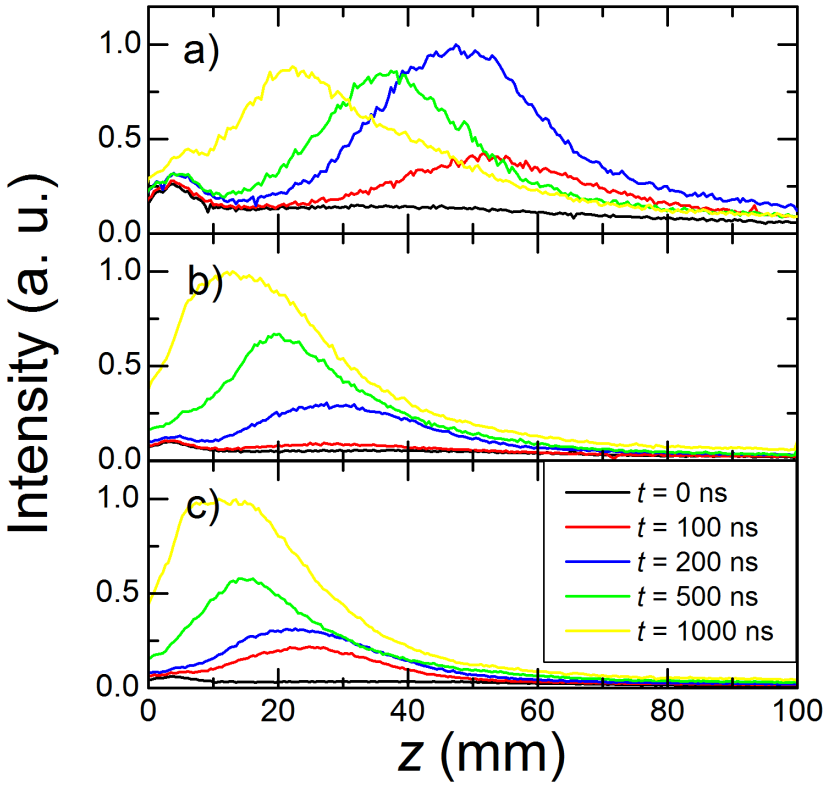

Figure 4.12: Axial intensity distribution during the ignition of HiPIMS discharges operated with a repetition frequency of a) 50 Hz, b) 75 Hz and c) 100 Hz observed for Ar(I) (filter 750 nm). The intensity was summed over all radial positions at a constant axial position.

Images were taken by the camera but this time not Abel-inverted as the information of interest is distributed along the axial direction. Instead, the intensity at a constant axial position z was summed up over all radial positions. The axial profile of the intensity for all three frequencies is shown in figure 4.12. One can see, that an intensity maximum is present in all three cases 100 ns after discharge ignition but for different axial positions. It is closest to the target ($z = 24$ mm) for frequency 100 Hz and can be observed further away from the target for 75 Hz ($z = 27$ mm) and 50 Hz ($z = 52$ mm). This seems to be correlated to the electron density at pulse initialisation, because a lower electron density leads to a thicker sheath and the intensity maximum is observed furthest away from the target ($f = 50$ Hz). However, this position does not coincide with the position of the sheath edge assuming either a matrix or a Child-Langmuir sheath (compare table 4.4).

Additional information was hoped to be obtained by using Langmuir and emissive probes (described in chapters 5.2.1 and 5.3.1). In order to be able to analyse Langmuir probe data, the sheath around the probe wire should be formed completely. This is determined by the slower species, the ions, and is described by the ion response time $\tau_{pi} = 2\pi\omega_{pi}^{-1}$ which was found to be too large to obtain reliable results during the ignition process. The temporal resolution of the emissive probe is also not suitable for the investigation of the ignition process (compare chapter 5.2.2) and the actively biased emissive probe strongly perturbs the ignition process because it can cause ionisation, if biased above the argon ionisation threshold. This discards this technique, as well.

With no further experimental data accessible by the aforementioned diagnostic tools, it was tried to describe the ignition process by a simple Monte Carlo model. The basic principles of the particle pusher and how collisions are treated is summarised in chapter 5.4. Only the changes made to adopt this model to the ignition process shall be given here. A time step of $\Delta t = 10^{-12}$ s was used to solve the equation of motion

$$\frac{d}{dt}\boldsymbol{v} = -\frac{e}{m_e}(\boldsymbol{E} + \boldsymbol{v} \times \boldsymbol{B}) \tag{4.18}$$

using the magnetic field measured for the magnetron and displayed in figure 3.2. The sheath was assumed to be a matrix sheath, due to the slow response of the ions. The axial electric field and the potential within the sheath write [35]:

$$V(z) = -\frac{en_e}{2\varepsilon_0}(d_s - z)^2, \tag{4.19}$$

$$E_z(z) = -\frac{en_e}{\varepsilon_0}(d_s - z), \tag{4.20}$$

with d_s being the sheath width. The radial and azimuthal electric field are generally neglected. Outside the sheath, both the potential and the electric field are zero. The finite rise

time of the target voltage is introduced by a linear increase of the target voltage from 0 V to V_t within a time of $\tau_r = 200$ ns. The sheath width, potential and electric field are then calculated for the target voltage present at the particular time. These conditions describe the motion of electrons which are left from the previous pulse. The electric field also accelerates positive argon ions towards the target which will release secondary electrons on impact. These electrons were treated in a separate simulation run with the sheath fully established and a constant target voltage. To simplify the number of collision processes, the predominant species present in the volume is supposed to be argon gas atoms. Three types of collisions were treated, namely elastic collisions, ionisation to Ar^+ and excitation. The cross-sections were taken from Hayashi [185] and are presented for a wide range of electron energies in figure 4.13. It shall be mentioned that an apparent excitation cross-section was used comprising cross-section of 25 excited states. If an electron collides with an argon, the energy is conserved in the case of an elastic collision (energy transfer is insignificant due to the large difference in the mass of the particles). The electron energy is reduced by 12 eV and 16 eV in the case of excitation or ionisation, respectively. The new direction of motion is calculated as

$$v_x = v \sin\theta \cos\phi, \tag{4.21}$$

$$v_y = v \sin\theta \sin\phi, \tag{4.22}$$

$$v_z = v \cos\theta, \tag{4.23}$$

with v being the speed of the electron after the collision and θ and ϕ two angles picked randomly in the interval $\theta \in (0;\pi)$ and $\phi \in (0;2\pi)$, respectively.

Electron-electron Coulomb collisions are described by its cross section

$$\sigma_{ee} = \frac{8}{\pi} b_0^2 \ln\Lambda_c, \tag{4.24}$$

with the impact parameter b_0:

$$b_0 = \frac{e^2}{4\pi\varepsilon_0 W_r}. \tag{4.25}$$

The kinetic energy of both electrons in the centre of mass system W_r. As the target electron is nearly at rest and the incident electron has an energy of E_{kin}, $W_r = 1/2E_{kin}$. The collision parameter is

$$\Lambda_c = \frac{2\lambda_d}{b_0}. \tag{4.26}$$

One can calculate the time between two collisions τ_c for electron-electron collisions using the discharge conditions summarised in table 4.4. The lowest value for τ_c is obtained

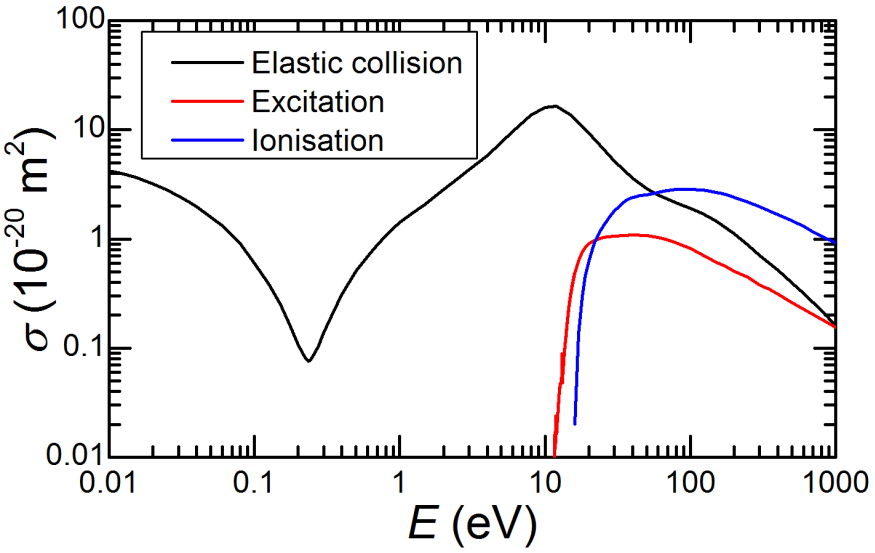

Figure 4.13: Cross-sections for elastic scattering, excitation and ionisation of argon by electron impact [185].

for highest electron densities ($f = 100$ Hz) and low electron velocities. But even with an incident energy of 1 eV the time between collisions is about 2.3 µs and increases to 1.6 ms for an incident energy of 100 eV. Electron-electron collisions are so infrequent that they are neglected here.

The starting point of the electrons was varied at the target surface ($z = 0$ mm) in steps of $\Delta r = 5$ mm from $r = 0$ mm to $r = 75$ mm. The outer-most position was set to 79 mm as the magnetic field was only measured up to $r = 80$ mm. While this approach is suitable for secondary electrons born at the cathode, it is only a simplification for the electrons that are distributed homogeneously throughout the discharge volume before pulse initialisation. On the other hand, the motion of the electrons is strongly influenced by the magnetic field. One can easily trace back the electron position to the target by following the magnetic field line starting at its initial position. The only difference an electron starting from the target would then be the kinetic energy because it will not be accelerated by the full target potential.

It was already mentioned that the electrons are assumed to be homogeneously distributed in the discharge volume and so are they in front of the target. Hence, the same amount of "test" electrons (1000) is started at every position to obtain sufficient statistic. Finally, the position of the electrons are stored for every step of its motion ($\Delta t = 10^{-12}$ s)

in a grid representing the r-z-plane. The mesh was 1 mm$\times$1 mm for $r = 0 \ldots 80$ mm and $z = 0 \ldots 100$ mm. Due to the constant time steps, the two-dimensional map obtained in this way represents the spatial distribution of the electron density.

The calculated electron density distribution profiles for the first 400 ns of the discharge pulse in steps of 100 ns are displayed in figure 4.14. These results were obtained for the expanding sheath, i. e. the target voltage is increased linearly within the first 200 ns of the pulse. One can see that the electrons are immediately repelled by the target voltage. However, their motion is strongly influenced by the magnetic field lines at the outer edge of the discharge, e. g. $r = 75$ mm and $r = 79$ mm. If the magnetic field lines close in front of the target, electrons gyrate around them and can only transfer to another field line by a collision with an argon atom. Especially, during the first 100 ns, one can see how close the electron motion follows the magnetic field lines. This changes with progressing time and an increasing amount of collisions. One can also see, that the electrons starting at the racetrack position ($r = 45$ mm) are well-confined close to the target by the magnetic field. Thus, a maximum of the electron density can be found at this position, which coincides with the intensity maximum close to the target observed in figure 4.12. This density maximum is also the reason why this simulation can only be considered a zero order approximation, because charge separation immediately results in the build-up of a potential and an electric field pointing towards the density maximum. This also implies a radial electric field which is neglected in this model. This potential distribution will of course influence the further development of the plasma during the ignition, as the ion motion is influenced by this radial field and the ions impinge preferably at or close to the racetrack area.

One can still see one remarkable difference between the spatial electron density distributions of the various repetition frequencies. The electrons starting at $r = 5$ mm shall be investigated now. It can be seen that the density originating from this position seems to form an arch above the target for 50 Hz. When looking at 75 Hz and 100 Hz electrons originating from the very same position follow the magnetic field line but do not extend to a full arch. As the electron density is the seem of multiple electron trajectories observed within a period of 100 ns, one can also see, that the electrons do not move so far in the cases of 75 Hz and 100 Hz. This implies that their kinetic energy is lower than for $f = 50$ Hz. This is somewhat counter-intuitive as the lower sheath width should result in a higher electric field resulting in a higher acceleration. The solution lies in the advancing sheath, which is fastest for $f = 50$ Hz, largest sheath thickness but the same target voltage rise time $\tau_r = 200$ ns. As the electron is accelerated by the electric field in the sheath it

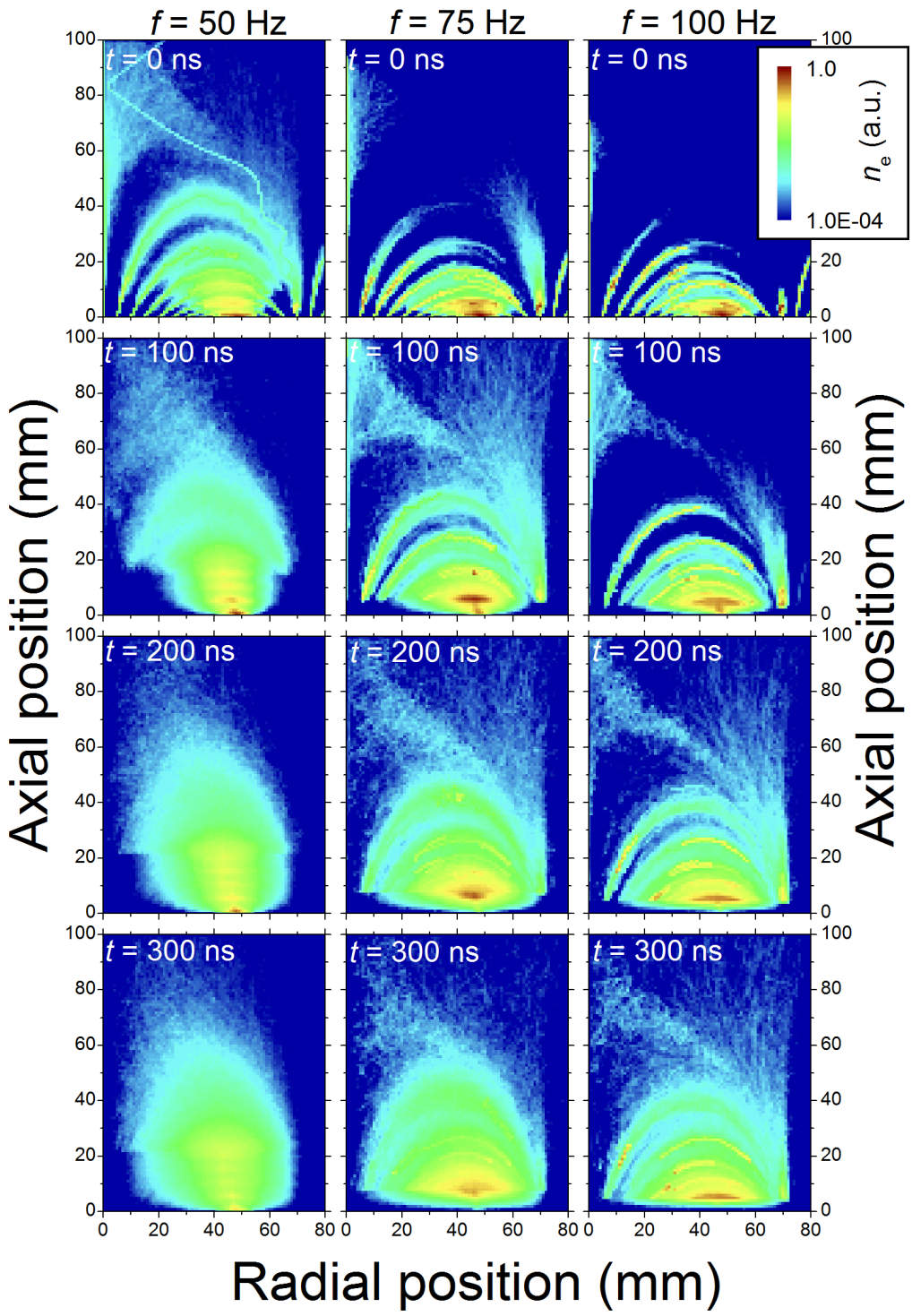

Figure 4.14: Spatial distribution of electrons calculated for the ignition of a HiPIMS discharge for repetition frequencies 50 Hz, 75 Hz and 100 Hz. The remnant electron density was measured by means of a Langmuir probe 10 µs before pulse initialisation.

might become fast enough to "overtake" the sheath edge. The velocity then remains constant unless collisions occur. This effect can for example be seen in the electron density distributions for later times, say $t = 300$ ns. A distinct step in the electron density can be found at the sheath edge. Electrons which were accelerated out of the sheath do not obtain the full energy equal to the target voltage equivalent to eV_t. Thus, they can only submerge into the sheath for a short distance only and not to the target.

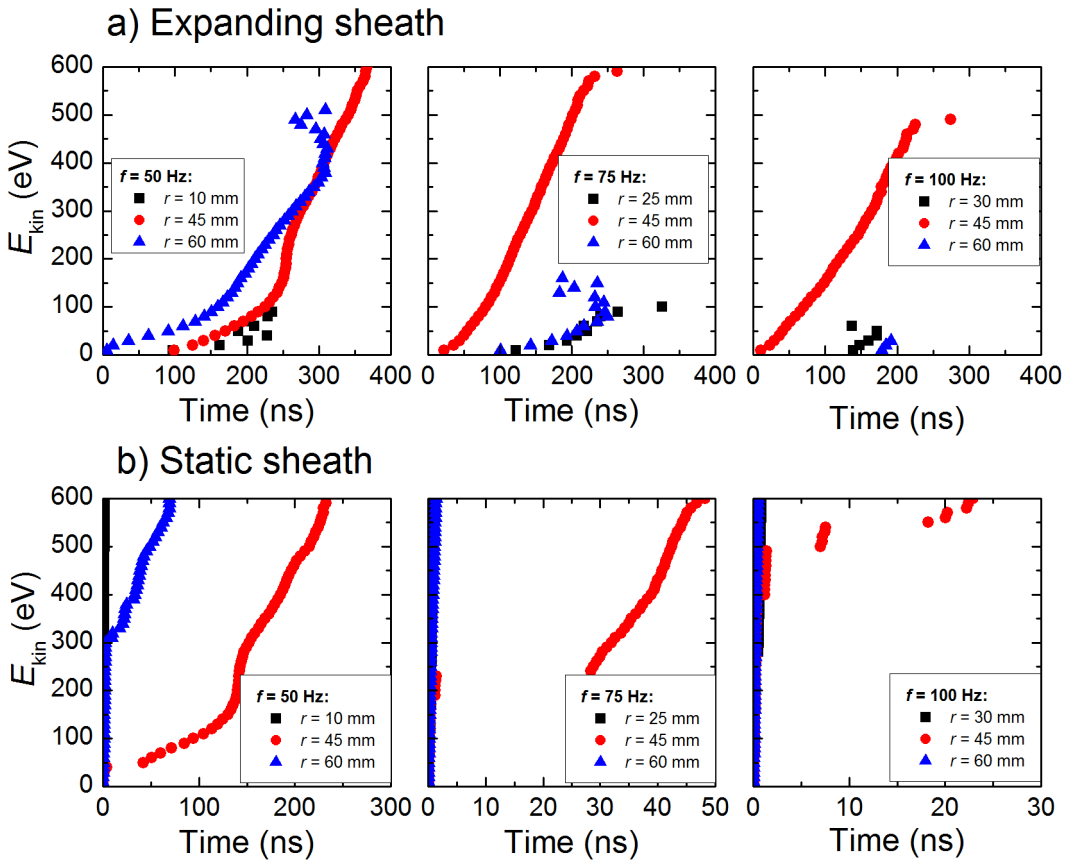

Figure 4.15: Temporal development of the electron energy during discharge ignition for electrons starting at selected radial positions.

This effect was studied in more detail by running the same simulation again and recording the time the electron need to exceed a certain kinetic energy. This time is obtained as an average over 1000 "test" electrons starting at each radial position. One can then display the kinetic energy of the electrons as a function of time, which is done for some example positions for both expanding and static sheath in figure 4.15. It shows that for repetition frequency 50 Hz, the acceleration of the electron is fastest at a starting posi-

tion of $r = 60$ mm, followed by electrons originating at 45 mm and 10 mm. It is worth noting, that electrons from $r = 10$ mm are rarely accelerated to more than 40 eV. The acceleration of electrons is fastest for $r = 45$ mm for $f = 75$ Hz, while the acceleration of electrons starting at 60 mm is strongly reduced. This is also the case for electrons starting at $r = 10$ mm. However, these electrons do not even reach the first threshold of 10 eV. Instead, a slow acceleration of electrons for $r = 25$ mm is shown. The case is worse when operating the discharge at 100 Hz. Acceleration of electrons can only be seen when they start close to the racetrack region. In summary, one can say that a lower electron density results into a thicker sheath, whose edge advances faster due to the same target voltage rise time of 200 ns. This allows electrons to be accelerated to higher energies even if the magnetic field is orientated perpendicular to the target. For higher initial electron densities, the sheath advances more slowly and not so far. The electron motion away from the target has to be impeded by a magnetic field component parallel to the target to allow for sufficient acceleration. Otherwise, electrons would just be repelled by the negative target potential and move away at low kinetic energy. If the sheath is well-established secondary electrons emitted from the target are accelerated to the full target voltage equivalent eV_t. This happens very quickly, within a few nanoseconds, as shown in figure 4.15 b).

The question remains, when the discharge phenomena are governed by the acceleration of remnant electrons and when secondary electrons emitted from the target play a major role. Thus, the ion current collected by the target I_{ion} was modelled by calculating the time argon ions starting at various distances from the target need to arrive at the cathode. For this purpose, the positive ions are regarded to be uniformly distributed in the discharge volume with a density $n_i = n_e$. Only an axial electric field shall be present described by the matrix sheath. Due to the given symmetry, all ions starting within $\Delta z = 0.01$ mm around a selected axial position z arrive at the target at the same time t. The number of ions collected at a given time N_i is simply the number of ions in the volume $\Delta V = \pi R^2 \Delta z$ and the ion density n_i:

$$N_i = n_i \Delta V. \tag{4.27}$$

The radius of the discharge is assumed to be the magnetron radius $R = 80$ mm. The collected charge is obtained by multiplying the result with the elementary charge e. The ion current is derived from the first temporal derivative of the charge. One can see in figure 4.16, that a large number of ions arrive very shortly, about 200 ns, after pulse initialisation when the remnant density is highest ($f = 100$ Hz). These ions cause emission of secondary electrons, which are accelerated by the full target potential and ionise the working gas.

Such high electron energies were measured by Poolcharuansin and Bradley using a Langmuir probe [91]. The plasma is ignited quickly and the onset of the discharge current is observed shortly after the target voltage is ramped up. The declining current after 200 ns is therefore not observed but a continuous increase due to more and more newly formed ions impinging on the target. For a low density of remnant electrons the ion current collected by the target is about an order of magnitude lower than calculated for $f = 100$ Hz. In addition, its maximum is observed with a delay of 500 ns in respect to the onset of the target voltage. The ignition of the discharge needs much more time and the onset of the discharge current shows a longer delay. The intensity profile of plasma-induced emission is therefore dominated by the acceleration of the remnant electrons rather than by secondary electron emitted from the cathode.

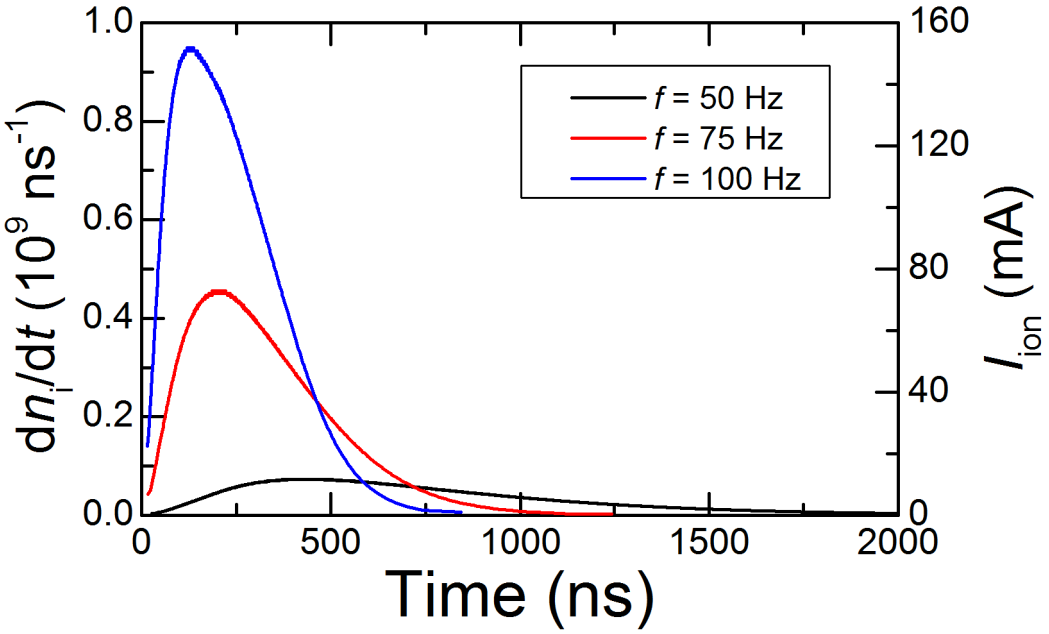

Figure 4.16: Calculated ion current collected by the target during discharge ignition.

In order to evaluate the effect of the electron motion on the plasma-induced emission, one has to look at the energy dependence of the excitation and ionisation processes. The excitation cross-section has a lower threshold energy and a lower maximum (≈ 40 eV) than the ionisation cross-section. However, the excitation cross-section is much lower than the ionisation cross-section for high electron energies (above 100 eV). The population of excited states is therefore preferred at low electron energies. The previous discussion allows to further specify where these particular electrons are found. For a low repetition

frequency, electrons close to the discharge axis $r \approx 10$ mm fulfil the criterion of a quick acceleration which is limited to lower energy levels < 50 eV. Following the motion of these electrons, one can find them at an axial position between 40 mm and 50 mm above the target, where they excite argon atoms which subsequently emit light. Is the repetition frequency and hence the remnant electron density higher, the region which exhibits electrons at favourable energy for excitation is found closer to the target as the start position of the electrons is closer to the racetrack where the magnetic field lines confine the electrons closer to the target. The intensity maximum can then also be expected closer to the target, which is indeed observed (compare figure 4.12). With increasing time, electrons closer to the target loose some of their energy due to inelastic collisions, mainly ionisation, until it is in a range for efficient excitation. The intensity maximum then steadily moves towards the target. However, the exact speed of this happening cannot readily be predicted with the present with the current simple model.

There is also an upper limit for the observation of an intensity maximum immediately after pulse initialisation. If the remnant electron density is too low, the sheath extends far away from the target and most of the electrons originating from most if not all radial positions are accelerated to too high energies too quickly and one cannot observe an intensity maximum within the first 200 ns of the pulse. This maximum might still occur at a later time after the electrons cooled down to an energy beneficial for frequent excitation. This might be the case, when sputtering the aluminium-doped zinc target, where the intensity maximum was observed with a delay of 800 ns but still about 50 mm above the target.

The upper limit for the axial position of the intensity maximum appears to be about 50 mm which is well below the magnetic null, the position of the last magnetic field lines still closing in front of the target. This can be explained by comparing the gyro radius between these two positions. The magnetic induction is 4.3 mT at $z = 50$ mm, which leads to a gyro radius of 7.8 mm for an electron energy of 100 eV. On this length, the magnetic field decreases further and the effective radius might well be even larger. If the guiding centre of the electron motion is at 70 mm, the gyro radius of an electron with the same energy is 39.7 mm ($B = 0.4$ mT). This value is so large that one can hardly speak of a magnetised electron and it can easily cross the magnetic field line.

In summary, the intensity maximum of the plasma-induced emission found remote from the target during discharge ignition is a unique feature of the ignition process. It was found that its position is not directly related to the position of the sheath edge. Analysing the trajectories and the energy of the electrons gives a hint, that the emission is caused by remnant electrons accelerated in the sheath during the initial time of the HiPIMS pulse.

It was shown, that the magnetic field configuration and the remnant electron density are the predominant influencing factors on where and when this maximum occurs. It could be demonstrated how the ignition process benefits from a high repetition frequency, i. e. a short off-time and thus a high density of electrons remaining from the previous pulse. Further investigation should include a self-consistent model to analyse the ignition process in more detail.

4.4.4 Stage B-C: Turbulent plasma

The stages B and C connect the discharge ignition with the fully established highly ionised discharge. This turbulent stage is characterised by a strong increase of the discharge current accompanied by an increase of the electron density [91]. The intensity profile emitted by the plasma during stage B, the plasma built-up is asymmetric but reveals characteristic similarities between all species investigated (compare figure 4.10 B). This leads to the conclusion that the phenomenon is caused by electrons rather than by an asymmetric distribution of the working gas or the sputtered metal vapour. Comparing images of one sequence, intensity maxima appear to change their lateral position and travel away from the target. This indicates the electron drift above the target superimposed with a motion in axial direction away from the target, similar to an ion acoustic wave.

Measurements of the plasma potential by means of an emissive probe showed the presence of strong electric fields in the order of $10\,\mathrm{kV\,m^{-1}}$ due to strong charge separation during this early stage of the discharge (compare figures 5.9 and 5.10). Electrons moving under the influence of such strong fields can gain enough energy to excite or ionise particles within a short distance of only a few millimetre. This condition is largely different from the later stage of the HiPIMS pulse or during continuous (DC) magnetron sputtering, where only secondary electrons emitted from the target gain sufficient energy as they are accelerated in the high voltage sheath adjacent to the target. The sheath has a typical width of a few millimetres, but it is much more advanced during the early stage of the discharge, compare table 4.4. It is therefore possible, that the asymmetric intensity distribution indicates the presence of avalanches, which are present during plasma built-up. One also to consider the electron transport during this stage of the pulse. The discharge current continuously increases during this time and has to be compensated by an equal current towards the grounded chamber walls. However, the electron density close to the walls is probably too low to balance the fluxes in (from the cathode) and out (to the grounded walls) of the plasma. This necessitates enhanced electron transport from the discharge volume towards

the chamber walls. It might be possible that a rather turbulent electron transport is required which manifests itself in the presence of very localised regions of ionisation.

Further studies were carried out to investigate the influence of the magnetic field configuration and the boundary conditions by rotating the magnetron source and by changing the pressure. These experiments were complicated by problems with the reproducibility of the measurements. The observed phenomenon is extremely sensitive to the exact stage of the discharge. The onset of the discharge current can change by about ± 0.5 µs from one set of measurements to another, which results in a change of the recorded image for the same temporal position. Further problems arise as the entire discharge drifts with time. Successively recording images for the same temporal position showed good agreement whereas images recorded 30 minutes later revealed a completely different distribution of the intensity. However, it was found that the phenomenon seemed to disappear when the pressure is reduced. For example, a decrease of the pressure from 0.53 Pa to 0.2 Pa resulted in symmetric images.

Further hints on a turbulent plasma stage can be found in the relatively large standard deviation of the measured plasma potential during the initial stage of the discharge and noisy current voltage characteristics recorded by Langmuir probes during this stage of the discharge. Due to the problems with the reproducibility of measurements, it is suggested to use a camera that allows for recording images with a high frame rate, e. g. a streak camera, to study the phenomenon in more detail.

The plasma-induced emission for argon neutrals (filter 750 nm) is found to appear very similar to a DCMS discharge (compare figures 4.7 and 4.9). The intensity is highest where the magnetic field lines are orientated parallel to the target and a high electron density can be found [76]. However, there is also a striking difference between this stage and a DCMS discharge. The overall intensity maximum is found detached from the target and moving away from it. The position of the intensity maximum of Ar(I) emission is displayed over time in figure 4.17 for HiPIMS discharges operated with a titanium target. One can see, that the position of highest intensity increases linearly with time and one obtains a velocity of $(1.62 \pm 0.09)\,\mathrm{km\,s^{-1}}$ and $(1.74 \pm 0.17)\,\mathrm{km\,s^{-1}}$ for a working gas pressure of 0.53 Pa and 1.33 Pa, respectively. The intensity maximum is probably caused by a travelling electron density maximum, not unlike an ion acoustic wave originating from the rapid sheath motion during discharge ignition, which was already described by Gyalfson et. al. [93]. One can compare the measured speed with the ion acoustic speed:

$$v_b = \sqrt{\frac{k_B T_e}{m_{Ar}}}, \tag{4.28}$$

which gives a value of 2.2 . . . 2.7 km s^{-1} for an electron temperature of 2 . . . 3 eV. This is in the same range as the measured value, which also does not show any pressure dependence just as it is suggested by equation 4.28.

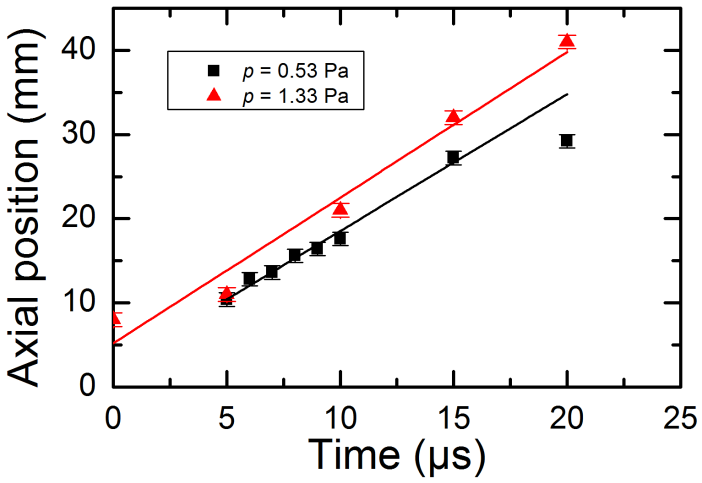

Figure 4.17: Position of the intensity maximum of the Ar(I) emission (filter 750 nm) during the turbulent plasma stage. The HiPIMS discharge was operated with a titanium target (see table 4.3 for discharge parameters).

As the high discharge current suggests a high sputtering rate, Hala et. al. found an expanding metal emission indicating the transport of sputtered metal vapour [95]. This could hardly be observed in the present study, maybe because of the ionisation of the sputtered particles immediately above the target, which is described in the next section.

The travelling intensity maximum can also be found in the emission of all species when sputtering the aluminium-doped zinc target. However, this feature is superimposed with a strongly asymmetric intensity profile which suggests the presence of a highly turbulent, non-uniform plasma. The intensity profile was found not to be stable in time but to vary more or less from discharge pulse to discharge pulse. It was recently found by Kozyrev et. al. and Anders et. al. that this behaviour is by no means an exception, but that the anomalous transport observed in HiPIMS discharges might be caused by localised ionisation regions drifting above the racetrack. The gate width and the exposure time was probably chosen too long to find this behaviour also at a later time of the discharge. It is not quite clear, why this asymmetric behaviour could still be observed between 5 µs and 15 µs, despite the not so suitable measuring parameters. Maybe, these ionisation regions

have not fully been formed at this time or do not drift fast enough to smear out the effect when observed time-averaged.

4.4.5 Stage D-F: Highly ionised discharge

This stage of the discharge is characterised by a large discharge current, which implies high electron densities and thus, a high degree of ionisation. It starts about 20 µs after pulse initialisation for sputtering titanium and after 30 µs for the Al_5Zn_95-target and comprised the labels D, E and F. The main features recognised in the spatial distribution of the intensity are rarefaction of the working gas, a high intensity of metal neutrals (Ti(I) and Zn(I)) emission revealing two distinct maxima, and the emission of argon and zinc ions close to the target, right above the racetrack.

The intensity is proportional to the electron density, the rate coefficient, which is a function of the electron temperature, and the density of particles in the ground state (compare eq. 4.8). In order to evaluate, the rarefaction, the spatial distribution of both the electron density and the temperature most be known to calculate the spatial distribution of the argon atoms. Without these quantities, obtained from a separate experiment, like a Langmuir probe measurement for example, no further conclusion can be drawn, but that there is gas rarefaction, due to lack of Ar(I) emission in front of the target (compare fig. 4.9 and 4.10). As the electron density was measured to be highest in the plasma torus [76] and the electron temperature is usually considered high in this region [54], too, the density of argon neutrals must be depleted.

The most important feature of the high-current, or metal-dominated, stage is the large sputtering and ionisation rate. Sputtering of target material is caused by ions impinging on the cathode with sufficient energy. The flux of sputtered particles reads:

$$\Gamma_s = Y_i(E)\Gamma_i, \tag{4.29}$$

with the sputtering yield $Y_i(E)$ and the flux of impinging ions Γ_i. These ions are also responsible of secondary electron emission from the cathode, which gain considerable energy in the sheath and sustain the discharge by either ionisation or dissipating their energy among the background electrons, hence heating the electron system. The measured current at the target I_d is given as:

$$I_d = A_t e\Gamma_i(1+\gamma_{see}), \tag{4.30}$$

with A_t being the target surface area and γ_{see} is the secondary electron emission coefficient. For simplicity, the ions are assumed to be singly ionised. As both the sputtered flux and

the discharge current are proportional to the impinging ion flux, the spatial distribution of the discharge current at the target shall be used as a measure of the impinging ion flux and hence the sputtered metal flux expanding in the plasma. The spatial distribution of the discharge current was measured by Clarke el. al. for sputtering a copper target [186]. As the target material and the temporal development of both the target voltage and the discharge current differ from the present study, the measured data cannot be used. However, it was found that the full width at half maximum (FWHM) w_d can quite accurately be described by a model proposed by Wendt et. al. for DC magnetron sputtering [187]. The width of the discharge current distribution w_d (in mm) depends on the discharge current I_d, the target voltage V_t and the magnetic induction (in Gauss):

$$w_d = 94.7 \frac{V_t^{1/10} I_d^{1/5}}{B^{4/5}}. \tag{4.31}$$

This so-called "thick sheath"-model requires the sheath thickness in front of the target to be larger than the gyration radius of an electron with a kinetic energy of the target potential equivalent ($E_{kin} = eV_t$). This condition is not necessarily fulfilled in this case, because the sheath is typically less than 1 mm thick (Child-Langmuir law) and a gyration radius of 2.4 mm can be calculated for an electron with a kinetic energy of 800 eV and a magnetic induction of (40 mT). However, the close agreement between measurement and Wendt's model reported in [186], justifies the use of this model as a benchmark for the spatial distribution of the emission profiles.

Figure 4.18 shows the calculated width of the discharge current distribution at the target calculated using Wendt's model, together with the time-resolved target voltage and the discharge current monitored by the oscilloscope and a magnetic field of 400 Gauss (40 mT). It is displayed against the instantaneous discharge power $P(t) = V_t(t)I_d(t)$. The width of the discharge current shall be compared to the distance between the two distinct maxima of the zinc neutrals emission and the width of emission of argon and zinc ions, as the discharge current comprises mainly these two species.

At a first glance, one can see, that the calculated width is much higher than any of the widths obtained from the optical measurements. This underestimation of the width is caused by the fact, that the clamp ring blocks the view to the initial 4.5 mm above the target. Thus, the intensity profile immediately above the target is not accessible. This setup is necessary to provide the target with sufficient contact to the cooling system to avoid overheating as instantaneous powers higher than 100 kW are applied to it. In addition, a large thermal load during sputtering can cause significant intrinsic stress leading to deformation of the target, which makes firm mechanical fitting necessary.

The width of the discharge current increases and decreases with increasing and decreasing discharge power, and so does the distance between the two maxima of Zn(I) emission and the width of the Ar(II) emission. On the contrary, the width of Zn(II) remains almost constant when increasing the discharge power and increases when the discharge power is decreased. However, the contribution of zinc ions to the discharge current and the sputtering process might be arguable as the discharge evolves into a more DC-like state when the discharge power decreases, indicating less ionisation of the sputtered flux which is also confirmed by the drop of Zn(II) emission in the second half of the discharge pulse. The majority of the discharge current and the sputtering might already be carried by argon ions again.

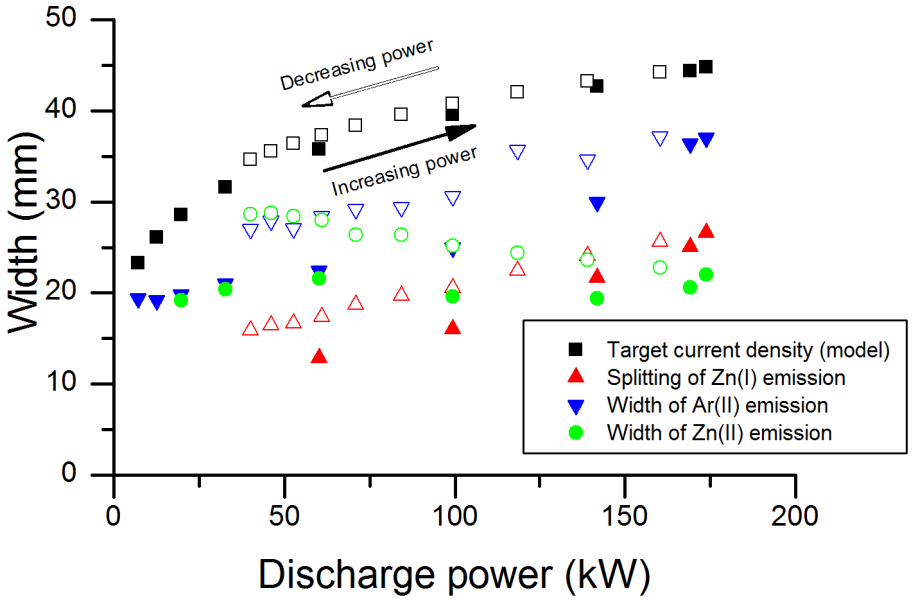

Figure 4.18: Comparison of the width of the discharge current with the spatial distribution of the plasma-induced emission. The solid symbols indicate increasing discharge power, while open symbols represent the development when the instantaneous discharge power decreases.

The increasing width of the argon ion emission profile with increasing power suggests that the density distribution of argon ions is getting wider. As the ions are extracted perpendicular to the target by the strong axial electric field present in the sheath and the extended magnetised pre-sheath. The wider distribution of argon ions leads then directly to a wider discharge current distribution and an increased width of sputtering and hence the racetrack,

as reported by Clarke et. al. [186]. The sputtered particles are preferably ejected in a direction perpendicular to the target surface. The actual distribution follows a cosine law eq. 4.17 [48], which makes particle ejection far off the normal direction of the target very unlikely. This allows the increased width of the sputtering profile to be observed in the optical emission of Zn(I). This is particularly true close to the target, where most of the sputtered particles have not suffered from collisions. The splitting of the Zn(I) emission profile is then a convolution of the wider sputtering profile and ionisation in front of the target.

When the discharge power is reduced, the opposite effect is observed. The width of the argon ion emission, the width of the target current distribution, the sputtering profile and finally the distance between the two intensity maxima in the emission of zinc atoms decrease. This decrease appears to be slower than predicted by the model for the target current width, which is plausible as it was developed for a stationary case, DC magnetron sputtering. In pulsed discharges, the time the plasma needs to adjust to altered boundary conditions must be considered. While the electron system can respond almost instantaneously, high plasma frequency, the time for sufficient ionisation, acceleration of the ions towards the target, sputtering and the motion of the sputtered particle into the area of detection can easily be in the microsecond range. Thus, the rise of the experimentally obtained widths is expected to be slower than predicted by Wendt's model and the decrease of the width, on the other hand, will also occur with a delay.

The splitting of the emission of titanium neutrals was found to be generally higher, up to 33 mm compared to 27 mm in the case of the aluminium-doped zinc target. This seems plausible due to the higher discharge current and the lower ionisation threshold for titanium (6.83 eV compared to 9.39 eV for zinc [177, 179]). Another effect, has yet been omitted: The change of the magnetic field due to large Hall currents, may alter the magnetic field configuration of the magnetron [27]. As plasmas are diamagnetic, these magnetic fields will reduce the field created by the permanent magnets, which will in turn reduce the magnetic confinement and might lead to an additional widening of the sputtering profile. Recent measurements on HiPIMS discharges have confirmed the temporal and spatial development of the intensity distribution of argon atoms and ions and metal atoms and ions for sputtering titanium, aluminium and chromium [133].

4.4.6 Stage G: Pulse termination

The discharge on-time ends with the termination of the high voltage applied to the cathode, which ends the production of energetic secondary electrons sustaining the discharge. One can now observe the plasma afterglow. Within 1 µs the target voltage increases to zero, whereas the discharge current slowly approaches zero, see figure 4.19 (sputtering Ti with a pressure of 0.53 Pa). This slow approach might be caused by positive ions reaching the target, which were accelerated towards the cathode in the discharge on-time and continue their motion due to their inertia.

Figure 4.19 also shows the temporal development of the intensity observed with filter 750 nm at the discharge axis 5 mm above the target. When the target voltage is terminated, the intensity immediately drops by about an order of magnitude before it decays more slowly. The process can be described by a double exponential decay characterised by the two time constants $\tau_1 = (0.53 \pm 0.05)$ µs and $\tau_2 = (3.5 \pm 0.4)$ µs. Assuming that electron impact excitation is still the dominant mechanism of populating the excited states of argon atoms, one has to consider the temporal development of the rate coefficient, the electron density and the density of particles in the ground state (compare eq. 4.8). The density of argon atoms in front of the target might still be depleted from the sputtering in the discharge on-time. However, it is thought the temporal variation of this density due to diffusion of argon atoms back into the discharge volume can be neglected on this short time scale of about 10 µs. Thus, the rate coefficient and the electron density remain. The two spectral lines observed with filter 750 nm are emitted by electron transition from the $2p_1$ into the $1s_2$ level (750.4 nm) and from the $2p_5$ into the $1s_4$ level (751.5 nm). Both levels are preferably populated by direct or cascade electron impact excitation out of the argon ground state, rather than out of one of the two metastable argon levels $1s_3$ and $1s_5$ [182]. This excitation process has a threshold energy of 13.48 eV and 13.27 eV for the $2p_1$ and the $2p_5$ state, respectively. It can therefore be concluded that this excitation and hence, the intensity observed for these spectral lines is very sensitive to the loss of energetic electrons [181]. Indeed, the electron density distribution functions measured by Poolcharuansin and Bradley by means of a Langmuir probe show this behaviour [91]. Figure 4 c) in that reference summarises EEDF's measured at 100 µs, i. e. shortly before pulse termination, and at 110 µs, in the early afterglow. It can be seen that the EEDF recorded at 100 µs has an energetic tail extending up to 20 eV, whereas at 110 µs a maximum energy of only 10 eV was obtained. At the same time the electron temperature only drops from 1.5 eV to 1.2 eV [91].

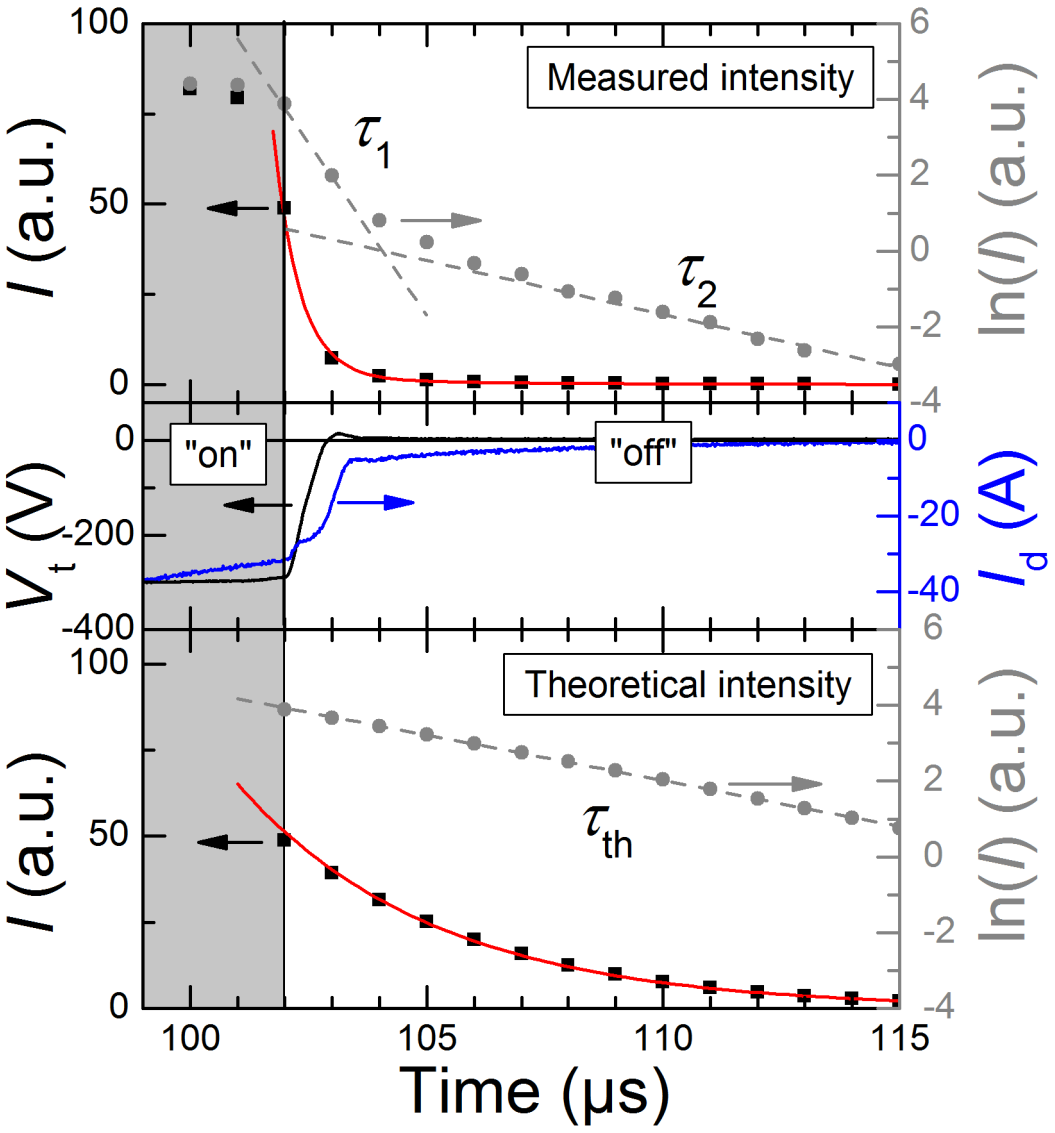

Figure 4.19: Temporal development of the plasma-induced emission of Ar(I) (filter 750 nm during pulse termination. The intensity was observed 5 mm above the target at the discharge axis. Discharge parameters for sputtering Ti at argon pressure 0.53 Pa can be found in table 4.3

The longer decay time of (3.5 ± 0.4) µs is usually attributed to the decay of metastable argon atoms [188] and mainly occurs for spectral lines where population out of the metastable argon levels plays a significant role, for example 763.5 nm and 811.5 nm. The main difference between this study on HiPIMS discharges and the investigations with optical emission spectroscopy on pulsed DC discharges [181, 188] is the by about two orders of magnitude higher electron density for HiPIMS. It is therefore possible to observe this additional decay because the intensity emitted is high enough. In order to investigate the second decay of the intensity further, one has to calculate the rate coefficient and the electron density in the interval 102 µs to 115 µs. For this purpose, the electron density and temperature reported in ref. [91] will be used, as these measurements were carried out in the same vacuum chamber, with the same magnetron sputtering source and power supply under very similar conditions. For a pressure of 0.53 Pa the electron density was measured to be 6.25×10^{17} m^{-3} and the electron temperature was 1.5 eV, just before pulse termination (at 100 µs). The decay times for the electron density and temperature were reported to be 30 µs and 52 µs, respectively. Using this data, the temporal development of both parameters in the first 15 µs of the afterglow can be calculated. The rate coefficient for the population of the excited argon states k_{2p} is calculated using an analytical formula as published in [35, 189]:

$$k_{2p} = 1.4 \times 10^{-14} \left(\frac{k_B T_e}{eV} \right)^{0.71} \exp - \frac{13.3eV}{k_B T_e}, \tag{4.32}$$

which gives the rate coefficient in $\mathrm{m^3\,s^{-1}}$. As the density of argon atoms is assumed to be constant during the early stage of the afterglow, the emitted intensity is proportional to the product of rate coefficient and electron density. This product is calculated from the experimental data for electron density and temperature and normalised to the intensity measured at 102 µs for better comparison. This theoretical intensity is also shown in figure 4.19. One can see, that this curve can be described by a single exponential decay with a time constant of (4.16 ± 0.04) µs, which agrees reasonably well with the measured decay (3.5 ± 0.4) µs. It can therefore be concluded, that the initial decay is caused by the efficient loss of energetic electrons, whereas the second time constant reflects the decay of both the electron density and temperature.

Figure 4.20 a) shows the two times constants obtained for the decay of the emission from argon and titanium atoms at different axial positions along the discharge axis. It can be seen, that the decay of the intensity of both species is characterised by a double exponential decay with the time constants τ_1 and τ_2, except for Ti(I) emission for axial po-

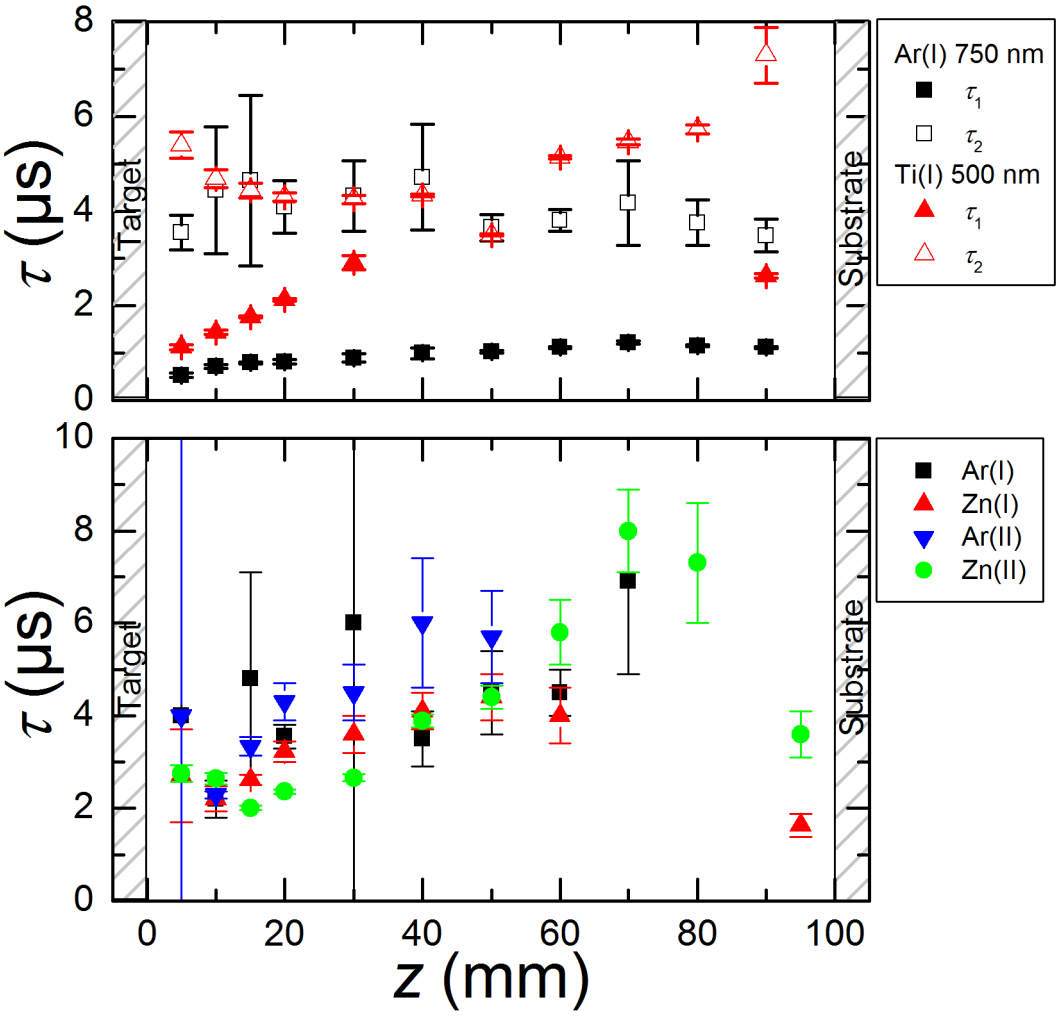

Figure 4.20: Spatial distribution of the decay of plasma-induced emission after pulse termination for a) sputtering titanium at 0.53 Pa and b) sputtering an aluminium-doped zinc target at 1.33 Pa.

sitions between 40 mm and 80 mm above the target. However, we shall start discussing the results for Ar(I) 750 nm, first. The first decay constant increases with increasing distance to the target from (0.53 ± 0.05) µs to (1.22 ± 0.03) µs obtained 70 mm above the target, which coincides with the position of the magnetic null. It then decreases approaching the substrate position, (1.12 ± 0.02) µs at $z = 90$ mm. The second decay time shows no clear trend but remains rather constant at 4 µs. The findings suggest, that energetic electrons are most efficiently lost at the boundaries, close to the target and the substrate, because of the short escape path for the electrons. The intensity development described by the theoretical consideration using data provided by Poolcharuansin and Bradley [91] seems to be applicable throughout the discharge volume, which suggests that the majority of electrons having lower energy is lost with similar rates everywhere in the discharge.

The decay process of the Ti(I) emission is more complex because the particle density of titanium atoms is not necessarily a constant in time. With the termination of the target voltage at the end of the HiPIMS pulse, the sheath in front of the cathode collapses. Positive ions are then no longer accelerated by the axial electric field in the sheath and pre-sheath region to kinetic energies of several 100 eV. Hence, sputtering, the source of titanium atoms, stops with the end of the pulse. Subsequently, the sputtered flux created just before pulse termination expands into the discharge volume. Macák et. al. measured a velocity of about 2500 $\mathrm{m\,s^{-1}}$ for this expansion [78]. This means, that titanium atoms can travel about 3 cm to 4 cm during the initial time of the afterglow, 13 µs are investigated here. It is worth noting, that the velocity given here is only the average of an extended ion velocity distribution function. Some atoms might be faster, others might move more slowly.

Close to the target, the initial decay of Ti(I) emission is fastest giving a first time constant of (1.12 ± 0.05) µs which is higher than observed for Ar(I). This might be caused by an increasing titanium atom density due to the passing sputtered flux and by the lower excitation threshold of only 3 eV (compare table 4.2). Both effects will slow down the initial decay. The second decay time is (5.4 ± 0.3) µs and probably represents the loss of intensity due to the decay of the electron density and temperature as explained for A(I). With increasing distance from the target, the first decay time increases while the second decreases. This effect is probably caused by the passing sputtered flux, which increases the titanium atom density when arriving at the position and decreases it after passing through. The arriving sputtered flux compensates for the rate loss, due to the decay of the electron density and temperature, which increases the first time constant. After the "packet" of sputtered particle has passed, the decreasing Ti(I) density enhances the decay of the emission and decreases the second time constant. At axial positions between 40 mm and

80 mm, these effects appear to cancel out. Only one decay time can be observed which lies in-between the initial and second time constant observed closer to the target. At 90 mm above the target, the influence of an oncoming flux of sputtered particles on the initial decay is only marginal, as the titanium atoms do not propagate fast enough to reach this position. Two decay constants can be measured again. The first one describes the loss of energetic electrons and the second one is the highest measured throughout the discharge volume and is probably affected by the oncoming sputtered flux, which slows down the second decay of intensity.

Investigations were extended to observe the spatial and temporal evolution of argon and metal (Zn) ions, when sputtering an aluminium-doped zinc target. The decay times calculated for all species at different axial positions along the discharge axis are shown in figure 4.20 b). In this case, the initial drop of the intensity can hardly be seen and the decay of the intensity is fitted by a single exponential decay with a time constant τ in the order of a few microseconds, as τ_2 observed for sputtering titanium. One can see, that the decay times strongly increase with increasing distance to the target. At several axial positions no decay time could be calculated. The intensity decreases at these positions, but so slowly that the decay appears to be linear rather than being exponential. This behaviour is particularly pronounced between the magnetic null ($z = 70$ mm) and the floating substrate. This suggests that the transport of electrons out of this region is strongly impeded.

For better analysis, the spatial intensity distributions for sputtering the Al_5Zn_{95}-target at various times after pulse termination are shown in figure 4.21. The intensity observed with each filter was normalised to its maximum which occurs at 102 µs for all species. A logarithmic scale was chosen to also visualise the spatial distribution of the intensity even 13 µs after switching off the discharge.

During the process of terminating the target voltage, which takes about 1 µs, the intensity of each species is predominantly emitted in the region adjacent to the target where energetic secondary electrons are confined by the combination of magnetic field and the negative target voltage. Except for emission observed for Ar(I), the intensity drops quickly towards the substrate (not so pronounced due to logarithmic scale). This confirms the idea, that secondary electrons emitted by the target gain substantial energy in the sheath and are able to ionise or excite particles right above the target. As the motion of these electrons is strongly influenced by the magnetic field, its configuration is represented by the spatial distribution of the intensity of the plasma-induced emission (compare DCMS discharge, chapter 4.3). When the target voltage is switched off, the source of energetic electrons

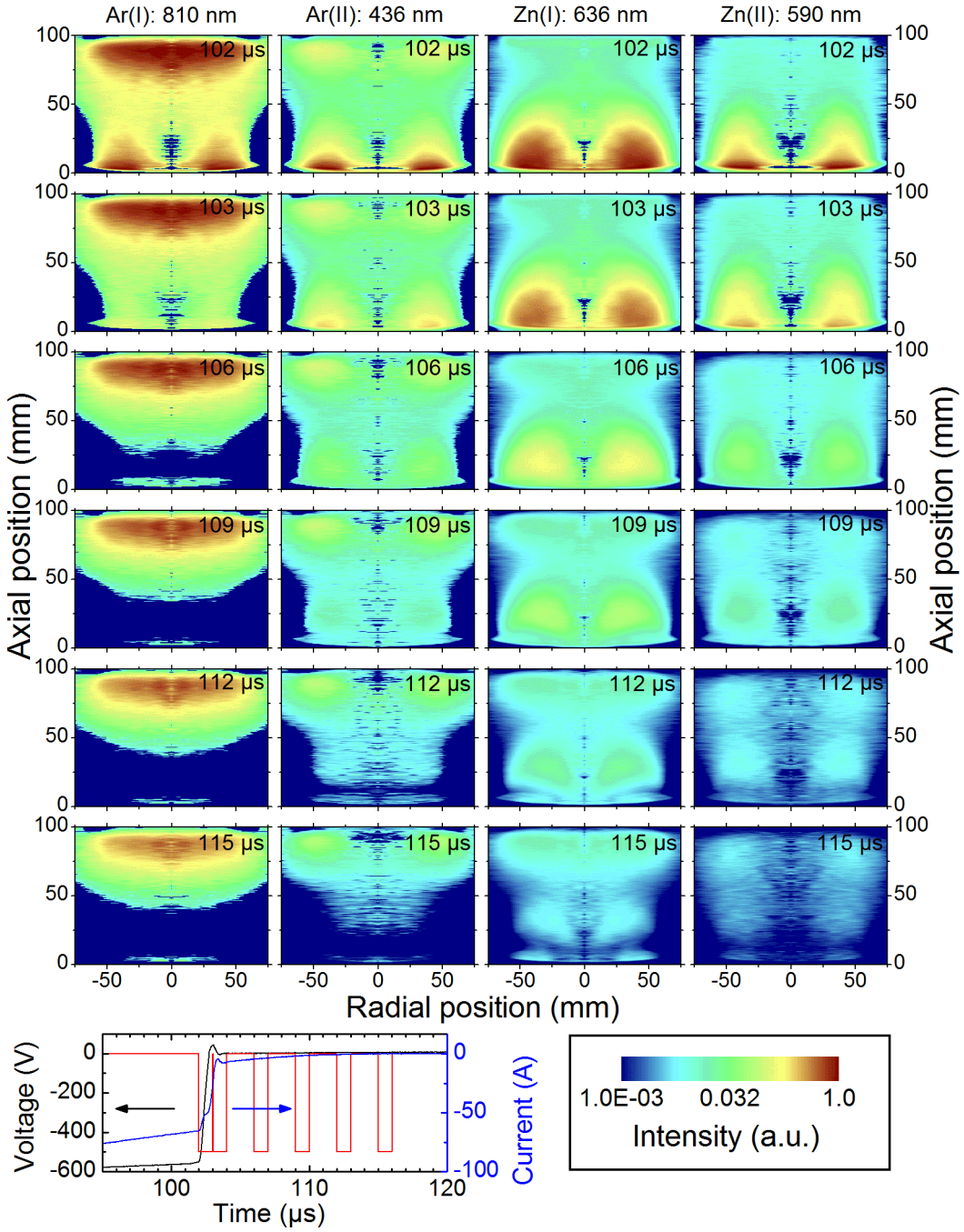

Figure 4.21: Spatial distribution of the plasma induced emission during the transition into the afterglow when sputtering an aluminium-doped zinc target at 1.33 Pa.

drains and the intensity in the vicinity of the target drops quickly, as it can be seen in figure 4.21. However, the emission close to the substrate is sustained for much longer.

The spatial distribution of the intensity emitted by argon atoms shall be considered first, because it is thought that it is related closest to the distribution of electron density and temperature. It is assumed, that the density of argon atoms is a constant in time for the 13 µs investigated. Furthermore, this density shall vary only little spatially close to the target, so that this influence can be neglected. The electron temperature was found to change only slightly during the discharge pulse (figure 5.19, which is also assumed for the early afterglow. The intensity distribution then directly reflects the electron density distribution, which shows a distinct maximum at about 80 mm above the target at the discharge axis. This is well between the magnetic null ($z = 70$ mm) and the floating substrate placed 100 mm away from the target. The maximum can be explained by investigating the transport of electrons in the potential and magnetic field configuration, which is depicted schematically in figure 4.22.

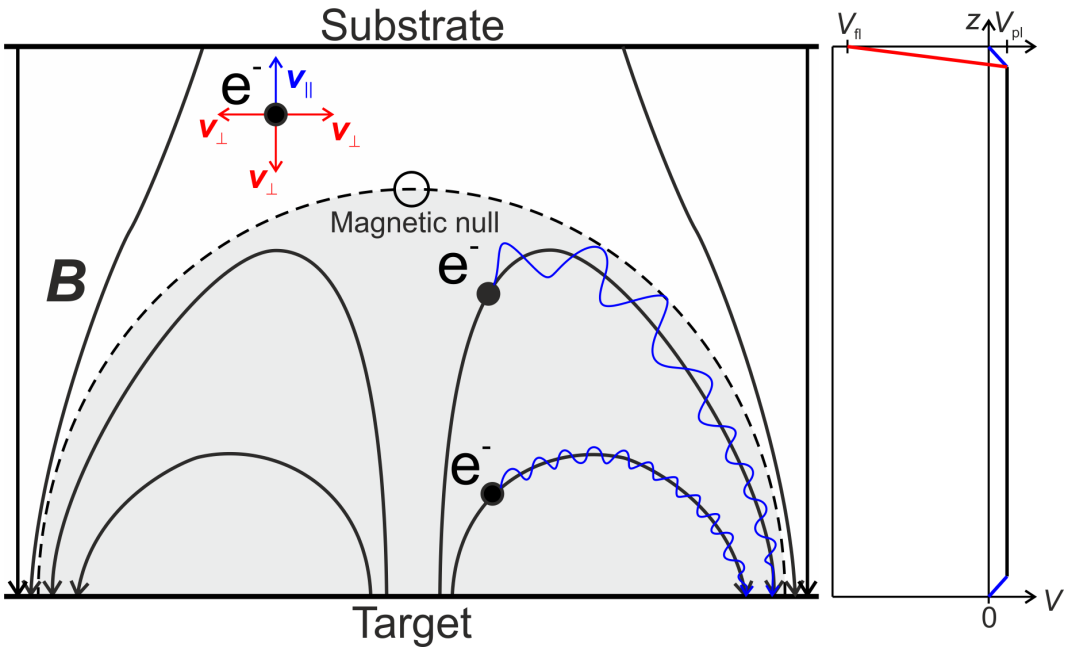

Figure 4.22: Schematic drawing of the magnetic field and potential distribution of the magnetron and the possible transport of electrons.

The space potential V_{pl} in the bulk plasma is usually considered to be situated above ground level by about $0.5 k_B T_e/e$ [35]. It varies little spatially in magnetron discharges during the pulse off-time as it was shown for pulsed-DC magnetron sputtering discharges

[190, 191]. Hence, the potential drop between the plasma and the grounded target is $0.5k_BT_e/e$, where as a higher potential barrier $\Delta V = V_{pl} - V_{fl} \approx 5.2k_BT_e/e$ exists towards the floating substrate. This reduces the flux towards the target by $\exp -0.5 \approx 0.61$ and much more significantly the flux to the substrate by $\exp -5.2 \approx 5.5 \times 10^{-3}$. The configuration of the magnetic field only allows electrons in front of the target where they intersect the target surface to be guided towards the target where they can escape the discharge if they have sufficient energy ($\geq 0.5k_BT_e$). This region is indicated by the grey background colour in figure 4.22 and possible electron trajectories are shown. The curved magnetic field lines increase the path of the electron towards the the grounded target which results in a retarded loss of electrons further away from from the target. This is the reason, why the decay constants increase with increasing distance to the target. Above the magnetic null, the situation is slightly different. A high potential barrier of $5.2k_BT_e/e$ prevents most electrons from escaping the discharge through the floating substrate. In addition, both the radial motion towards the chamber walls and the axial motion towards the target are impeded because of the transverse magnetic field. There appear to be escape routes along the discharge axis and at large radial positions where the magnetic field is orientated perpendicular to the target. As the magnetic field strongly increases towards the target, some electrons might also be reflected by a magnetic-mirror effect, which makes it arguable how efficient this escape route actually is. The effect of the magnetic field configuration on the motion of the electrons above the magnetic null has nicely been visualised by Welzel et. al. [192]. In summary, the combination of the magnetic field configuration of the strongly unbalanced magnetron and the potential barrier towards the floating substrate causes a local maximum of electron density between the magnetic null and the substrate.

The emission of the other species, argon ions, zinc atoms and ions, also decay most slowly close to the substrate, which is also caused by the impeded transport of electrons out of this region. However, the case is more complex for these species, because one cannot assume that these particles are distributed homogeneously in front of the substrate. Furthermore, the density might also vary temporally, for example due to the arrival of the sputtered flux of zinc atoms. This sputtered flux is also supposed to be largest in the direction perpendicular to the target surface. One would therefore expect, that the emission of both zinc atoms and ions has its maximum above the racetrack ($r = 45 \ldots 50$ mm) close to the substrate. Indeed, such a behaviour is found but not to great extent, because the cosine distribution of the direction of the sputtered flux and collisions make this effect less pronounced. The intensity maximum was found at a radial position of 42 mm and was about 25 % higher than the emission at the center. The intensity maximum in the

vicinity of the substrate is even easier to recognise for zinc ions and particularly for argon ions. The radial position of the maximum was found to be 50 mm. This is slightly higher than the radial position of the racetrack which lies between 45 mm and 50 mm. As this intensity maximum must be caused by a locally increased density of argon and zinc ions, it is necessary to ask why this maximum appears. The origin of the zinc ions might give a hint. These ions are born as atoms at the target surface by the sputtering process, which gives these atoms a prefered direction perpendicular to the target surface and an initial velocity, which lies somewhere in the velocity distribution function [175]. The particle motion towards the substrate is influenced by collisions with the background gas, and once the atom is ionised by the electric field in the discharge. This process will be analysed in detail in chapter 5.4.2. It was found that most metal ions arrive at the substrate at a radial position of 50 mm (figure 5.30, chapter 5.4.2). These calculations were made for the pulse on-time, but the intensity maxima discussed here can also be found during the HiPIMS pulse. However, their intensity is so much lower compared to the intensity emitted adjacent to the target, that they are not easily spotted in the intensity plots. The same observation can also be made for argon ions: An intensity maximum present at radial position 50 mm. Argon ions might be moved to this position by momentum transfer with the directed sputtered flux. Unlike argon atoms which can be pushed out of the discharge volume by the sputtering wind [96], the motion of argon ions is influenced by the electric field. The axial field is easier to overcome as the sputtered particles mainly transfer a momentum in the axial direction towards the substrate, while the radial component of the incident sputtered particle differs from collision to collision and most likely averages out over several events. While this explanation may seem plausible, more modelling of the motion of argon atoms and ions is necessary to understand this behaviour, even though results from Monte Carlo simulations reported by Kadlec suggest a somewhat directed motion of argon atoms towards the substrate during the HiPIMS pulse [23].

4.4.7 Stage H: Afterglow

Several authors have reported on ultralong decay times of the plasma in the afterglow of HiPIMS discharges with decay times of the electron density in the millisecond range [91]. It shall be noted that already Bäcker et. al. observed very long decay times for pulsed-DC magnetron sputtering. This feature is therefore not limited to HiPIMS discharges, but it might be observed easily in these discharges due to the high degree of ionisation of the plasma. Hecimovic and Ehiasarian reported on the presence of ions of both the

working gas and the sputtered material [83, 104]. Anders and Yushkov speculated on the influence of long-living metastable argon atoms which would slowly release their stored energy and sustain the plasma [105]. In fact, a large amount of metastable states can be found in all species present in the discharge, e. g. argon ions [193], titanium atoms [194] and titanium ions [195]. Vitelaru et. al. have recently reported measurements on the density of metastable states of argon atoms investigated by using optical absorption spectroscopy. However, due to the strong decrease of the density within the first few 100 µs of the afterglow, the metastable argon atoms might only play a minor role in sustaining the plasma.

The influence of the density of metastable argon atoms in the afterglow was investigated numerically by Wenig et. al. [196]. They showed that inelastic processes, such as chemoionisation

$$\begin{aligned} Ar^m + Ar^m &\rightarrow Ar^+ + Ar + e^- \quad \Delta E = 7.34\,eV \\ Ar^m + Ti &\rightarrow Ti^+ + Ar + e^- \quad \Delta E = 4.71\,eV, \end{aligned}$$

and superelastic collisions

$$Ar^m + e^- \rightarrow Ar + e^- \quad \Delta E = 11.55\,eV$$

can reheat the electron gas, i. e. sustain the mean energy of the electrons, or even create new electrons. The electron energy distribution function was measured in the afterglow of a pulsed RF-discharge by DeJoseph et. al. [197]. They confirm the presence of peaks in the EEDF at energies which are characteristic for chemoionisation and superelastic collisions. However, both studies (theory and experiment) were carried out at an operating pressure which was an order of magnitude higher than what is typically used in HiPIMS. A low pressure results in a higher mean free path which makes collision processes especially chemoionisation less likely. In addition, the density of metastable states at the beginning of the afterglow assumed for the modelling [196] was equal to the electron density. In HiPIMS discharges, this ratio is more likely 100:1 favouring the electron density [91, 100]. One cannot completely rule out the effect of sustaining the electron temperature during the afterglow by the aforementioned processes. However, it is arguable if reactions involving metastable states can produce electrons in a rate sufficiently high to cause the high electron densities that were observed [91].

Time-resolved optical 2d-imaging may help shedding some light on this mystery by observing the spatial and temporal evolution of the plasma-induced emission. To compensate for the low intensity in the afterglow, the gate width was increased to 100 µs, which

still gave a reasonable temporal resolution considering the duration of the afterglow to be 9.9 ms, at least. The gain was set to 7 to further enhance the measured intensity and the exposure time was increased, as well. The temporal development of the intensity of argon atoms and ions, titanium atoms, as well as zinc atoms and ions recorded 50 mm above the target is shown in figure 4.23. One can see, that after an initial drop of the intensity by about four to six orders of magnitude compared to the intensity recorded during the HiPIMS pulse, an additional intensity maximum can be seen in the emission of argon and metal (Ti or Zn) several 100 µs after the HiPIMS pulse has ended. No such maximum can be observed for argon or zinc ions. The further decay can the be described by a single exponential function. The appearance of the maximum and the decay times, typically in the order of 1 ms, are summarised in table 4.5.

Target	**Species**	**Filter** (nm)	**Pressure** (Pa)	**Maximum** (µs)	**Decay time** (µs)
Titanium	Ar(I)	750	0.53	(560 ± 200)	(1240 ± 190)
	Ti(I)	500	0.53	(800 ± 120)	(960 ± 180)
	Ar(I)	750	1.33	(560 ± 60)	(1440 ± 40)
	Ti(I)	500	1.33	(890 ± 130)	(1440 ± 80)
Aluminium-doped zinc	Ar(I)	810	1.33	(360 ± 80)	(1000 ± 110)
	Ar(II)	436	1.33	—	(810 ± 100)
	Zn(I)	636	1.33	(320 ± 100)	(1040 ± 90)
	Zn(II)	590	1.33	—	(900 ± 80)

Table 4.5: Compilation of decay times and temporal position of the maximum in the afterglow.

The temporal evolution of the intensity for Ar(I), Ar(II), Zn(I) and Zn(II) observed at the discharge axis for different axial distances from the target are depicted in figure 4.24. The intensity observed generally increases with distance to the target, which was already observed immediately after pulse termination. The additional intensity maximum seems to appear earliest close to the target and with more delay closer to the substrate, where the intensity also decays more slowly. As it was previously mentioned, no additional maximum in the emission of argon and zinc ions can be observed. In summary, the temporal

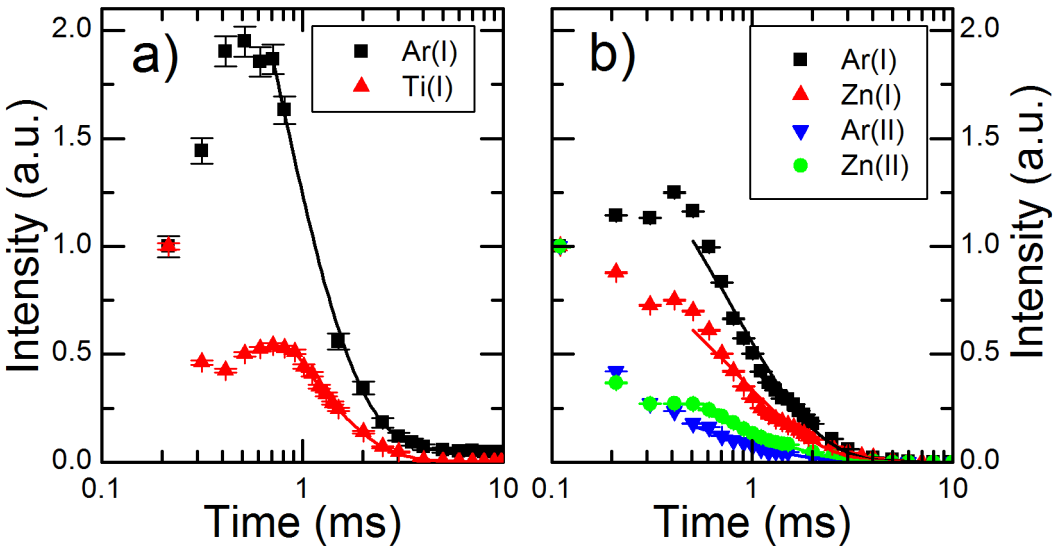

Figure 4.23: Temporal development of the plasma-induced emission in the afterglow of HiPIMS discharges recorded at the discharge axis 50 mm above the target. Discharge parameters are found in table 4.3

development of the plasma-induced emission in the afterglow reveals two key phenomena: The additional intensity maximum only observed for the emission of neutral species, and a large time constant in the order of 1 ms for the decay of the intensity of all species.

The intensity maximum shall be investigated first, as it gives a hint on the population mechanism of the excited states, and hence the origin for the emission of light. Ohebsian et. al. investigated the temporal development of the population of argon atoms and ions, as well as titanium atoms and ions in the afterglow of a hollow cathode plasma, by means of emission and absorption spectroscopy [198]. They found maxima in the density of excited argon and titanium states 150 µs to 200 µs in the afterglow, but not in their ions. The population mechanism made responsible for this behaviour was electron-ion recombination. Nafarizal et. al. studied the afterglow of a pulsed RF-discharge and found a maximum in the intensity emitted by argon atoms as well as a maximum in the population of metastable argon states. This was explained by a three body electron-ion recombination with the third body being an electron [199]. Further reports on this phenomenon were published by DesJoseph et. al. [200] and Bogaerts et. al. [201].

For sake of simplicity, the temporal development of the intensity of only Ar(I) shall be discussed, because it is well-studied and sufficient data (cross-sections, rate coefficients)

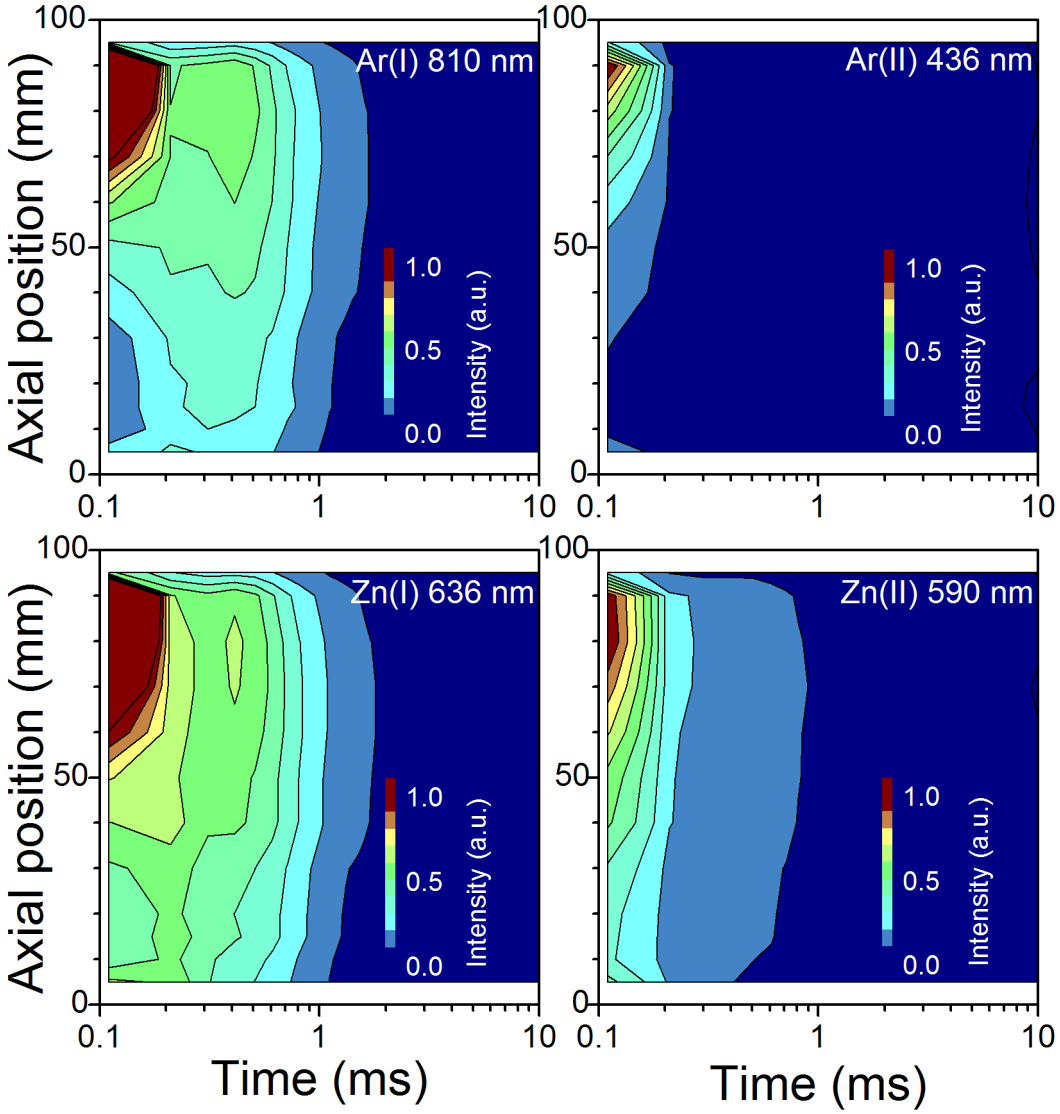

Figure 4.24: Spatial distribution of the temporal development of the plasma-induced emission in the afterglow of a HiPIMS discharge with aluminium-doped zinc target. Discharge parameters are found in table 4.3

can be found to explore the recombination process. Four of these processes shall be discussed and evaluated, here. A first remark shall be made towards momentum conservation, which prohibits that an electron is just "absorbed" by an argon ion. There must always be a particle to balance the momentum equation. In the case of radiative decay

$$Ar^+ + e^- \quad \rightarrow \quad Ar + h\nu,$$

this particle is a photon, usually in the UV range. As such low wavelengths were neither detected nor an excited argon state is created, this process will be neglected. The momentum conservation can be fulfilled, if a third particle is involved in the process. This can be a heavy particle P, such as an argon or titanium ion:

$$\begin{aligned} Ar^+ + e^- + P \quad &\rightarrow \quad Ar^* + P \\ \tfrac{dn_{Ar^+}}{dt} &= -k_{ner} n_e n_{Ar^+} \qquad . \end{aligned}$$

The density of argon ions is denoted as n_{Ar^+} and the rate coefficient (in $\mathrm{cm}^3\,\mathrm{s}^{-1}$) for this neutral electron-ion-recombination is

$$k_{ner} = 10^{-11} p, \tag{4.33}$$

with the pressure p given in Torr [202]. Alternatively, an electron can serve as the third body during the collision:

$$\begin{aligned} Ar^+ + e^- + e^- \quad &\rightarrow \quad Ar^* + e^- \\ \tfrac{dn_{Ar^+}}{dt} &= -k_{eer} n_e^2 n_{Ar^+} \qquad . \end{aligned}$$

The rate coefficient k_{eer} (in $\mathrm{cm}^6\,\mathrm{s}^{-1}$) for this electron-electron-ion recombination process strongly depends on the electron temperature [202]:

$$k_{eer} = 10^{-19} \left(\frac{T_e}{300\,K} \right)^{-9/2}. \tag{4.34}$$

Finally, a rather exotic process shall be mentioned, requiring the presence of the argon molecular ion Ar_2^+:

$$\begin{aligned} Ar_2^+ + e^- \quad &\rightarrow \quad Ar^* + Ar \\ \tfrac{dn_{Ar_2^+}}{dt} &= -k_{dr} n_e n_{Ar_2^+} \qquad , \end{aligned}$$

with $n_{Ar_2^+}$ being the density of argon molecular ions. The rate coefficient k_{dr} (in $\mathrm{cm}^3\,\mathrm{s}^{-1}$) for this dissociative recombination process is [203]:

$$k_{dr} = 9 \times 10^{-7} \left(\frac{T_e}{300\,K} \right)^{-0.61}. \tag{4.35}$$

Bogaerts reported on the afterglow of a glow discharge and summarised several production routes of the Ar_2^+ molecule [204]. All of these involve collisions between two or three argon atoms and/or ions, which is much more likely when operating at higher pressure due to the smaller mean free path, 133 Pa in that study compared to 1.33 Pa in the present case. Hardly any report on the density of Ar_2^+ ions can be found, but its density lies probably in the range of $10^{-2} \times n_{Ar^+}$ and $10^{-3} \times n_{Ar^+}$ [41]. With such a low density the rate equation 4.35 can be simplified by setting $k_{dr} n_e \approx const.$ because the loss of the electron density compared to the loss rate of the argon molecular ion can be neglected. The solution of this decoupled differential equation is an exponential decay with a time constant $\tau_{dr} = (k_{dr} n_e)^{-1}$. Given an electron density of 10^{17} m^{-3} and an electron temperature of 1 eV which are typical values for the plasma in the beginning of the afterglow, the decay time is calculated to be 100 µs. This means, that these ions are quickly destroyed without having a significant effect on the electron density and the development of the plasma-induced emission several 100 µs into the afterglow.

The two remaining three-body recombination processes shall be compared. For this purpose, the electron density and temperature measured in the afterglow of several HiP-IMS discharges operated at an argon pressure of 0.53 Pa, 1.06 Pa and 1.60 Pa were taken [91], the rate coefficients for both recombination processes calculated and the decay rates dn_{Ar^+}/dt plotted against time in figure 4.25. For the calculations, it was assumed that the majority of ions are singly charged and that the density of argon ions is a constant fraction of the electron density, as it might not be the only singly charged ion species present. The excited states of argon are thought to be populated by the recombination process, in a way that the production rate of excited states is proportional to the recombination rate. This is plausible, because the created argon atom is randomly created in some highly-excited state and the subsequent decay is a statistic process described by the transition probabilities. As the measured intensity is proportional to the density of particles in the excited state, which are created by a rate proportional to the recombination rate, the intensity is also proportional to the recombination rate. This consideration is only true, if the deexcitation process of the excited states is fast enough, to prevent build-up of the particle density in the excited state. As the radiative decay is a very fast process, this condition is fulfilled. One can see, that the rate at the beginning of the afterglow is highest for recombination involving a heavy particle, but it is arguable, that the rate coefficient for this process does not depend on the electron temperature. One would expect slower electrons to be more easily collected by argon ions than fast electrons. After about 200 µs to 300 µs the recombination with an electron as third body is higher than neutral-electron-ion recombination.

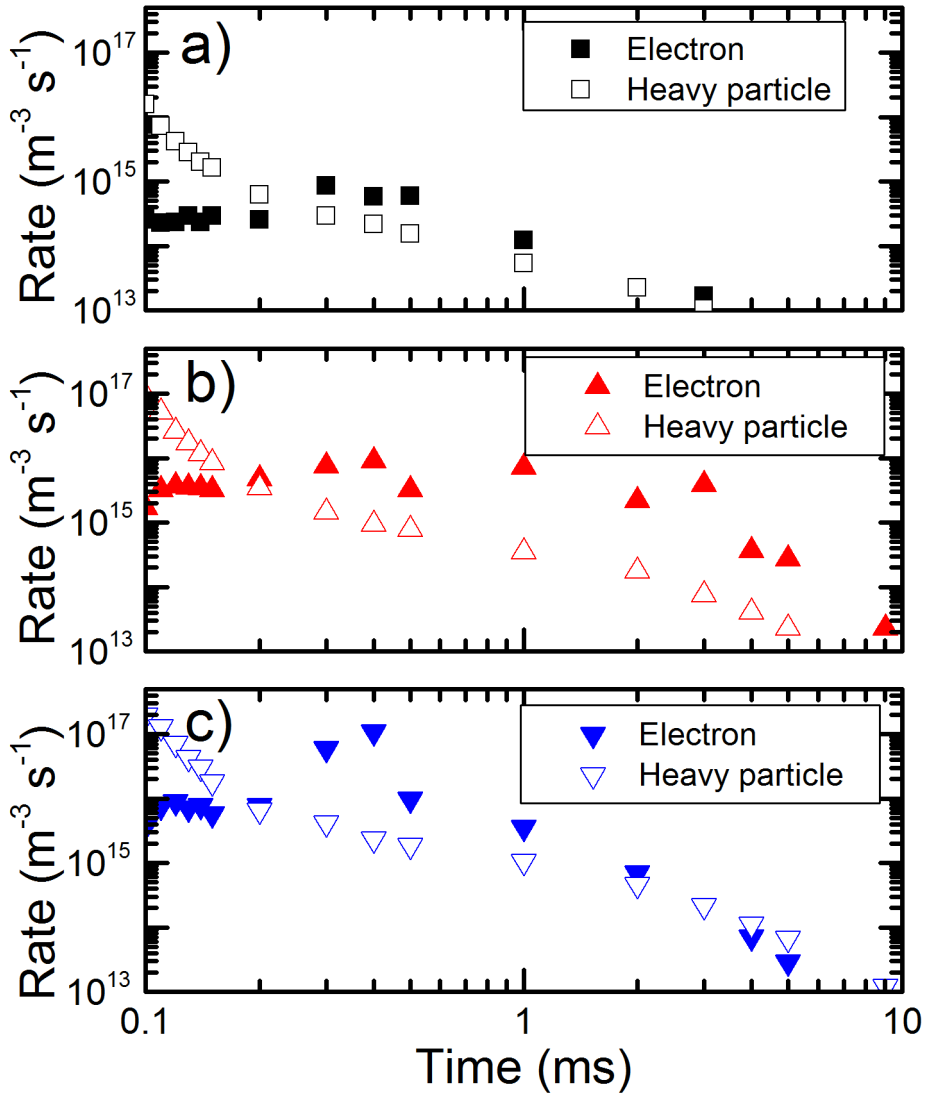

Figure 4.25: Calculated electron-ion recombination rates of argon ions Ar^+ in the afterglow of HiPIMS discharges operated at a) 0.53 Pa, b) 1.06 Pa and c) 1.60 Pa, using the electron density and temperature reported by Poolcharuansin and Bradley [91].

Furthermore, the decrease of the electron temperature causes the rate coefficient to rise so dramatically that it overcompensates for the loss of electron density and a maximum can be observed at temporal positions 300 µs to 400 µs, slightly earlier for lower pressure than for higher pressures. The maximum in the recombination rate manifests itself in a maximum of the plasma-induced emission, as it was observed in the experiments. One can see from figure 4.25, that the maximum rate is increased by a factor of 3, 5 and 20 compared to the initial rate for argon pressure 0.53 Pa, 1.06 Pa and 1.60 Pa, respectively. This trend is confirmed by the present data; the intensity maximum was found to be more pronounced for higher pressure. After its maximum, the rate decays with the decaying electron density, as the rate coefficient does not change anymore, due to constant electron temperature. The decay of the measured intensity therefore represents the decay of the electron density.

A similar electron-ion-recombination mechanism was also reported to populate the excited states of titanium atoms with titanium ions as the parent particle [198]. The titanium ions were reported to be created by charge exchange collisions between titanium atoms and argon ions. It is not clear, if this process is necessary in the afterglow of HiPIMS, as a vast amount of metal ions are created during the pulse on-time. No intensity maxima were observed for argon or metal ions, because the density of particles in the next higher charge state, Ar^{2+} and $Ti^{2}+/Zn^{2+}$, is too low. However, the existence of these charge states was reported by Ehiasarian et. al. [82]. The intensity emitted by singly-charged argon and metal ions can therefore also be explained by the population of excited states by electron-ion recombination.

It was found that electron-electron-ion recombination is the dominant mechanism to create excited states in the HiPIMS afterglow. The population rate is proportional to the recombination rate and hence the loss rate of argon ions dn_{Ar^+}/dt, which is proportional to n_e^3, if the density of argon ions is proportional to the electron density. In an ideal plasma with singly charged argon ions being the only ion species $n_{Ar^+} = n_e$, but due to the presence of metal ions only proportionality can be demanded. Poolcharuansin and Bradley reported on a single exponential decay of the electron density while the electron temperature remained constant in the late afterglow [91]. The electron density in the late afterglow can be written as:

$$n_e(t) = n_{e0} \exp - \frac{t}{\tau_{n_e}}, \tag{4.36}$$

with τ_{n_e} being the time constant in the range of 3.5 ms to 4.5 ms. The intensity of the plasma induced emission is proportional to the population rate of excited states, which is proportional to the recombination rate which in turn is proportional to n_e^3. This means that

the intensity is proportional to n_e^3:

$$I(t) \propto n_{e,0}^3 \exp -\frac{3t}{\tau_{n_e}}. \tag{4.37}$$

The decay time obtained for the intensity $\tau_i \approx \tau_{n_e}/3$. Applying this formula to the decay times summarised in table 4.5, one can calculate decay times of (3.7 ± 0.6) ms for 0.53 Pa and (4.3 ± 0.2) ms for 1.33 µs, when using Ar(I) emission as benchmark. These values agree very well with the Langmuir probe measurements [91]. This confirms once more, that electron-electron-ion recombination is the dominant excitation mechanism in the HiPIMS afterglow.

The population processes have successfully been described and the decay of the plasma-induced emission could be related to the decay of the electron density. However, the reason for the unusually low loss of electrons out of the discharge is still not understood, but some thoughts shall be summarised now. First, the loss of electron density by recombination in the discharge volume will be examined, as this process does not only populate excited states but also decreases both the electron and ion density. The rate equation for electron-electron-ion recombination for the electrons reads:

$$\frac{dn_e}{dt} = -k_{eer} n_e^3, \tag{4.38}$$

in the presence of only singly charged ions. The rate coefficient k_{eer} is an average value if several species of singly charged ions are present (Ar^+, Ti^+ or Zn^+). The highest rate coefficient can be calculated for the lowest electron temperature of 0.2 eV, which gives $k_{\mathrm{eer}} = 1.0 \times 10^{-35}\ \mathrm{m^6\,s^{-1}}$. One can linearise the aforementioned rate equation by keeping n_e^2 as a constant, which gives an exponential decay of the electron density with a time constant $\tau_{eer} = (n_e^2 k_{eer})^{-1}$. This approximation only holds for a short time interval and gives a crude overestimation of the decay rate. Assuming an upper limit of the electron density in the afterglow of $10^{18}\ \mathrm{m^{-3}}$, one obtains a decay time of 0.1 s, which is a huge exaggeration of the actual loss rate of electrons. However, it proves that electrons are not efficiently lost by volume recombination in the HiPIMS afterglow.

Fluid dynamics shows that a flux of charged particles Γ is caused by an applied electric field and/or by a density gradient:

$$\Gamma = \pm \mu n \boldsymbol{E} - D \nabla n, \tag{4.39}$$

with μ and D being the particle mobility and diffusion constant, respectively. As no external field is applied during the afterglow, the mobility term can be dropped and one has to

solve Fick's second law of diffusion to obtain the temporal and spatial development of the particle density:

$$\frac{dn}{dt} = D\nabla^2 n. \tag{4.40}$$

A solution for a cylindrical symmetry was already presented in chapter 2.2 [35]. The decay of the electron density follows an exponential law and the time constant τ_d can be calculated using the dimensions of the cylinder, R for its radius and l for its length:

$$\tau_d = \frac{\Lambda_d^2}{D}, \tag{4.41}$$

$$\Lambda_d = \left(\frac{2.405^2}{R^2} + \frac{\pi^2}{l^2}\right)^{-1/2}, \tag{4.42}$$

with Λ_d the characteristic diffusion length obtained from the spatial density distribution. Inserting the chamber radius $R = 200$ mm and the distance between target and substrate $l = 100$ mm, the characteristic diffusion length can be calculated as $\Lambda_\mathrm{d} = 29.7$ mm. If this result is used and the decay times calculated for the electron density is used, one obtains a very low diffusion constant of $0.3\ \mathrm{m^2\,s^{-1}}$ and $0.2\ \mathrm{m^2\,s^{-1}}$ for a working gas pressure of 0.53 Pa and 1.33 Pa, respectively.

The decay of the density of titanium ions in the afterglow of a HiPIMS discharge was both measured by means of absorption spectroscopy and modelled by de Poucques et. al. [106]. They assumed transport by ambipolar diffusion and obtained a diffusion constant of $D_\mathrm{a} = 0.80\ \mathrm{m^2\,s^{-1}}$ to fit best their experimentally obtained data. While this value lies close to the diffusion constants calculated in the present study, the authors did not give a comparison to a theoretically obtained diffusion constant. It is therefore difficult to scale this value obtained for a pressure of 4 Pa to the working gas pressure used in this study. In order to investigate ambipolar diffusion in the presence of a magnetic field, diffusion constants and particle mobilities have to be known for electron transport along and across magnetic field lines. The ions are generally considered not to be magnetised, hence only one set of transport coefficients is required for describing both their motion along and across magnetic field lines.

For the electrons the well-known classic diffusion constants for transport parallel to the magnetic field

$$D_{||} = \frac{k_B T_e}{m\nu_c}, \tag{4.43}$$

and perpendicular to it

$$D_\perp = \frac{D_{||}}{1 + \left(\frac{\omega_c}{\nu_c}\right)^2} \tag{4.44}$$

are used, with ω_c and ν_c being the cyclotron and collision frequency [35], respectively. Electrons can either collide with the background gas or with ions. As an electron temperature of 0.2 eV, reported by [91], suggests a mean energy which would lie in or close to the Ramsauer minimum of the cross-section, electron-neutral collisions can be neglected. The collision frequency of electrons with ions can be calculated using the Spitzer formula [34]:

$$\nu_c = \frac{\pi e^4}{(4\pi\varepsilon_0)^2\sqrt{m_e}} n_e (k_B T_e)^{-3/2} \ln\Lambda_p, \tag{4.45}$$

with the vacuum permittivity ε_0, the electron mass m_e and the plasma parameter:

$$\Lambda_p = 12\pi n_e \lambda_d^3. \tag{4.46}$$

The electron density 2 ms in the afterglow of a HiPIMS discharge operated at an argon pressure of 0.53 Pa was measured as $n_\mathrm{e} = 3.5\times10^{16}\ \mathrm{m}^{-3}$ and the electron temperature was 0.2 eV [91]. The electron-ion collision frequency is then $9.52\times10^6\ \mathrm{s}^{-1}$, which results in a diffusion constant parallel to the magnetic field of $D_{\mathrm{e}||} = 3.69\times10^3\ \mathrm{m}^2\,\mathrm{s}^{-1}$. The gyration frequency for a magnetic induction of 2 mT is $3.52\times10^8\ \mathrm{s}^{-1}$; the electrons have to cross the axial magnetic field at the edge of the discharge volume (radial position 80 mm). This gives a diffusion constant across the magnetic field of $D_{\mathrm{e}\perp} = 2.70\ \mathrm{m}^2\,\mathrm{s}^{-1}$. The corresponding electron mobilities are $\mu_{\mathrm{e}||} = 1.85\times10^4\ \mathrm{m}^2\,\mathrm{V}^{-1}\,\mathrm{s}^{-1}$ and $\mu_{\mathrm{e}\perp} = 13.5\ \mathrm{m}^2\,\mathrm{V}^{-1}\,\mathrm{s}^{-1}$, having made use of the Einstein relation (eq. 2.45).

The ion diffusion constant can be calculated using:

$$D_i = \sqrt{\frac{\pi}{8}\frac{k_B T_i}{m_i}}\lambda, \tag{4.47}$$

with λ being the mean free path of the positive ions (after [35]. The mean free path is calculated as $\lambda = (n_g\sigma)^{-1}$ with n_g the density of the background gas and σ the charge exchange cross-section for argon ions ($\sigma = 7.2\times10^{-19}\ \mathrm{m}^2$ [205]). The gas density is obtained by applying ideal gas law with a pressure of 0.53 Pa and a temperature of 300 K. The diffusion constant also depends on the ion temperature, which is unknown at this point. Due to the long time (2 ms) after pulse termination, most energetic ions are already lost to the walls and only a small fraction of thermalised ions are present [83]. An ion temperature slightly above room temperature of 0.1 eV is assumed. This gives a diffusion constant of $D_\mathrm{i} = 3.34\ \mathrm{m}^2\,\mathrm{s}^{-1}$ for a pressure of 0.53 Pa. The corresponding ion mobility is $\mu_\mathrm{i} = 33.4\ \mathrm{m}^2\,\mathrm{V}^{-1}\,\mathrm{s}^{-1}$. Due to the largely different transport of the electrons along and across magnetic field lines, the ambipolar diffusion is also considered in respect to the

orientation of the magnetic field. The ambipolar diffusion constant for particle transport exclusively perpendicular to the magnetic field reads:

$$D_{a\perp} = \frac{\mu_i D_{e\perp} + \mu_{e\perp} D_i}{\mu_i + \mu_{e\perp}}. \tag{4.48}$$

The diffusion constant $D_{a||}$ is calculated in the same way by simply replacing the electron diffusion constant and mobility with the values for the transport parallel to the magnetic field. In this way, the diffusion constants were obtained $D_{a||} = 9.98\ \mathrm{m^2\,s^{-1}}$ and $D_{a\perp} = 2.88\ \mathrm{m^2\,s^{-1}}$. The diffusion constants for an argon pressure of 1.33 Pa were calculated using an electron density of $8.0 \times 10^{16}\ \mathrm{m^{-3}}$ (interpolated from the Langmuir probe measurements for 1.06 Pa and 1.60 Pa reported by Poolcharuansin and Bradley [91]), an electron temperature of 0.2 eV and otherwise the same conditions. The diffusion constants obtained, were $D_{a||} = 3.98\ \mathrm{m^2\,s^{-1}}$ and $D_{a\perp} = 2.74\ \mathrm{m^2\,s^{-1}}$. In summary, these values are still one order of magnitude too high.

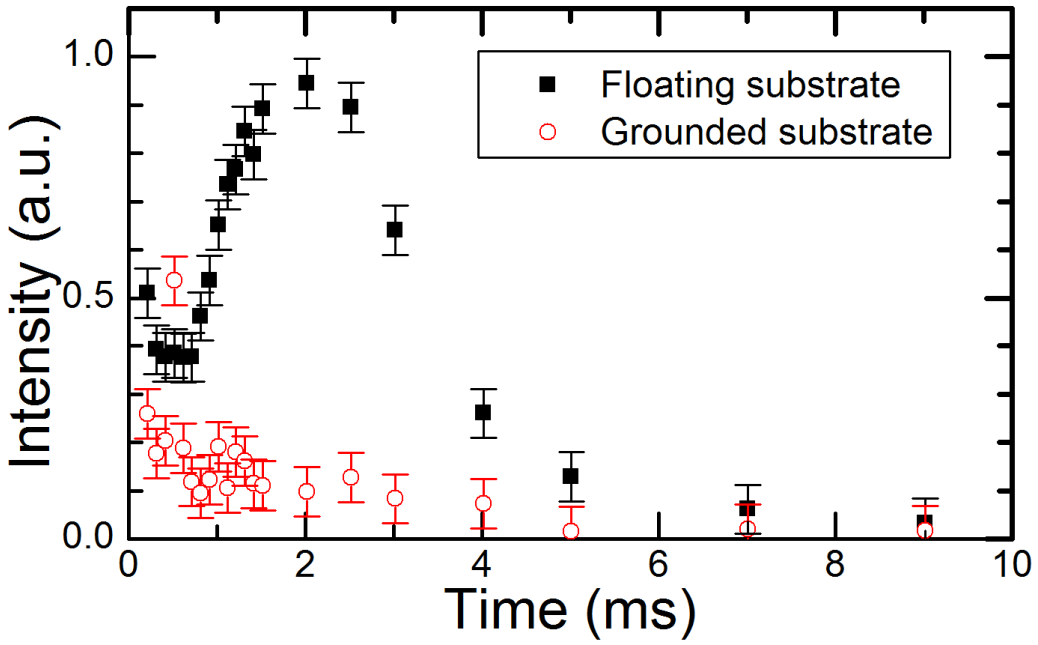

Figure 4.26: Temporal development of the intensity of the plasma-induced emission of Ar(I) filter 750 nm in the afterglow for a floating (black, solid squares) and a grounded substrate (red, open circles). The intensity was recorded 90 mm above the target at the discharge axis. The discharge conditions for sputtering titanium at an argon pressure of 1.33 Pa can be found in table 4.3.

It was discussed in the previous chapter that the electron flux to the floating substrate is impeded by the potential barrier $\Delta V = V_{pl} - V_{fl} \approx 5.2 k_B T_e / e$ (compare figure 3.15). This leads to a decrease of the flux to the substrate to a fraction of 9.1×10^{-3} . Applying this consideration reduces the effective diffusion constant along the magnetic field lines to less than 0.1 $m^2 s^{-1}$, but the different temporal behaviour between floating and grounded substrate has to be proven, as well.

The spatial distribution of the plasma-induced emission in the afterglow was investigated for sputtering a titanium target at an argon pressure of 1.33 Pa, as it was already shown, that a higher pressure emphasises the phenomena observed in the afterglow. This time, two different substrate configurations, floating and grounded, shall be compared. Figure 4.26 shows the temporal development of the intensity recorded with filter 750 nm for Ar(I) emission 90 mm above the target along the discharge axis. One can clearly see the influence of the substrate configuration. While the intensity observed with the grounded substrate drops immediately after pulse termination and remains at a rather constant level, the intensity recorded for the floating substrate reveals generally higher intensities and the characteristic maximum at about 2 ms. The image recorded by the iCCD at this time is shown in figure 4.27 for both substrate configurations. The image was not Abel-inverted because of the low intensity, i. e. low signal-to-noise ratio, and because the algorithm can cause inaccuracies at the discharge axis, as it was demonstrated in chapter 4.3.

It is known, that the spatial solution for the density $n_e(r,z)$ of Fick's law for a cylindrical geometry is [35]:

$$n_e(r,z) = n_{e0} J_0 \left(\frac{2.405}{R} r \right) \cos \frac{\pi}{l} z, \tag{4.49}$$

with J_0 being the zero order Bessel function. Keeping the axial position z constant, one can study the radial distribution of the electron density. As the population of excited states is caused by electron-electron-ion recombination, the locally emitted intensity $i(r) \propto n_e^3$. The intensity measured by the detector at position x_0 is integrated over the optical path as described in chapter 4.1.2:

$$I(x_0) = 2 \int_{x_0}^{R} \frac{i(r) r}{\sqrt{r^2 - x_0^2}} dr. \tag{4.50}$$

Using the proportionality of the locally emitted intensity and the radial distribution of the electron density (eq. 4.49), gives the measured intensity as:

$$I(x_0) = 2C \int_{x_0 - x_c}^{R} \frac{\left[J_0 \left(\frac{2.405}{R} r \right) \right]^3 r}{\sqrt{r^2 - (x_c - x_0)^2}} dr, \tag{4.51}$$

with x_c being the centre of the intensity profile and C a constant to fit the profile to the intensity measured by the iCCD. This equation can be used to fit to the radial intensity distribution for a given axial position z and a given time t. The fitting parameters are the constant C, the centre coordinate of the intensity profile x_c and the radius R. This fitting procedure was used for a number of axial and temporal positions. It was found that the centre of the intensity profile during the afterglow of the HiPIMS discharge is about 10 mm off the geometric discharge axis. However, the centre of the intensity, and hence of the radial electron density distribution, is strongly influenced by the distance to the plasma boundaries, the chamber walls, rather than depending on the magnetron itself. As the magnetron might not be exactly at the centre of the cylindrical vacuum chamber, an off-set of 10 mm seems to be possible. The characteristic radius was fitted to about (175 ± 5) mm which differs little from the radius of the vacuum chamber ($R = 200$ mm). The theoretical curve fitted to the experimental data for an axial position of 90 mm is also shown in figure 4.27 for both the grounded and the floating substrate, which confirms that the experimental data can be fitted by this function quite well.

The intensity distribution along an axis at constant radial position is also shown in figure 4.27. One can clearly see, that it does not resemble any cosine-like function, thus, it was not tried to fit a cosine function to it. However, as it was shown that the measured intensity $I \propto n_e^3$, it can be deduced that $n_e \propto \sqrt[3]{I}$. Calculating $\sqrt[3]{I}$ gives an almost constant result for both substrate configurations, especially in the vicinity of the substrate ($z > 50$ mm). This means, that there is hardly any density gradient in the axial direction, and without a density gradient there is no diffusion. The solution of Fick's law has to be altered to account for this finding by dropping the axial term:

$$n_e(r) = n_{e0} J_0 \left(\frac{2.405}{R} r \right), \tag{4.52}$$

which is the solution for an infinitely long cylinder. The characteristic diffusion length Λ_d also changes:

$$\Lambda_d = \frac{R}{2.405}. \tag{4.53}$$

The diffusion length is much longer than originally assumed (29.7 mm) and be calculated to 73 mm and 83 mm, when using the radius calculated from the radial intensity profile (175 mm) and the chamber radius (200 mm), respectively. The time constant of ambipolar diffusion across magnetic field lines yields 1.8 ms and 2.4 ms for the two characteristic diffusion lengths and a pressure of 0.53 Pa. The time constants for pressure 1.33 Pa are 1.9 ms and 2.5 ms. This is close to the decay times observed in this study as well as by

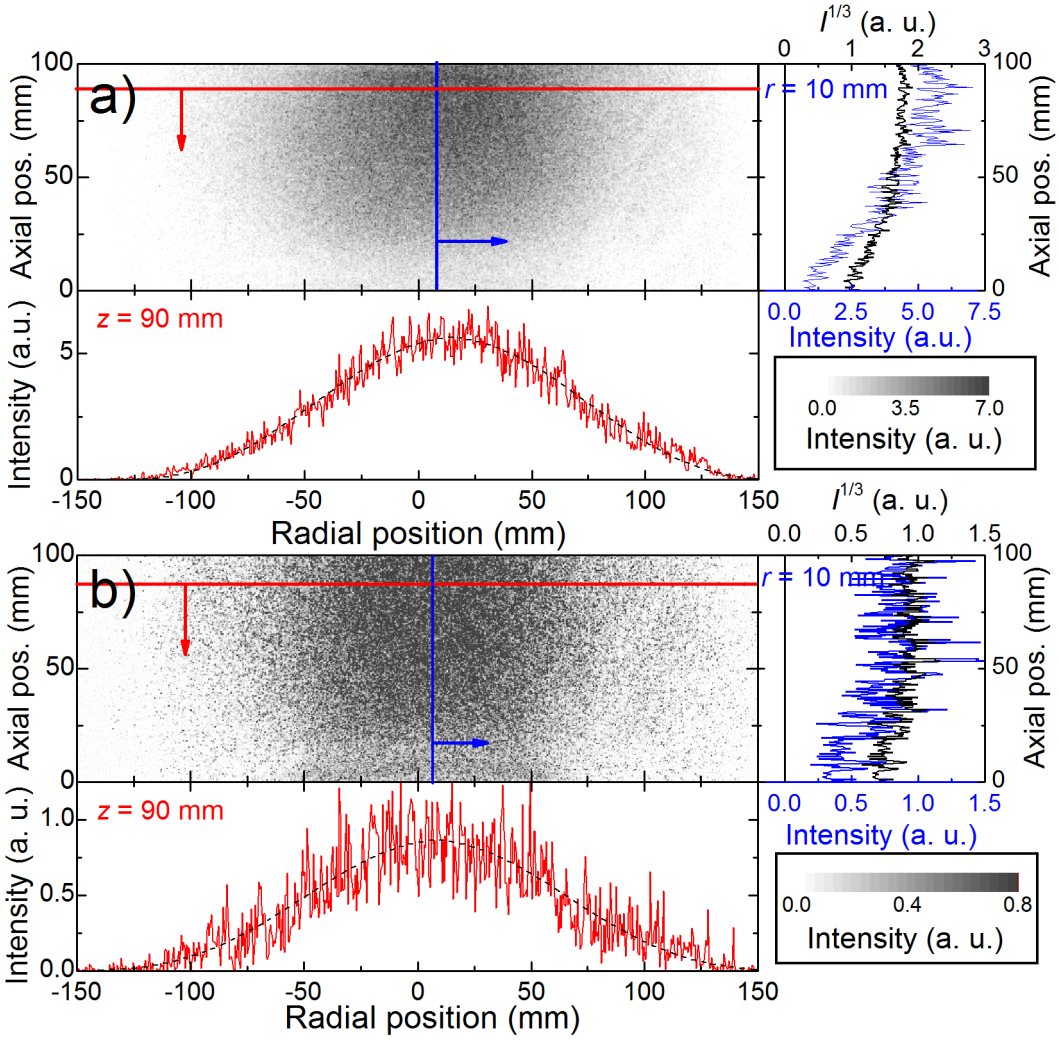

Figure 4.27: Spatial distribution of the plasma-induced emission of Ar(I) observed with filter 750 nm, 2 ms in the HiPIMS afterglow for a) a floating substrate and b) a grounded substrate. The discharge conditions for sputtering titanium at an argon pressure of 1.33 Pa can be found in table 4.3.

Poolcharuansin and Bradley [91]. However, the pressure dependence of the time constants is not fully reproduced. An increase by about 20 % was reported for the Langmuir probe measurements, whereas the time constants calculated here almost stay the same. More studies have to be carried out, focussing on accurate measurements of the electron and ion temperature in the afterglow, as well as further clarification of the influence of long-living species, such as argon metastable atoms.

4.5 Chapter conclusions

The temporal and spatial evolution of the plasma-induced emission studied by means of optical 2d-imaging gave an overview over phenomena present throughout the HiPIMS pulse and in the afterglow. The discharge ignition is accompanied by an intensity maximum observed remote from the cathode and quickly moving towards it. A simple Monte Carlo model applied to the discharge conditions showed that this phenomenon is probably caused by the motion of remnant electrons in the presence of the advancing sheath and the static magnetic field of the unbalanced magnetron. The ignition is followed by another transient stage of the discharge where the intensity maximum was found to travel away from the target not unlike an ion acoustic wave. This phenomenon is superimposed by an asymmetric intensity profile indicating a turbulent, highly non-uniform discharge. As the pulse progresses this unstable stage is not observed anymore. The highly ionised stage is characterised by a high discharge current and a high degree of ionisation. It could be shown, that the working gas is strongly depleted in front of the target by the sputtering wind. Ionisation of the sputtered flux also occurs immediately above the racetrack and is so efficient that hardly any metal atoms can pass this region without being ionised. This manifests in the loss of intensity emitted by metal atoms and the observation of two distinct intensity maxima whose position is related to the discharge current. Furthermore, the emission of argon ions, metal atoms and ions indicates a wider sputtering profile due to the high discharge current. The HiPIMS discharge develops into a more DC-like stage at the end of the pulse after the target voltage has dropped significantly.

The transition from the pulse on-time to the afterglow plasma is accompanied by a sharp drop of the plasma-induced emission, which was found most pronounced close to the target and somewhat impeded in the vicinity of the floating substrate. The decay is caused by the quick loss of energetic electrons followed by a slightly more slowly cooling of the entire electron population. The extremely slow decay of the intensity between the magnetic

null and the floating substrate could be explained by the confining arrangement of the magnetic field and the potential barrier between the bulk plasma and the floating substrate. The intensity in the afterglow is predominantly caused by excited states populated by a three body recombination process, involving two electrons and an ion. The additional intensity maximum observed in the afterglow in the emission of neutral particles is due to the slow decay of the electron density in combination with a strong increase of the recombination rate coefficient due to the drop in the electron temperature. The spatial intensity profile in the late afterglow suggests that the decay of the electron density and thus the plasma-induced emission is caused by ambipolar diffusion of electrons and ions across the magnetic field of the unbalanced magnetron.

5 Transport of sputtered particles

The transport of sputtered particles is an important feature to study when depositing thin films with HiPIMS. Various authors reported on the apparently low deposition rates observed with HiPIMS compared to DCMS and their possible origin, see for example [22,29, 89,111,113,116–118,206,207]. On the other hand, it is usually claimed that the moderate kinetic energy of ions of the sputtered material are beneficial for the film growth [86,87]. Christie [118], Sarakinos et. al. [206] and Vlcek and Burcalova [119] developed semi-empirical models to describe the film deposition by considering the sputtering process, the ionisation probability, back-attraction of ionised sputtered particles to the target and the transition of these particles through the entire discharge. These effects are described by probabilities calculated from discharge by probabilities calculated from discharge properties considered on global scale. For example, the probability of ionised sputtered particles returning to the target is usually varied over a wide range to fit measured fluxes and ion energy distribution functions. In the real discharge, a sputtered particle is ejected from the target with a certain velocity. It can get ionised somewhere in the discharge volume and the created ion then has to move against the electric field. Depending on the initial conditions, the spatial distribution of the electric field and where the ionisation takes place, the particle reaches the substrate or is attracted back to the target. In addition, the ion can also be deflected by an azimuthal force arising from the presence of a two-stream instability as pointed out by Lundin et. al. [29].

The semi-empirical transport model used here includes all these effects plus scattering of sputtered particles on the background gas. Instead of solving the problem of a fully self-consistent model, the plasma potential, the electron density and temperature were measured by means of emissive and Langmuir probes, respectively. These measurements serve as input parameters to calculate the trajectory of "test" particles ejected from the target.

This chapter is divided into three sections, dedicated to the emissive probe and Langmuir probe measurements, as well as the actual transport model.

5.1 Experimental setup

The experimental setup is depicted in figure 5.1. It was used for all probe measurements with the only difference being the probe itself, which was either an emissive or a single Langmuir probe. They were inserted from a flange at the side of the vacuum chamber. This allows for changing the radial position of the probe, only. The axial position was altered by moving the magnetron and the substrate together to keep the distance between both of them at 10 cm. In this way, the axial position was varied from $z = 10$ mm to $z = 95$ mm. Positions closer to the target were not accessible as the probe significantly disturbed the plasma, ultimately leading to the extinction of the discharge. The upper limit is determined by the minimum distance of the probe to the substrate. The radial position was varied from $r = 0$ mm to $r = 80$ mm for the Langmuir probe and up to $r = 90$ mm for the emissive probe which allows for more accurate calculation of the electric field at the edge of the discharge, $r = 80$ mm. It was made use of the assumption of an cylindrically sym-

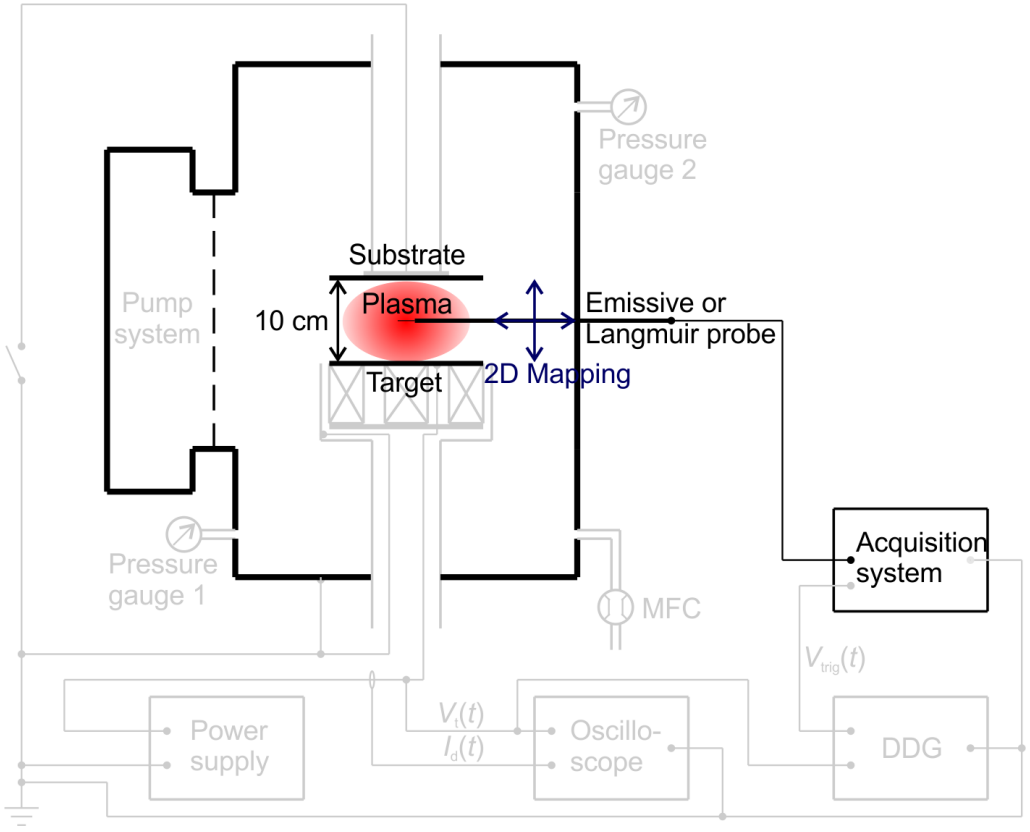

Figure 5.1: Schematic drawing of the experimental setup for probe measurements.

metric discharge, which only requires to measure plasma properties for positive and not for negative radial positions, which saves a lot of experimental time. The step size of positioning the probe was 5 mm for both the radial and axial direction, which results in a grid of 306 and 342 data points for the Langmuir probe and the emissive probe measurements, respectively.

The discharge was operated at a pressure of 0.53 Pa and an argon flow rate of 30 sccm. The target was made of titanium, purity 99.95 %, supplied by Pi-Kem. The purpose-built power supply was used to ignite the HiPIMS discharge with a pulse length of 100 µs and a repetition frequency of 100 Hz. The target voltage was adjusted to obtain the same energy per pulse of $E_{\text{pulse}} = 7$ J for all substrate and magnetic field configurations, resulting in an average power of 700 W. Further discharge parameters are summarised in table 5.1.

Setting	**No substrate**	**Floating substrate**	**Grounded substrate**	**More balanced**	**More unbalanced**
Pressure (Pa)			0.53		
Argon flow (sccm)			30		
Set voltage (V)	-690	-710	-720	-740	-725
Average power (W)			700		
Frequency (Hz)			100		
Pulse width (µs)			100		
Peak current density (A cm^{-2})	1.05	1.20	1.12	1.02	1.02
Peak power density (kW cm^{-2})	0.51	0.56	0.56	0.55	0.54

Table 5.1: Discharge parameters for probe measurements. The magnetic field configuration was only changed when the substrate was grounded

The substrate was either floating or grounded. The balance of the magnetic field was varied by moving either the inner or the outer permanent magnet. The configuration with both magnets being as close to the target as possible is called the standard configuration, also shown in figure 3.2. The G-factor is 1.0 in this case and the magnetron "very unbalanced". When the outer permanent magnet is pulled out by 10 mm, the configuration gets more balanced. With the magnetic null found at an axial position of 80 mm, the magnetron is still "very unbalanced", $G = 1.1$. When only the inner magnet is pulled out by 10 mm, the magnetic null is found 65 mm above the target and the magnetron is then "extremely

unbalanced", $G = 0.9$. These two configurations are named "more balanced" and "more unbalanced" in figure 5.2. The influence of the magnetic field was only investigated for the grounded substrate, as it was found that the discharge was much more stable when operated with the substrate grounded. The purpose of these measurements was to find whether a more unbalanced magnetron can lead to higher deposition rates.

5.2 Emissive probe

5.2.1 Theoretical background

An emissive probe is essentially a Langmuir probe that emits electrons, usually by thermoionic emission. The electron emission current I_{e0} is then described by the Richardson-Dushman equation (reference [208] ch. 8):

$$I_{e0} = CA_w T_w^2 \exp \frac{E_w}{k_B T_w}, \tag{5.1}$$

with C being the Richardson constant ($\approx 6 \cdot 10^5\ \mathrm{A\,m^{-2}K^{-2}}$ for all pure metals) and E_w is the work function, 4.54 eV for tungsten. The surface area of the probe and the probe temperature are denoted as A_w and T_w, respectively. The total current measured by the probe can be written as [209]:

$$I_p(V_b) = \begin{cases} I_c(V_b) + I_{e0}, & V_b < V_{pl} \\ I_c(V_b) + I_{e0} \exp -\frac{e(V_b - V_{pl})}{k_B T_w} g(V_b - V_{pl}), & V_b \geq V_{pl}, \end{cases} \tag{5.2}$$

with $I_c(V_b)$ being the probe collection current in the absence of emission (cold Langmuir probe) and $g(V_b - V_{pl})$ describes the influence of the geometry of the probe, e. g. the probe radius.

For an ideal probe, the $I_p - V_b$ characteristic for a probe bias higher than the plasma potential of both the cold and the hot probe are identical. Both characteristics diverge somewhere close to the plasma potential, with the hot, i. e. electron-emitting, probe showing more negative currents. This emission current increases with increasing wire temperature, as expected from the Richardson-Dushman law. However, the point of divergence between the probes does not seem to alter much. Hence, it was proposed by Langmuir to use this point to identify the plasma potential [210]. However, it was later demonstrated that the using this so-called separation point method can lead to quite significant error [211]. This

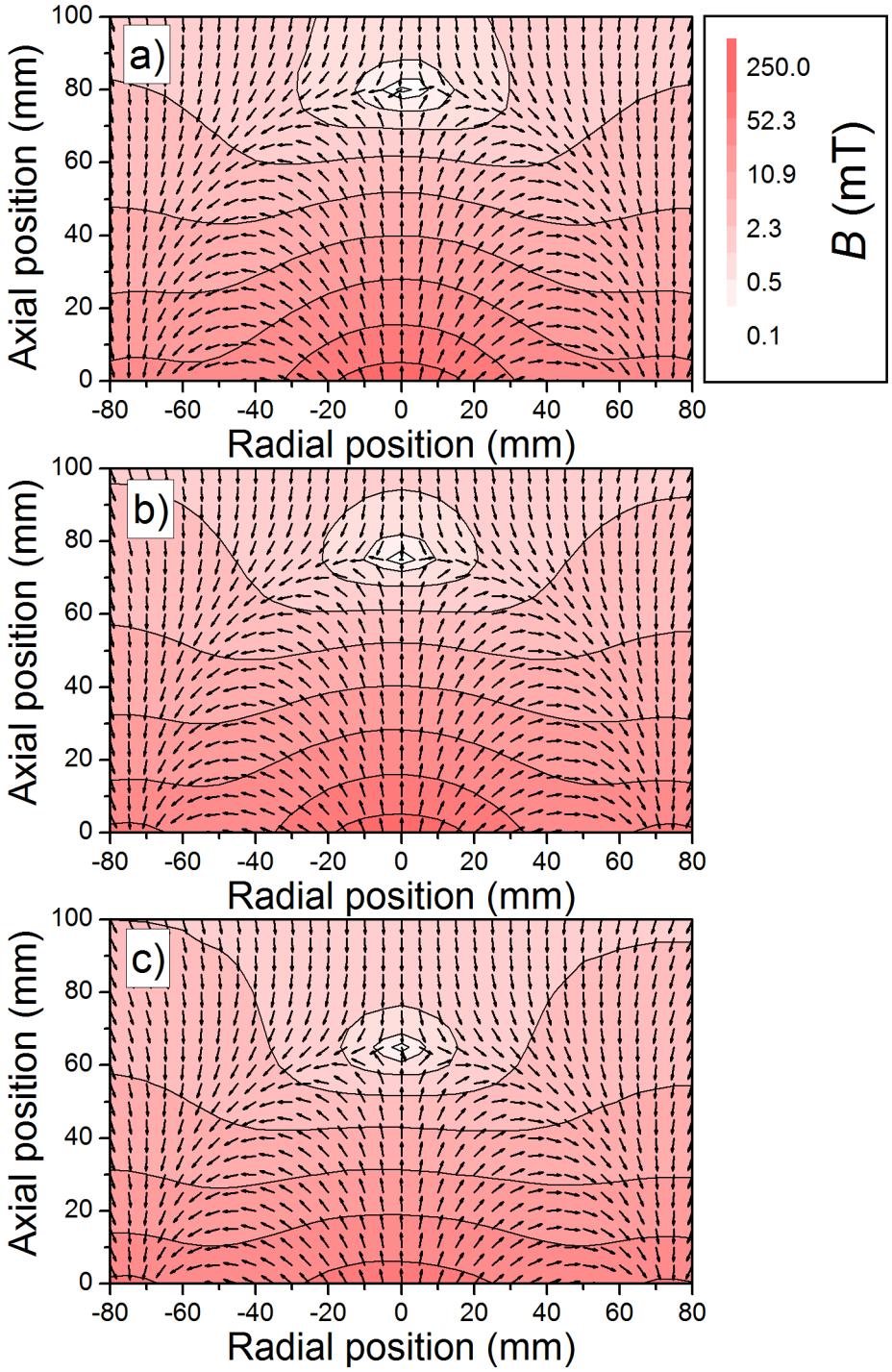

Figure 5.2: Three different magnetron configurations were used for Langmuir and emissive probe studies: a) A more balanced magnetic field, b) the standard configuration and c) a more unbalanced configuration. The magnetic field for the more balanced and the more unbalanced configuration were calculated as described in chapter 3.2.

is due to space charge effects; the vicinity or sheath around the probe is different for emitting or non-emitting probes, hence the two $I_p - V_b$ characteristics never lie on top of each other. Surface contaminations can degrade the results even further.

The floating potential, identified by $I_p = 0$, moves towards more positive values when the wire temperature increases. However, it can never rise above plasma potential, because all electrons would immediately be attracted back to the probe. The method published by Kemp and Sellen makes use of this observation [212]. They suggested to use a probe insulated from ground, hence floating point technique, and heat it until the measured probe potential saturates. This potential can then be identified as the plasma potential. This method has a number of advantages. Keeping the probe floating in the plasma minimises its disturbance. It is also a very fast technique as only one value, the probe potential at large emission, has to be recorded. Hence, it is an excellent tool for spatial measurements, because the probe can be designed to move through the plasma. On the other hand, one loses information on the electron density and temperature.

Finally, the inflection point method makes use of the "full" $I_p - V_b$ characteristic of a weakly emitting probe. It was proposed by Smith et. al. to use the maximum in the first derivative to identify the plasma potential [213]. The main benefit of this method is the higher accuracy, which is claimed to be in the order of $0.1 k_B T_e/e$ [211, 214], whereas the floating point method gives consistently too low values for the plasma potential. The error of the floating point method is given as either $k_B T_e/e$ by Ye and Takamura [214] or even as $1.5 k_B T_e/e$ reported by Schwager and also by Hobbs and Wesson [215, 216].

A number of techniques have been developed for heating the probe. Joule heating is the most commonly used, because it simply requires sufficient current to flow through the probe to heat it to thermoionic emission [210]. Hence, the probe is formed into a closed loop in contrast to the straight Langmuir probe. The choice of probe material is made very easy, because it needs to be a conductive material with a very high melting point. Hence, tungsten is commonly used, often doped with a few percent thorium oxide. The wire is usually formed into a hairpin and then connected to the probe holder either by welding [212] or mechanically clamped [217, 218]. Of course, the same considerations concerning the size and the experimental setup as discussed for (non-emitting) Langmuir probes apply.

Other heating methods include indirect heating [219], i. e. probe and heating circuit are separated, self-emission by the heat flux coming from the plasma [220] and laser-heating [221, 222]. For very high plasma temperatures secondary electron emission can be the dominant effect, Wang et. al. [223].

Additional information on a variety of emissive probe setups and analysis methods have recently been summarised by Sheehan and Hershkowitz [224]. This paper also contains information on when best to use which technique. The plasma densities encountered during these experiments are typically in the range of $10^{18} \ldots 10^{19}$ m^{-3}. This is the very upper limit of using the floating point method. This is why, Sanders et. al. recently developed an emissive probe with a pulsed heating current [225], in order to obtain higher wire temperatures while keeping the average thermal load of the wire low.

The current to a Langmuir single probe can be strongly altered in the presence of the magnetic field. Especially, the electron current can be impeded substantially. The emissive probe relies on electrons emitted thermoionically to leave the probe. Of course, these electrons can be influence by the magnetic field, too. However, a number of publications used an emissive probe in combination with the floating point method to record plasma space potentials without reporting any malfunction of the probe or "suspicious" results, e. g. references [226–231], and particularly for magnetron discharges published by various authors [53, 191, 232, 233]. Electrons emitted by the probe will certainly be influenced by the magnetic field and can eventually be recollected. This would reduce the effective emitting surface area. However, for cylindrical probes emitted electrons almost always have a velocity component parallel to the magnetic field except in the worst case, when the probe is parallel to the magnetic field [224].

Emissive probes are a well-established diagnostic tool to measure the plasma space potential. The floating point method will be used to investigate the spatial and temporal evolution of the plasma potential in the discharge.

5.2.2 Experimental setup

The general experimental setup and measuring parameters are described in chapter 5.1. The emissive probe was mounted on top of a stem made of stainless steel and inserted at the side of the vacuum chamber. Positioning of the probe was done by moving the stem in axial direction at a constant distance from the target. The axial position of the probe above the target was changed by moving the magnetron together with the substrate. Emissive probe data was recorded for positions $r = 0 \ldots 90$ mm and $z = 10 \ldots 95$ mm with a step size of 5 mm. The temporal evolution of the plasma potential was measured at 342 spatial positions. By extracting information of the plasma potential for a given temporal position, spatially resolved plots of the plasma potential can be obtained.

The tip of the emissive probe is shown schematically in figure 5.3 [191]. The emitting part of the probe is a thoriated tungsten wire (99.4 % W, 0.6 % Th), (50 ± 5) µm in diameter and a length of (8 ± 1) mm. It was formed in a semi-circle and pushed into an alumina sleeve (inner diameter 0.5 mm, outer diameter 1.0 mm and length 8 mm), which facilitates mechanical and electrical connection to a tungsten rod (purity 99.9 %) (500 ± 50) µm in diameter and a length of about 12 cm. The opposite end of the tungsten rods is pushed into brass pins which then connect to the probe stem which has two copper wires running through it to enable connecting the probe tip to the heating and measuring circuit. The entire probe, except for the emitting wire at its tip, is housed in alumina tubes, which are clamped into a socket made of PEEK. The socket is formed of two custom-made parts joined by two screws. This enables easy maintenance and replacement of components. The most important task in designing the probe was to avoid deposition of a conductive titanium layer establishing an electrical connection between the hot probe and the cold probe holder, which would falsify the measurements. The plasma density in HiPIMS discharges is generally high and can easily exceed 10^{18} m^{-3}, which results in very small Debye lengths in the order of a few micrometers. Hence, the plasma can penetrate into trenches and cause deposition. The ceramic sleeve was therefore pushed into the alumina holder by 0.5 mm. Further improvement was achieved by filing the ceramic sleeve into a conical shape which avoids direct contact between the sleeve and the inner wall of the alumina holder. Both the alumina sleeve and the holding tube are cleaned whenever the thoriated tungsten wire was renewed and replaced on a regular basis. The resistance of the probe mounted inside the vacuum chamber was measured prior to each experiment to be $1.0 \ldots 1.5\ \Omega$ to assure proper connectivity of the probe.

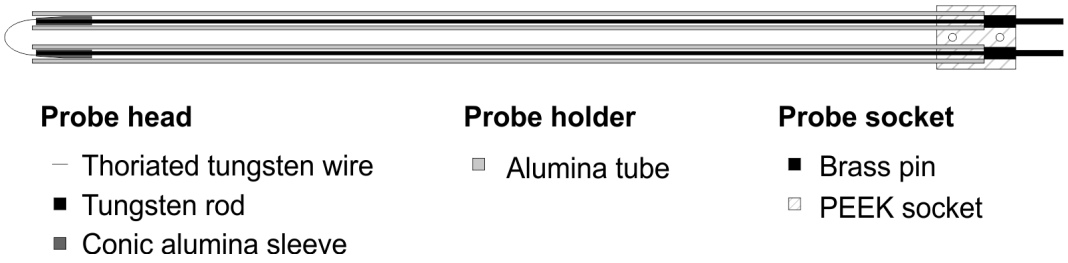

Figure 5.3: Schematic diagram of the tip of the emissive probe (after [191]).

The heating and measuring circuit is shown in figure 5.5. The entire circuit was disconnected from ground as the floating point method was used. A 12 V battery (7.2 Ah) provided energy to heat the filament of the probe. The heating current was adjusted by a

variable resistor and measured by a multimeter UT70A supplied by UNI-T. The accuracy of the heating current is about ±50 mA [234]. In order to avoid perturbation of the measured plasma potential by the voltage drop across the probe, the potential was measured in parallel to the probe in the centre of two 47 Ω resistors. A high voltage probe Tektronix P6015A was chosen to measure the plasma potential, because of its high input impedance of 100 MΩ [235]. The delay of the voltage measurements is 18 ns (oscilloscope and probe combined) and the accuracy of the measured voltage is 5 %.

The temporal resolution of the probe is critical for analysing the probe data, as one has to be sure that the measuring circuit can follow fluctuations in the plasma potential fast enough. This is particularly important for measurements at the beginning of the pulse. Fujita and Yagura [237] showed, that the temporal resolution can be expressed by means of the resistance across the sheath around the probe R_s, the measuring resistor R_m and the capacitance of the insulated circuit to ground C_g. Bradley et. al. also introduced the impedance of the sheath Z_s due to its capacitance, but also showed that this impedance is usually higher than the sheath resistance [236]. The measuring resistor R_m is 100 MΩ in the present case and currents through it can be neglected. As a result, the temporal resolution τ can be estimated as:

$$\tau \approx R_s C_g. \tag{5.3}$$

In other words, the capacitance of the measuring circuit has to be charged to have the measured potential being the plasma potential. This means, that minimising the capacitance of the heating circuit is the key to optimise for a fast response of the plasma potential measurements. This is the reason, why a very simple DC heating circuit was used with all cables reduced to a minimum length. The capacitance to ground was measured to be (180 ± 60) pF. Welzel et. al. used the random thermal current of electrons and a voltage drop equal to $k_B T_e/e$ across the sheath to calculate the sheath resistance [191]. Typical values during the HiPIMS pulse are an electron density of 10^{18} m^{-3} to 10^{19} m^{-3} and an electron temperature of $1 \ldots 3$ eV, which gives a response time of less than 10 ns. Thus, the probe follows quickly any changes of the plasma potential. At the beginning of the pulse, the conditions are largely different. The remnant electron density is likely in the range of $10^{14} \ldots 10^{15}$ m^{-3} and the electron temperature is about 0.3 eV. The response time of the probe then lies in the range of several microseconds. This is plausible considering the extreme case of measuring the space potential in vacuum, as reported by Diebold et. al. [238]. No negative potentials could be measured with the floating point method, because the filament only emits electrons and hence, only biases itself positive in respect to

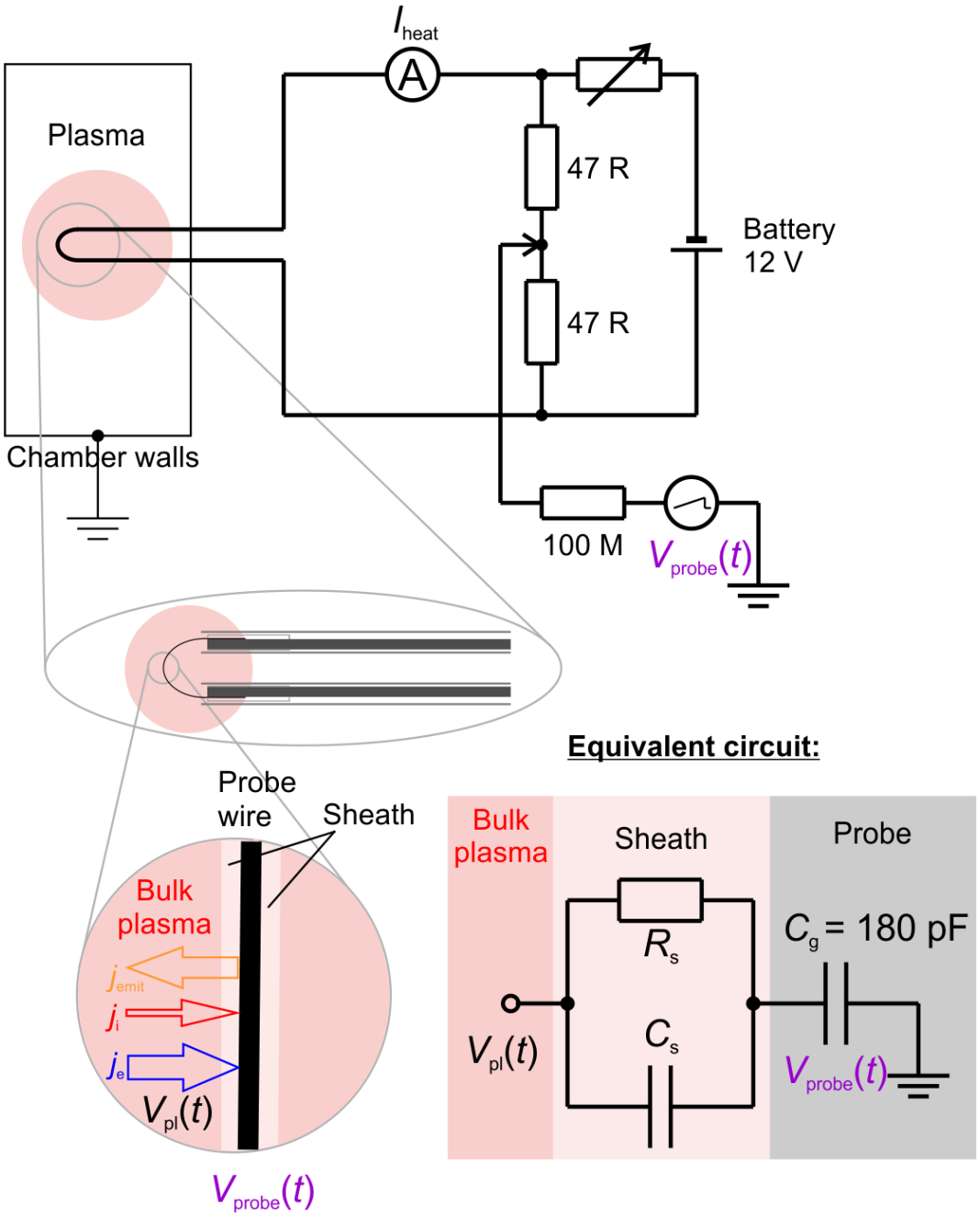

Figure 5.4: Heating and measuring circuit of the emissive probe measurements. The response time of the probe is determined by the resistance R_s and the impedance Z_s of the sheath and the capacitance of the circuit to ground C_g (after [191, 236]).

ground. Negative charges, however, have to be collected from the plasma. The lower the electron density, the slower the charging process.

It was tried to improve the situation by actively biasing the probe to negative voltages and measuring the current flowing to ground. As before, the plasma potential would be identified from the floating point, when the measured current is zero. The method showed promising results for measurements carried out in vacuum, but a problem occurred when investigating the HiPIMS discharge. When the filament is biased to -20 V or below, the probe itself creates charged particles by emitting electrons with kinetic energies above the ionisation threshold of argon. This sustains the plasma in the off-time, which strongly influences the ignition process and seriously alters the plasma conditions. Even pulsing the probe bias led to no satisfying result, because the probe was either still too slow to follow the plasma potential or disturbed the ignition process. Only the passive probe was used in the experiments.

5.2.3 Preliminary Experiments

A series of experiments was conducted to characterise the emissive probe. The most important task is to find the right heating current for which the probe potential saturates and which can be identified as the plasma potential. The temporal evolution of the probe potential was recorded for two characteristic positions when the heating current was varied. The HiPIMS discharge was operated with the substrate floating and the discharge parameters as stated in table 5.1. The first position labelled b) in figure 5.5 is in the dense plasma zone right above the racetrack, $r = 45$ mm and $z = 10$ mm, and the second position shown in figure 5.6 c) is in the plasma column, $r = 0$ mm, $z = 80$ mm, where the plasma density is lower. The heating current was varied between 0 A and 0.9 A, the maximum, which can only be applied for a short time before the wire evaporates. Three points in time are shown for both positions, the initial voltage peak, the stable stage of the discharge at $t = 70$ µs and the voltage overshoot during the transition from discharge on- to off-time. One can see, that the probe potential saturates during the stable stage when the discharge is investigated far away from the dense plasma zone (position c)). In the dense plasma, however, the probe potential does not fully saturate. The floating potential ($I_{\text{heat}} = 0$ A) is -30 V and the electron temperature at this position measured by means Langmuir probe to be 2 eV (compare figure 5.19). With the plasma potential being $V_{pl} \approx V_{fl} + 5.2 k_B T_e$, the theoretical plasma potential would be -20 V. The experimentally obtained value is $-(21.5 \pm 0.5)$ V for a heating current of 0.9 A. Considering the fact, that the plasma potential cannot be

approached by more than $1 \ldots 1.5 k_B T_e/e$ [214–216], the obtained value is what could be expected, theoretically. The same is true when studying the voltage overshoot, time labelled III. The initial peak shows quite a contradictory behaviour. The measured probe potential decreases with increasing heating current. The initial peak is very sensitive to the onset of the discharge current because this temporal position marks the increase of the electron density and thus allows the probe to be charged to the negative plasma potential. If this onset occurs earlier, as observed in this experiment, the response time of the probe is decreased and the plasma potential is measured at an earlier point in time, when it is still more negative. The delay of the discharge current changes by only 0.5 µs and it is not entirely clear if this shift is caused by the increased heating current. However, a drift by 0.5 µs is only marginal if it occurs in the same way for all measurements. In conclusion, a heating current of 0.85 A will be used for all experiments. This allows for measuring all radial positions $0 \ldots 90$ mm for one axial position before the probe has to be replaced. The probe breaks much earlier when a higher heating current is applied.

The error bars introduced in figure 5.5 were obtained from repeated probe measurements with a heating current of 0.85 A. The measurements of the initial peak have a low accuracy of about ± 20 V whereas the plasma potential during the stable stage of the discharge only varies by ± 0.5 V.

Another important feature to be investigated is the influence of the magnetic field on the measured probe potential, as the most practical approach on moving the emissive probe is by keeping its orientation in respect to the target constant. This means, all experiments were carried out with the loop of the thoriated tungsten wire parallel to the target. Due to the complex shape of the magnetic field, the loop is intersected by magnetic field lines with an angle between 0° and 90°. If the orientation of the probe has strong influence on the measured plasma potential as suggested by Mishra et. al. [89], mapping the plasma potential distribution can quite severely be disturbed by this effect. In order to evaluate the influence of the magnetic field, the probe was placed at two characteristic positions, in the dense plasma zone $r = 45$ mm, $z = 20$ mm and far away from the target $z = 100$ mm at the discharge axis $r = 0$ mm. The probe was then rotated around its own axis. The measurements were carried out with the HiPIMS discharge operated by the Sinex power supply ($E_{\text{pulse}} = 7$ J, $\tau = 100$ µs, $f = 50$ Hz) with otherwise same conditions as summarised in table 5.1. The substrate had to be removed to enable the probe to be inserted through the end flange. This is necessary to rotate the probe in respect to the magnetic field. The angle α shall describe the angle between the magnetic field and the normal of the loop of the emissive probe. An angle of $\alpha = 0^\circ$ means that the probe is intersected by magnetic field

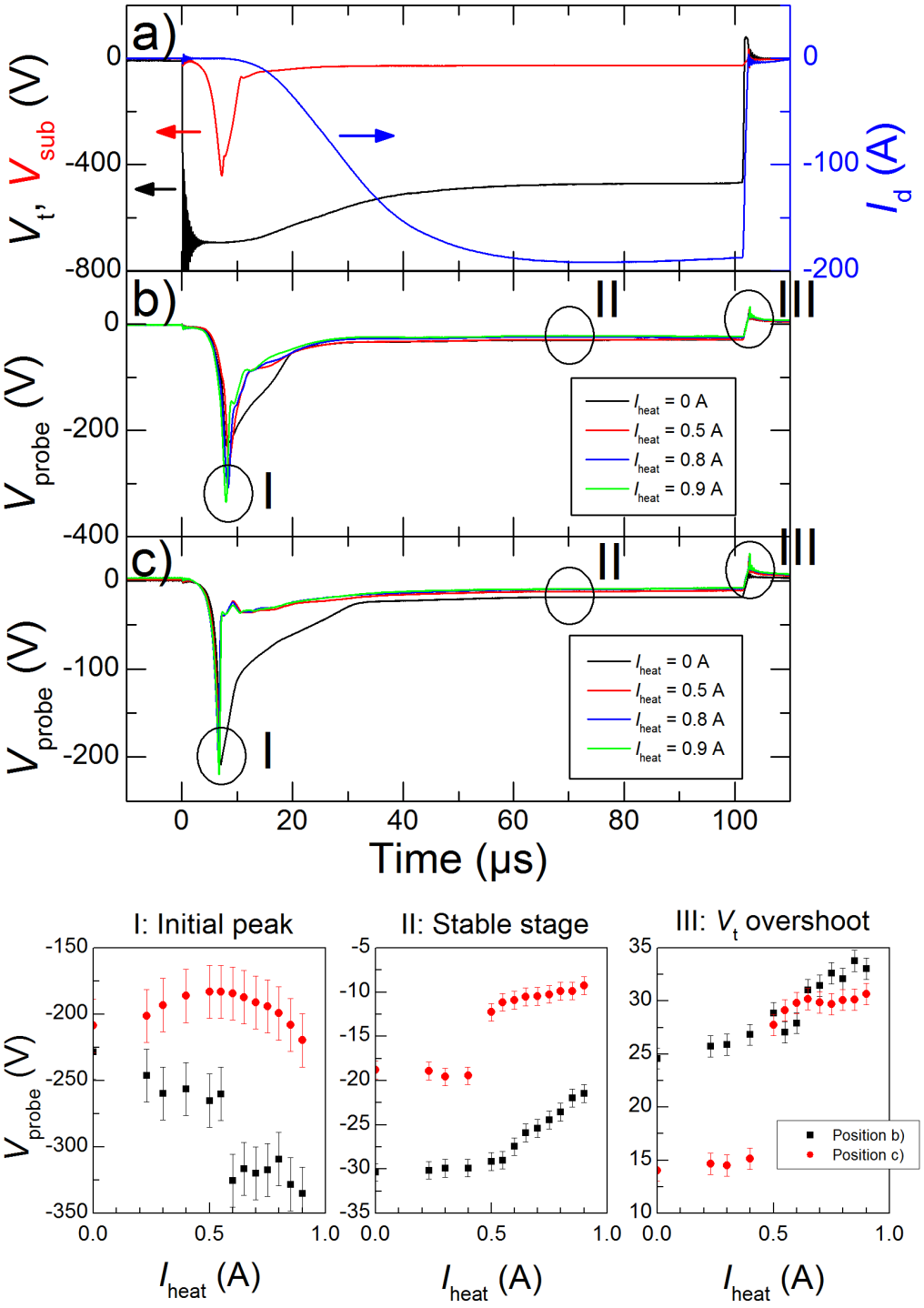

Figure 5.5: Influence of the heating current on the measured probe potential in the dense plasma zone, $r = 45$ mm, $z = 10$ mm b), and the plasma column, $r = 0$ mm, $z = 80$ mm c). The substrate was kept floating; further discharge parameters are summarised in table 5.1.

lines perpendicular to the loop surface. The temporal development of the probe potential for both positions in the discharge for three angles 0°, 45° and 90° are shown in figure 5.6. One can see that a significant change can only be observed for the initial peak of the plasma potential close to the target. It was found, that it changes by about 10 V when rotating the probe from 0° to 360° in steps of 45°. During the rest of the pulse, the change is rather small, only ± 0.6 V which is close to the accuracy of the probe potential observed during the same time. Changing the orientation of the probe far away from the target only changes the measured potential by ± 0.3 V. In conclusion, the measured plasma potential is hardly influenced by the orientation of the probe in respect to the magnetic field. This is plausible because some part of the filament always emits electrons in a direction parallel to the magnetic field in which electron transport is not impeded. One should also mention that the electric field in the sheath around the probe is rather large. With a voltage drop of $1 \ldots 3$ V across the sheath in the order of the Debye length which is about 10 µm, the electric field is in the order of $10^5\ \mathrm{V\,m^{-1}}$. This strong electric field should even transport electrons across the magnetic field and prevent electrons from being recollected by the probe.

A final remark shall be made on the influence of the probe on the HiPIMS discharge. This is particularly critical when the probe is immersed into the plasma close to the target. It was observed, that the discharge current is reduced by about 12 % in the stable stage, when the probe is inside the discharge compared to the case when no probe is placed into the plasma. The power supply helps sustaining the discharge current, because the voltage drop across the limiting resistor decreases with decreasing discharge current. This increases the voltage applied to the target and helps sustaining the discharge current. In addition, the delay of the discharge current onset can be increased by 2 µs to 3 µs. Thus, the recorded data of the plasma potential was first normalised to the onset of the discharge current, as it was done by Rauch et. al. [239]. The time axis was then recalibrated with the delay of the discharge current onset observed when no probe was placed into the plasma. As this delay is stable in respect to the initialisation of the target voltage, the initialisation of the target voltage is used to define the temporal position $t = 0$. The influence of the slightly lower discharge current during the stable stage of the discharge on the measured plasma potential can usually be neglected, because the plasma potential distribution is a result of charge separation and not of the charge carrier density itself. Measurements in a DCMS discharge reported by Bradley et. al. showed that the plasma potential did not change even though the discharge current was varied over one order of magnitude [53].

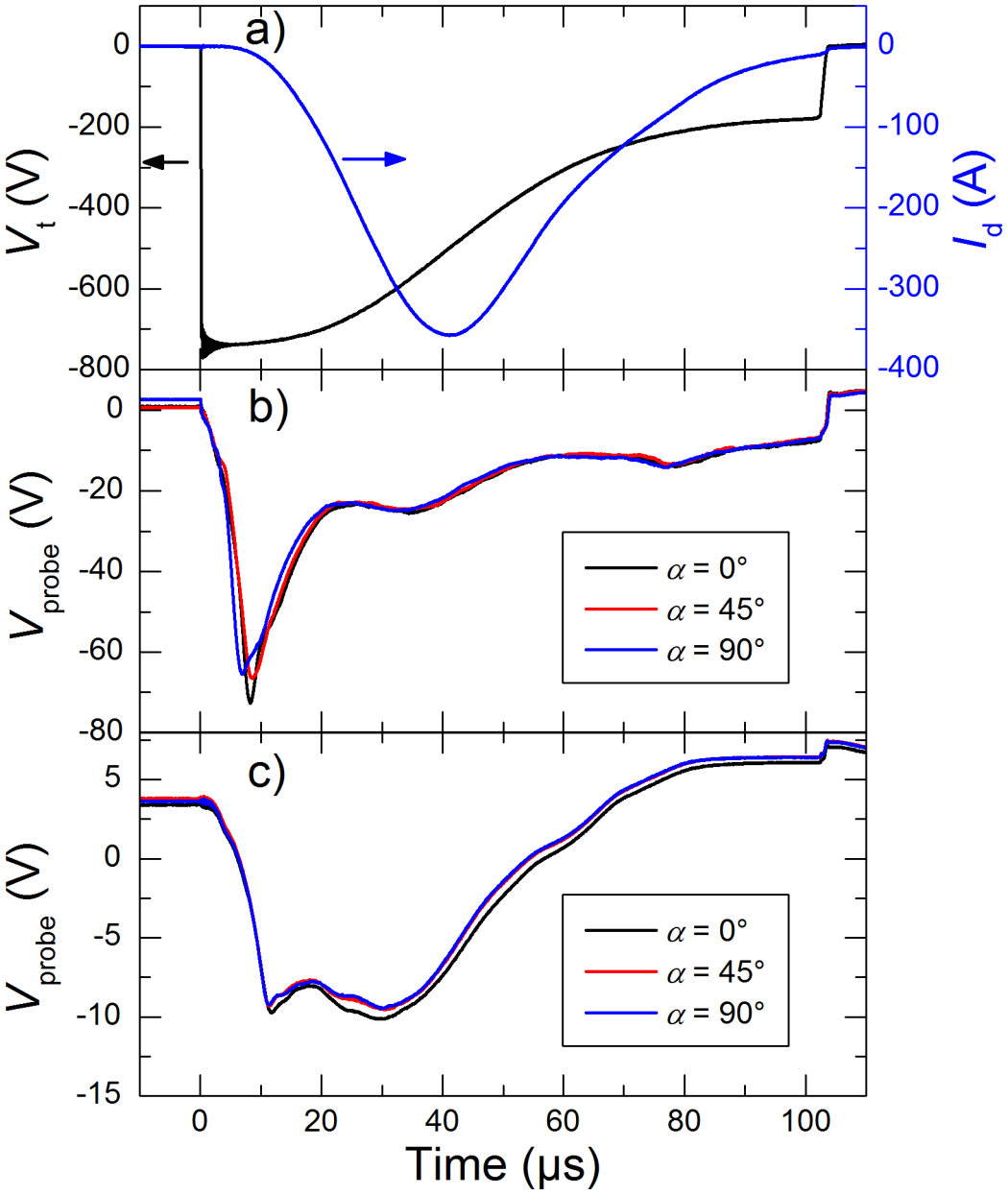

Figure 5.6: Influence of the magnetic field on the measured plasma potential in the dense plasma zone, $r = 45$ mm, z = 20mm b), and the plasma column, $r = 0$ mm, $z = 100$ mm c). No substrate was used and the discharge was operated with the Sinex power supply ($E_{\text{pulse}} = 7$ J, $\tau = 100$ µs, $f = 50$ Hz) and further conditions as summarised in table 5.1.

5.2.4 Measuring procedure

The vacuum chamber was conditioned prior to each experiment by running a DCMS discharge with 200 W for about 10 min until the target voltage and the discharge current stabilised. At the same time, the emissive probe was heated by a current of 0.5 A to clean the wire surface from oxides and other contaminations. Then, the home-made HiPIMS power supply was connected to the magnetron and the discharge was run with the desired settings for 15 min in order to stabilise. Afterwards, the probe was immersed into the plasma and placed at the discharge axis. The heating current was increased to 0.85 A and radial positions from 0 mm to 90 mm were measured at a constant distance from the target. When the probe was removed from the chamber, the resistance between the alumina tube at the tip of the probe and the brass connector pins was measured to check whether or not the probe got coated during the experiment. Only if the measured resistance was beyond the measuring range of the multimeter of 2000 MΩ, the plasma potential measurements were analysed. Otherwise, they were discarded and the experiment repeated with a new probe.

5.2.5 Temporal development

Two substrate configurations, floating and grounded, were investigated. The target voltage, substrate potential (for the floating substrate only) and the discharge current are shown in figure 5.7 a). It can be seen, that the initially applied target voltage is nearly the same for both configurations. The delay of the discharge current onset is about 7 µs in both cases and the current shows only little difference. It increases rapidly and stays roughly constant in the second half of the pulse just as the target voltage does. The ignition of the discharge is accompanied by a strongly negative peak in the potential of the floating substrate of $-(510 \pm 30)$ V indicating the presence of very energetic electrons as seen from Langmuir probe measurements [90, 91]. Poolcharuansin and Bradley even reported potentials beyond -600 V necessary to repel even the most energetic electrons. The exact temporal development of the floating potential measured at the substrate might, however, also be influenced by the response time similar to the emissive probe, described by equation 5.3. The capacitance to ground was measured to be (370 ± 70) pF, but the surface area is much bigger compared to the probe which makes the substrate follow changes of the potential much faster as pointed out by Bradley et. al. [236]. The floating potential quickly increases to more positive values which are constant during the stable stage of the discharge, $-(25 \pm 1)$ V. It should be mentioned that the potential of the grounded substrate is not perfectly zero. Despite the use of thick copper wiring used to ground the substrate

a voltage of -2 V could be observed during the stable stage of the discharge, increasing with the discharge current. The electron current flowing to ground can be calculated using the electron density and temperature measured in the vicinity of the substrate (see figure 5.19). The electron current would about 200 A, resulting in a resistance of 10 mΩ, caused by the cable and joints. This has to be kept in mind when discussing the measured data. The pulse termination is characterised by overshoots in all parameters, the target voltage, the discharge current, as well as the substrate and plasma potential.

The temporal development of the plasma potential for the substrate floating and grounded of two characteristic spatial positions are shown in figure 5.7. Figure 5.7 b) depicts the evolution of the probe potential in the dense plasma zone, $r = 45$ mm, $z = 10$ mm, whereas 5.7 c) was recorded far away from the target at the discharge axis, $r = 0$ mm, $z = 90$ mm. During discharge ignition one can observe three distinct maxima in the plasma potential as it was already reported by Mishra et. al. [89,240]. The first of these is most striking. Close to the target, peak values of -200 V and -300 V were recorded when the substrate was grounded and floating, respectively. A negative space potential of about -100 V can even be observed 90 mm away from the target, when the substrate is floating, which is much lower than observed for the grounded substrate -6 V. It is very likely that these negative space potentials are related to the expansion of the sheath during the ignition process. The electron density in the late afterglow was below the measuring threshold for the Langmuir probe system, thus, the sheath width cannot be calculated, but a matrix sheath may well be extended up to several centimetres above the cathode, as summarised in table 4.4. If the substrate is floating, there is an additional negative electrode, the substrate, which is also surrounded by an extended sheath. This might cause the more negative plasma potential observed with the substrate floating. However, one also has to consider the low temporal resolution during discharge ignition, which causes the initial peak to occur consistently after the onset of the discharge current is detected. It seems that the increase of the electron density is a necessary condition to allow the probe to be charged to negative values. For example, about 10^{11} electrons are necessary to charge the probe from 0 V to -300 V. This is only possible, if a descent electron density is already established. The built-up of the electron density also varies between different spatial positions which makes it very different to produce a two-dimensional map of the plasma potential during discharge ignition. It might even be possible, that the plasma potential is even more negative during the ignition. In the limit of no remnant electron density, the potential distribution would be that of a capacitor. In this case, the space potential 10 mm above the cathode (position b) in figure

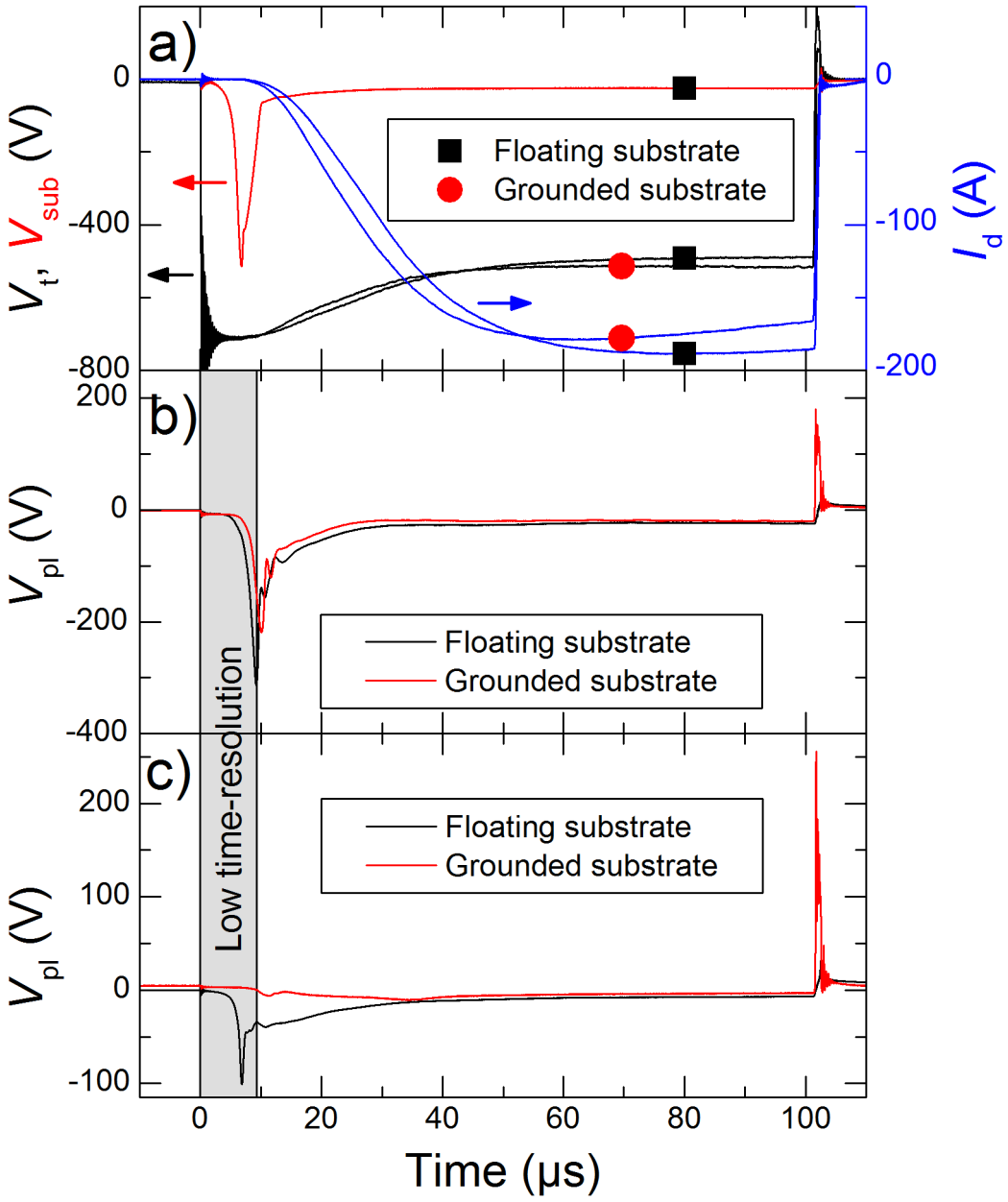

Figure 5.7: Temporal development of the plasma potential during the HiPIMS pulse observed in the dense plasma zone in the vicinity of the target $r = 45$ mm, $z = 10$ mm, b) and close to the substrate $r = 0$ mm, $z = 90$ mm c). The substrate was either floating (black line) or grounded (red line). Discharge conditions are summarised in table 5.1.

5.7) would be about −600 V. However, the low temporal resolution leaves the question of the spatial distribution during the discharge ignition unanswered.

The further maxima in the development of the plasma are strongly related to the highly turbulent transport of electrons and ions during the rapid increase of the discharge current as observed by optical [31, 32] and plasma potential measurements [239]. They originate from the averaging process and can be described as the (average) time when drifting ionisation zones pass the probe position. Thus, they occur at different times at different positions. Proper analysis would require to measure the spatial distribution of the plasma potential for each single pulse. This is not possible with the present setup, because it would require a set of probes immersed into the plasma somewhat similar to the arrangement used by Horwat and Anders to study the ion flux [241, 242].

The strongly negative peaks of the plasma potential during the initial stage of the discharge are succeeded by a rather stable stage of the plasma, during which the potential only varies slightly. Close to the target, a constant value of −19 V and −22 V was found when the substrate was grounded and floating, respectively. The plasma potential is more positive when measured further away from the target as seen in figure 5.7 c). However, it does not go positive for most positions as observed by Mishra et. al. [89, 240]. This is due to a difference in the discharge current, which levels at an almost constant value in the present study but drops significantly at the end of the pulse when the Sinex power supply is used.

Overshoots like in the present case are well-known from mid-frequency pulsed-DCMS discharges [190, 191, 232, 236, 243]. They are usually caused by the stray capacitance of the setup, comprising the power supply, wiring and the magnetron.

Usually, the plasma potential measured during the overshoot is found to be well above the target potential [190, 191, 232, 236, 243]. It was also reported, that a high probe temperature is necessary to achieve full saturation. Together with the investigation of the heating current, shown in figure 5.5, it can be concluded, that full saturation was not achieved for the overshoot in the dense plasma zone adjacent to the target. The measured probe potential for position b) is therefore found to be below the target potential at about +180 V for the grounded and at +35 V for the floating substrate. When the probe potential is measured in the vicinity of the substrate, figure 5.7 c), it is found to be more positive than the potential of the nearest electrode, the substrate. In the case of the grounded substrate, the plasma potential is with +250 V even higher than the target potential. The plasma potential measured with the floating substrate is only +35 V and thus higher than the substrate potential (+20 V). It is still below the target potential, but Welzel et. al. showed that

there is still a potential gradient in the axial direction, even in the off-time [191]. After the voltage overshoot, the plasma potential remains at a slightly positive value of +2 V to +5 V throughout the discharge volume. Hence, hardly any electric field can be found in the HiPIMS afterglow.

One shall also note, that the plasma potential was consistently measured more positive when the grounded substrate was used. This difference will be discussed in the next chapter, when the spatial distribution of the plasma potential, the electric field and the inferred drift speeds are shown.

5.2.6 Spatial distribution

The spatial plasma potential distribution is a fundamental parameter of any plasma discharge. It is as much the result of the spatial distribution of positive and negative charge carriers as it is to balance the flux of both species to fulfil quasineutrality. This is, on the one hand, described by the Poission equation

$$\nabla^2 V_{pl} = -\frac{e}{\varepsilon_0}\left(\sum_i Z_i n_i - n_e\right), \tag{5.4}$$

with Z_i being the charge of the positive ion species and n_i their respective density. The electric field given by

$$\boldsymbol{E} = -\nabla V_{pl}, \tag{5.5}$$

influences the flux of particles

$$\boldsymbol{\Gamma} = \pm\mu n\boldsymbol{E} - D\nabla n. \tag{5.6}$$

As quasineutrality is a fundamental property of all plasmas, the plasma potential has to adjust itself to balance the flux of positive ions and electrons to the walls of the plasma's container. For example, without the presence of a magnetic field, an ambipolar potential is established, which is positive in respect to ground, to impede the transport of electrons and enhance the transport of positive ions. In the presence of a magnetic field, the particle transport is strongly altered as both the electrons and the positive ions can be magnetised. In the present case, the magnetic field is too weak to have an effect on the trajectory of the ions, thus, only the electron transport can be impeded by the magnetic field. In the case of magnetron sputtering discharges, the plasma potential is inhomogeneous and strongly influenced by the magnetic field. This has been extensively studied both theoretically [45, 244–246] and experimentally [89, 190, 191, 232, 236, 239, 240, 243].

After the temporal evolution of the plasma potential was discussed for two characteristic positions in the discharge, its spatial distribution shall be investigated. Four temporal positions were selected to demonstrate the spatial distribution of the plasma potential V_{pl}, the inferred electric field $\boldsymbol{E}$, the net charge density Δn and the $E \times B$ drift speed. The discharge ignition is represented by spatial distributions given for $t = 10$ µs, while the rise of the discharge current is investigated for $t = 20$ µs. The discharge current recorded for the grounded substrate shows a maximum at about $t = 50$ µs and the stable stage of the discharge is shown for $t = 70$ µs, for which supplemental Langmuir probe data was collected, see chapter 5.3.4.

Figure 5.8 shows the plasma potential distribution for the standard magnetic field configuration for a floating and a grounded substrate installed 10 cm above the target. While axial positions from $z = 10$ mm to $z = 95$ mm are measured by the emissive probe, the substrate potential was recorded by a separate probe connected to the substrate and included as measured value for $z = 100$ mm. One can see the influence of the magnetic field and the negative target voltage in all images. The most negative potentials are found adjacent to the cathode right above the racetrack. The plasma potential increases both radially and axially. As discussed in the previous chapter, the plasma potential is strongly negative during the ignition of the discharge, $t = 10$ µs, and gradually increases with time. The potential profile also appears to widen close to the target when the discharge current rises. Comparing both substrate configurations, one can see that the plasma potential is consistently more negative when the substrate is floating, as it was observed for mid-frequency pulsed-DCMS discharges [191]. This is to enhance the electron transport across magnetic field lines, because the electron flux to the substrate is decreased due to the potential barrier $\Delta V = V_{pl} - V_{fl}$. Hence, only a small fraction of electrons can escape from the discharge via the substrate. The current is essentially limited by the ions, as zero net current is drawn from the insulated substrate. It is worth mentioning, that the major part of the target voltage of about -500 V drops in the region $z < 10$ mm. Mishra et. al. reported fairly low plasma potentials $V_{\mathrm{pl}} > -30$ V for axial positions as close as 2 mm above the target, giving an upper approximate of the cathode sheath width of < 2 mm. It can therefore be concluded, that the current emissive probe measurements only allow for investigating the plasma potential in the extended, magnetised pre-sheath. The potential drop recorded for this region is only about 5 % of the target voltage, which is consistent with emissive probe measurements reported by other authors [89, 239, 240].

The electric field was calculated from the measured plasma potential $\boldsymbol{E} = -\nabla V_{pl}$. The measured data was smoothed by a Savatzky-Golay algorithm of order three before the gra-

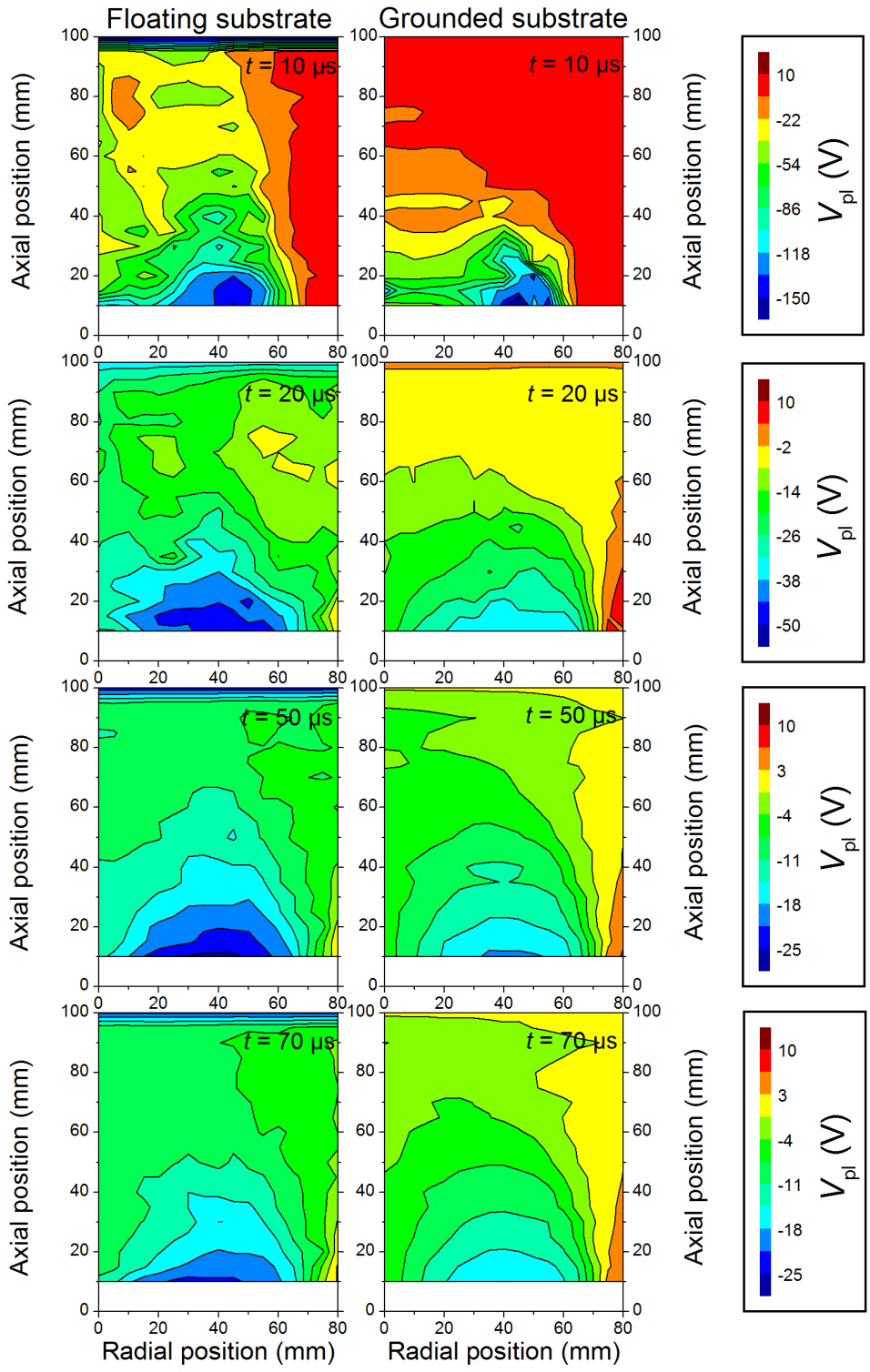

Figure 5.8: Spatial distribution of the plasma potential during a HiPIMS discharge pulse with a floating and a grounded substrate. Discharge conditions are summarised in table 5.1.

dient was calculated. The resulting electric field is shown in figure 5.9. During discharge ignition, extremely large radial and axial fields in the order of $10^4\ \mathrm{V\,m^{-1}}$ can be observed in the vicinity of the target, which was also reported by Mishra et. al. [89]. Such behaviour was already inferred when modelling the motion of remnant electrons when the target voltage is applied at the beginning of the pulse (see figure 4.14). Electrons starting close to the discharge axis or at the outer edge of the discharge are accelerated away from the target leaving a positive charge (ions) behind. The magnetic field orientated parallel to the target prevents electrons from moving far from the target. The difference in charge causes high gradients of the plasma potentials, see equation 5.4. It should be mentioned, that the major part of the plasma bulk ($z > 60$ mm) remains nearly field-free, especially when the substrate is grounded. This might be attributed to the different substrate potential present during this stage of the discharge. The grounded substrate is of course at a potential of 0 V, whereas the potential of the floating substrate peaks at -510 V. The floating substrate is then probably also surrounded by an advanced sheath which causes high electric fields in the bulk of the discharge. An additional contribution may come from the time response of the emissive probe, which is not necessarily the same everywhere in the discharge, because the electron density and temperature and hence, the sheath resistance can differ (compare equation 5.3). The electron density in the vicinity of the grounded substrate is expected to be particularly low during pulse ignition, as electrons can easily escape the discharge volume, as shown for the stable stage of the discharge in figure 5.19. The low electron density may result in a very poor temporal resolution of the emissive probe. In consequence, the probe may not follow the plasma potential close enough and the negative values which might be present cannot be recorded. The electric field would then be calculated too low.

With progressing time, the electric field is not only reduced to a maximum of about $1.5 \times 10^3\ \mathrm{V\,m^{-1}}$ but this maximum is also moved to higher radial positions, from $r = 60$ mm to $r = 70$ mm. One can also nicely see the influence of the magnetic field when looking at the electric field during the stable stage of the discharge. It is found to be maximal where it has to transport electrons out of the discharge volume across a strong magnetic field. If the substrate is grounded, electrons only have to be transported into the region where magnetic field lines do not close in front of the target anymore but guide the electrons towards the substrate where they can escape the discharge. This loss mechanism is strongly impeded by the floating potential if the substrate is insulated from ground. Thus, the electric field is nearly parallel to the target at the outer edge of the discharge $r = 80$ mm, as electrons have to be transported across the magnetic field in this region. Considering the motion of positive ions, one can see from both the plasma potential and the electric field that they

are accelerated towards the target by the axial field and towards the racetrack, $r \approx 45$ mm, by the radial field component. This means, on the other hand, that a significant amount of ionised sputtered particles is attracted back to the target, which can significantly reduce the deposition rate as pointed out by Mishra et. al. [89]. The spatial distribution of the electric field measured during the rise of the discharge current, $t = 20$ µs, reveals quite a few positions where the field is reversed, pointing to the substrate. This behaviour coincides with the asymmetric intensity profiles found for the plasma-induced emission during the plasma built-up stage. Some suggestion on the development of the plasma are summarised in chapter 4.4.4. The axial field in the vicinity of the floating substrate is high throughout the entire discharge pulse, 3×10^3 V m^{-1}, due to its negative potential. Ions impinging on the floating substrate therefore gain an extra kinetic energy equivalent to the voltage drop between the plasma and the floating potential.

In the next step, the difference in the particle density between positive and negative charge carriers

$$\Delta n = \sum_i Z_i n_i - n_e \tag{5.7}$$

is calculated by using

$$\Delta n = \frac{\varepsilon_0}{e} \nabla \cdot \boldsymbol{E}. \tag{5.8}$$

A positive value of Δn indicates an excess of positive ions, whereas a negative value is obtained where more electrons than positive ions are present. The spatial distribution of the net charge density Δn is shown in figure 5.10. The red contour line indicates the change from a positive to a negative net charge. During the discharge ignition a large charge separation in the order of 10^{14} m^{-3} can be found close to the target. A large negative charge is found above the racetrack, $r \approx 45$ mm, where the magnetic field confines the electrons most efficiently. A positive net charge can be seen at the discharge axis and at the outer edge of the discharge. This confirms the assumption that positive ions are left behind, whereas electrons can easily be accelerated away from the target by the advancing sheath. This happens in regions where the magnetic field is predominantly orientated perpendicular to the target. On the other hand, electrons are well-confined above the racetrack where the electron density might be increased further by secondary electrons originating from the target in the racetrack region. Even though the charged particles might be distributed homogeneously in the discharge volume just before discharge ignition, the strong radial electric field accelerates the positive ions towards the racetrack area, where they impinge on the target and release secondary electrons. One should also note that the electron density is in the range of $10^{14} \ldots 10^{15}$ m^{-3} during discharge ignition. The charge separation

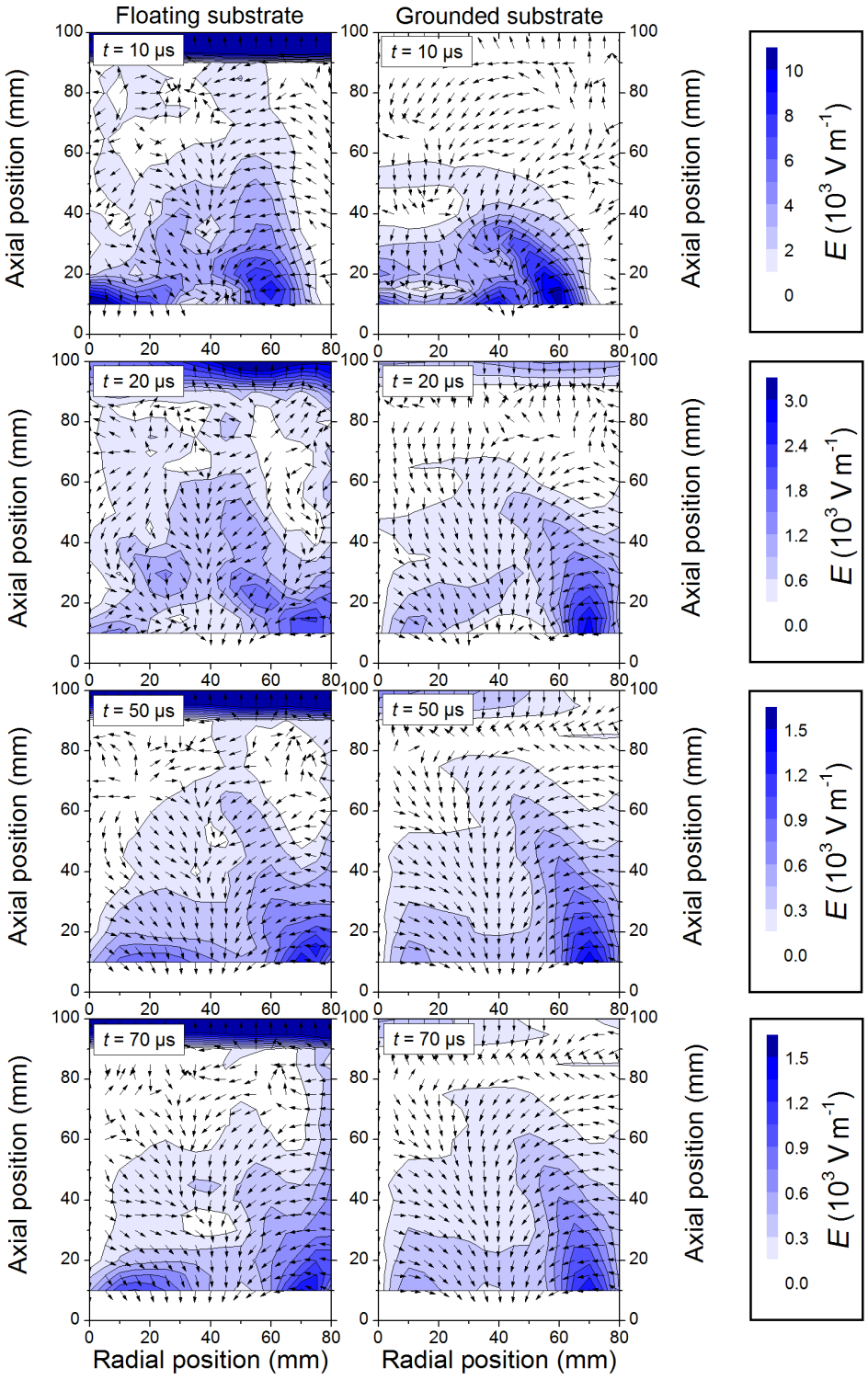

Figure 5.9: Spatial distribution of the electric field during a HiPIMS discharge pulse with a floating and a grounded substrate. Discharge conditions are summarised in table 5.1.

is therefore significant. In other words, the areas of positive net charge are almost exclusively populated by ions whereas electrons is the predominant species where a negative net charge is observed. This changes dramatically when the discharge develops into the stable stage. The net charge density does not only drop by an order of magnitude but the relative charge separation, i. e. the net charge density divided by the electron density, decreases to 10^{-6}. Thus, separation of charges is important to create the plasma potential distribution but has hardly any influence on the quasineutrality as $\sum_i Z_i n_i - n_e << n_e$. This agrees very well with the common assumption made for the pre-sheath. One can see that a negative excess charge is found in the magnetically confined region adjacent to the target independent of the substrate configuration. Here, the magnetic field confines electrons very efficiently. Close to the discharge axis and at the outer edge of the discharge, the net charge is positive close to the target but gets more negative towards the substrate. This behaviour is particularly pronounced when the substrate is floating, which is again a result of the confining nature of the insulated substrate (diameter 20 cm), which poses a high potential barrier for the electrons. As electrons have to be transported radially out of the discharge volume, their density is slightly increased at the outer edge of the discharge. The region in the vicinity of the substrate reveals the most striking difference between the floating and the grounded substrate. The net charge close to the floating substrate is positive whereas it is negative when the substrate is grounded. The negative potential of the floating substrate repels electrons and attracts positive ions, which causes a slight shift in the net charge favouring positive ions. When the substrate is grounded, one can observe a negative net charge density at the discharge axis right above the magnetic null. Electrons which are scattered and subsequently transported out of the magnetically confined region close to the target are guided by the magnetic field lines towards the substrate. These field lines are bent towards the discharge axis as shown schematically in figure 4.22. Guiding the electrons towards the discharge axis slightly increases the electron density compared to the density of positive ions in this area. The area of the magnetic null is not readily accessible by electrons as they would have to cross magnetic field lines. They are more likely guided around this area.

Finally, the calculated $E \times B$ drift speeds shall be examined for the temporal positions 10 µs, 20 µs, 50 µs and 70 µs after pulse initialisation, displayed in figure 5.11. The direction of the drift is clockwise, negative azimuthal direction, for all times and all positions. The areas of investigation is limited to $z \leq 80$ mm, because electrons are only confined by the magnetic field in this region where the magnetic field lines close in front of the target. Electrons closer to the substrate can easily leave the discharge volume with-

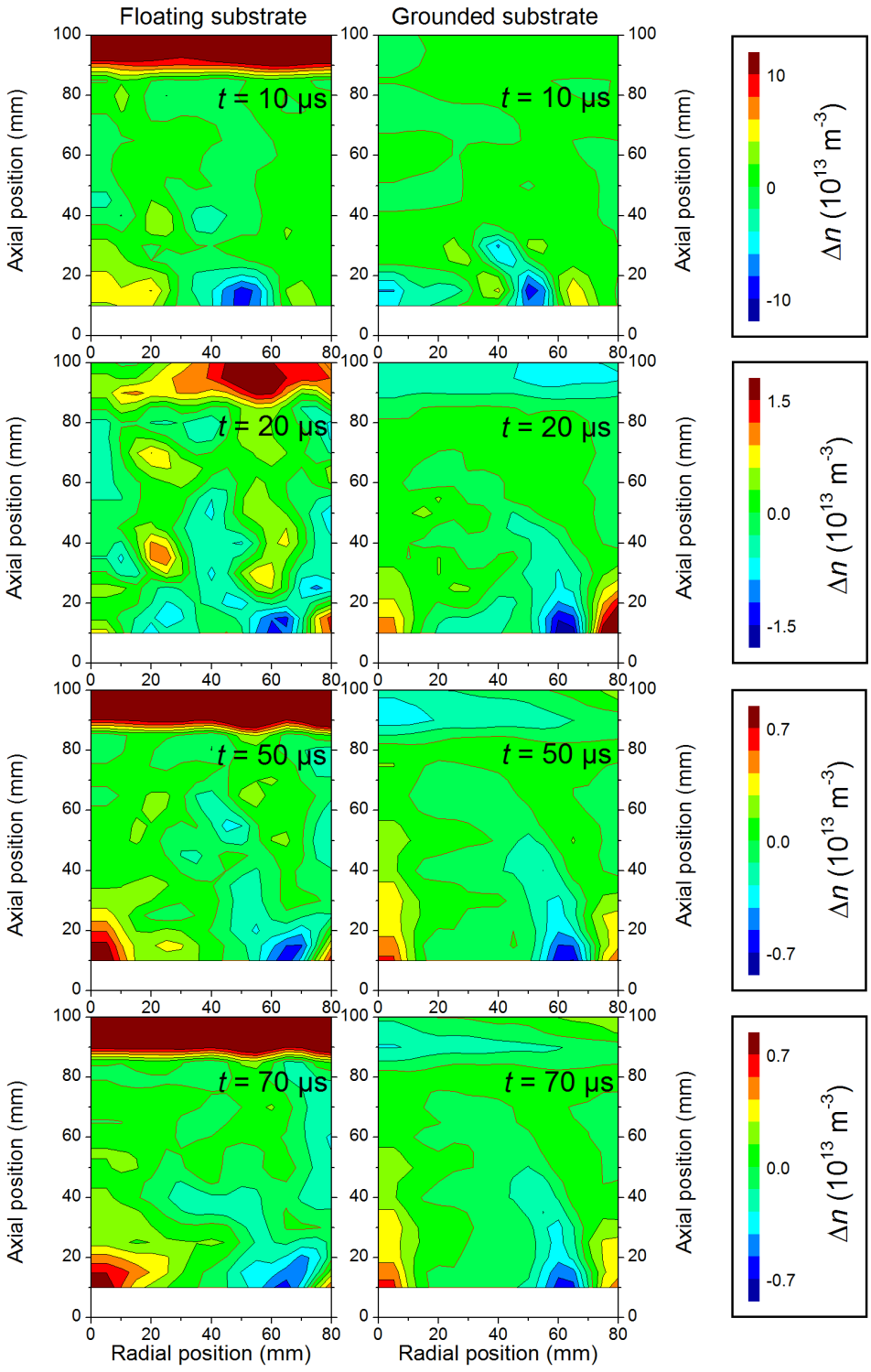

Figure 5.10: Spatial distribution of the net charge density during a HiPIMS discharge pulse with a floating and a grounded substrate. Discharge conditions are summarised in table 5.1.

out a large drift component in their motion. One can see, that the maximum of the drift speed is found along the curved magnetic field lines remote from the target. It is observed closer to the target during discharge ignition, due to the higher electric field close to the target. With progressing time, it moves away from the target and closer to the discharge axis where the magnetic field is rather low, $v_{E\times B} \propto B^{-1}$. This has also been reported by Mishra et. al. [240]. There is some difference between the floating and the grounded substrate. While the calculated $E \times B$ drift speed nicely follows the curved magnetic field lines when the substrate is grounded, a substantial drift speed at the outer edge of the discharge, $r = 80$ mm, is observed when the substrate is floating. This reflects the increased electric field in the case of a floating substrate necessary to transport electrons radially out of the discharge.

Data recorded by the emissive and the Langmuir probe for a temporal position $t = 70$ µs was used together with magnetic field measurements to also calculate the magnetic field gradient and curvature drift v_B according to equations 2.31 and 2.32 and the diamagnetic drift v_{dia}, equation 2.38. All three drift speeds were summed up and the azimuthal current density calculated

$$j_\phi = -en_e v_d, \tag{5.9}$$

with v_d the total drift speed. The drift speeds and azimuthal current density are shown for a temporal position of 70 µs in figure 5.12. The drift speeds are clockwise just as the $E \times B$ drift, while the azimuthal drift current is counter-clockwise. All drift speeds are in the range of 10^5 m s^{-1} and show their maximum remote from the target. The maximum of the curvature and gradient drift speed is found 60 mm above the target at a radial position of $r = 20$ mm. This is the place where the radius of curved magnetic field is smallest. The spatial distribution of the curvature and gradient drift speed hardly hardly show any difference between the two substrate configurations because the magnetic field is the same and the distribution of the electron temperature is very similar in both cases, see figure 5.19. It agrees well with the measurements carried out for a DCMS discharge [54]. The diamagnetic drift speed is the smallest contribution to the total drift speed. It is about 50 % higher in the case of the grounded substrate due to the higher gradient of the electron pressure, figure 5.19. The calculated drift current density is highest, about 1.2×10^5 A m^{-2} when the substrate is insulated from ground. Its maximum is found 60 mm and agrees with the maximum of the curvature and gradient drift speed is found. However, the drift current above the target is not negligible, about 4×10^4 A m^{-2}, as the high electron density compensates for the relatively low drift speeds. The azimuthal current density j_ϕ was

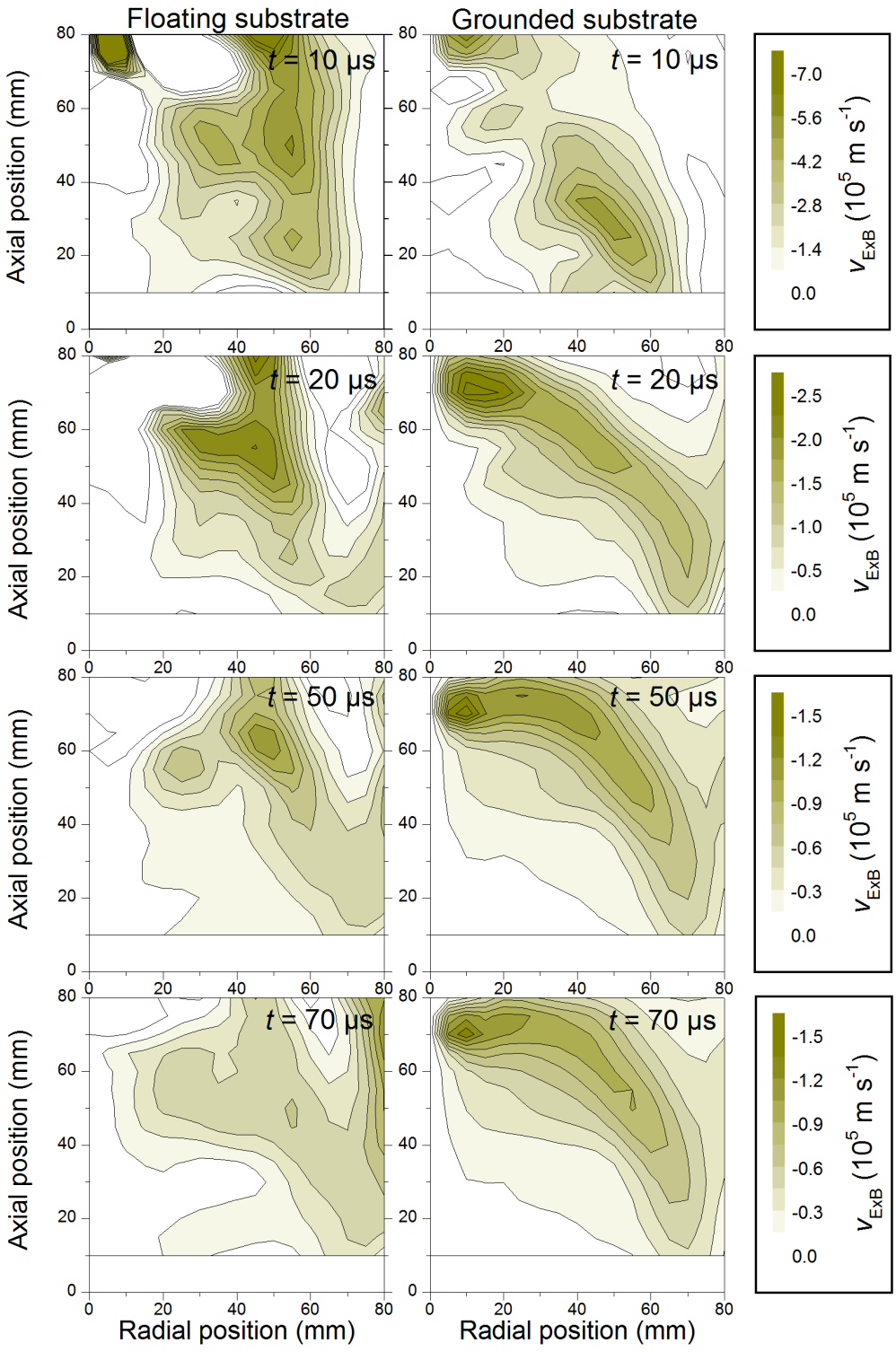

Figure 5.11: Spatial distribution of the $E \times B$ drift speed during a HiPIMS discharge pulse with a floating and a grounded substrate. Discharge conditions are summarised in table 5.1.

also recently studied by means of a B-dot probe by Lundin et. al. [247]. Comparing the present results and the results published by this group is somewhat cumbersome, because no substrate was used, the magnetic field is more balanced in that study and the power supply was a Sinex, hence no stable discharge level is observed. As in the present study, the maximum position of the azimuthal current density is found where the magnetic field is orientated parallel to the target. However, the overall maximum is found at an axial position closest to the target which is not the case in the present study. The current density is also about three times lower than in the present calculations. It is not quite clear, if the difference is due to the different discharge parameters or caused by the different measuring methode.

The extraordinarily high peak of the magnetic field curvature and gradient drift is the main reason for the maximum of the drift current density being found remote from the target (compare figure 5.12). However, the error can be estimated to be 16 %, with the major part of 10 % coming from the accuracy of the electron temperature measurement. By contrast, the accuracy of the magnetic induction is only 1 % for each component, radial and axial, yielding a total error of less than 1.5 % of the absolute value of the magnetic induction. In conclusion, the calculation of the curvature drift is rather accurate and as the electrons are still magnetised ($r_c = 2.5$ mm for $B = 1.5$ mT and $k_B T_e = 2.5$ eV) the obtained drift is expected to occur. However, it should be mentioned that similar discrepancies in the drift current density were reported for DCMS and MF-pulsed DCMS [53, 248]. B-dot probe measurements carried out in a pulsed DCMS discharge [248] agree very much with the results of Lundin et. al. [247], who both found the maximum of the azimuthal current density closest to the target, whereas this maximum was found remote from the target when it was calculated from the drift speeds and the plasma density, this study and references [53, 54]. It appears, that the differences observed between the measured current density and the calculated value are systematic in nature. However, the reason for this behaviour is not clear. Vetushka et. al. suggested inaccuracies in the measurement of the spatial distribution of the electron density due to the presence of the magnetic field used in [53, 54] and the use of a different target material in their study. Both arguments do not hold, because the electron density was deduced from quasineutrality and the measured ion density [53, 54]. The ion current collected by the Langmuir probe is not influenced by the magnetic field in magnetron sputtering discharges because the magnetic induction is too low and the gyroradius of the ions to large due to their large mass. The target material, on the other hand, should not have any influence on the spatial distribution of the azimuthal

current density, especially when considering the generally low degree of ionisation of the sputtered flux in DCMS and MF-pulsed DCMS.

In summary, the calculated drift speeds agree quite well with references [239, 240] for HiPIMS discharges and reference [54] for the curved and gradient B drift. However, the total drift current density does not agree well with direct measurements by means of a B-dot probe [247]. This discrepancy seems to be repeatable as one can see from previous reports on the measured and calculated drift current density, see references [53, 54, 248]. The reason for this behaviour is not yet understood, but might partly be attributed to relatively high uncertainties of both methods, which are in the order of 40 % for the calculation (combined drift speeds and electron density) and up to 50 % given by Lundin et. al. [247]. Further investigations would need to be carried out to clarify this issue, which should start with a comparison of both techniques in a DCMS discharge under same conditions.

The current density calculated in the present study will be used for modelling the transport of sputtered particles.

The influence of the balance of the magnetic field was investigated for three magnetic field configurations while the substrate was grounded. Figure 5.13 shows the magnetic field, the measured plasma potential, the electric field, the net charge density and the calculated $E \times B$ drift speed for temporal position $t = 70$ µs. The position of the magnetic null shifts by 15 mm from $z = 65$ mm to $z = 80$ mm, while the magnetic induction at the racetrack position increases from 35 mT to 40 mT. The plasma potential shows only little difference between the magnetic field configurations, but the influence is easier to be observed in the electric field distribution. One can see, how the electric field at radial position $r = 15$ mm reduces when the imbalance of the magnetron is increased. At the same time, the electric field at the outer edge of the discharge $r = 70$ mm is increased to facilitate electron transport across the magnetic field close to the target. The net charge density confirms these trends. It is positive at the discharge axis right above the target and decreases with the imbalance of the magnetron. On the other hand, the negative net charge at the radial position $r = 60$ mm increases with the imbalance of the magnetron, which increases the electric field in this region. The negative excess charge observed for the grounded substrate in figure 5.10, is also found in all three configurations. The influence of the position of the magnetic null can be seen as the position of the negative net charge moves closer to the target when the magnetic null is closer to the target, i. e. when the magnetron is more unbalanced. The axial position of the negative charge moves from $z = 85$ mm to $z = 80$ mm and $z = 70$ mm, when the position of the magnetic null changes from $z = 80$ mm to $z = 75$ mm and $z = 65$ mm. This demonstrates how the electron trans-

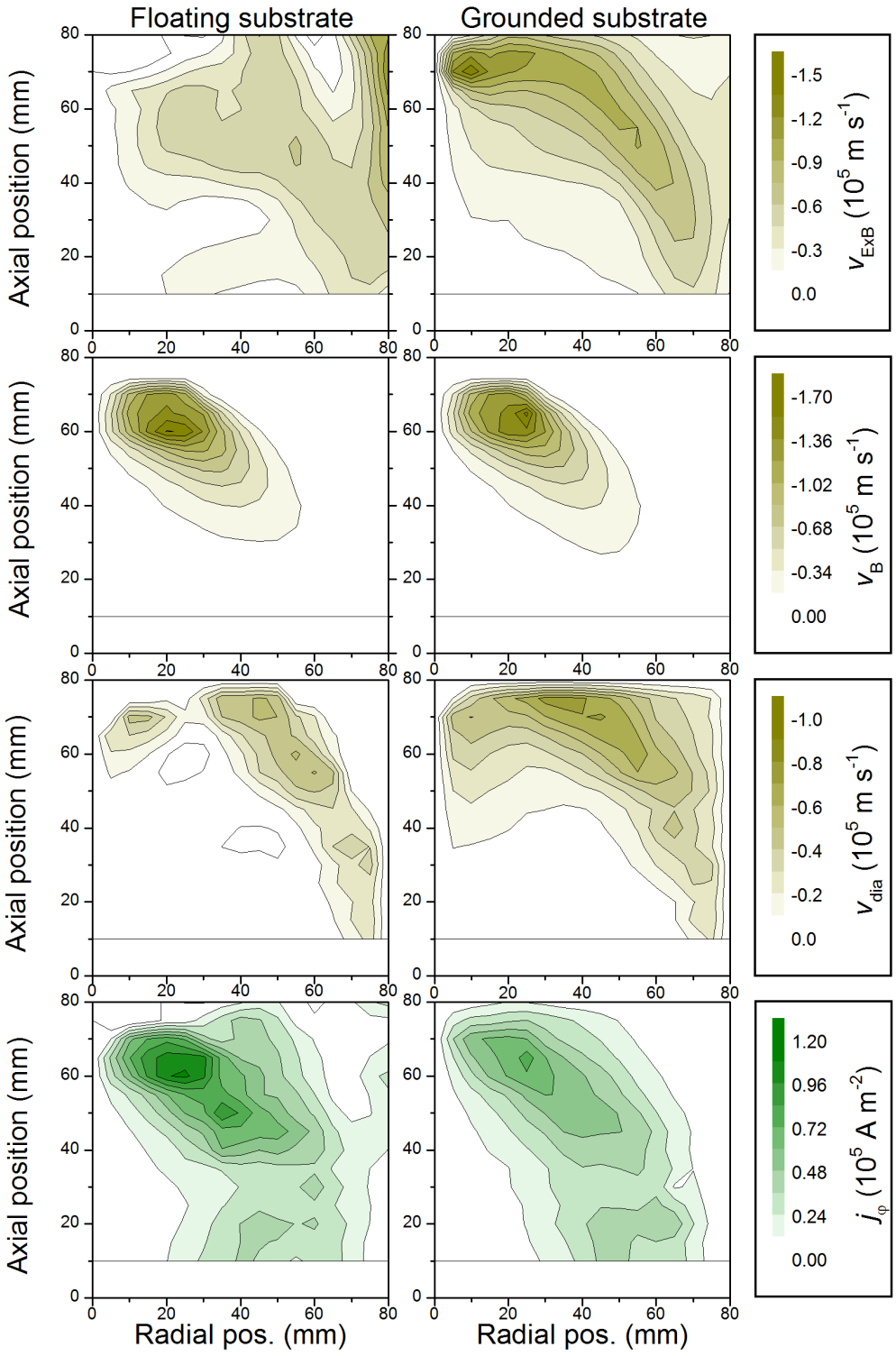

Figure 5.12: Spatial distribution of the drift speeds and the azimuthal current density during the stable stage of a HiPIMS discharge ($t = 70$ µs) with a floating and a grounded substrate. Discharge conditions are summarised in table 5.1.

port works, when the substrate is grounded. The strong radial electric field transports the electrons across the closed magnetic field lines into the region where the magnetic field guides them towards the substrate. Finally, the $E \times B$ drift speed shows an arch-like distribution with the highest speed obtained close to the discharge axis. The axial position, however, changes with the balance of the magnetron. The most balanced configuration shows the maximum $E \times B$ at $z = 75$ mm, while it is moved to $z = 70$ mm and $z = 60$ mm when the unbalance of the magnetron is increased. The maximum can be found at the outermost magnetic field lines which still close in front of the target.

In summary, the changes of the plasma conditions are rather subtle when investigating the influence of the balance of the magnetic field. This is simply because the position of the inner and the outer magnet can be adjusted slightly, but not the entire spectrum from a balanced to a very unbalanced configuration is accessible. The transport model will therefore focus mainly on the different substrate configurations with the standard magnetic field configuration.

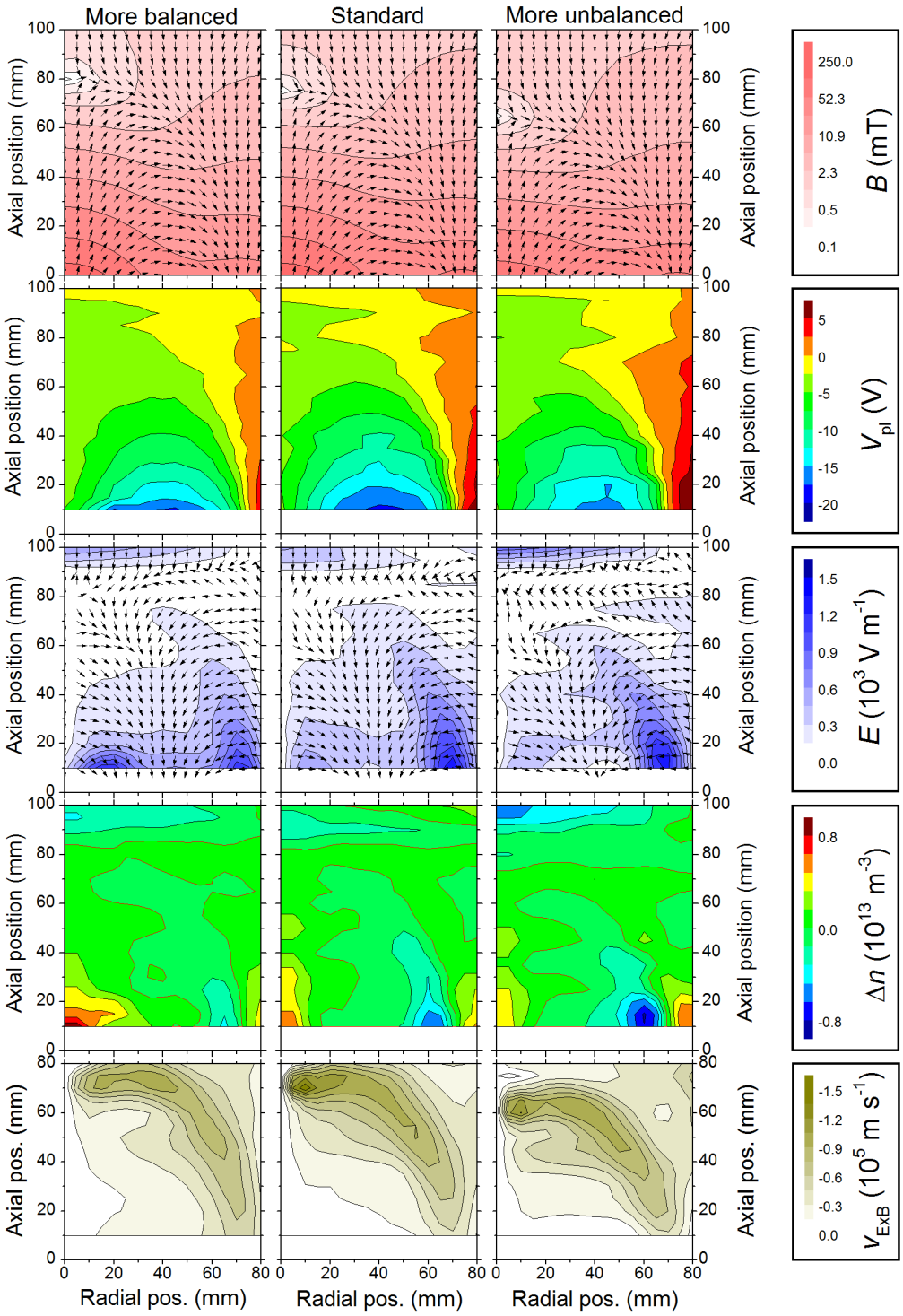

Figure 5.13: Investigation of the stable stage of the HiPIMS discharge ($t = 70$ µs) for different magnetic field configurations with a grounded substrate. Discharge conditions are summarised in table 5.1.

5.3 Langmuir single probe

5.3.1 Theoretical background

A simple approach of a Langmuir probe is to immerse a body, which is usually called a probe, into the plasma and to measure the current through the probe I_p when sweeping the probe bias voltage V_b in respect to ground. While the probe could have any shape, analytical or numerical solutions are only available for three major shapes, namely planar, cylindrical and spherical probes. The cylindrical probe is the most commonly used arrangement, because it simply represents a wire immersed into the plasma. Typical dimensions are a length l_p of a few millimetre and a radius r_p in the sub millimetre range. Hence, such a probe is usually seen as a negligible disturbance to the plasma.

The little influence on the plasma can be shown by investigating the sheath around the probe. Kiel published a formula for the sheath width d_s of a cylindrical probe [249]:

$$d_s = \sqrt{2}\tau(\alpha)\lambda_d \left(\frac{r_p}{\lambda_d}\right)^{1/4} \left(\frac{e\left|V_b - V_{pl}\right|}{k_B T_e}\right)^{1/2}, \tag{5.10}$$

with λ_d being the Debye length and $\tau(\alpha)$ is a parameter depending on the temperature ratio of the repelled and the attracted species. When the probe bias voltage is below the plasma potential, $V_b < V_{pl}$, electrons are repelled and $\tau(\alpha) = 1.54$, whereas $\tau(\alpha) = 1$ in the electron collection regime, $V_b > V_{pl}$. Maxwellian velocity distribution functions for both the electrons and the positive ions were assumed and in our particular case the ions shall be in rest $T_i = 0$. For a typical effective probe voltage $\left|V_\mathrm{b} - V_\mathrm{pl}\right| = 50\,\mathrm{V}$, i. e. the probe is biased $\pm 50\,\mathrm{V}$ in respect to the plasma potential, a particle density of $10^{19}\,\mathrm{m}^{-3}$ and an electron temperature of $k_\mathrm{B}T_\mathrm{e} = 3\,\mathrm{eV}$ a sheath width of 44 µm and 67 µm can be derived for the electron saturation and the ion saturation region, respectively.

A current-voltage $I_p - V_b$-characteristic of a cylindrical probe is shown in figure 5.16. For strongly negative bias voltages the probe repels electrons and the current is purely an ion current. This region is called ion saturation. For the probe being strongly positively biased, no ions but only electrons are collected, i.e. electron saturation region. The region between ion and electron saturation is a transition where both electrons and ions are collected. As soon as the probe is biased more negative than the plasma space potential V_{pl}, electrons are being repelled. However, only the electrons in the distribution with too little energy cannot reach the probe anymore. A Boltzmann factor is commonly used to describe this behaviour for Maxwellian electrons. The potential where electron and ion

current equal, i. e. no net current in or out of the plasma, is the aforementioned floating potential, see chapter 2.3. The transition region extends further to more negative probe bias until hardly any electron is collected by the probe and the ion saturation region is reached. One should mention that a decrease of the ion current described by a Boltzmann factor must also exist for bias voltages above the plasma space potential. However, due to the low ion temperature $T_i << T_e$ and the already low ion current the Langmuir probe is insensitive to the ion temperature. In conclusion, the current-voltage characteristic can give us information on the electron density n_e and temperature T_e, the ion density n_i and the floating V_{fl}, as well as the plasma space potential V_{pl}. However, we will describe a more accurate way of determining the plasma potential in chapter 5.2.

The two potentials, floating and plasma potential, can readily be obtained from the $I_p - V_b$-characteristic. The electron temperature is found analysing the electron current I_e in the electron repulsion region, i. e. $V_b < V_{pl}$. It can be shown, that the electron density is described by a Boltzmann function:

$$n(\boldsymbol{r}) \approx n_0 \exp - \frac{e(V_{pl} - V(\boldsymbol{r}))}{k_B T_e}. \tag{5.11}$$

The electron density in the bulk is denoted as n_0 and $n(\boldsymbol{r})$ and $V(\boldsymbol{r})$ are the electron density and the potential at position $\boldsymbol{r}$, respectively. It is worth noting, that this expression holds for any shape of probe. However, this approximation only holds in the case of sufficiently negative probe bias, $e(V_{pl} - V_b) >> k_B T_e$ [36]. This is required to assure that the Langmuir probe does not draw to high electron current which would deplete the electron density in the probe vicinity. As the approximation can usually be fulfilled, the electron temperature can be calculated from the inverse slope of the linear fit in an $\ln I_e - V_b$-diagram. Another possibility of measuring not only the electron temperature but the whole electron energy distribution function (EEDF) $f_e(V)$ was published by Druyvesteyn [250]:

$$f_e(V) = \frac{2m_e}{e^2 A_p} \left(\frac{2eV}{m_e} \right)^{1/2} \frac{d^2 I_e}{dV^2}, \tag{5.12}$$

where $V = V_{pl} - V_b$. The Druyvesteyn formula is only applicable in the transition regime $V_b < V_{pl}$. The electron density and temperature can be obtained by:

$$n_e = \int_0^\infty f_e(E) dE, \tag{5.13}$$

$$k_B T_e = \frac{2}{3 n_e} \int_0^\infty E f_e(E) dE. \tag{5.14}$$

Measuring the EEDF directly is a huge advantage over the electron temperature measurements mentioned before. However, the analysis requires very smooth $I_p - V_b$-characteristics and is extremely sensitive to noisy data due to the derivative of the electron current. A review on this method has recently been published by Godyak and Demidov [251].

Deriving the electron or ion density from the electron or ion saturation currents is a much more complex task. Despite almost one century of experimental application and theoretical treatment, starting with Mott-Smith and Langmuir 1926 [252], the collection of particles is still in discussion and a number of theories exist, most of which are not readily applicable to experimental data because they are only available in numerical form. To further complicate the matter, several regimes of operation exist. The collection of particles by the probe is strongly affected by particle collisions. One can distinguish between

- a collisionless sheath, if $\lambda_d < \lambda_c$, or
- a collisional sheath, if $\lambda_d < \lambda_c$.

Here, λ_d is the Debye length which is commonly used to express the thickness of the sheath surrounding the probe. Magnetic fields are also often present in technological plasmas, such as magnetron sputtering discharges. Depending on the magnetic field strength, one distinguishes between three conditions:

- weak magnetic fields with $r_{ce}, r_{ci} > \lambda_d$,
- intermediate magnetic fields with $r_{ce} < \lambda_d$ but $r_{ci} > \lambda_d$,
- strong magnetic fields with $r_{ce}, r_{ci} < \lambda_d$,

with r_{ce} and r_{ci} being the gyro radii of electrons and ions, respectively. In this work, we will encounter the first and the second case, i.e. the ions are never magnetised, but the electrons are magnetised close to the target as is discussed in chapter 2.4.

Finally, a number of probe theories were developed relating the measured currents to the particle densities and the bias voltage for collisionless sheaths and no magnetic fields. The main criterion to describe the particle trajectory is the ratio of probe radius and sheath thickness, the Debye length, r_p/λ_d. For thick sheaths $r_p/\lambda_d << 1$ not all particles entering the sheath will eventually be collected by the probe, some will only be deflected. This condition is known as Orbital Motion Limited theory (OML), which was first analysed by Mott-Smith and Langmuir [252]. Their original work actually assumed an infinite sheath width. In contrast, ABR theory, named after the authors Allen, Boyd and Reynolds, is

applicable for large probes with small sheaths $r_p/\lambda_d >> 1$ [253]. In this case, the particle motion can be assumed as radial towards the probe. Further improvements on these theories were published over decades, also including collisions and defining the parameter range r_p/λ_d for which each theory is valid. A major extension of the original OML theory was made by Bernstein and Rabinowitz who analysed particle motion in a finite probe sheath, allowing for orbital motion [254]. Their work was continued by Laframboix who used Maxwellian velocity distribution functions in his analysis in contrast to monoenergetic particles, that were used by Bernstein and Rabinowitz [255]. The ABR theory was refined by Chen to also describe cylindrical probes [135]. The first efforts to include collisions was published by Chou [256], who analysed Laframboix' equations. Further experimental and theoretical investigations can be found in references [257–262], most of which contain a large amount of computational work, e. g. Monte Carlo simulations, which are far too complex to be applied to analysing the $I_p - V_b$-characteristic of the probe.

Allen et. al. as well as Chen reviewed the progress of probe theory in recent years also emphasising on the validity of each of them [263–268]. While Allen stresses the limitations of the OML theory, Chen reports on the "surprising validity of OML theory". Both authors report on Langmuir probe measurements in RF discharges. Allen et. al. used an arrangement of parallel plates to excite the plasma, whereas Chen used helicon discharges. The results could hardly be any more different: Allen et. al. displayed their results in a so-called Sonin plot [269] and showed how well experiments agree with ABR theory, i. e. radial motion towards the probe [268]. On the other hand, Chen showed that OML theory can be used up to a ratio $r_p/\lambda_d \approx 3$ [266]. In a series of experiments published in 2009, he found OML theory to be valid over a wide range of plasma parameters, also for very high densities in the order of 10^{18} m^{-3} [267]. He finds that a key criterion, the absence of an absorption radius [135], is fulfilled in his measurements even for $r_p/\lambda_d = 10$. The absorption radius is a distance from the probe, below which the attracted particle will inevitably be collected by the probe independent of the particles initial velocity. This means an effective increase in the probe radius, which can be set equal to the absorption radius. Another mechanism, that can destroy the orbital motion of an attracted particle are collisions. Allen and Annaratone et. al. give a condition when OML theory fails:

$$\lambda_c < r_p \sqrt{\frac{-eV_b}{k_B T_i}}. \tag{5.15}$$

They report $\lambda_c = 4$ mm for a 0.5 Pa argon plasma. This suggests, that using a probe with a small diameter can help sustain OML theory. The RHS of equation 5.15 can be calculated

to be well below 3 mm for a maximum probe bias $V_\mathrm{b} = -100$ V and an ion temperature close to room temperature $k_\mathrm{B}T_\mathrm{i} = 0.03$ eV. As both conditions, the absorption radius and the collisions, favour the validity of OML theory, it will be used throughout the experiments.

Figure 5.14 shows the motion of a particle, ion or electron, collected by a cylindrical probe. For a long probe, i. e. $l_p >> r_p$, the particle motion can be analysed in a plane perpendicular to the probe axis. As it was already discussed, the thickness of the sheath d_s must be much larger than the probe radius, $d_s >> r_p$. If no collisions occur, energy and angular momentum of the particle are conserved [35]:

$$\frac{1}{2}(v_r^2 + v_\varphi^2) + e\left|V_{pl} - V_b\right| = \frac{1}{2}m(v_r'^2 + v_\varphi'^2), \tag{5.16}$$

with v_r and v_φ being the initial and v_r' and v_φ' the final radial and azimuthal velocity components, respectively.

$$d_s v_\varphi = r_p v_\varphi'. \tag{5.17}$$

For a particle to be collected by the probe requires the radial component of its velocity to be directed towards the probe, $v_r, v_r' < 0$. However, the radial component of the particle velocity at the probe v_r' is rather small, i. e. the velocity is almost tangential to the probe, hence, $v_r'^2 \approx 0$. Using this consideration and combining equations 5.16 and 5.17, one obtains a condition for the initial azimuthal velocity of the particle $v_\varphi \leq \left|v_{\varphi 0}\right|$ with

$$v_{\varphi 0} = \left(\frac{v_r^2 + 2e\left|V_{pl} - V_b\right|/m}{d_s^2/r_p^2 - 1}\right)^{1/2}. \tag{5.18}$$

This means, that only particles with a sufficiently small azimuthal velocity can be collected, while particles with to high azimuthal velocity will only be deflected but not collected by the probe. If the velocity distribution function at the sheath edge is known, one can solve for the collected current I_c:

$$I_c = -2\pi d_s l_p n_0 e \int_{-\infty}^{0} v_r dv_r \int_{-v_{\varphi 0}}^{v_{\varphi 0}} f(v_r, v_\varphi) dv_\varphi. \tag{5.19}$$

Assuming a Maxwellian distribution function

$$f(v_r, v_\varphi) = \frac{m}{2\pi k_B T_0} \exp -\frac{m(v_r^2 + v_\varphi^2)}{k_B T_0}, \tag{5.20}$$

with n_0 and T_0 being the particle density and temperature at the sheath edge, one obtains:

$$I_c = 2en_0 r_p l_p \left(\frac{2e\left|V_{pl} - V_b\right|}{m}\right)^{1/2}. \tag{5.21}$$

This result can be used for both species electrons and ions. However, a few assumption were made to solve the integration. Firstly, the sheath thickness must be large $r_p/d_s << 1$, but that was the condition started with. Secondly, the initial velocity in radial direction must be small $1/2mv_r^2 << e\left|V_{pl} - V_b\right|$, so that the particle motion is orbital rather than radial. Finally, the azimuthal velocity for particle collection must be small compared to the thermal velocity in the azimuthal direction, $1/2mv_{\varphi 0} << 1/2k_BT_s$. Hence, only a small part of the velocity distribution function contributes to the integral 5.19. The particle motion across magnetic field lines can be strongly impeded as discussed in chapter 2.2.2. This strongly alters the collection in particular of the easy to magnetise electrons. Some theoretical analysis can be found in references [36, 135, 270, 271]. However, a fully comprehensive theory has not been published, yet. It was therefore made use of the fact that only the electrons but not the ions are magnetised and the aforementioned analysis was applied to the ion saturation regime only.

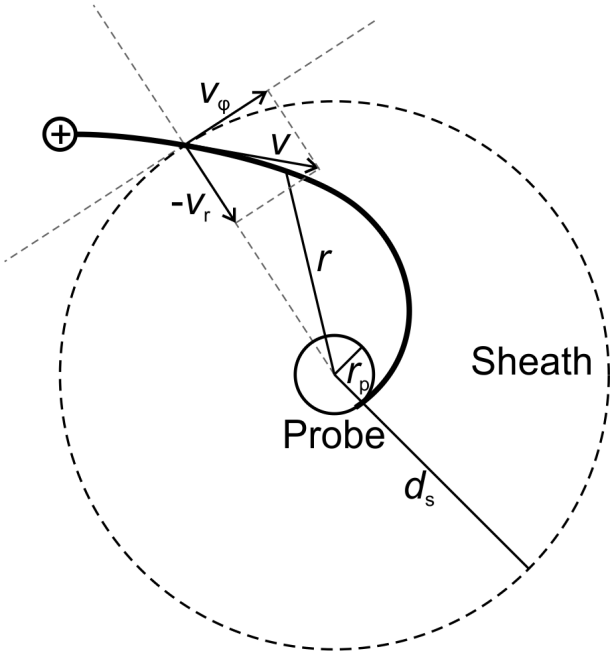

Figure 5.14: Particle collection by long cylindrical probe in the orbital motion limited regime, after [35].

Finally, some practical considerations for the experimental setup shall be summarised. The probe must be sufficiently small to not disturb the plasma. In their recent review on Langmuir probes Godyak and Demidov state, that the following inequations concerning

the probes dimensions, as well as its electrical properties have to be fulfilled [251, 272]:

$$r_p \ln \frac{\pi l_p}{4 r_p}, r_h, \lambda_d \quad << \quad \lambda_c, \tag{5.22}$$

$$I_p << I_d, I_{ch}. \tag{5.23}$$

Here, r_h is the radius of the probe holder and λ_c the mean free path for collisions of the collected species. One can calculate the characteristics lengths to be $r_\mathrm{p} \ln(\pi l_\mathrm{p}/4 r_\mathrm{p}) = 0.21$ mm, $r_\mathrm{h} = 0.5$ mm and $\lambda_\mathrm{d} = 3.3$ µm. Several collision processes were evaluate, namely electrons colliding with either argon or titanium atoms or ions, as well as charge exchange collisions between argon ions and argon atoms and titanium ions and titanium atoms. The cross-sections for electron-neutral collisions were taken from Hayashi [185] and Lotz [273], the electron-ion collision was analysed by using cross-sections for Coulomb scattering (equations 4.24 to 4.25) and the charge-exchange cross sections were taken from the summary given by Smirnov [205]. Mean free paths for characteristic kinetic energies of the incident particles are summarised in table 5.2. One can see, that aforementioned equation is almost in all cases fulfilled. Only the radius of the probe holder might violate this equation. However, the Langmuir probes described by Godyak and Demidov [251] were not used in deposition plasmas. In the present study, a setup (compare figure 5.15) had to be used to avoid deposition of a conductive titanium layer between probe and holder which would falsify the measurements. The current drawn by the probe I_p is usually negligible compared to the discharge current I_d and the current flowing to the grounded chamber walls I_{ch}. The probe current is limited to 250 mA which is three orders of magnitude lower than the discharge currents typically observed for HiPIMS discharges which lie above 100 A. The situation is more complex in the afterglow plasma. The resistance to the chamber walls was calculated from the decay of the electron density, shown in figure 5.18 and table 5.3. This gives a current flowing to the chamber walls of about 300 mA which is two orders of magnitude higher than the typical electron collection current observed during this time. Another condition arises when looking at the probe circuit. The probe bias voltage is measured against ground, which is the same potential as the chamber walls. To assure that the entire bias voltage drops in the sheath of the probe rather than in the sheath of the chamber walls. Hence, the resistance of the probe sheath R_p has to be large compared to the resistance of the chamber wall sheath R_{ch}. Godyak and Demidov found [251]:ashi [185] and Lotz [273], the electron-ion collision was analysed by using cross-sections for Coulomb scattering (equations 4.24 to 4.25) and the charge-exchange cross sections were taken from the summary given by Smirnov [205]. Mean free paths for

characteristic kinetic energies of the incident particles are summarised in table 5.2. One can see, that aforementioned equation is almost in all cases fulfilled. Only the radius of the probe holder might violate this equation. However, the Langmuir probes described by Godyak and Demidov [251] were not used in deposition plasmas. In the present study, a setup (compare figure 5.15) had to be used to avoid deposition of a conductive titanium layer between probe and holder which would falsify the measurements. The current drawn by the probe I_p is usually negligible compared to the discharge current I_d and the current flowing to the grounded chamber walls I_{ch}. The probe current is limited to 250 mA which is three orders of magnitude lower than the discharge currents typically observed for HiP-IMS discharges which lie above 100 A. The situation is more complex in the afterglow plasma. The resistance to the chamber walls was calculated from the decay of the electron density, shown in figure 5.18 and table 5.3. This gives a current flowing to the chamber walls of about 300 mA which is two orders of magnitude higher than the typical electron collection current observed during this time. Another condition arises when looking at the probe circuit. The probe bias voltage is measured against ground, which is the same potential as the chamber walls. To assure that the entire bias voltage drops in the sheath of the probe rather than in the sheath of the chamber walls. Hence, the resistance of the probe sheath R_p has to be large compared to the resistance of the chamber wall sheath R_{ch}. Godyak and Demidov found [251]:

$$\frac{A_p n_p}{A_{ch} n_{ch}} \sqrt{\frac{m_i}{2\pi m_e}} << 1, \tag{5.24}$$

with A_p and A_{ch} being the surface area of the probe and the chamber, respectively. The electron density in the vicinity of the probe is denoted as n_p and n_{ch} is the electron density close to the chamber wall. One can give an upper limit for the left-hand side of this equation by assuming the probe to measure at the position of highest electron density, which is close to the sheath edge above the target. It determines the discharge current by:

$$I_d = 0.61 A_t e n_p \sqrt{\frac{k_B T_{et}}{m_i}}, \tag{5.25}$$

with A_t being the target surface area and T_{et} the electron temperature at the sheath edge. The discharge current also has to flow through all grounded chamber walls, which gives:

$$I_d = 0.61 A_{ch} e n_{ch} \sqrt{\frac{k_B T_{ech}}{m_i}}, \tag{5.26}$$

with T_{ech} the electron temperature close to the chamber walls. Combining equations 5.24 to 5.25 and using 100 as an approximation for the square root expression in equation 5.24,

one obtains:

$$\frac{A_p}{A_t}\sqrt{\frac{T_{ech}}{T_{et}}} << 0.01, \tag{5.27}$$

The probe surface area is $A_\mathrm{p} = 1.3 \times 10^{-6}$ m^2 and the target area is 1.8×10^{-2} m^{-2}. As the electron temperature within the discharge volume is usually higher than at the chamber walls, equation 5.27 can always be fulfilled.

Collision process	**Kinetic energy of incident particle**		
	1 eV	10 eV	100 eV
Electron-argon	0.55 m	0.049 m	0.14 m
Electron-titanium	—	0.20 m	0.14 m
Electron-ion	6.1×10^{-4} m	0.047 m	3.8 m
Argon charge exchange	0.011 m	0.016 m	—
Titanium charge exchange	4.1×10^{-3} m	5.2×10^{-3} m	—

Table 5.2: Mean free paths given for typical collision events influencing Langmuir probe measurements. Ionisation cross-sections were used for electron-titanium collisions, assuming similar cross-sections as for argon in the case of elastic collisions.

In addition, the plasma can also contaminate the probe, which is a very important fact in deposition plasmas, such as magnetron sputtering. This can lead to insulating layers on the probe surface or to a conductive layer between the probe and its holder. The probe can also degenerate in etching plasmas. The emission of secondary electrons from the probe surface as well as the presence of negative ions can also influence the measurements and have to be accounted for in the probe theory. In high density plasmas the electron current can cause heating of the probe to thermoionic electron emission. Therefore, the probe bias must be kept low too avoid falsified measurements, which poses an additional difficulty for measuring the electron saturation current in high density plasmas. Finally, inaccuracy can arise from particle density gradients along the probe. The spatial resolution is therefore limited by the probe length, which cannot be made arbitrarily small, because the condition of an infinitely long cylinder is required for OML theory to work.

More probe techniques have been developed over the years. A floating double probe measures the current flowing between two probes immersed into the plasma and biased in respect to each other. The probe is insulated from ground and hence does draw any net

current from the plasma. This makes this tool very useful in decaying plasmas [274]. It also overcomes the heating problem caused by high electron currents, because the probe current is limited by the ion current. A triple probe for instantaneous display of electron temperature and electron density was developed by Chen and Sekiguchi [275]. A disadvantage of the probes mentioned before, is their incapability to measure the ion energy distribution function (IEDF). In a retarding field analyser (RFA), an additional negatively biased electrode is installed which repels electrons and makes the IEDF accessible for measurements [276]. An alternative method to measure the electron density, not relying on the particle fluxes, makes use of the plasma (electron) resonance frequency. This so-called hairpin probe is discussed in detail by Chabert and Braithwaite (chapter 10 [42]) and references therein.

In summary, Langmuir (single) probes are one of the standard tools for plasma diagnostics. The experimental setup is simple and some of the most important plasma properties, such as electron and ion density, the electron temperature, as well as the floating and plasma potential, can be measured. A short summary on probe theory was given, which was focused on OML theory and its conditions. OML theory will be used for all probe analysis, but only on the ion saturation current due to the magnetic field, that causes the electrons to be magnetised in most parts of the discharge. The ion density will be calculated from the slope of the graph in the $I_p^2 - V_b$ diagram. The electron temperature can still be derived from a Boltzmann plot [36] and the floating potential can still be found at $I_p = 0$. However, the plasma potential measured by the probe is already strongly affected by the impeded electron current and cannot be used for further analysis. A direct method of measuring the plasma potential is the emissive probe described in chapter 5.2.

5.3.2 Experimental setup

The principal experimental setup is shown in figure 5.1 and is the same as for the emissive probe measurements. The probe is connected to a stainless steel stem which is inserted into the plasma via a feed-through at the side of the vacuum chamber. Moving the stem in the axial direction allows for changing the radial position of the probe, i. e. the distance from the discharge axis. The magnetron was moved together with the substrate to change the axial position, the distance to the target.

The main difference in the experimental setup lies of course in the probe and the acquisition system. The setup of the probe is shown in figure 5.15 [91, 277]. It consists of the probe head, the probe holder and the socket, which allows to connect the probe to the

stainless steel stem, 6 mm in diameter. The most important part of the probe is the collecting electrode which is a straight tungsten wire (purity 99.95 %) supplied by Goodfellow. It has a diameter of (100 ± 10) µm and the collecting area of the wire protrudes the protective alumina tube by about 4 mm. As the wire was cut by hand, the actual probe length differed from probe to probe and was measured by means of a calliper. It ranged from 3.7 mm to 4.3 mm, measured with an accuracy of ± 0.05 mm. The length of the individual probe was used to calculate the electron and ion density. The tungsten wire is held in place by a spacer. This is an alumina tube with an inner diameter of 0.2 mm and an outer diameter of 0.5 mm, which is pushed into the protective tube by about 1 mm. This prevents it from being coated by a conductive layer of titanium which may lead to a connection to the grounded probe stem and thus to compromise the measurements. This approach works very well far away from the target, but the probe had to be replaced frequently in the vicinity of it, where the plasma can penetrate into the gap. The protective tube (inner diameter 0.5 mm, outer diameter 1.0 mm, length 3 cm) was inserted into the probe holder, yet another alumina tube (inner diameter 1.0 mm, outer diameter 2.0 mm, length 10 cm, and fixed by polyimide (PI) tape. The probe holder was push-fitted into the probe socket, made of PEEK 6 mm in diameter and 10 mm long. Within the socket, the tungsten wire was brazed to a connector pin made of brass and pushed into the PEEK socket from the opposite side. The pin allows for both mechanical and electrical connection with the stainless steel stem which has an insulated copper wire run through it. The mechanical bond was enhanced by using polyimide tape.

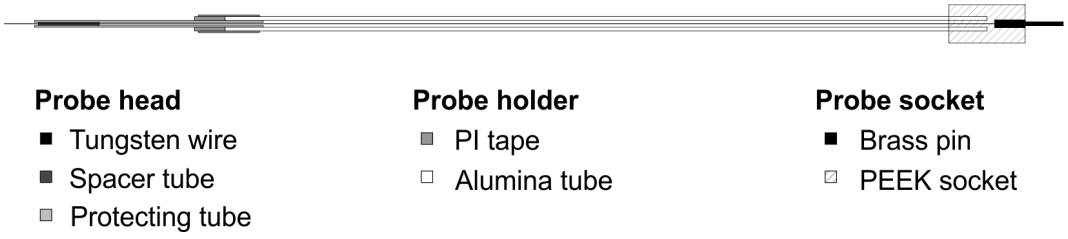

Figure 5.15: Schematic drawing of the Langmuir probe [91, 277].

The probe is connected to a commercial acquisition system Smartprobe supplied by Scientific Systems [278], which records the probe current I_p in dependence on the bias voltage V_b. Each measurement comprises 200 $I_p - V_b$ pairs equally spaced within the adjustable limits of the probe bias V_b. The maximal bias voltage is ± 95 V and the probe current is limited to 250 mA. The accuracy of the measurements is 25 mV and 0.1 µA (measuring range 0.25 mA) for the bias voltage and the probe current, respectively. Due

to the high electron density in HiPIMS discharges, the measuring range is more likely to be 250 mA and the accuracy 0.1 mA.

For time-resolved measurements a delay generator DG 535 or DG 645 manufactured by Stanford Research Systems was used to deliver a TTL signal synchronised to the discharge pulse to trigger the measurement. The bias voltage is applied to the probe continuously and the probe current measured in an interval of 1 µs, triggered by the TTL signal. The probe current is averaged over ten discharge pulses. After all current measurements are recorded for a certain probe bias, the bias voltage is increased by one step (200 steps within the set range) and the procedure is repeated. The result is an $I_p - V_b$ characteristic taken for a particular temporal position. Three of these characteristics were averaged before plasma parameters, such as electron and ion density, electron temperature, floating and grounded potential.

The measuring procedure started with recording the load line of the Langmuir probe, an $I_p - V_b$ characteristic without a plasma. Afterwards, the vacuum chamber was conditioned by running a 200 W DCMS discharge for 10 min until the target voltage and the discharge current displayed at the Advanced Energy Pinnacle Plus power supply did not change anymore. During this time, the probe was retracted to avoid deposition. Probe characteristics of the DC discharge were then recorded at the discharge axis ($r = 0$ mm) and above the racetrack ($r = 45$ mm). The HiPIMS power supply was then connected to the magnetron, the discharge set to the desired parameters and stabilised for 15 min. Measurements were then carried out for radial positions 0 mm to 80 mm while the axial distance of the probe to the target was kept constant. In order to check whether the probe got coated during the process, the radial position $r = 0$ mm was measured again, as well as the load line and the two positions of the DCMS discharge. Only if all repeated measurements agree with the initially recorded data, the $I_p - V_b$ characteristic was analysed. Otherwise, the data was discarded and the measurement repeated with a new probe. Preliminary experiments were carried out to find suitable upper limits for the bias voltage. This is particularly important for measurements in the dense plasma zone above the racetrack where the probe current can easily exceed the limit of 250 mA. The drawback of this approach is that both the plasma potential and electron collection region, i. e. the electron density, were not accessible.

The $I_p - V_b$ characteristics such as the one shown in figure 5.16 is analysed by first finding the floating potential V_{fl}, the probe bias where the probe current is zero. The plasma potential V_{pl} was obtained by finding the zero of the second derivative $d^2 I_p / dV_b^2$. The electron and the ion density were calculated by analysing the $I_p^2 - V_b$ plot in the respective

saturation regime. A linear fit to the graph in the interval of the probe bias from -95 V to -80 V was used to calculate the ion density:

$$n_i = \sqrt{\frac{m_i A}{8e^3 l_p^2 r_p^2}}, \tag{5.28}$$

with A being the slope of the linear fit and m_i is the mass of the ions. It was assumed, that the collected ion species is singly charged argon. The small difference in the mass between argon and titanium ions can lead to an underestimation of the ion density by up to 10 %. On the other hand, the gas and thus the ion composition are distributed inhomogenuously in the volume. While argon gas is replaced by sputtered titanium in the vicinity of the target as indicated by optical measurements shown in chapter 4.4.2 and by Monte Carlo simulations [23], the gas and ion composition close to the substrate might still be dominated by argon. In addition, the assumption of singly charged ions is rather cruel, because multiply charged ions up to Ti^{4+} could be observed [84, 85]. However, the operating conditions in these studies favour higher ionisation states then in the present study. While Andersson et. al. operate at about three times the peak current density, Poolcharuansin et. al. observed multiply charged ions only for an operating pressure about an order of magnitude lower than in the current experiment. Ehiasarian et. al. used Langmuir probes, atomic absorption spectroscopy and mass spectrometry to investigate the ion composition in the vicinity of the substrate. They found the fraction of Ti^{2+} ions to be less than 10 % of the total ion population. Though the fraction of doubly charged ions is expected to be rather low, one shall discuss its influence on the obtained ion density. Equation 5.28 has to be corrected by a factor of $Z^{-3/2}$, with Z being the charge state. Neclecting multiply charged ions would lead to an overestimated ion density, because the ion collection current is artificially high, as some ions carry double the charge. This condition might be somewhat fortunate: While the presence of a large amount of titanium ions gives an underestimated ion density, it is more likely that some of these ions are doubly charged compared to the chance of finding doubly charged argon ions, due to the large difference in the ionisation threshold (Ti^{2+} 13.58 eV [279] and Ar^{2+} 27.64 eV [280]). The latter effect would at least partly compensate for the effect of the ion mass, unless an extraordinarily high fraction of ions is doubly charged.

The electron density is obtained in analogue way. The slope of the linear fit in the $I_p^2 - V_b$ diagram in the electron collection region, $V_b > V_{pl}$ was used to determine the electron density, using equation 5.28 but replacing the ion mass with the electron mass. In a last step, the ion current is subtracted from the probe current and the resulting electron current

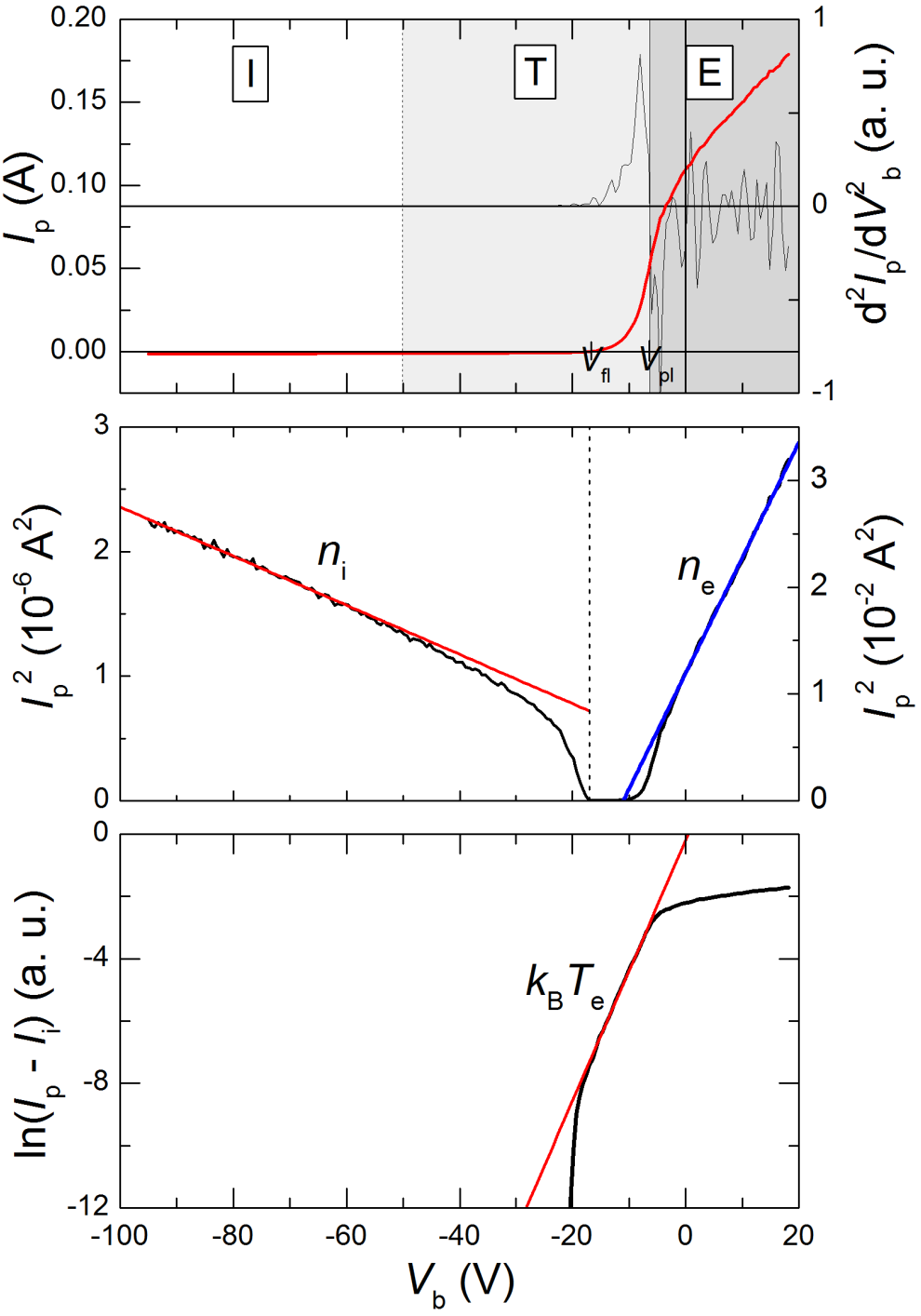

Figure 5.16: Analysing procedure of the $I_p - V_b$ characteristic measured by a Langmuir probe, 90 mm above the target at the centre of the discharge. The discharge was operated with grounded substrate and standard magnetic field configuration. Discharge parameters are summarised in table 5.1

is plotted in a semi logarithmic graph. The inverse slope of the linear fit for $V_b < V_{pl}$ is then the electron temperature $k_B T_e$ in eV.

The accuracy of the electron and ion density is determined by the accuracy of the probe radius, the probe length and the slope of the linear fit. The biggest contribution has the probe radius with 10 % according to the manufacturers specification. The relative error of the probe length is 1 % and the accuracy of calculating the slope in the $I_p^2 - V_b$ diagramme is approximated to be 5 %. The maximum error is therefore 16 % of the value obtained in the experiments. For the ion density, the maximum error has an additional component as discussed before, due to the mass and the charge of the collected ion species. Th $I_p - V_b$ characteristics are recorded in voltage steps of about 0.6 V. Both the floating and the plasma potential cannot more accurate than half of this step width, ± 0.3 V. Finally, the accuracy of the electron temperature was estimated from the maximum error of the slope of the linear fit in the semi-logarithmic plot to be ± 0.1 eV. The temporal resolution is 1 µs which is the measuring intervall of the acquisition system [278].

5.3.3 Results: Temporal development

The temporal evolution of plasma parameters, such as electron density and temperature, the ion density, as well as the floating and the plasma potential were studied for different substrate configurations. The titanium target was sputtered with operating conditions summarised in table 5.1. The magnetic field was kept in the standard configuration and the substrate was either grounded or floating or removed completely. Particular emphasis was put on the temporal development during the discharge on-time, because the spatial distribution of the ion density and the electron temperature at temporal position $t = 70$ µs will be used for the particle transport model.

Results of the Langmuir probe measurements during the discharge on-time are displayed in figure 5.17. One can see, that there is some difference in the target voltage and the discharge current waveforms. When no substrate is used, the delay of the onset of the discharge current in respect to the target voltage is less than 1 µs. As the discharge current starts almost immediately, the target voltage had to be reduced in order to keep the average power the same. Thus, the observed peak current density is slightly lower with 1.05 $\mathrm{A\,cm^{-2}}$ compared to 1.12 $\mathrm{A\,cm^{-2}}$ and 1.20 $\mathrm{A\,cm^{-2}}$ when a grounded or a floating substrate was used, respectively. The onset of the discharge current is delayed most when a grounded substrate was used (delay 11 µs), and slightly less for the floating substrate,

8 µs. The reason for this difference will become clear when investigating the afterglow of the discharge, but the pulse on-time shall be considered first.

The very initial time after pulse initialisation was omitted because the probe response time, i. e. the ion plasma period τ_{pi}, may not be sufficient. It is about 1 µs when no substrate was used, but no response time could be calculated, as the ion density was below the detection limit immediately before discharge ignition. In addition, this highly transient stage has already been intensively studied by Poolcharuansin and Bradley [91]. Both the electron and ion density start at very low levels of about 10^{15} m^{-3} at the beginning of the pulse. It quickly starts rising after pulse initialisation without a substrate installed, just as the discharge current does. The electron density peaks just before the target voltage is switched off at the end of the HiPIMS pulse. The density at this time is 1.3×10^{19} m^{-3}. When the substrate is installed, the onset of the discharge current is delayed and so is the onset of the electron density. It also reveals its maximum just before pulse termination at values of 1.0×10^{18} m^{-3} and 1.5×10^{18} m^{-3} for the grounded and the floating substrate, respectively. The electron density is highest for the floating substrate because the loss of electrons to the substrate is impeded by the potential barrier $\Delta V = V_{pl} - V_{fl} \approx 5.2 k_B T_e/e$, as already described in chapter 4.4.6. This potential barrier is reduced to $0.5 k_B T_e/e$ when the substrate is grounded. Electrons are then more quickly lost and the electron density is lower. The case of not using a substrate is somewhat similar to the grounded substrate, as the grounded chamber walls serve as boundary. However, the path to these walls is significantly longer than when the grounded substrate is installed.

The ion density n_i follows the same trend but is generally 20 % higher than the calculated electron density. This might have two reasons. Firstly, OML theory usually gives a slightly overestimated ion density as pointed out by Iza and Lee [262] and Chen [267]. Secondly, even the weak magnetic field 90 mm above the target influences the electron collection current [281].

The electron temperature $k_B T_e$ is highest shortly after discharge ignition as it was previously reported [90, 91]. It cools down to values of about 2.8 eV during the stable stage of the discharge and no difference between the substrate configurations can be observed.

The plasma potential V_{pl} seems to start close to 0 V when the target voltage is ramped up. When the discharge current starts rising it shows a shallow dip until it stabilises at an almost constant level during the second half of the pulse. These measurements using a Langmuir probe are clearly less sensitive to changes than the emissive which one can see, for example, in the initial minimum measured to be -25 V. The emissive probe gives values less than -100 V. However, the minimum occurs for the same reason. The rapid

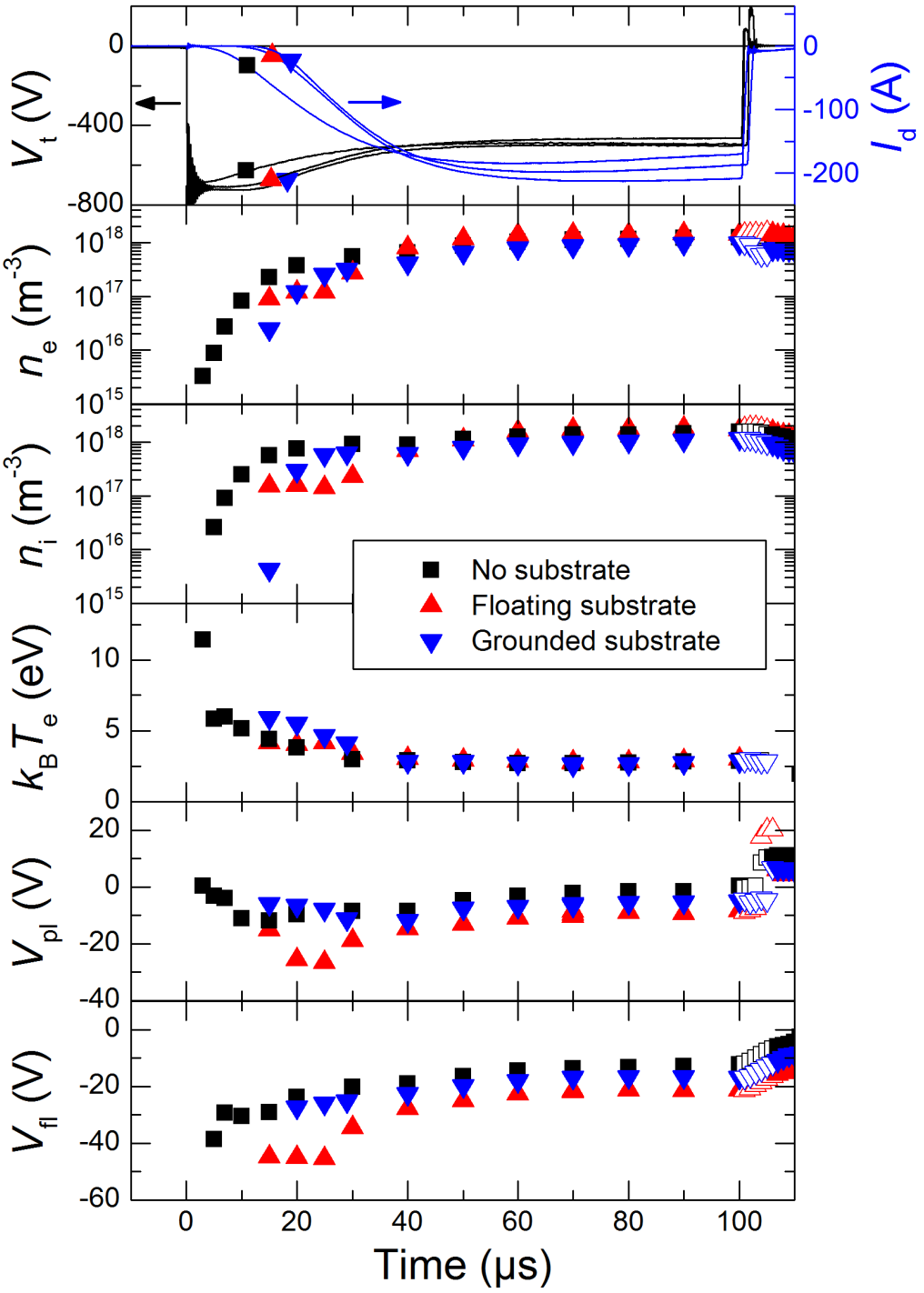

Figure 5.17: Temporal development of the plasma parameters during the HiPIMS pulse operated with different substrate configurations. Discharge parameters are summarised in table 5.1.

increase of the discharge current without sufficient electron density close to the grounded walls and the anode cup, requires a strongly negative plasma potential to facilitate electron transport across the magnetic field to balance the electron and ion flux. One clear difference between the different substrate configurations can be observed during the second half of the pulse. The plasma potential is highest if no substrate is used, followed by the grounded substrate whereas lowest plasma potentials are obtained with the floating substrate. This can also be explained considering the transport of the electrons. The floating substrate creates a potential barrier for the electrons, which results in a more negative plasma potential, because a large amount of electrons have to be transported across the magnetic field lines towards the chamber walls. Without the potential barrier towards the substrate, the electron transport needs to be enhanced less and the resulting plasma potential is more positive when the substrate is grounded. The conditions are somewhat different when no substrate is used. The surface area of the walls is larger because the whole chamber now serves as anode. In many cases, this results in positive plasma potentials as reported by Mishra et. al. using an emissive probe [89]. In the present study, the plasma potential is still negative but the most positive values were measured in this set of experiments.

The floating potential V_{fl} is linked to the plasma potential and depends, unlike the plasma potential, on the local electron temperature. As the electron temperature is high during pulse initialisation, the floating potential is most negative during this time. The floating potential then increases to more positive values when the electron temperature decreases. In the second half of the pulse, a stable level is observed which reveals the same order as the plasma potential, i. e. the floating potential is most negative with a floating substrate, slightly more positive when the substrate is grounded and has the highest value if no substrate is used. This is not surprising, because the electron temperature is the same for all three configurations and the plasma potential reveals the same order.

It is worth noting, that stable levels of all plasma parameters are observed in the second half of the pulse (for $t > 50$ µs). The spatial measurements recorded for $t = 70$ µs are therefore thought to be a good representative of the plasma conditions during the stable stage of the HiPIMS discharge.

The temporal development of the electron density and the electron temperature measured during the discharge off-time is shown in figure 5.18. The plasma and the floating potential quickly drop to zero after the target voltage is switched off and the ion density follows the development of the electron density. The transition from discharge on- to off-time is accompanied by an overshoot of the target voltage which compromises the Langmuir probe measurements. This lasts for about 5 µs and the plasma parameters recorded

during this time are indicated by using open instead of solid symbols in figure 5.17 and 5.18. The electron density first decreases quickly with time constants ranging from 30 µs to 40 µs as summarised in table 5.3. This agrees well with the temporal development reported by Poolcharuansin and Bradley [91], who suggest Bohm diffusion as the main loss mechanism.

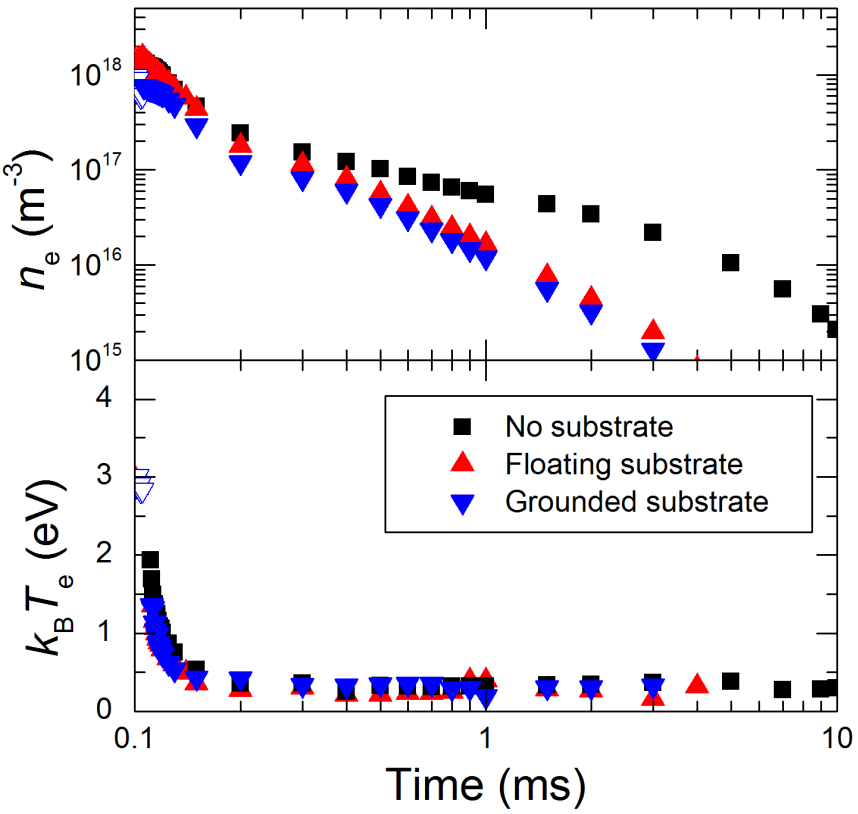

Figure 5.18: Temporal development of the plasma parameters in the HiPIMS afterglow operated with different substrate configurations. Discharge parameters are summarised in table 5.1

The second time constant is in the millisecond range and reveals a clear difference between the discharge with or without a substrate. The decay is significantly slower when no substrate is used, (2790 ± 80) µs, compared to (1030 ± 50) µs and (1130 ± 40) µs when the substrate is grounded and floating, respectively. The decay time obtained for no substrate is in the same range as reported in [91]. The faster decay observed with a substrate installed is consistent with the longer delay of the discharge current onset, as the lower

density of remnant electrons slows down the ignition process, as shown in chapter 4.4.3. However, these results do not fit well with the decay constants observed for the plasma-induced emission in chapter 4.4.7. On the first glance, the experimental setup remained the same, but within the two years lying between these experiments almost all devices were replaced; the power supply, the target and the magnetic field of the magnetron. These two experiments are therefore less comparable than one would expect. From the present experiments, it can be concluded that installing a substrate causes a faster decay of the plasma in the afterglow. One would expect, that the characteristic diffusion length decreases with the substrate in place which leads to the faster decay as observed. However, the electron density remains about a factor of two higher when the substrate is floating compared to the grounded substrate. The lower density of remnant electrons then leads to a longer delay of the discharge current onset, 8 µs for the floating substrate and 11 µs for the grounded substrate.

		No substrate	**Floating substrate**	**Grounded substrate**
Electron density	initial	(33.1 ± 1.5) µs	(37.7 ± 0.7) µs	(40.8 ± 0.6) µs
	longterm	(2790 ± 80) µs	(1130 ± 60) µs	(1030 ± 50) µs
Electron temperature		(17.9 ± 0.8) µs	(16.7 ± 0.9) µs	(17.2 ± 0.6) µs

Table 5.3: Time constants of the decay of the electron density and temperature in the afterglow of HiPIMS discharges with different substrate configurations.

The electron temperature drops quickly after the target voltage is switched off and remains at about 0.2 eV to 0.3 eV during the entire afterglow. The decay can be described by a single time constant which appears to be the same for all substrate configurations as seen in table 5.3. In summary, one can say that the presence of the substrate allows for a more efficient loss of electrons but has no influence on the temporal development of the electron temperature.

5.3.4 Results: Spatial distribution

The spatial distribution of the ion density, electron density and the floating potential were measured with the Langmuir probe at a temporal position of $t = 70$ µs, which is considered to be representative for the discharge in the second half of the HiPIMS pulse. The plasma was mapped in a grid shown in figure 5.21. The radial position was varied between

$r = 0$ mm and $r = 80$ mm in steps of $\Delta r = 5$ mm. The same step size was used for the axial position, which was varied between $z = 10$ mm and 95 mm. Distances closer to the target were not accessible because the probe significantly disturbed the plasma. For comparison with the emissive probe measurements, the plasma was calculated using the floating potential and the electron temperature:

$$V_{pl} \approx V_{fl} + 5.2\frac{k_B T_e}{e}. \tag{5.29}$$

The plasma potential could not be measured directly in the vicinity of the target due to the high probe current. The substrate was always used in either grounded or floating, when the standard magnetic field configuration of the magnetron was studied. The more unbalanced magnetic field was investigated with the substrate grounded, because the discharge was found to be more stable with grounded substrate than when the floating substrate was used.

The spatial distribution of the ion density and the electron temperature are shown in figure 5.19. The ion density reveals features typical for magnetron discharges. The maximum of about 1×10^{19} m^{-3} is found right above the racetrack where the magnetic field, orientated parallel to the target, confines the electrons most efficiently. The density drops towards the discharge axis and the outer edge of the plasma and also with increasing distance to the target. These characteristics agree very well with the electron density measurements reported by Böhlmark et. al. [76]. One can also observe a clear difference between the floating and the grounded substrate. The ion density in the vicinity of the floating substrate is about a factor of five higher than when the substrate is grounded (both magnetic field configurations). This behaviour is caused by the potential barrier electrons have to overcome when they want to reach the substrate. This about $5.2k_B T_e/e$ for the floating but only $0.5k_B T_e$ for the grounded substrate. The different magnetic field configurations do not show a large difference but one can notice that the ion density is slightly lower for the more unbalanced case. The difference in the maximum close to the target is about 7 % and is probably caused by a decrease of the magnetic induction at this position from 40 mT to 38 mT. A feature of the more unbalanced magnetic field is, that the magnetic null is closer to the target ($z = 65$ mm) and that more magnetic field lines guide electrons towards the substrate. This reduces the region of magnetic confinement. The ion density distribution appears therefore to be slightly bent towards the discharge axis.

The electron temperature was found to vary little temporally as seen in figure 5.17, but also exhibits only a slight spatial variation. It generally stays in a range between 1 eV to 3.5 eV and only one electron temperature was observed. The spatial distribution ap-

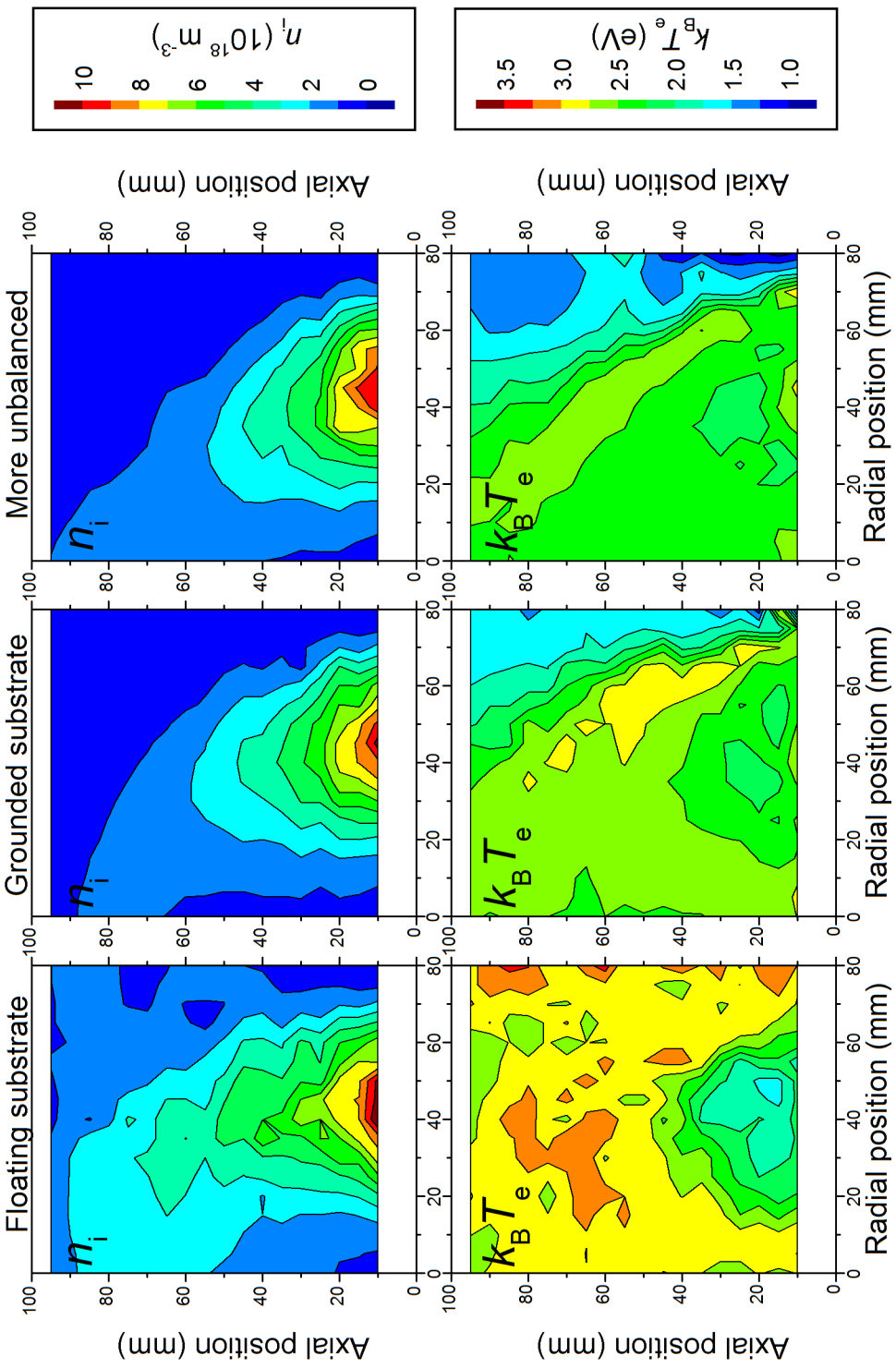

Figure 5.19: Spatial distribution of the ion density and the electron temperature during the HiPIMS discharge pulse ($t = 70$ µs) operated with different substrate configurations. Discharge parameters are summarised in table 5.1

pears quite atypical for a magnetron discharge, where the highest electron temperature is expected in the confined region close to the target [54]. On the contrary, the electron temperature seems to be lowest in exactly that region above the racetrack. This can be explained by the efficient loss of the electron energy by inelastic collisions with the sputtered titanium particles. This requires little more than 2 eV for the spectral lines summarised in table 4.2. In addition, the time between two collisions of an energetic secondary electron originating from the target with the thermalised electron gas is about 600 ns for an electric kinetic energy of 100 eV, using equation 4.24 to 4.26. This means, that energetic electrons quickly lose their energy to the electron gas and only one group of electrons by one temperature is observed. The electron temperature seems to increase slightly for the axial position closest to the target. It is at the moment not clear whether this effect reflects an increase of the electron energy towards the target or if it is simply an artefact. It was already observed for measurements with the emissive probe, that the presence of the probe in the vicinity of the target causes the discharge current to drop. This results in a lower sputtering rate, a lower density of titanium particles in front of the target which lowers the loss rate of the electron energy as inelastic collisions become less frequent. The electron temperature is then measured too high.

Again, the floating substrate impedes the loss of electrons to the substrate even with high energy which results in an overall increased electron temperature. One can therefore observe a higher electron temperature in the vicinity of the floating substrate and at the edge of the discharge, whereas a much lower electron temperature is observed when the substrate is grounded. It appears that for the grounded substrate, one can find a region of slightly higher electron temperature along the outermost magnetic field lines which still close in front of the target. Energetic electrons are scattered into this region and suffer from less inelastic collisions with titanium particles which have highest density above the racetrack and can sustain their higher energy. If these electrons are scattered beyond this area, they are guided towards the grounded substrate and are subsequently lost from the discharge.

The floating and the calculated plasma potential are shown in figure 5.20. As the electron temperature only shows little spatial variation, the floating and the plasma potential almost look identical except for a shift of the actual values. The spatial distributions generally confirm the measurements carried out with the emissive probe. The most negative potential is found close to the target, due to the excess of negative charge, i. e. electrons. More negative potentials are observed in the case of the floating substrate. This is to facilitate electron transport across the magnetic field in the radial direction as the flux towards the

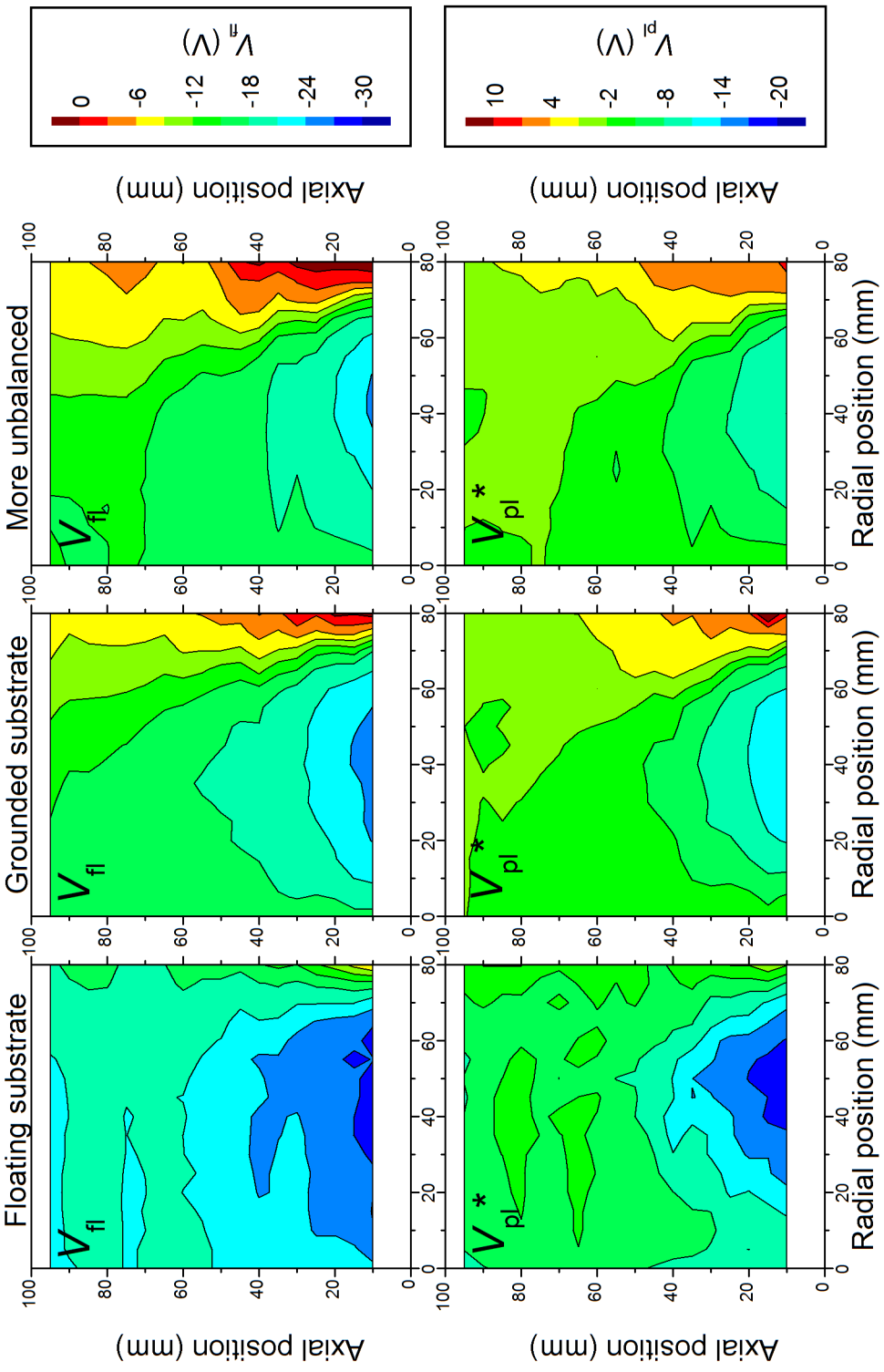

Figure 5.20: Spatial distribution of the floating and the plasma potential during the HiPIMS discharge pulse ($t = 70$ µs) operated with different substrate configurations. Discharge parameters are summarised in table 5.1

floating substrate is impeded by the potential barrier. The effect of changing the magnetic field can also be seen for both potentials. The equipotential lines are bent more towards the discharge axis when the more unbalanced configuration is investigated.

5.4 Transport model

The transport of particles sputtered from the target is an important field of study for HiPIMS discharges. On the one hand, the flux of ionised, sputtered particles to the substrate, which is significantly higher than for conventional DCMS, was found to be beneficial for the film growth. On the other hand, it is the high degree of ionisation of the sputtered flux which causes the deposition rate to be reduced as the ionised particles have to overcome the plasma potential barrier towards the substrate [89]. Several studies were conducted to investigate the origin of the apparently lower deposition rates and to overcome this disadvantage of depositing films with HiPIMS.

Among these studies are also transport models such as the pathway model proposed by Christie [118]. This model describes the transport by evaluating the processes involved. It starts with the sputtering of the target, which is either caused by working gas or metal ions impinging on the target. The total sputtering rate depends on the composition of the ion flux to the target, as well as on the sputtering yield for the respective ion-target material combination. The sputtered particles can then be ionised in the vicinity of the target with a probability β. Once ionised, the motion of the sputtered particles is influenced by the electric field present in the plasma. Ions can be attracted back to the target with a probability σ and are thus lost for the deposition process. Two characteristic parameters, η and ξ, describe subsequent losses of particles due to the chamber geometry and scattering. Vlcek et. al. added an ionisation probability for particles in the plasma bulk as they used a highly unbalanced magnetron enhancing this process [119, 282]. In a recent review by Gudmundsson et. al., the transport probabilities were related to external parameters, such as the target voltage. They found, that the fraction of sputtered particles which are ionised and attracted back to the target is proportional to $V_t^{-1/2}$ [72]. This means, that increasing the target voltage allows for more ions to be transported to the substrate. It appears, that a given deposition system can be optimised in terms of deposition rate and degree of ionisation of the flux of particles arriving at the substrate. This was studied further by Brenning et. al. [207], who related these key properties to external parameters such as the target voltage, the discharge current, the discharge pulse length, the pressure, the target material and the magnetic field configuration. It is suggested, that optimum conditions exist for operating HiPIMS discharges which should be found by a combined approach of experimental and numerical studies. They also stressed the importance of the plasma potential distribution, as well as the fact that the sputtered particles show a characteristic velocity distribution.

A special case of the aforementioned model is the work published by Sarakinos et. al. [206]. They used optical emission spectroscopy to estimate the composition of ions impinging on the target. This was the first time, that not all transport parameters were varied over a wide range to study their influence but also experimental data was used in the model. However, one drawback still remains, that most transport probabilities are global averages and need to be varied over a wide parameter range. For example, the ionisation probability, as well as the back attraction of particles to the target were only studied as global estimates.

Modelling the particle trajectories in magnetron sputtering discharges is a well-established research area, which already allows to fully model DCMS discharges [246, 283–286]. However, the computational effort for HiPIMS discharges is significantly higher due to the higher particle density and the resulting higher plasma frequency requiring finer time steps for the calculations. One can overcome this drawback by replacing the time-consuming self-consistent model by experimental data and concentrate on the motion of "test particles", in the present case the sputtered metal atoms, under the given conditions. The deposition of particles onto the substrate, the sidewalls and the target have already been studied for DCMS both experimentally [287, 288] and numerically [289]. In summary, the presented model shall fill the gap between the global transport models mentioned before and the fully self-consistent but computationally expensive models known for DCMS.

5.4.1 Description of the model

The transport model presented in this study uses a large number of test particles (2.4 million) which are metal particles sputtered from the target, until they reach either one of the boundaries, target or side wall. The calculation time is 40 µs and particles which have not reached any of these boundaries are thermalised, i. e. too slow to cover the distance to any of the chamber walls. The following processes are taken into account when calculating the trajectory of the test particles:

- Ionisation,
- the electrical field acting on ions,
- the force caused by the modified two stream instability as suggested in [1, 28, 29],
- collisions with other heavy particles (working gas or sputtered particles).

A schematic drawing of the discharge is shown in figure 5.21. One can see, that the coordinates range from $r = 0$ mm to $r = 80$ mm and in axial direction from $z = 0$ mm to $z = 100$ mm. It was made use of the cylindrical symmetry even though recent publications indicate a rather turbulent and thus asymmetric behaviour during the HiPIMS pulse [31–33]. Measured discharge properties, such as the plasma potential, the electron density and temperature as well as the vacuum magnetic field are used as input data to calculate the trajectories of the sputtered particles. The sputtering process determines the initial velocity and the starting position of the sputtered particle, which is followed through the discharge volume. The trajectory of the particle itself is not stored as the data would be rather large. Instead, the main information of its motion is recorded. For example, the position and the kinetic energy is saved for each particle arriving at any wall. In addition, the discharge volume is also investigated, by recording the spatial distribution of ionisation events, the thermalised particles and the relative density. The influence of the two-stream instability shall also be studied, which requires to also analyse the velocity of the particles in the discharge volume. The algorithm for moving particles is presented first, followed by the input in the format prepared for the calculations.

The motion of particles in the presence of an electric and magnetic is described by

$$m\frac{d\boldsymbol{v}}{dt} = q\left(\boldsymbol{E} + \boldsymbol{v} \times \boldsymbol{B}\right). \tag{5.30}$$

The leap-frog algorithm as described by Birdsall and Langdon was used to solve the equation of motion [40], as direct integration is prone to errors. The key feature of this approach is, that the velocity and the position of the particle are not calculated for the same time but with half a time step $\Delta t/2$ difference. The calculation procedure in cylindrical coordinates starts by a half time step acceleration:

$$\boldsymbol{v}^{-} = \boldsymbol{v}(t - \Delta t/2) + \frac{q}{m}\boldsymbol{E}\frac{\Delta t}{2}, \tag{5.31}$$

with $\boldsymbol{v}(t - \Delta t/2)$ is the velocity at time $t - \Delta t/2$. In the next step, the velocity is rotated due to the influence of the magnetic field.

$$\boldsymbol{v}' = \boldsymbol{v}^{-} + \boldsymbol{v}^{-} \times \boldsymbol{t}, \; with \tag{5.32}$$

$$\boldsymbol{t} = \frac{q}{m}\frac{\Delta t}{2}\boldsymbol{B}, \tag{5.33}$$

$$\boldsymbol{v}^{+} = \boldsymbol{v}^{-} + \boldsymbol{v}' \times \boldsymbol{s}, \; with \tag{5.34}$$

$$\boldsymbol{s} = \frac{2}{1 + t^2}\boldsymbol{t}. \tag{5.35}$$

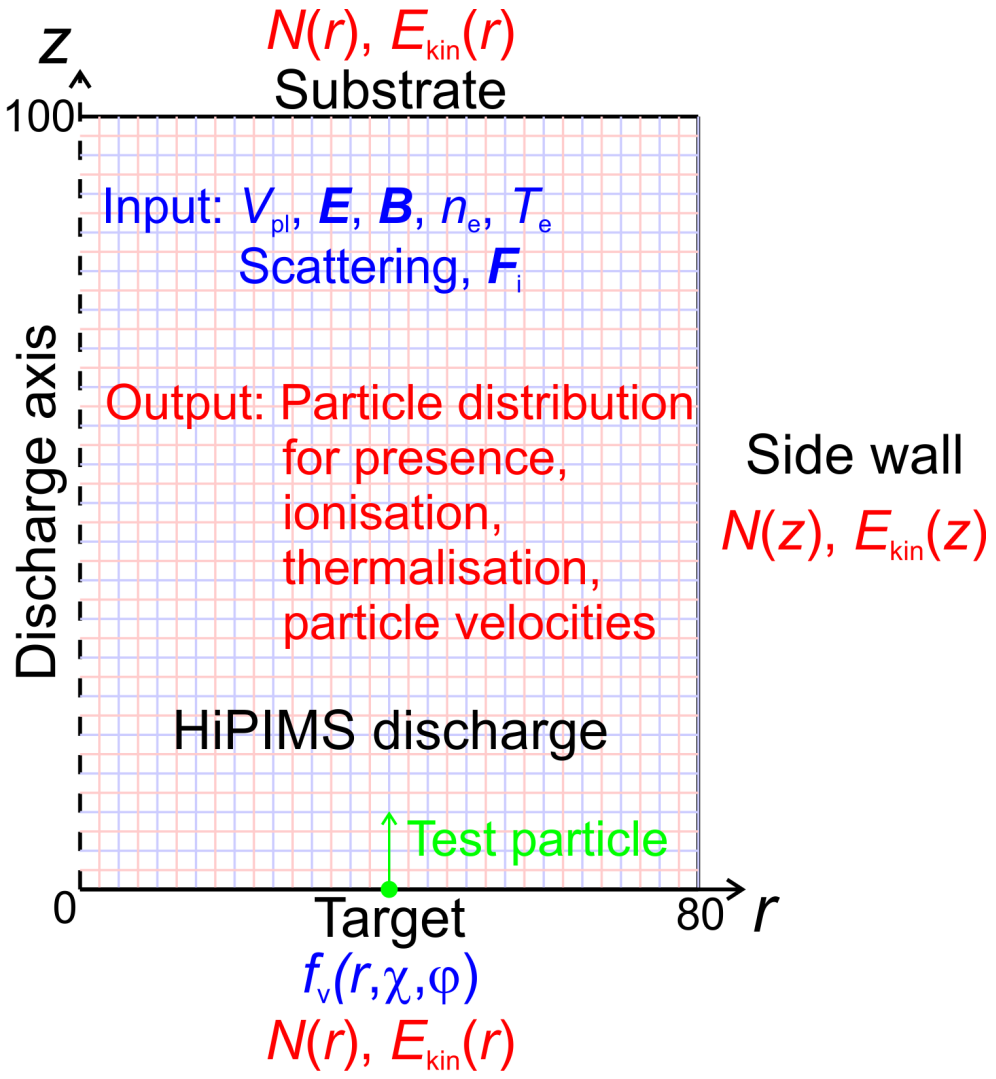

Figure 5.21: Schematic drawing of the particle transport model showing the input data (blue) and the calculated data (red). The plasma properties are measured for the light blue grid, whereas for the calculated distribution of, for example, the relative particle density the grid is shifted by 2.5 mm.

Another acceleration by half a time step follows

$$\boldsymbol{v}'(t+\Delta t/2) = \boldsymbol{v}^{+} + \frac{q}{m}\boldsymbol{E}\frac{\Delta t}{2}. \tag{5.36}$$

After iterating the velocity, the now particle position has to be calculated which requires special treatment, as conventional Cartesian coordinates would lead to large errors when moving the particle close to the discharge axis $r = 0$ mm. Thus, the coordinates x, y and z are calculated, first,

$$x = r(t) + v'_r(t+\Delta t/2)\Delta t, \tag{5.37}$$
$$y = v'_\varphi(t+\Delta t/2)\Delta t, \tag{5.38}$$
$$z = z(t) + v'_z(t+\Delta t/2)\Delta t, \tag{5.39}$$

before transforming them into cylindrical coordinates r, φ and z

$$r(t+\Delta t) = \sqrt{x^2+y^2}, \tag{5.40}$$
$$\varphi(t+\Delta t) = \varphi(t) + \alpha, \tag{5.41}$$
$$z(t+\Delta t) = z, \tag{5.42}$$

with α being $\sin\alpha = y/r(t+\Delta t)$ or $\cos\alpha = x/r(t+\Delta t)$. In the case, that $r(t+\Delta t/2) = 0$ the motion is all radial and α is set to zero. Finally, the direction of the velocity has to be rotated by α

$$\begin{pmatrix} v_r(t+\Delta t/2) \\ v_\varphi(t+\Delta t/2) \\ v_z(t+\Delta t/2) \end{pmatrix} = \begin{pmatrix} \cos\alpha & \sin\alpha & 0 \\ -\sin\alpha & \cos\alpha & 0 \\ 0 & 0 & 1 \end{pmatrix} \begin{pmatrix} v'_r(t+\Delta t/2) \\ v'_\varphi(t+\Delta t/2) \\ v'_z(t+\Delta t/2) \end{pmatrix} \tag{5.43}$$

The time step Δt was set to 10^{-7} s for all calculations. The magnetic field was neglected for the model calculations run for sputtered particles, but it was incorporated in modelling the electron trajectories during discharge ignition (chapter 4.4.3).

Two kinds of collisions have to be implemented. One representing elastic collisions of the sputtered particles with the background gas or thermalised metal vapour. The other being ionisation of the sputtered titanium atoms up to charge state two. This is usually the highest charge state commonly reported for HiPIMS discharges [82, 290]. Only under extremely high current densities or low operating pressure, higher charge states were observed [84, 85].

The collision of sputtered particles with the background gas or with each other is quite complex, as the density of both species is not known for the present discharge. Kadlec

showed that a substantial amount of argon is replaced by sputtered particles in the vicinity of the target [23]. He also demonstrated that particles also exhibit a velocity pointing away from the target, which increases difficulties because one would have to know the relative velocity between two colliding particles. In addition, one also has to accommodate collisions between titanium ions and other particles which includes charge exchange collisions. While elastic collisions have a cross-section of about 3×10^{-19} m^2 as used by Bultinck et. al. [246], the charge exchange collision cross-section is 2.2×10^{-18} m^2 [205]. Due to the largely different cross-sections and an unknown particle density, the mean free path

$$\lambda = \frac{1}{n\sigma} \tag{5.44}$$

is varied over a wide range. The lower limit was calculated by using the charge exchange collision cross-section and a particle density obtained from ideal gas law $n = p/k_B T_g$ ($p = 0.53$ Pa, $T_\mathrm{g} = 300$ K). The minimum mean free path is 3.5 mm and is varied up to 350 mm or collisions are completely discarded to study the influence of collisions. The probability of a collision to occur is

$$P_{el} = 1 - \exp -\frac{s}{\lambda}, \tag{5.45}$$

with s being the pathway the particle has moved. A uniform random number $RN \in (0,1)$ was calculated and compared to the collision probability (function *"ran2"* in reference [291]). A collision has occurred if

$$RN < P_{el}. \tag{5.46}$$

It is checked for collisions after each step of moving the particle. In case of a collision, the altered velocity is calculated.

The absolute value of the particle velocity after the collision is readily obtained from eq. 2.70

$$v_i' = v_i \cos\theta, \tag{5.47}$$

with $\theta \in (0, \pi/2)$ being the angle between the initial direction of the incident particle and the direction of the particle after scattering. Assuming particles of equal mass, which is the case for collisions of sputtered particles with the thermalised metal vapour and still a good approximation for collisions between titanium particles and argon atoms, due to their similar mass, the actual direction of the velocity can be calculated as shown in figure 5.22:

$$\boldsymbol{v_i'} = v_i' \cos\theta \frac{\boldsymbol{v_i}}{v_i} + v_i' \sin\theta \frac{\boldsymbol{q}}{q}, \tag{5.48}$$

with $\boldsymbol{q}$ being a direction perpendicular to the initial direction of the velocity $\boldsymbol{i}$

$$\boldsymbol{q} = \begin{pmatrix} v_y v_z + v_z \\ -v_x v_z + v_z \\ -v_x - v_y \end{pmatrix}. \tag{5.49}$$

This direction still has one degree of freedom. It can be rotated by $\delta \in (0, 2\pi)$ around the direction of the initial particle velocity. The two angles θ and δ are calculated using the same random number generator as mentioned before:

$$\theta = \frac{\pi}{2} RN, \tag{5.50}$$

$$\delta = 2\pi RN. \tag{5.51}$$

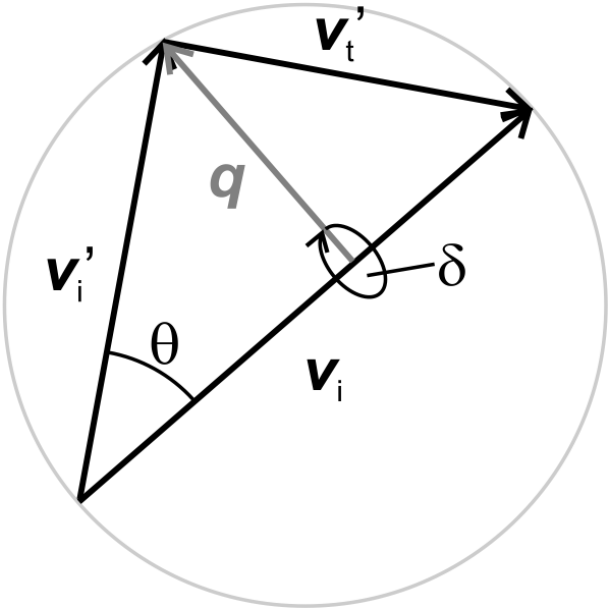

Figure 5.22: Direction of the particle after elastic scattering for the special case of equal masses.

The ionisation process is described by the ionisation cross-section as reported by Lotz [273]. However, equation 5.45 cannot be applied to calculate whether a sputtered particle is ionised or not, because it describes the process from the electron point of view. Instead, the rate equation shall be used

$$\frac{dn_{ion}}{n_0} = n_e k_{ion}(T_e) dt, \tag{5.52}$$

with n_0 being the density of particles in the respective ground state (Ti or Ti^+). Both the number of ionisation processes and the density of particles in the ground state are not known, but the expression dn_{ion}/n_0 gives the fraction of ionisation processes in respect to the density of particles in the ground state in a time interval. This can be used as the probability for ionisation processes, as long as the time interval dt is short enough to not largely deplete the density of particles in the ground state. Again, the ionisation probability

$$P_{ion} = n_e k_{ion}(T_e) dt \tag{5.53}$$

is compared to the random number and in case of an ionisation event, the charge is increased by one, but no changes on the particle density were made, as the momentum transfer from electron to heavy particle is negligible.

After describing the particle moving algorithm, the arrangement of the input data shall be presented. This comprises, the plasma potential, the electric field, the force acting on the ions due to the modified two-stream instability, the ionisation rates, as well as the radial and velocity distribution of sputtered particles. Both the electric field, determined from the emissive probe measurements by $\boldsymbol{E} = -\nabla V_{pl}$, and the additional force are required for the particle moving algorithm. The plasma potential and the electric field were used for the stable stage of the HiPIMS discharge ($t = 70$ µs).

The drift instability was studied by Lundin et. al. [1], who obtained electric fields of some 10 $\mathrm{V\,m^{-1}}$ in the azimuthal and the radial direction oscillating with a frequency in the low MHz range. Such oscillation could not be measured by the present emissive probe setup, simply because measurements were carried out sequentially and not simultaneously for several positions in the discharge. The model developed by Hurtig et. al. shows nicely the mechanisms involved in the particle transport [292], but it is too complex to be applied in the current study. Instead, the volume-averaged force acting on the positive ions is used [29, 293]

$$\left\langle \boldsymbol{F}_{i\varphi} \right\rangle = \eta_\perp q \boldsymbol{j}_\varphi, \tag{5.54}$$

with $\eta_\perp$ being the transverse resistivity. Using $\eta = B/\omega\tau e n_e$, $q = Ze$ and $\boldsymbol{j}_\varphi = -e n_e \boldsymbol{v}_d$, the azimuthal force on the ions reads:

$$\boldsymbol{F}_{i\varphi 0} = -\frac{B}{\omega\tau} Z e v_d \boldsymbol{e}_\varphi, \tag{5.55}$$

with v_d the absolute value of the drift speed as shown in figure 5.12. More recently, Anders et. al. suggested the presence of a force in axial direction enhancing the ion transport [32].

Considering the azimuthal force on the ions is a drag force of the drifting electron fluid, a force must also act on the electrons with the same amplitude but opposite direction [293].

This force is perpendicular to the magnetic field which causes the electrons to drift perpendicular to both the force and the magnetic field (see eq. 2.30). The drift velocity $\boldsymbol{v}_{\perp B}$ can be calculated as

$$\boldsymbol{v}_{\perp B} = -\frac{v_d}{\omega\tau}\boldsymbol{e}_{varphi} \times \boldsymbol{e}_B, \tag{5.56}$$

with $\boldsymbol{e}_B$ the direction of the local magnetic field. This drift has both a radial and an axial component directed away from the target. The force on the ions associated with it, has the same direction and, thus, enhances the transport of ions away from the target, as proposed by Anders et. al [32]. The force can be written as:

$$\boldsymbol{F}_{i\perp B} = -\frac{F_{i\varphi}}{\omega\tau}\boldsymbol{e}_{varphi} \times \boldsymbol{e}_B. \tag{5.57}$$

Yet again, this force would cause an electron drift, which is directed in azimuthal direction, opposite to the initially determined drift speed. This causes a force on both the electrons and ions, which in turn would imply further drifts and forces. Following this thought, one obtains an altered force

$$\boldsymbol{F}_{i\varphi} = -F_{i\varphi 0}\boldsymbol{e}_\varphi \left(1 - (\omega\tau)^{-2} + (\omega\tau)^{-4} \mp \ldots\right), \tag{5.58}$$

$$\boldsymbol{F}_{i\perp B} = -F_{i\varphi 0}\boldsymbol{e}_\varphi \times \boldsymbol{e}_B \left((\omega\tau)^{-1} - (\omega\tau)^{-3} + (\omega\tau)^{-5} \mp \ldots\right). \tag{5.59}$$

The sum on the right hand side converges for $\omega\tau < 1$, which is usually fulfilled, and the forces read:

$$\boldsymbol{F}_{i\varphi} = -F_{i\varphi 0}\frac{(\omega\tau)^2}{1+(\omega\tau)^2}\boldsymbol{e}_\varphi \tag{5.60}$$

$$\boldsymbol{F}_{i\perp B} = -F_{i\varphi 0}\frac{\omega\tau}{1+(\omega\tau)^2}\boldsymbol{e}_\varphi \times \boldsymbol{e}_B. \tag{5.61}$$

In order to somewhat account for the statistic nature of the volume-averaged force, the absolute value $F_{i\varphi 0}$ is modified further by introducing a Gaussian distribution with its centre at $F_{i\varphi 0}$ and a standard deviation of $0.5F_{i\varphi 0}$. This is to represent the fact, that not all ions are subject to a large acceleration by the full force, but it depends on the coupling between the oscillating electric field caused by the fluctuation of the electron density due to the electron drift and the positive ion.

The last remaining parameter is $\omega\tau$, which was subject to several experiments on highly ionised plasmas [28]. It was found to be in the range of 2 to 2.7. The azimuthal forces calculated when using a grounded and a floating substrate are displayed in figure 5.23. The input data is provided as bilinear interpolation to allow for calculating the force at any

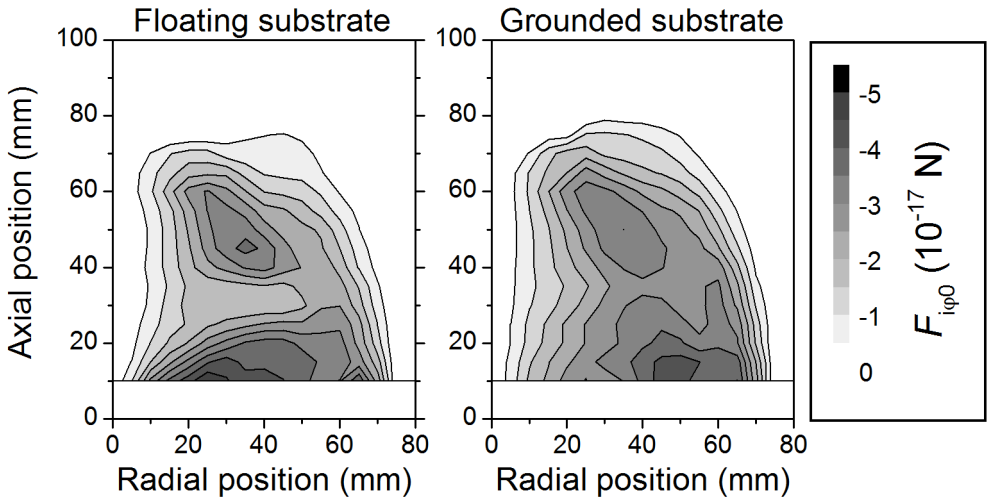

Figure 5.23: Spatial distribution of the force caused by the modified two-stream instability calculated from combined emissive and Langmuir probe measurements for $t = 70$ µs.

position in the discharge volume. A bilinear interpolation was also used for the direction $-\boldsymbol{e}_\varphi \times \boldsymbol{e}_B$.

Ionisation cross-sections for creating Ti^+ and Ti^{2+} ions are used as published by Lotz [273]. The rate coefficient $k_{ion}(T_e)$ was calculated using equation 2.63. The spatial distribution of the ionisation rates, $n_e k_{ion}(T_e)$, for both the grounded and the floating substrate are shown in figure 5.24. They were also interpolated bilinearly before used in the calculations.

In order to model the transport for the entire discharge volume, measured plasma parameters such as the plasma potential, ionisation rates etc. have to be extrapolated between $z = 0$ mm, position of the target, and $z = 10$ mm, position of measurements closest to the target. In addition, the position up to which the extrapolation has to be made is unknown, as the extension of the sheath is unknown, too. But even without knowing the exact sheath position, one can already expect that the electron density falls dramatically in the sheath as most of the target potential of several 100 V drops in this region. With only a few electrons in the sheath, ionisation does not occur and both the electric field and the force caused by the two-stream instability do not act on the sputtered particle. One can therefore set the electron density and the instability force to zero. Okazawa et. al. showed that the sheath width varies radially in front of the target due to the magnetic field with the thinnest sheath observed right above the racetrack where the magnetic field is orientated

parallel to the target [294]. However, the parameter range in that study does not cover HiPIMS discharges. Due to the lack of experimental or theoretical data, the sheath width

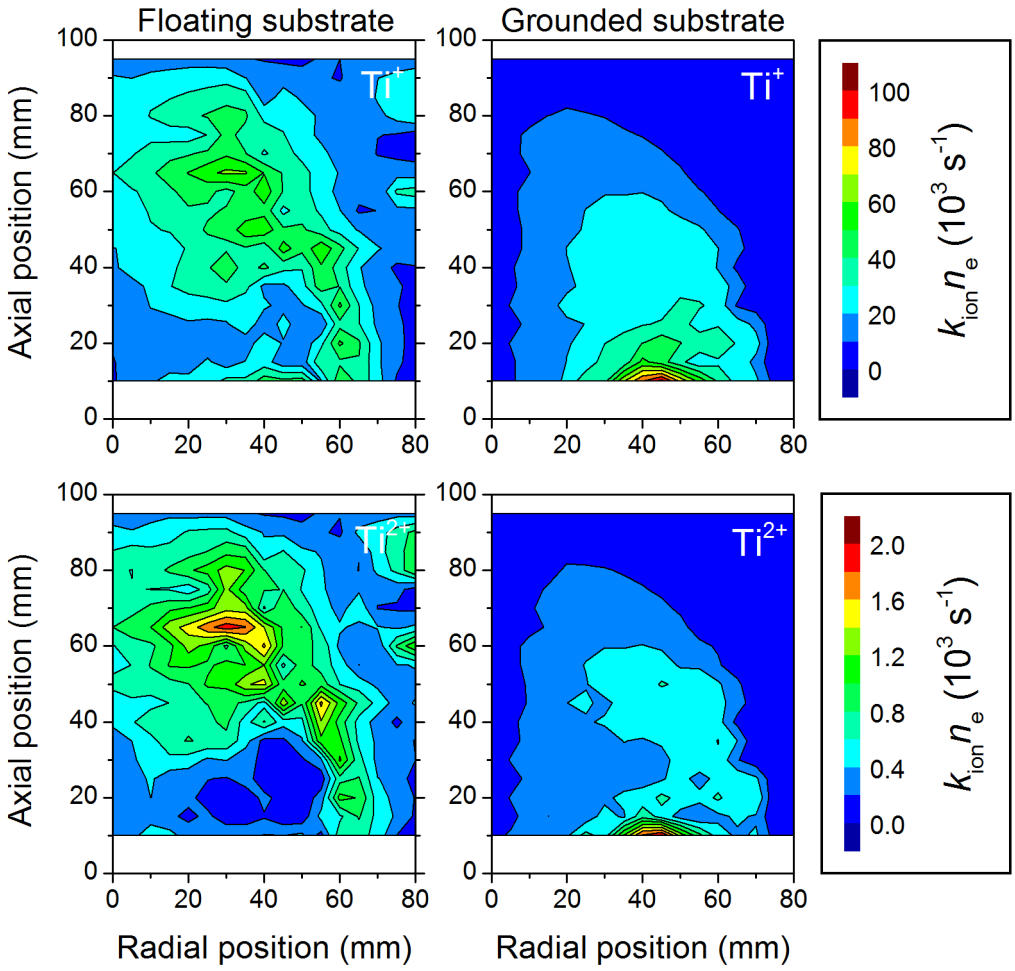

Figure 5.24: Spatial distribution of the titanium ionisation rate calculated from Langmuir probe measurements for $t = 70$ µs.

is set to be 2 mm, as emissive probe measurements showed, that the sheath was not entered at this position. The axial distribution of the plasma potential suggests a linear function to extrapolate the measured data up to $z = 2$ mm. An additional boundary condition is the target potential as summarised in table 5.4, which was set as the plasma potential for $z = 0$ mm. The electric field was not extrapolated separately but the extrapolated plasma potential was used for its calculation. The force caused by the two-stream instability was also extrapolated linearly up to $z = 2$ mm. The ionisation rate comprises two components,

the electron density and the rate coefficient, determined by the electron temperature. The latter is shown to vary only slightly within the HiPIMS discharge, see figure 5.19. The electron temperature is therefore assumed to be constant. The electron density was extrapolated by a linear function, but also has to fulfil a boundary condition. The ion flux, determined by the ion density and the Bohm speed at the sheath edge, has to carry the discharge current measured at the target

$$I_d = \int_{A_t} Z_{eff} e n_i \sqrt{\frac{k_B T_e}{m_i}} dA. \tag{5.62}$$

The effective charge state of the ions Z_{eff} also accounts for other contributions to the discharge current, such as multiply charged ions and secondary electron emission. It was assumed to be 1.1. The slope was multiplied by the same factor for all radial positions until the calculated current agreed with the measured value. Once, the electron density was calculated, the ionisation rate was extrapolated and used as input data for the model. Examples for the extrapolation of the measured plasma potential, the instability force and the electron density are shown in figure 5.25.

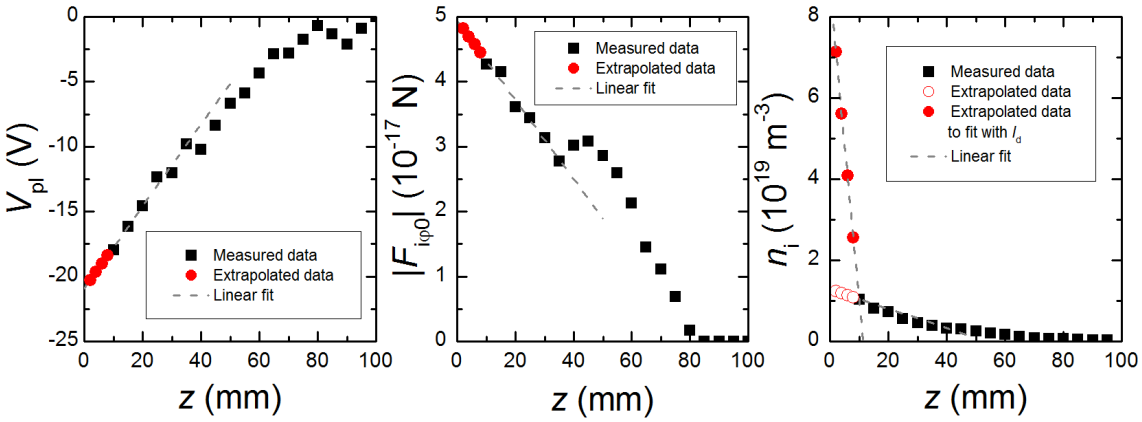

Figure 5.25: Interpolation of experimental data for the plasma potential, the instability force and the electron density towards the target. The substrate was grounded in all examples displayed and the radial position is $r = 45$ mm.

A final consideration must be made on the initial velocity and radial position of the titanium atoms ejected from the target. Titanium atoms sputtered from the target have an energy distribution as given by [50]:

$$f_s(E) = \begin{cases} 2\left(1+\frac{E_s}{\Lambda_e E_i}\right)\frac{E_s E}{(E_s+E)^3}, & E \leq \Lambda_e E_i \\ 0, & E > \Lambda_e E_i, \end{cases} \tag{5.63}$$

with E_s being the surface binding energy (3.30 eV for titanium [295]) and E_i being the energy of the incident ions which is assumed to be the target voltage equivalent, $E_i = -eV_t$, for singly charged ions. The parameter Λ_e represents the ratio of the masses of incident ions m_i and target atoms m_t:

$$\Lambda_e = \frac{4m_i m_t}{(m_i + m_t)^2}, \tag{5.64}$$

which is about 1 due to the very similar mass of argon and titanium. The velocity distribution function is obtained by

$$f(v) = \frac{m_t v}{e} f(E). \tag{5.65}$$

The velocity distribution function for sputtering a titanium target in HiPIMS for $t = 70$ µs is shown in figure 5.26 a). One can easily see, that it ranges from velocities just above zero to several 10^4 m s^{-1}, with both the lower and higher end of the distribution sparsely populated. An initial approach, representing the entire velocity distribution function with a constant step size for the velocity, was found to need too many particles to be calculated to achieve sufficient resolution at the peak of the distribution. Instead, the velocity distribution was divided in 100 intervals with equal population. The boundaries $v_0 \dots v_{100}$ were calculated as:

$$v_0 = 0, \tag{5.66}$$

$$0.01 = \frac{\int_{v_i}^{v_{i+1}} f(v)dv}{\int_{v_0}^{v_{100}} f(v)dv}. \tag{5.67}$$

Each interval is then represented by its mean velocity

$$\bar{v}_i = \frac{\int_{v_{i-1}}^{v_i} v f(v)dv}{\int_{v_{i-1}}^{v_i} f(v)dv}. \tag{5.68}$$

As an example, the representative velocities using 10 intervals are shown in figure 5.26, too. One can see, how the velocities are denser close to the maximum of the distribution.

Particles can also be ejected by the target in a non-normal direction. Using the angle χ, counted from the target normal, a cosine distribution is usually reported [51]. The angular distribution is also converted into discrete values as it was done for the velocity distribution. In this case, 20 intervals were used. The particle can also have a velocity component in the azimuthal direction φ between 0° and 360° and is varied in steps of 6°. The initial velocity of the sputtered titanium atom is then given as

$$\boldsymbol{v}_i = \begin{pmatrix} \bar{v}_i \sin\chi \cos\varphi \\ \bar{v}_i \sin\chi \sin\varphi \\ \bar{v}_i \cos\chi \end{pmatrix}. \tag{5.69}$$

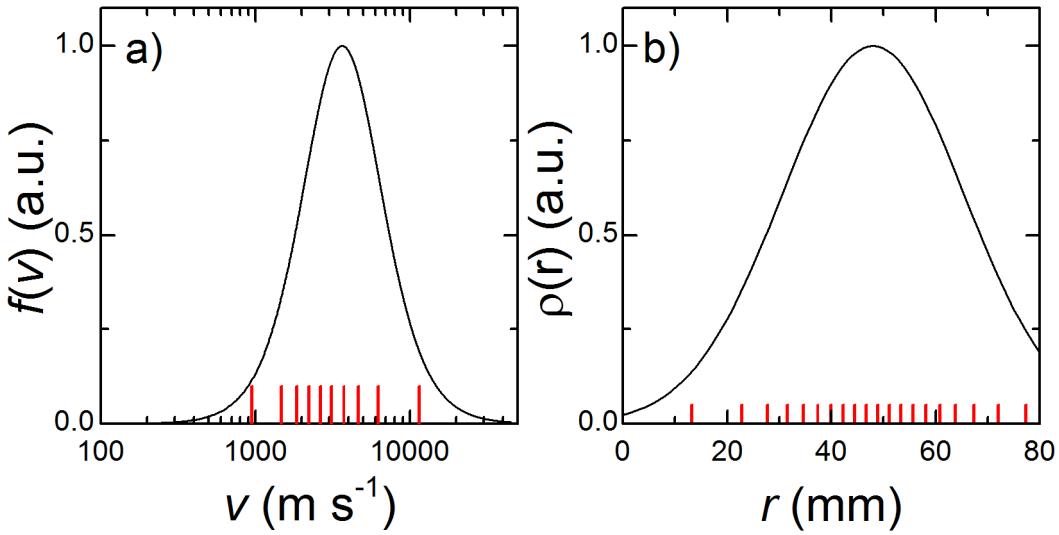

Figure 5.26: Velocity (a) and radial distribution (b) of particles sputtered from the target for $t = 70$ µs using discharge conditions as summarised in table 5.4. The black curves represent the actual distribution function, whereas the red lines show the representative velocities and radial positions for the test particles.

The initial radial position of the sputtered particle is determined by the radial distribution of ions impinging on the target $\rho(r)$. As these ions do not only cause sputtering but also constitute to the major part of the measured discharge current, the radial distribution of the target current density can be used as a measure for the radial distribution of the initial particle position. Clarke et. al. [186] measured the target current density distribution for a HiPIMS discharge and demonstrated, that the theoretical distribution published by Wendt et. al. describes the experimental data quite well [187]. This allows to scale the target current density distribution to the conditions found in the present discharge. The full width half maximum of the distribution w_d in millimetre is given by [187]

$$w_d = 94.7 \frac{V_t^{1/10} I_d^{1/5}}{B^{4/5}}, \tag{5.70}$$

with the magnetic induction B given in Gauss. The target voltage and discharge current recorded by the oscilloscope 70 µs after pulse initialisation were used, as well as the magnetic field measured above the target surface above the racetrack. All these parameters are summarised in table 5.4. A Gaussian distribution was assumed for the radial distribution of sputtered particles with the centre $r_{||B}$, the radial position above the target where the

magnetic field is orientated parallel to the target and the standard deviation σ_d calculated by

$$\sigma_d = \frac{w_d}{2.3548}. \tag{5.71}$$

This distribution was once again represented by 20 intervals with equal probability. It is shown in figure 5.26 b) together with the original sputtering distribution.

Configuration	B **(mT)**	V_t **(V)**	I_d **(A)**	σ_d **(mm)**	$r_{\|\|B}$ (mm)
Floating	40	480	192	17.7	48
Grounded	40	512	176	17.5	48
More unbalanced	38	525	176	18.3	51

Table 5.4: Discharge conditions for modelling the particle transport.

5.4.2 Results of the transport model

The trajectories of three test particles with initial velocities of 5×10^3 m s^{-1}, 10×10^3 m s^{-1} and 20×10^3 m s^{-1} perpendicular to the target are shown in figure 5.27. All three particles start at the target surface in the racetrack area at $r = 45$ mm and the model is run for conditions of a grounded substrate, a mean free path of 35 mm and $\omega\tau = 2$, which was used for all simulations unless explicitly stated different. The target is indicated by the grey circle. The sputtered titanium atom is ionised right above the target within the first 1 µs of motion. This means, that the motion of the particle is largely determined by the electric field and the force caused by the two-stream instability. The influence of the latter one can be seen in the projection of the trajectory in the x-y plane. All three particles gain velocity in the azimuthal direction which initially was zero. For example, the particle starting with an initial velocity of $v_z = 5 \times 10^3$ m s^{-1} makes about half a turn above the target before it is attracted back to the cathode. In contrast, the other two test particles have sufficient energy to overcome the plasma potential barrier and reach the substrate. Trajectories of 24 million test particles were calculated just as demonstrated and their distribution, velocity and kinetic energy recorded. Storing all trajectories require too much memory. Thus, the individual particles are only represented in the distributions and average velocities shown in the following chapters.

Every particle ejected from the cathode is counted into the statistics at either one of the boundaries, target, sidewall, substrate, or as thermalised, if the particle has not reached any

boundary within the calculation time of 40 µs. One can further detect the composition of particles at each of the four possible outcomes, which means that the particle composition at all boundary walls can be given. One can also follow, where particular species move to. For example, the fraction of singly charged positive titanium ions deposited on the substrate can be calculated. The results shown and discussed in this chapter were obtained by using the discharge conditions for a grounded substrate.

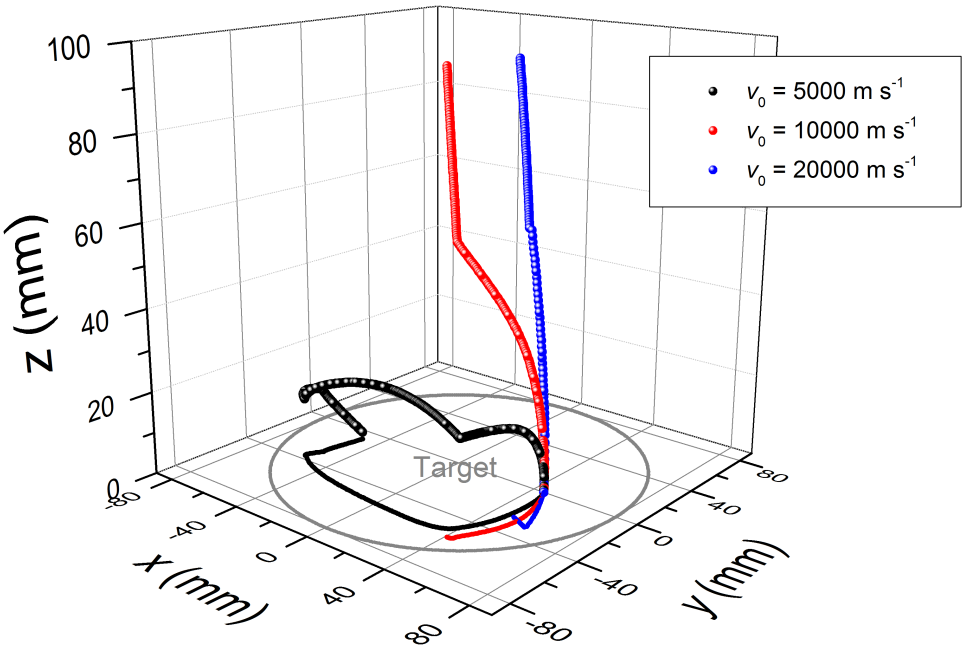

Figure 5.27: Calculated trajectories of three test particles for a grounded substrate.

First, the influence of collisions shall be studied by varying the mean free path over a wide range. The particle distribution and the composition of the flux to the walls is depicted in figure 5.28 using $\omega\tau = 2$. One can see, that with increasing mean free path or less frequent collisions, more and more particles can travel through the discharge volume and reach the substrate. For a mean free path of only 3.5 mm (charge-exchange processes) more than 60 % of the titanium atoms and more than 97 % of the charged particles (Ti^+, Ti^{2+}) are scattered and attracted back to the target. This number reduces to zero for Ti when no collisions occur, while still more than half the ionised particles (Ti^+: 54 %, Ti^{2+}: 93 %) are attracted back to the cathode by the electric field. At the same time, the

fraction of titanium atoms reaching the substrate increases from 0 % to 35 %, while only a maximum of 21 % of Ti^+ and 2 % of Ti^{2+} arrive at the substrate. More particles are seen to be deflected to the sidewalls, which constitutes 64 % of the titanium atoms, 23 % of Ti^+ and 4 % of Ti^{2+} when no collision occurs. In total, 55 % of the particles are attracted back to the target, 19 % can reach the substrate, while 24 % of the particles are detected at the sidewalls and 2 % are thermalised, i.e. they have not reached any of the walls. In the intermediate range of the mean free path, $\lambda = 35$ mm, more particles are attracted back to the target, 78 %. This is caused by the energy transfer to the background gas due to collisions. Charged particles then have less kinetic energy to overcome the potential barrier to the substrate, where only about 4 % of the particles arrive. 10 % of the particles are detected at the sidewalls and 8 % are thermalised.

The composition of the flux to the target is largely dominated by Ti^+ ions, which is at least 62 % for $\lambda = 3.5$ mm and increases to 76 % if no collision occurs. One can also observe a significant contribution of doubly charged titanium ions, 28 % to 24 %, as most of these ions are attracted back to the target. They would need to overcome twice the potential $2e\Delta V$ compared to Ti^+. The flux to the sidewall becomes dominated by Ti^+ with increasing mean free path way, increases from 3 % to 74 %, whereas the flux to the substrate is dominated by these ions for all mean free paths, contribution 70 % to 82 %. This demonstrates, how efficient particles are ionised in the discharge volume. In the case of frequent collisions, 15 % of the particles are neutral, 59 % are singly charged ions and the rest, 26 %, are doubly charged. This composition changes with increasing mean free path, fewer collisions. The fraction of Ti and Ti^{2+} both decrease to 9 % and 14 %, respectively, while the fraction of Ti^+ increases to 77 %. This is plausible, because particles quickly lose kinetic energy by frequent collisions and remain in the dense plasma zone adjacent to the cathode. Here, they do not only get ionised but also have a high probability to be ionised a second time, which explains the increased fraction of Ti^{2+}. As scattering does not only change the kinetic energy of the particle but also changes its direction, frequent collisions can lead to back-scattering of the incident flux of titanium atoms before they even get ionised. This is confirmed by the rather large amount of titanium atoms detected at the target for low mean free paths.

The return probability of titanium ions to the target is calculated to be in the range of 54 % to 97 % ($\lambda = 35$ mm: 79 %), which is in the same range as the return probability used by Brenning et. al. [207]. Vlcek et. al. found a return probability of titanium ions of 70 % at a degree of ionisation of 80 %, which also confirms the present data [119]. However, recent measurements of the ionised metal flux to the substrate in a very similar

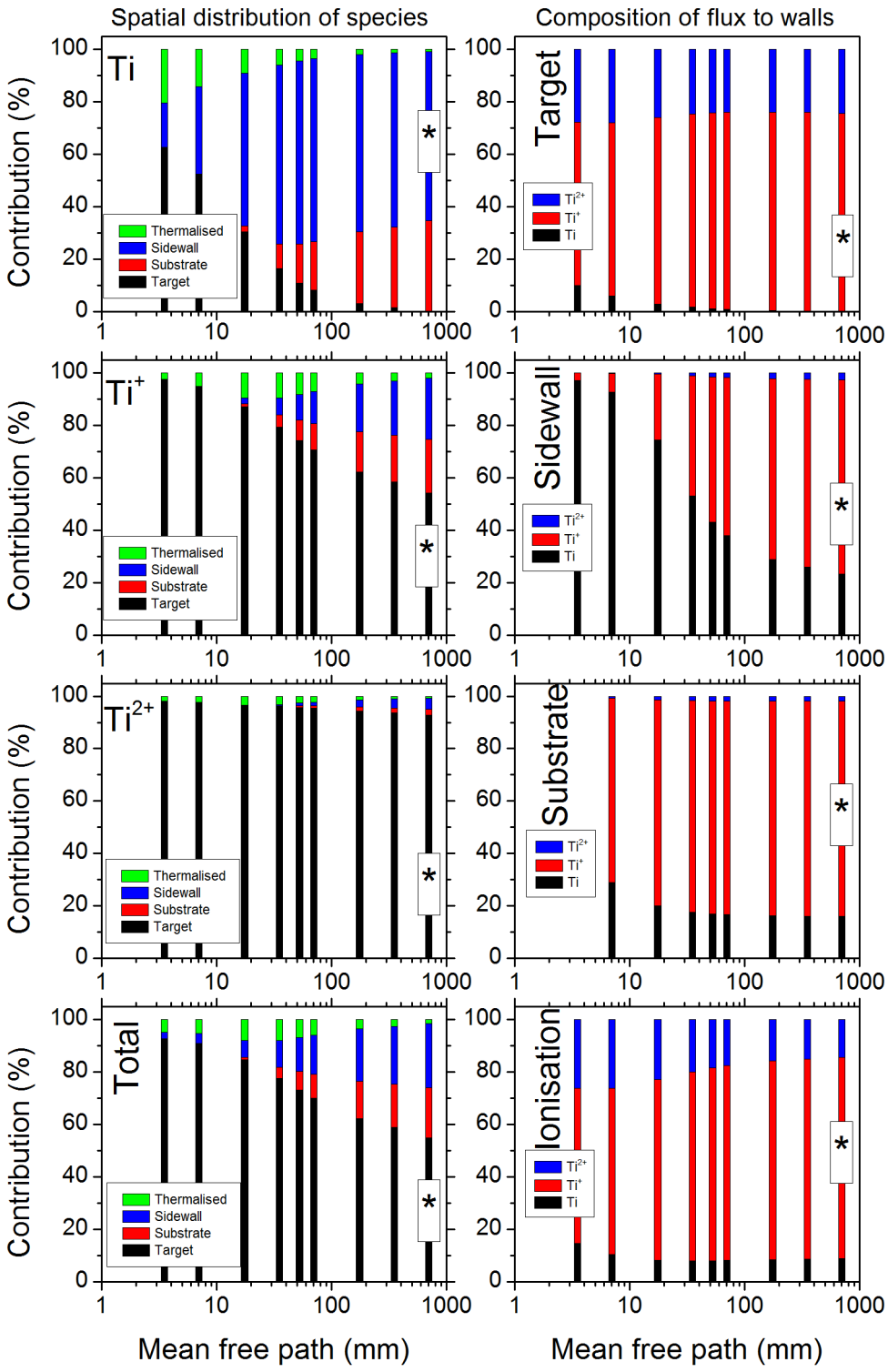

Figure 5.28: Particle distributions calculated for a grounded substrate for varying the collision mean free path.

experimental setup as in this current study revealed the fraction of titanium ions to the substrate to be in the range of 30 % to 40 % [296]. This is much lower than calculated by the model, which gives a value of up to 80 %. One also has to keep in mind, that only 4 % of the total sputtered particles arrive at the substrate during the discharge pulse. It might be possible that a significant fraction of the deposition is due to condensation of sputtered metal vapour in the off-time. This vapour would mainly consist of titanium atoms and not of ions. An investigation on this problem will be discussed at a later time.

Once the titanium atom is ionised, the electric field acts on the particle, as well as the force caused by the modified two-stream instability. The influence of the latter one shall be studied now. The force was varied globally by altering the collision parameter $\omega\tau$ from 1.2 (which is below the value typically reported for HiPIMS discharges [28]), to 16, which represents Bohm diffusion. In addition, the case of no force was also included. Figure 5.29 shows the spatial distribution and the composition of the flux to the walls. The spatial distribution for titanium atoms and the degree of ionisation are not shown, because the force has no influence on both of them. However, an influence on the ions Ti^+ and Ti^{2+} can be seen. With increasing force, decreasing $\omega\tau$, the fraction of particles arriving at the sidewalls and the substrate increases from 4 % to 14 % and from 4 % to 7 % for Ti^+ and from 0 % to 5 % and 0 % to 1 % for Ti^{2+}. At the same time, the fraction of particles kept in the discharge volume, thermalised particles, increase from 3 % to 27 % for Ti^+ and from 1 % to 17 % for Ti^{2+}. The increased sideway deflection due to the force caused by the two-stream instability as suggested by Lundin et. al. [29]. However, the transport of ions towards the substrate is only enhanced slightly, indicating that the components of the force in the axial direction is not high enough to largely increase the ion transport. The increased fraction of thermalised particles can be explained by the fact that the axial and radial component of the force compensate for a part of the axial and radial component of the electric field. This increses the duration of particles to stay within the discharge volume, as they are neither accelerated towards the target nore to the substrate or sidewalls.

The composition of the flux changes less significantly. At the target, the fraction of Ti^+ decreases from 78 % to 70 % when increasing the force, while more Ti^{2+} ions are attracted back to the target, constituting 21 % to 28 % of the flux. The composition at the sidewall confirms the trend, that more ions are deflected to the sidewalls by the two-stream instabilty. The fraction of Ti^+ increases from 35 % to 61 % and the fraction of Ti^{2+} increases from 0 % to 6 % while the amount of titanium atoms is reduced from 64 % to 32 %. The influence of the force on the transport of ions to the substrate is by far

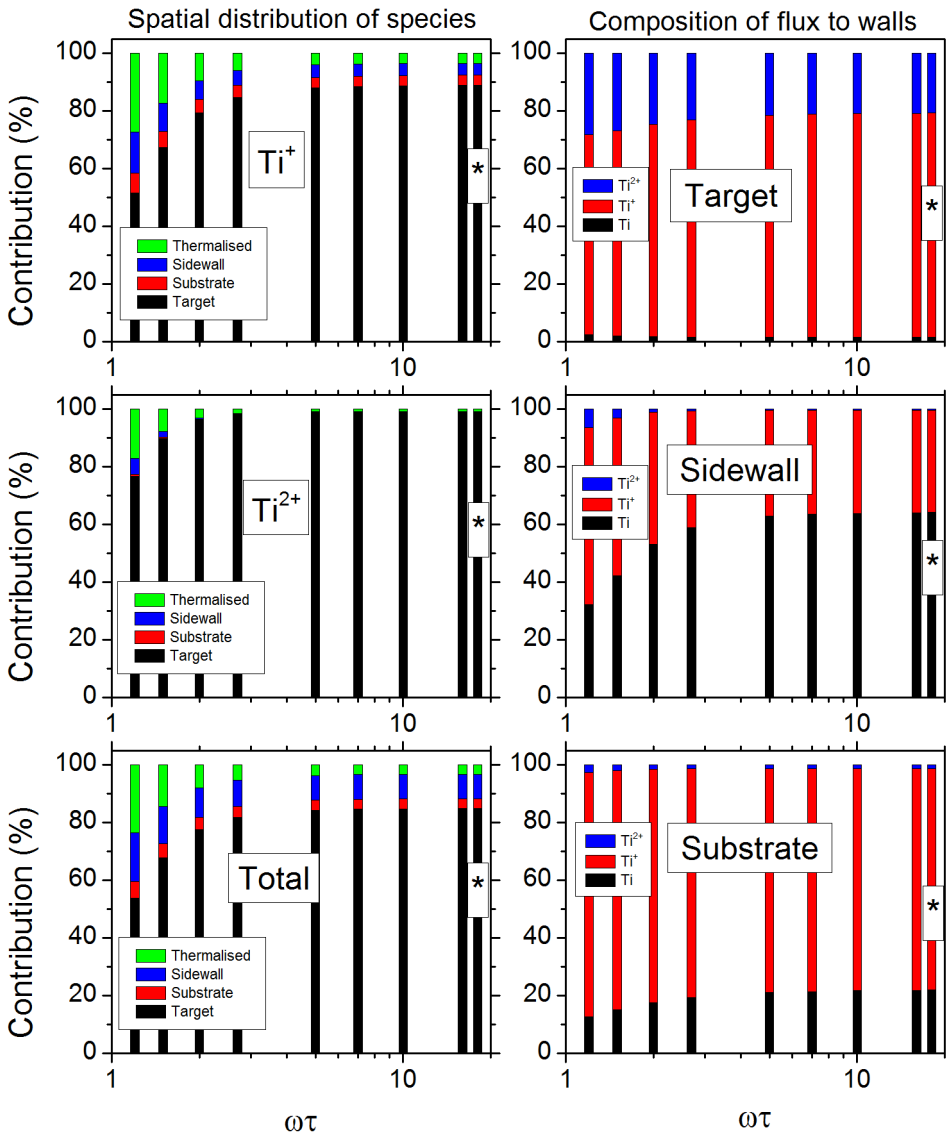

Figure 5.29: Particle distributions calculated for a grounded substrate for varying the force caused by the two-stream instability.

less pronounced. The fraction of Ti^+ only increases from 77 % to 85 % and the fraction of Ti^{2+} from 1 % to 3 %. It shall be noted, that a force in only the azimuthal direction leads to a far lower enhancement of the ion transport to both the sidewalls and the substrate. For example, the fraction of Ti^+ ions detected at the substrate is not influenced and stays at 4 %, while the fraction of Ti^+ at the sidewall only increases from 4 % to 9 %.

Finally, the influence of the magnetic field and the substrate configuration shall be investigated. Not the entire set of parameters, varying the mean free path and the force caused by the two-stream instability, will be presented here, but key parameters for the case $\lambda = 35$ mm and $\omega\tau = 2$ are summarised in table 5.5. These parameters only differ slightly between the different configurations. The highest flux to the substrate is calculated for the floating substrate. At the same time, the fraction of particles attracted back to the target and the particles deflected to the sidewall are decreased. This is caused by a lower ionisation rate in front of the target, when the floating substrate is used (see figure 5.24). This means, that more particles are ionised further away from the target. Thus, the ionised sputtered particles do not need to overcome the entire potential barrier to the substrate. The increased electron density in the vicinity of the floating substrate still allows for a high degree of ionisation of the metal flux. Increasing the unbalance of the magnetic field does not seem to have too much of an effect. The flux towards the substrate is increased, but only slightly. On the other hand, the balance of the magnetron can only be varied slightly. The influence certainly needs more investigation with a much wider a range of varying the magnetic field.

The axial and radial distribution of particles detected at the target, the sidewall and the substrate are shown in figure 5.30. One can clearly see most titanium ions to impinge at the target in the racetrack region, as it would be expected. The radial distribution of particles at the target also reveals a slight asymmetry with more ions impinging at higher radial positions. This feature is enhanced further when increasing the force caused by the two-stream instability, which suggests that ionised titanium particles are accelerated radially outwards before they impinge on the target. A slightly asymmetric distribution was also reported by Clarke et. al. for the target current distribution [186]. The axial distribution of particles arriving at the sidewall show a clear maximum for the titanium atoms close to the target $z = 5$ mm. This suggests, that titanium atoms arrive at the sidewall, only if they were ejected from the target under a rather large angle χ. It appears, that it is only under this condition, that sputtered titanium atoms are not ionised. It is, however, questionable if one can observe this maximum experimentally as the target clamp ring exceeds the target surface by 5 mm. The flux calculated for this axial position might just be deposited at the

	Floating	**Grounded**	**Unbalanced**
Substrate	6.6 %	4.2 %	4.7 %
Sidewall	9.3 %	10.2 %	10.8 %
Target	74.7 %	77.7 %	73.8 %
Thermalised	9.4 %	7.9 %	10.7 %
Ionisation in volume	92 %	92 %	90 %
Ionisation at substrate	89 %	81 %	77 %
Ionisation at sidewall	45 %	46 %	42 %

Table 5.5: Comparison of fluxes to the walls for different substrate and magnetic field configurations.

clamp ring. The axial distribution of Ti^+ ions is rather uniform. The radial distribution at the substrate is dominated by the arriving flux of Ti^+. The wide distribution shows its maximum above the racetrack at $r = 45$ mm, which suggests that the initial conditions, starting position and initial velocity, still have a large influence on the deposition at the substrate despite the influence of the electric field, the force caused by the two-stream instability and scattering. The radial distribution also confirms the observations made by optical 2d-imaging. Throughout the entire discharge pulse, the intensity maximum of metal ions in the vicinity of the substrate was found above the racetrack $r \approx 45$ mm. This feature is most striking during pulse termination shown in figure 4.21. The flux of titanium atoms shows its maximum at the outer edge of the discharge, as most particles arriving closer to the centre of the discharge are ionised in the discharge volume.

Figure 5.31 shows the axial and the radial distribution of the kinetic energy of Ti^+ ions arriving at the sidewall and the substrate, respectively. One can see, that particles arrive with kinetic energies of more than 40 eV. For particles detected at the sidewall, the energy distribution is widest close to the target with the maximum of the particle distribution found at 15 eV close to the target, $z = 10$ mm, and at 5 mm further away, $z = 75$ mm. A similar finding was reported by Lundin et. al. [29]. However, they also find a large maximum of the particle distribution close to zero kinetic energy, which might be caused by fully thermalised ions. The presence of this species could not be confirmed by the present

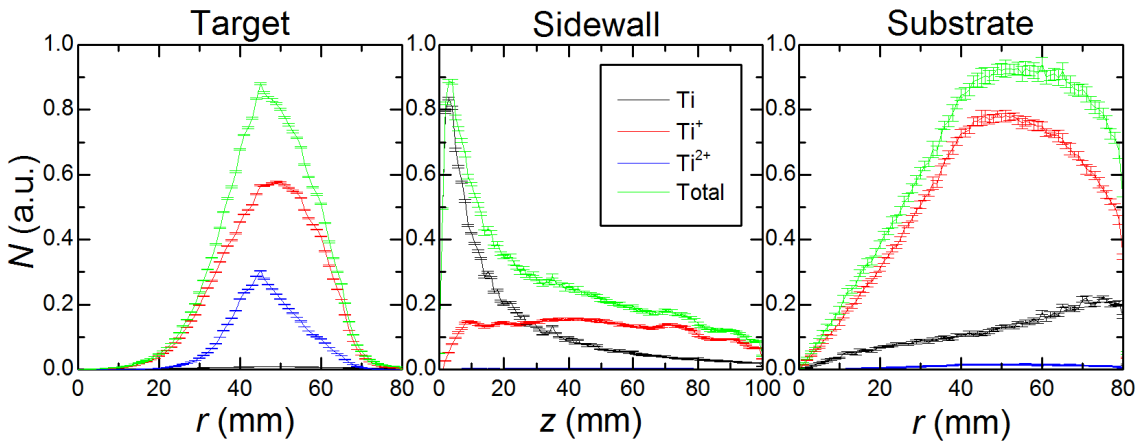

Figure 5.30: Particle distributions calculated at the target, the sidewall and the substrate for a grounded substrate ($\lambda = 35$ mm, $\omega\tau = 2$).

study, but treatment of particle collisions were largely simplified and in particular charge-exchange collisions widely neglected. In addition, the grounded front cap accommodating the orifice of the mass spectrometer might also change the plasma potential in its vicinity allowing more ions of low energetic ions. However, the maximum of the distribution is found for low kinetic energies of $2 \ldots 3$ eV for all radial positions. The energy distribution reveals an additional energy of about 16 eV which originates from the potential drop from the plasma potential to the substrate when it is floating.

The influence of the force caused by the two-stream instability is investigated for the sidewall, $z = 20$ mm, and the substrate at $r = 60$ mm. The distribution of the kinetic energy is shown in figure 5.32. The number of particles arriving at the sidewall increases with increasing force as it is observed in figure 5.29. While the distribution's onset is found for the same energy, $E_{\mathrm{kin}} = 5$ eV, which coincides with the plasma potential at the outer edge of the discharge, the position of the maximum moves to higher energies. In addition, more particles are ejected out of the discharge to sidewall with higher kinetic energy. This nicely demonstrates, that ions can be transported out of the discharge volume by the two-stream instability force. The influence of the instability is not so pronounced when looking at the energy distribution calculated for the substrate. More particles are transported towards it but the energy distribution hardly changes. The maximum is always found for $E_{\mathrm{kin}} = 2$ eV, and the distribution mainly follows the sputtering distribution $f(E)$. However, the energy distribution seems to be largely depleted for particles at low energy. Particles ejected from the cathode with such a low energy are attracted back to the target once they are ionised and

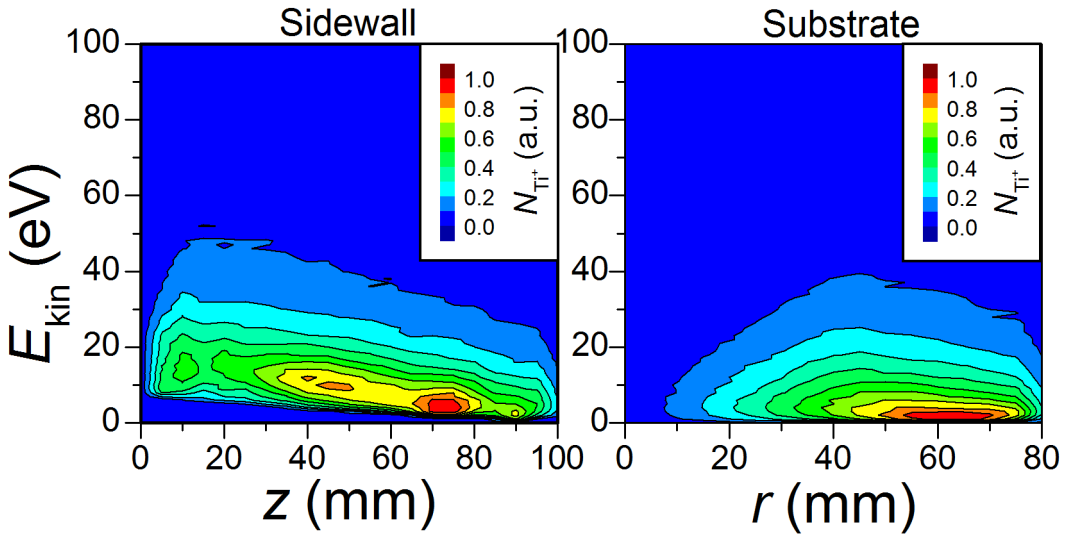

Figure 5.31: Energy distributions calculated the sidewall and the substrate for a grounded substrate ($\lambda = 35$ mm, $\omega\tau = 2$).

do not contribute to the deposition at the substrate. Even though the two-stream instability does not alter the energy distribution significantly, it still enhances the transport of particles through the discharge volume

The spatial distribution of the particle density, the radial, azimuthal and axial velocity are shown in figure 5.33. The relative particle density is calculated by recording the position of each particle after each time step Δt. It can be seen, that the density of titanium atoms is concentrated close to the target. This is confirmed by optical 2d-imaging, which shows a clear minimum in the emission of metal atoms right above the racetrack (see figure 4.9). The density of titanium atoms is reduced by ionisation immediately above the racetrack due to the high electron density in this region. The density of titanium ions Ti^+ is highest close to the target above the racetrack $r = 45$ mm. It decreases towards the discharge axis, the outer edge of the discharge, as well as to the substrate. In comparison, the density of Ti^{2+} ions is more concentrated to the target due to the electric which poses double the force on these ions compared to Ti^+. The radial velocity of the ions Ti^+ and Ti^{2+} is directed towards the outer edge of the discharge throughout most of the discharge volume. This is probably due to the two-stream instability which accelerates ions out of the discharge. Close to the discharge, however, a negative value can be seen for a radial position of about 60 mm to 70 mm.

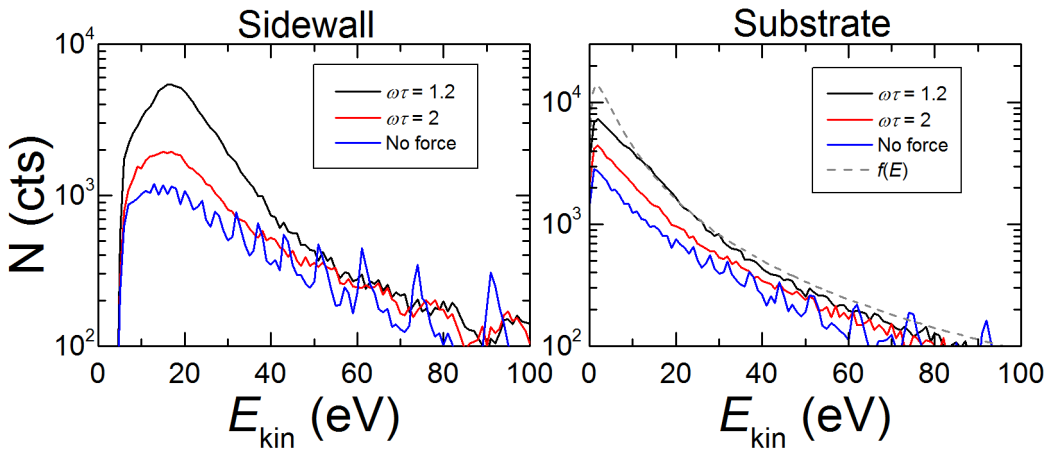

Figure 5.32: Energy distributions calculated at $z = 20$ mm and $r = 60$ mm for varying the force caused by the two-stream instability.

The radial electric field present in this area accelerates ions towards the racetrack region. The entire outer edge of the discharge is characterised by an average radial velocity close to 3×10^3 m s^{-1}. This does not represent an electric field accelerating the ions in this regions, but it is caused by the averaging process. As the ions with low kinetic energy are repelled by the plasma potential barrier, only the energetic part of the sputtering distribution passes into this region, causing an elevated average velocity. There is an additional area adjacent to the substrate which reveals a negative radial velocity of the ions. This area coincides with the region of lower plasma potentials located between the magnetic null and the substrate, as seen in figure 5.13.

The azimuthal force of the titanium atoms is close to zero because no force acts in the azimuthal direction and the initial distribution averages to zero. An effective azimuthal velocity can be seen for both ionic species Ti^+ and Ti^{2+} with its maximum close to the target. The force caused by the two-stream instability accelerates the ions to a maximum average velocity of 3×10^3 m s^{-1} and 7×10^3 m s^{-1} for Ti^+ and Ti^{2+}, respectively. This value increases to 4.5×10^3 m s^{-1} and 9×10^3 m s^{-1} when the force is increased by setting $\omega\tau$ to 1.2. This velocity is in the same order as the azimuthal velocity reported for drifting ionisation zones reported by Anders et. al. [32].

The axial velocity is found to be largely positive for titanium atoms. This means, that only the fastest atoms can pass the dense plasma zone, while the slow atoms get ionised because they remain in the region of high electron density for a longer time. The axial velocity of Ti^+ ions is positive in most regions of the discharge volume, represent-

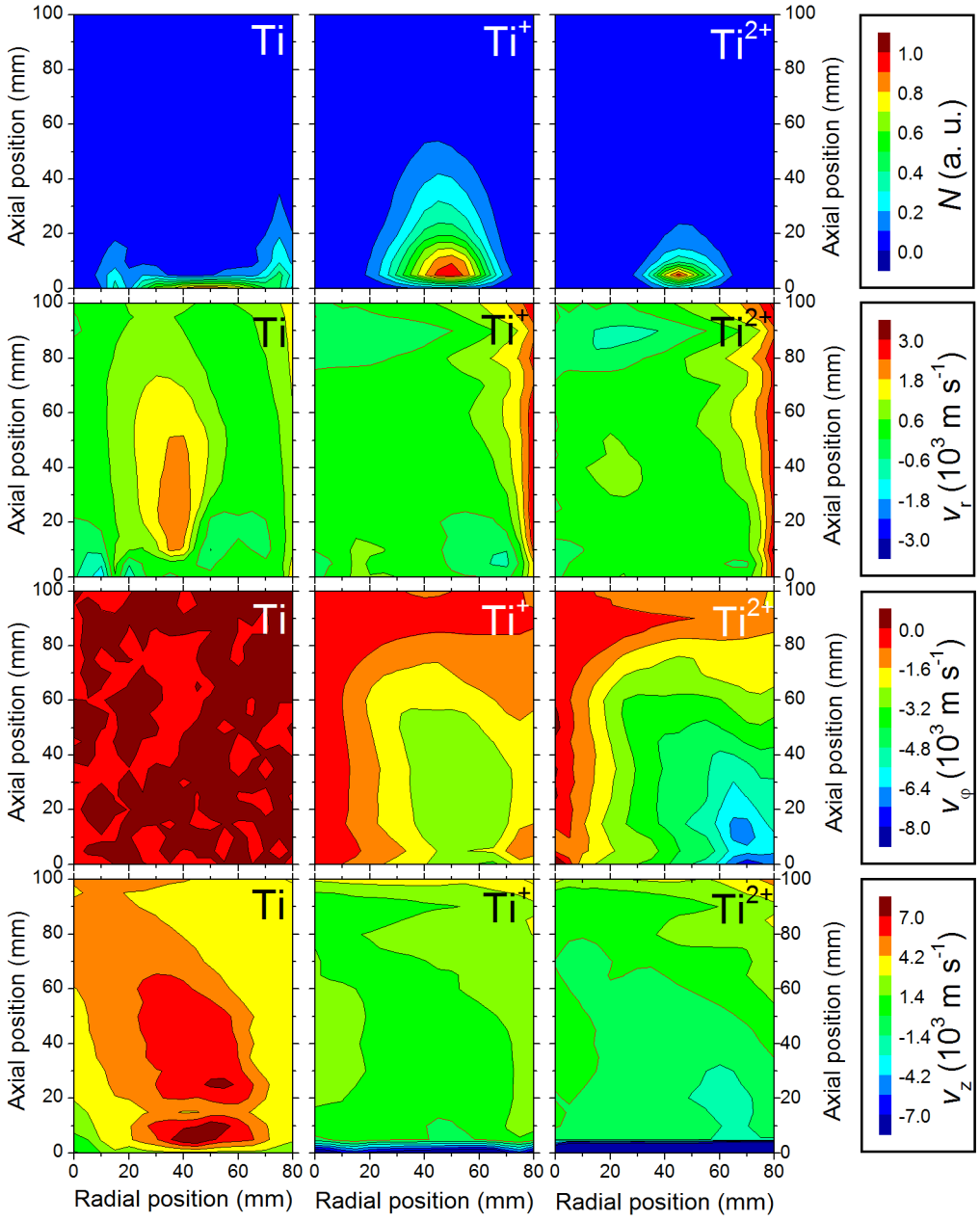

Figure 5.33: Relative particle distribution and velocity distribution calculated for a grounded substrate ($\lambda = 35$ mm, $\omega\tau = 2$).

ing ions travelling towards the substrate with an average speed of about $1 \times 10^3\,\mathrm{m\,s^{-1}}$ to $1.5 \times 10^3\,\mathrm{m\,s^{-1}}$, similar to the values reported by Macak et. al. [78]. The strong axial electric field in the sheath adjacent to the target accelerates the ions towards the cathode. This manifests itself in large negative ion velocities of several $10^4\,\mathrm{m\,s^{-1}}$. The velocity of Ti^{2+} is mainly directed towards the target, even 60 mm above the target. This demonstrates once again, how efficient the plasma potential attracts these ions back to the cathode.

Due to the apparently low flux of particles to the substrate, it seems reasonable that the deposition on the substrate should also be investigated in the discharge off-time. For this purpose, the model was run as before but the plasma potential, the electric field, the ionisation and the instability force are set to zero after a set amount of time. The spatial distribution of particles for all species, Ti, Ti^+ and Ti^{2+}, is shown in figure 5.34 as well as the composition of species. One can see, that after switching off the discharge, an increased amount of particles arrives at the substrate, at the sidewall or is thermalised and subsequently transported to one of the walls. The fraction of particles arriving at the substrate increases by a factor of 4 from 4 % to 17 %, when the discharge is switched off after 1 µs. A similar increase from 10 % to 44 % is observed for the deposition to the sidewall. It is worth noting, that the composition of particles, the ionisation, is not greatly altered unless the discharge is switched off after less than 2 µs. This is due to the immediate ionisation of sputtered particles close to the target.

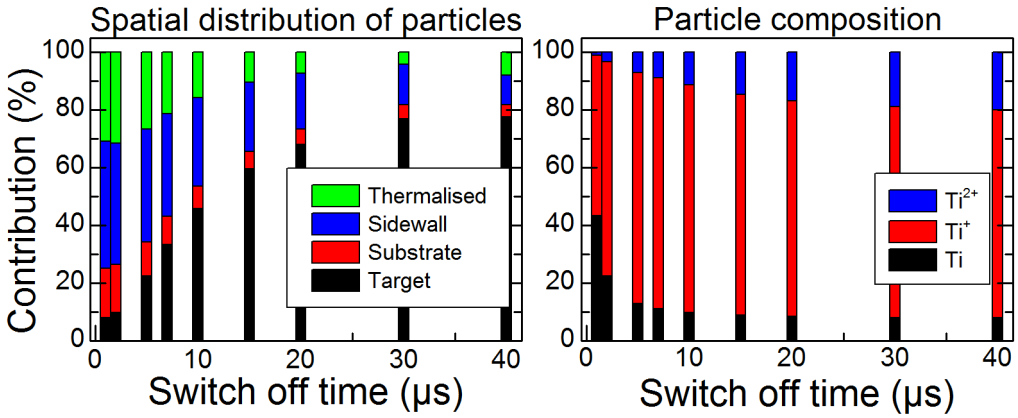

Figure 5.34: Particle distributions calculated for a grounded substrate for varying the switch off time ($\lambda = 35$ mm, $\omega\tau = 2$).

5.5 Chapter conclusions

Measurements carried out by means of emissive probe showed that the discharge ignition is accompanied by a deeply negative plasma potential and strong radial and axial electric fields caused by the acceleration of remnant particles away from the target where the magnetic field is orientated perpendicular to the target and a zone of confined electrons above the racetrack where the magnetic field runs parallel to the target. With progressing time the plasma potential becomes more positive but still reveals a distribution characteristic for magnetron discharges. The plasma potential is most negative above the racetrack in front of the target to enhance electron transport across magnetic field lines. Consistently lower potentials were measured when the substrate was insulated from ground compared to the substrate grounded. This is necessary, because the electron transport has to be enhanced further as the loss at the floating substrate is limited by the ion current.

A stable regime was found in the second half of the discharge pulse, for which the spatial distribution of the ion density and the electron temperature were recorded. An ion density peak was found closest to the target where the magnetic field is orientated parallel to the target. As the loss of electrons through a floating substrate is limited, an increased electron and ion density could be recorded in its vicinity compared to a grounded target. The electron temperature was found to be rather uniformly distributed due to frequent Coulomb collisions between the electrons and a strong depletion of their energy by ionisation and excitation collisions with the sputtered metal particles.

The combination of plasma potential, electron density and electron temperature measurements facilitated a transport model for sputtered titanium atoms, including ionisation, motion in the electric field and the force caused by the modified two-stream instability. Results show, that a high degree of ionisation of the sputtered flux is achieved, about 80 %. This causes most of the sputtered particles to return to the target, as the ionised particles are attracted back by the negative plasma potential in the expanded pre-sheath. It could be confirmed that the two-stream instability can lead to deflection of particles to the sidewalls. However, the extremely low deposition rate, only 4 % of the sputtered flux arrive at the substrate, needs further investigation. This was partly started by investigating the transport of particles after the discharge, electric field, ionisation and instability force, are switched off.

6 Summary

6.1 Conclusions

The aim of this thesis is to provide a better understanding of High Power Impulse Magnetron Sputtering (HiPIMS) discharges by applying spatially and temporally resolved diagnostics, such as optical 2d-imaging in combination with Abel-inversion, emissive and Langmuir probe measurements, as well as modelling the transport of sputtered particles based on the experimentally obtained plasma properties. The results of the individual diagnostic tools can be summarised:

- Optical 2d-imaging provided an overview over the entire discharge pulse including the development in the afterglow. It was found, that applying a high negative target potential during pulse initialisation leads to the acceleration of remnant electrons under the influence of the magnetic field. Electrons starting in a region where the magnetic field is orientated perpendicular to the target are efficiently lost, whereas electrons starting in the magnetic trap are confined by the magnetic field. A simple model for the motion of remnant electrons during sheath expansion revealed that the intensity maximum recorded remote from the target is caused by the acceleration of electrons up to an energy preferable for electron impact excitation but not for ionisation. The rise of the discharge current is accompanied by a turbulent transport of particles manifesting itself in an asymmetric emission profile and an intensity maximum travelling away from the target with the ion acoustic speed indicating the presence of an ion solitary wave. At high discharge currents, the density of the working gas is depleted which is seen in a lack of intensity of argon neutrals emission adjacent to the target. It could further be demonstrated that sputtered particles are efficiently ionised right above the racetrack, while the emission of both argon and metal ions is concentrated close to the target and shows an increased width of its radial emission profile indicating sputtering from a wider racetrack. This suggests better target utilisation. The transition from discharge on- to off-time is characterised by a fast drop of the plasma-induced emission which was found to be characterised by a two-fold

exponential decay. The first time constant calculated to be less than 1 µs indicates the efficient loss of electrons in the electron distribution function, whereas the second time constant is in the order of several microseconds and shows the decay of both the electron density and temperature. Spatially resolved investigation of the switching process revealed that electrons get lost most quickly close to the target and that their transport is impeded by the magnetic field in combination with the floating substrate leading to a much slower decay of the intensity in its vicinity. The plasma-induced emission in the late afterglow shows a ball- or cloud-like structure with no influence of the magnetic field observed. Electron-impact excitation is replaced by electron-electron-ion recombination as dominant mechanism to populate excited states. Ultralong decay time constants for the intensity in the order of 1 ms were found and could be explained by ambipolar diffusion of electrons and ions radially across the magnetic field.

- An emissive probe was used to study the spatial and temporal evolution of the plasma potential. It was found, that the temporal resolution of the floating probe is determined by the impedance of the surrounding sheath and the capacitance of the measuring circuit to ground. The latter one was optimised by using a battery to heat the probe and reduce the length of the cable to a minimum. The so improved setup occur

- Time-resolved Langmuir probe measurements in the plasma bulk showed that the ignition process of the discharge is accompanied by high electron temperatures and floating potentials. All plasma parameters stabilise during the second half of the discharge pulse. The measured electron density at this time is about 10^{18} m^{-3} and the electron temperature is 2.5 eV. While the electron temperature is the same for all substrate configurations, the electron density was found found to be 50 % higher when the substrate is floating compared to a grounded substrate. The development in the afterglow revealed significant differences in the ultralong decay time. While the time constant is about 3 ms if no substrate is used it reduces to about 1 ms with a substrate in place leading to a significantly lower density of remnant electron density and a longer delay of the discharge current onset. Spatially resolved measurements of the ion density and electron temperature showed a density maximum is the magnetically confined region up to 10^{19} m^{-3}, which reduces both radially and towards the target. It was found that a floating substrate confines electrons in the discharge volume better than a grounded substrate. This leads to the observed increased electron density in the vicinity of the floating substrate. The electron temperature was

found to be almost uniformly distributed throughout the discharge with values ranging from 1 eV to 3 eV. A slight dip in the temperature above the racetrack was observed which is probably caused by efficient cooling of the electrons by inelastic collisions with sputtered metal particles.

- The measured plasma potential, ion density and electron temperature were used in a quasi-stationary model analysing the transport of sputtered particles by following the trajectories through the discharge. It was found that the ionisation process is very efficient leading to a degree of ionisation of the sputtered flux of about 80 % with most ionisation events taking place in the dense plasma zone adjacent to the target. The majority of ionised particles is attracted back to the target while only 4 % of the sputtered particles arrive at the substrate. This fraction can be increased to 6 % by using a floating substrate for which more ionisation events occur in the discharge volume due to the increased electron density in the plasma bulk. It is suggested, that a significant fraction of the deposition might be due to condensation of thermalised metal vapour during the off-time of the discharge. The force caused by the modified two-stream instability was extended by a term directed perpendicular to both the azimuthal direction and the magnetic field. It could be demonstrated, that this force leads to a significant deflection of particles sideways out of the discharge volume and a resulting energy distribution function with a maximum at 15 eV above the target and only 5 eV further away from it. However, no significant influence on the ion energy distribution at the substrate could be seen. This suggests that the high energetic tail mainly originates from the sputtering distribution with particles at the low energetic end being ionised and attracted back to the target. The spatial distribution of particles indicates ionisation of the sputtered flux immediately above the target and azimuthal velocities of the ions of $3 \times 10^3\,\mathrm{m\,s^{-1}}$ for Ti^+ and $7 \times 10^3\,\mathrm{m\,s^{-1}}$ due to the azimuthal component of the instability force.

6.2 Suggestions for future work

More intensive studies on optical 2d-imaging also including Abel-inversion have recently been published concentrating on further target materials [133] and on the asymmetric behaviour recorded during the stage of rising discharge current [31–33]. It was found that this phenomenon is present throughout the entire discharge pulse and greatly alters the particle transport in HiPIMS discharges. Further investigations might concentrate on the

discharge ignition by using a model also including a solver for the Poisson equation to completely clarify why the initial intensity maximum occurs detached from the target. An absolutely calibrated system might also give a hint on the absolute particle density distribution of argon and metal atoms and ions, leading to more quantitative information than the one discussed in the present study.

Future work should also concentrate on refining the particle transport model to improve the results obtained. Particular emphasis should be put on the particle collisions by supplying additional data on the particle density of argon and metal atoms. This would help to better evaluate the influence of charge exchange collisions, which is widely neglected in the present version of the model. This process has a rather large cross-section which means that the titanium ion does not change its direction during this "collision" but only strips off an electron from a nearby titanium atom. This would leave a rather fast titanium atom and a thermalised titanium ion behind. The influence of this effect is not yet understood. A second point is that the particle whose trajectory is followed loses kinetic energy during a collision. At the same time, another particle must gain this energy. As this other particle could also be a sputtered titanium atom or ion, the presence of such a collective stream of titanium particles might enhance the transport towards the substrate.

The force caused by the modified two-stream instability was introduced ad-hoc as a force acting on all particles. References [31], [32] and [33], however, point out that this continuous picture of HiPIMS discharges might probably not be true, but that the plasma is concentrated in ionisation zones moving above the racetrack disturbing the average plasma properties, such as the plasma potential, the electron density and temperature, locally. This might enhance the transport of sputtered and ionised particles towards the substrate. In order to investigate this process numerically the plasma needs to be treated in a self-consistent manner. It might be possible that the averaged plasma parameters can still be used and only the deviation of the particle density from the average state and the electric fields associated with it needs to be calculated. This would save a large amount of computational time compared to the more sophisticated solution of modelling the entire discharge in a fully self-consistent way. Finally, the current transport model is more a case study as it is tailored for sputtering a titanium target under the conditions obtained experimentally. An extension to other target materials would be desirable, preferably without the time-consuming process of measuring all plasma parameters by hand. This last step would require adequate scaling laws including the magnetic field, the target material, the pressure and working gas, as well as the waveform of the power supply.

Bibliography

[1] D Lundin, U Helmersson, S Kirkpatrick, S Rohde, and N Brenning. Anomalous electron transport in high power impulse magnetron sputtering. *Plasma Sources Science and Technology*, 17(2):025007+, May 2008.

[2] W. R. Grove. On the Electro-Chemical Polarity of Gases. *Philosophical Transactions of the Royal Society of London*, 142:87–101, January 1852.

[3] T. A. Edison. Process of coating phonograph-records. U.S. Patent #713,863, 1902.

[4] R. F. Bunshah. *Handbook of Deposition Technologies for Films and Coatings*. Noyes Publications, New Jersey, 1994.

[5] S. M. Rossnagel, J. J. Cuomo, and W. D. Westwood. *Handbook of Plasma Processing Technology: Fundamentals, Etching, Deposition and Surface Interaction*. Noyes Publications, New Jersey, 1990.

[6] F. M. Penning. Die glimmentladung bei niedrigem druck zwischen koaxialen zylindern in einem axialen magnetfeld. *Physica*, 3(9):873–894, November 1936.

[7] J. F. Corbani. Cathode sputtering apparatus. U.S. Patent #3,878,085, 1975.

[8] J. S. Chapin. Sputtering process and apparatus. U.S. Patent #4,166,018, 1979.

[9] N. Savvides and B. Window. Unbalanced magnetron ion-assisted deposition and property modification of thin films. *Journal of Vacuum Science & Technology A: Vacuum, Surfaces, and Films*, 4(3):504+, May 1986.

[10] G. Este and W. D. Westwood. A quasi-direct-current sputtering technique for the deposition of dielectrics at enhanced rates. *Journal of Vacuum Science & Technology A: Vacuum, Surfaces, and Films*, 6(3):1845+, May 1988.

[11] M. Scherer, J. Schmitt, R. Latz, and M. Schanz. Reactive alternating current magnetron sputtering of dielectric layers. *Journal of Vacuum Science & Technology A: Vacuum, Surfaces, and Films*, 10(4):1772+, July 1992.

[12] D. A. Glocker. Influence of the plasma on substrate heating during low-frequency reactive sputtering of AIN. *Journal of Vacuum Science & Technology A: Vacuum, Surfaces, and Films*, 11(6):2989+, November 1993.

[13] S. Schiller, K. Goedicke, J. Reschke, V. Kirchhoff, S. Schneider, and F. Milde. Pulsed magnetron sputter technology. *Surface and Coatings Technology*, 61(1-3):331–337, December 1993.

[14] M. Konuma. *Plasma Techniques for Film Deposition*. Alpha Science International, Oxford, 2005.

[15] B. Schultrich. Beschichtungsverfahren: 9 Vakuumbogen 1. *Vakuum in Forschung und Praxis*, 19(3):38–39, 2007.

[16] V. Kouznetsov, K. Macák, J. M. Schneider, U. Helmersson, and I. Petrov. A novel pulsed magnetron sputter technique utilizing very high target power densities. *Surface and Coatings Technology*, 122(2-3):290–293, December 1999.

[17] A. P. Ehiasarian, W. D. Münz, L. Hultman, U. Helmersson, and I. Petrov. High power pulsed magnetron sputtered CrNx films. *Surface and Coatings Technology*, 163-164:267–272, January 2003.

[18] A. P. Ehiasarian, J. G. Wen, and I. Petrov. Interface microstructure engineering by high power impulse magnetron sputtering for the enhancement of adhesion. *Journal of Applied Physics*, 101:054301+, 2007.

[19] J. Paulitsch, P. H. Mayrhofer, C. Mitterer, W. D. Münz, and M. Schenkel. Mechanical and Tribological Properties of CrN Coatings Deposited by aSimultaneous HIPIMS/UBM Sputtering Process. *SVC - 50th Annual Technical Conference Proceedings*, 50:150–154, 2007.

[20] A. Ehiasarian. Comparison of microstructure and mechanical properties of chromium nitride-based coatings deposited by high power impulse magnetron sputtering and by the combined steered cathodic arc/unbalanced magnetron technique. *Thin Solid Films*, 457(2):270–277, June 2004.

[21] V. Sittinger, F. Ruske, W. Werner, C. Jacobs, B. Szyszka, and D. Christie. High power pulsed magnetron sputtering of transparent conducting oxides. *Thin Solid Films*, 516(17):5847–5859, July 2008.

[22] M. Samuelsson, D. Lundin, J. Jensen, M. A. Raadu, J. T. Gudmundsson, and U. Helmersson. On the film density using high power impulse magnetron sputtering. *Surface and Coatings Technology*, 205(2):591–596, October 2010.

[23] S. Kadlec. Simulation of Neutral Particle Flow During High Power Magnetron Impulse. *Plasma Processes and Polymers*, 4(S1):S419–S423, April 2007.

[24] J. Andersson and A. Anders. Gasless sputtering: Opportunities for ultra-clean metallization, coatings in space, and propulsion. *Applied Physics Letters*, 92(22):221503+, 2008.

[25] J. Andersson and A. Anders. Self-Sputtering Far above the Runaway Threshold: An Extraordinary Metal-Ion Generator. *Physical Review Letters*, 102(4):045003+, January 2009.

[26] A. Anders, J. Andersson, and A. P. Ehiasarian. High power impulse magnetron sputtering: Current-voltage-time characteristics indicate the onset of sustained self-sputtering. *Journal of Applied Physics*, 102(11), 2007.

[27] J. Bohlmark, U. Helmersson, M. VanZeeland, I. Axnas, J. Alami, and N. Brenning. Measurement of the magnetic field change in a pulsed high current magnetron discharge. *Plasma Sources Science and Technology*, 13(4):654–661, 2004.

[28] N. Brenning, R. L. Merlino, D. Lundin, M. A. Raadu, and U. Helmersson. Faster-than-Bohm Cross-B Electron Transport in Strongly Pulsed Plasmas. *Physical Review Letters*, 103(22):225003+, November 2009.

[29] D. Lundin, P. Larsson, E. Wallin, M. Lattemann, N. Brenning, and U. Helmersson. Cross-field ion transport during high power impulse magnetron sputtering. *Plasma Sources Science and Technology*, 17(3):035021+, August 2008.

[30] P. Poolcharuansin, B. Liebig, and J. W. Bradley. More evidence for azimuthal ion spin in HiPIMS discharges. *Plasma Sources Science and Technology*, 21(1):015001+, December 2011.

[31] A. V. Kozyrev, N. S. Sochugov, K. V. Oskomov, A. N. Zakharov, and A. N. Odivanova. Optical studies of plasma inhomogeneities in a high-current pulsed magnetron discharge. *Plasma Physics Reports*, 37(7):621–627, July 2011.

[32] A. Anders, P. Ni, and A. Rauch. Drifting localization of ionization runaway: Unraveling the nature of anomalous transport in high power impulse magnetron sputtering. *Journal of Applied Physics*, 111(5):053304+, 2012.

[33] A. P. Ehiasarian, A. Hecimovic, T. de los Arcos, R. New, V. Schulz von der Gathen, M. Böke, and J. Winter. High power impulse magnetron sputtering discharges: Instabilities and plasma self-organization. *Applied Physics Letters*, 100(11):114101+, 2012.

[34] F. F. Chen. *Introduction into Plasma Physics and Controlled Fusion*. Springer Science + Business Media, New York, 2006.

[35] M. A. Lieberman and A. J. Lichtenberg. *Principles of Plasma Discharges and Materials Processing*. John Wiley & Sons, Hoboken, New Jersey, 2005.

[36] I. H. Hutchinson. *Principles of Plasma Diagnostics*. Cambridge University Press, Cambridge, 1987.

[37] D. Depla and S. Mahieu. *Reactive Sputter Deposition*. Springer Verlag, Heidelberg, 2008.

[38] R. A. Powell and S. M. Rossnagel. *Thin Films: PVD for Microelectronics: Sputter Deposition Applied to Semiconductor Manufacturing*. Academic Press, San Diego, 1999.

[39] F. F. Chen and J. P. Chang. *Lecture Notes on Principles of Plasma Processing*. Plenum/Kluwer Publishers, Los Angeles, 2002.

[40] C. K. Birdsall and A. B. Langdon. *Plasma Physics via Computer Simulation*. Institute of Physics Publishing, Bristol, 1991.

[41] B. N. Chapman. *Glow Discharge Processes*. John Wiley, New York, 1980.

[42] P. Chabert and N. Braithwaite. *Physics of Radio-Frequency Plasmas*. Cambridge University Press, Cambridge, 2011.

[43] K. U. Riemann. The Bohm criterion and sheath formation. *Journal of Physics D: Applied Physics*, 24(4):493+, April 1991.

[44] J. W. Bradley and H. Amemiya. Plasma-Sheath Boundary in Plasmas Containing Thermal and Beam Electrons. *Japanese Journal of Applied Physics*, 33(Part 1, No. 6A):3578–3585, June 1994.

[45] E. Bultinck and A. Bogaerts. The effect of the magnetic field strength on the sheath region of a dc magnetron discharge. *Journal of Physics D: Applied Physics*, 41(20):202007+, October 2008.

[46] R. N. Franklin. The plasma-sheath boundary region. *Journal of Physics D: Applied Physics*, 36(22):R309, October 2003.

[47] J. L. Vossen and W. Kern. *Thin Film Processes II*. Academic Press, San Diego, 1991.

[48] R. Behrisch and W. Eckstein. *Sputtering by Particle Bombardement: Experiments and Computer Calculations from Threshold to MeV Energies*. Springer Verlag, Heidelberg, 2007.

[49] M. W. Thompson. II. The energy spectrum of ejected atoms during the high energy sputtering of gold. *Philosophical Magazine*, 18(152):377–414, August 1968.

[50] V. V. Serikov and K. Nanbu. Monte Carlo numerical analysis of target erosion and film growth in a three-dimensional sputtering chamber. *Journal of Vacuum Science & Technology A: Vacuum, Surfaces, and Films*, 14(6):3108+, November 1996.

[51] Y. Matsuda, Y. Yamamura, Y. Ueda, K. Uchino, K. Muraoka, M. Maeda, and M. Akazaki. Energy Dependence of Angular Distributions of Sputtered Particles by Ion-Beam Bombardment at Normal Incidence. *Japanese Journal of Applied Physics*, 25(Part 1, No. 1):8–11, January 1986.

[52] G. Bräuer, B. Szyszka, M. Vergöhl, and R. Bandorf. Magnetron sputtering - Milestones of 30 years. *Vacuum*, 84(12):1354–1359, June 2010.

[53] J. W. Bradley, S. Thompson, and Y. Aranda Gonzalvo. Measurement of the plasma potential in a magnetron discharge and the prediction of the electron drift speeds. *Plasma Sources Science and Technology*, 10(3):490–501, August 2001.

[54] Y. Aranda-Gonzalvo. *Hollow Cathode Magnetrons for Deposition Systems*. PhD dissertation, University of Manchester Institute of Science and Technology, 2003.

[55] A. E. Wendt, M. A. Lieberman, and H. Meuth. Radial current distribution at a planar magnetron cathode. *Journal of Vacuum Science & Technology A: Vacuum, Surfaces, and Films*, 6(3):1827+, May 1988.

[56] R. Kukla, T. Krug, R. Ludwig, and K. Wilmes. A highest rate self-sputtering magnetron source. *Vacuum*, 41(7-9):1968–1970, January 1990.

[57] W. De Bosscher and H. Lievens. Advances in magnetron sputter sources. *Thin Solid Films*, 351(1-2):15–20, August 1999.

[58] M. Wright and T. Beardow. Design advances and applications of the rotatable cylindrical magnetron. *Journal of Vacuum Science & Technology A: Vacuum, Surfaces, and Films*, 4(3):388+, May 1986.

[59] J. A. Thornton. High Rate Thick Film Growth. *Annual Review of Materials Science*, 7(1):239–260, 1977.

[60] R. Messier, A. P. Giri, and R. A. Roy. Revised structure zone model for thin film physical structure. *Journal of Vacuum Science & Technology A: Vacuum, Surfaces, and Films*, 2(2):500+, 1984.

[61] P. B. Barna and M. Adamik. Fundamental structure forming phenomena of polycrystalline films and the structure zone models. *Thin Solid Films*, 317(1-2):27–33, April 1998.

[62] A. Anders. A structure zone diagram including plasma-based deposition and ion etching. *Thin Solid Films*, 518(15):4087–4090, May 2010.

[63] H. Fujita, S. Yagura, H. Ueno, and M. Nagano. Plasma production with DC discharge planar magnetron device for thin film preparation. *Journal of Physics D: Applied Physics*, 19(9):1699+, November 2000.

[64] B. Window and J. Savvides. Unbalanced dc magnetrons as sources of high ion fluxes. *Journal of Vacuum Science & Technology A: Vacuum, Surfaces, and Films*, 4(3):453+, May 1986.

[65] S. Berg, H. O. Blom, M. Moradi, C. Nender, and T. Larsson. Process modeling of reactive sputtering. *Journal of Vacuum Science & Technology A: Vacuum, Surfaces, and Films*, 7(3):1225+, May 1989.

[66] S. M. Rossnagel and J. Hopwood. Metal ion deposition from ionized mangetron sputtering discharge. *Journal of Vacuum Science & Technology B: Microelectronics and Nanometer Structures*, 12(1):449+, January 1994.

[67] U. Helmersson, M. Lattemann, J. Bohlmark, A. P. Ehiasarian, and J. T. Gudmundsson. Ionized physical vapor deposition (IPVD): A review of technology and applications. *Thin Solid Films*, 513(1-2):1–24, August 2006.

[68] J. Alami, S. Bolz, and K. Sarakinos. High power pulsed magnetron sputtering: Fundamentals and applications. *Journal of Alloys and Compounds*, 483(1-2):530–534, August 2009.

[69] K. Sarakinos, J. Alami, and S. Konstantinidis. High power pulsed magnetron sputtering: A review on scientific and engineering state of the art. *Surface and Coatings Technology*, 204(11):1661–1684, February 2010.

[70] A. Anders. Discharge physics of high power impulse magnetron sputtering. *Surface and Coatings Technology*, March 2011.

[71] D. Lundin and K. Sarakinos. An introduction to thin film processing using high-power impulse magnetron sputtering. *Journal of Materials Research*, 27(05):780–792, 2012.

[72] J. T. Gudmundsson, N. Brenning, D. Lundin, and U. Helmersson. High power impulse magnetron sputtering discharge. *Journal of Vacuum Science & Technology A: Vacuum, Surfaces, and Films*, 30(3):030801+, 2012.

[73] J. W. Bradley and T. Welzel. Physics and phenomena in pulsed magnetrons: an overview. *Journal of Physics D: Applied Physics*, 42(9):093001+, April 2009.

[74] J. Lin, J. J. Moore, W. D. Sproul, B. Mishra, and Z. Wu. Modulated pulse power sputtered chromium coatings. *Thin Solid Films*, 518(5):1566–1570, December 2009.

[75] J. Lin, W. Sproul, J. Moore, Z. Wu, S. Lee, R. Chistyakov, and B. Abraham. Recent advances in modulated pulsed power magnetron sputtering for surface engineering. *JOM Journal of the Minerals, Metals and Materials Society*, 63(6):48–58, June 2011.

[76] J. Bohlmark, J. T. Gudmundsson, J. Alami, M. Latteman, and U. Helmersson. Spatial electron density distribution in a high-power pulsed magnetron discharge. *IEEE Transactions on Plasma Science*, 33(2):346–347, April 2005.

[77] B. M. Dekoven, P. R. Ward, R. E. Weiss, D. J. Christie, R. A. Scholl, W. D. Sproul, F. Tomasel, and A. Anders. Carbon Thin Film Deposition Using High Power Pulsed Magnetron Sputtering. 2003.

[78] K. Macák, V. Kouznetsov, J. Schneider, U. Helmersson, and I. Petrov. Ionized sputter deposition using an extremely high plasma density pulsed magnetron discharge. volume 18, pages 1533–1537. AVS, 2000.

[79] J. Vlcek, A. D. Pajdarova, P. Belsky, J. Lukas, P. Kudlacek, and J. Musil. Characterization of High-power Pulsed dc Magnetron Discharges for Ionized High-rate Sputtering of Copper Films. *Society of Vacuum Coaters 48th Annual Technical Conference Proceedings*, 48:465–469, 2005.

[80] J. Bohlmark, J. Alami, C. Christou, A. P. Ehiasarian, and U. Helmersson. Ionization of sputtered metals in high power pulsed magnetron sputtering. *Journal of Vacuum Science & Technology A: Vacuum, Surfaces, and Films*, 23(1):18–22, 2005.

[81] J. Bohlmark, M. Lattemann, J. T. Gudmundsson, A. P. Ehiasarian, Y. Aranda Gonzalvo, N. Brenning, and U. Helmersson. The ion energy distributions and ion flux composition from a high power impulse magnetron sputtering discharge. *Thin Solid Films*, 515(4):1522–1526, December 2006.

[82] A. P. Ehiasarian, Y. A. Gonzalvo, and T. Whitmore. Time-Resolved Ionisation Studies of the High Power Impulse Magnetron Discharge in Mixed Argon and Nitrogen Atmosphere. *Plasma Processes and Polymers*, 4(S1):S309–S313, April 2007.

[83] A. Hecimovic and A. P. Ehiasarian. Time evolution of ion energies in HIPIMS of chromium plasma discharge. *Journal of Physics D: Applied Physics*, 42(13):135209+, July 2009.

[84] J. Andersson, A. P. Ehiasarian, and A. Anders. Observation of Ti[sup 4+] ions in a high power impulse magnetron sputtering plasma. *Applied Physics Letters*, 93(7):071504+, 2008.

[85] P. Poolcharuansin, B. Liebig, and J. W. Bradley. Plasma Parameters in a Pre-Ionized HiPIMS Discharge Operating at Low Pressure. *IEEE Transactions on Plasma Science*, 38(11):3007–3015, November 2010.

[86] S. M. Rossnagel and J. J. Cuomo. Ion beam bombardment effects during films deposition. *Vacuum*, 38(2):73–81, January 1988.

[87] J. S. Colligon. Energetic condensation: Processes, properties, and products. *Journal of Vacuum Science & Technology A: Vacuum, Surfaces, and Films*, 13(3):1649+, May 1995.

[88] G. Y. Yushkov and A. Anders. Origin of the Delayed Current Onset in High-Power Impulse Magnetron Sputtering. *IEEE Transactions on Plasma Science*, 38(11):3028–3034, November 2010.

[89] A. Mishra, P. J. Kelly, and J. W. Bradley. The evolution of the plasma potential in a HiPIMS discharge and its relationship to deposition rate. *Plasma Sources Science and Technology*, 19(4):045014+, August 2010.

[90] A. D. Pajdarova, J. Vlcek, P. Kudlacek, and J. Lukas. Electron energy distributions and plasma parameters in high-power pulsed magnetron sputtering discharges. *Plasma Sources Science and Technology*, 18(2):025008+, 2009.

[91] P. Poolcharuansin and J. W. Bradley. Short- and long-term plasma phenomena in a HiPIMS discharge. *Plasma Sources Science and Technology*, 19(2):025010+, April 2010.

[92] C. G. Goedde, A. J. Lichtenberg, and M. A. Lieberman. Self-consistent stochastic electron heating in radio frequency discharges. *Journal of Applied Physics*, 64(9):4375–4383, 1988.

[93] K. B. Gylfason, J. Alami, U. Helmersson, and J. T. Gudmundsson. Ion-acoustic solitary waves in a high power pulsed magnetron sputtering discharge. *Journal of Physics D: Applied Physics*, 38(18):3417–3421, September 2005.

[94] J. Alami, J. T. Gudmundsson, J. Bohlmark, J. Birch, and U. Helmersson. Plasma dynamics in a highly ionized pulsed magnetron discharge. *Plasma Sources Science and Technology*, 14(3):525–531, August 2005.

[95] M. Hala, N. Viau, O. Zabeida, J. E. Klemberg-Sapieha, and L. Martinu. Dynamics of reactive high-power impulse magnetron sputtering discharge studied by time- and space-resolved optical emission spectroscopy and fast imaging. *Journal of Applied Physics*, 107(4):043305+, 2010.

[96] D. W. Hoffman. A sputtering wind. *Journal of Vacuum Science & Technology A: Vacuum, Surfaces, and Films*, 3(3):561–566, 1985.

[97] S. M. Rossnagel. Gas density reduction effects in magnetrons. *Journal of Vacuum Science & Technology A: Vacuum, Surfaces, and Films*, 6(1):19–24, 1988.

[98] A. Ehiasarian, R. New, W. D. Münz, L. Hultman, U. Helmersson, and V. Kouznetsov. Influence of high power densities on the composition of pulsed magnetron plasmas. *Vacuum*, 65(2):147–154, April 2002.

[99] J. Vlcek, A. D. Pajdarová, and J. Musil. Pulsed dc Magnetron Discharges and their Utilization in Plasma Surface Engineering. *Contributions to Plasma Physics*, 44(5-6):426–436, 2004.

[100] C. Vitelaru, D. Lundin, G. D. Stancu, N. Brenning, J. Bretagne, and T. Minea. Argon metastables in HiPIMS: time-resolved tunable diode-laser diagnostics. *Plasma Sources Science and Technology*, 21(2):025010+, March 2012.

[101] A. Anders. Self-sputtering runaway in high power impulse magnetron sputtering: The role of secondary electrons and multiply charged metal ions. *Applied Physics Letters*, 92(20):201501+, 2008.

[102] D. Lundin, N. Brenning, D. Jädernäs, P. Larsson, Erik Wallin, M. Lattemann, M. A. Raadu, and U. Helmersson. Transition between the discharge regimes of high power impulse magnetron sputtering and conventional direct current magnetron sputtering. *Plasma Sources Science and Technology*, 18(4):045008+, November 2009.

[103] W. M. Posadowski and Z. J. Radzimski. Sustained self-sputtering using a direct current magnetron source. *Journal of Vacuum Science & Technology A: Vacuum, Surfaces, and Films*, 11(6):2980–2984, 1993.

[104] A. Hecimovic and A. P. Ehiasarian. Temporal Evolution of the Ion Fluxes for Various Elements in HIPIMS Plasma Discharge. *Plasma Science, IEEE Transactions on*, 39(4):1154–1164, April 2011.

[105] A. Anders and G. Y. Yushkov. Plasma "anti-assistance" and "self-assistance" to high power impulse magnetron sputtering. *Journal of Applied Physics*, 105(7):073301+, 2009.

[106] L. de Poucques, J. C. Imbert, C. Boisse-Laporte, J. Bretagne, M. Ganciu, L. Teulé-Gay, and M. Touzeau. Study of the transport of titanium neutrals and ions in the post-discharge of a high power pulsed magnetron sputtering device. *Plasma Sources Science and Technology*, 15(4):661–669, November 2006.

[107] K. Bobzin, N. Bagcivan, P. Immich, S. Bolz, R. Cremer, and T. Leyendecker. Mechanical properties and oxidation behaviour of (Al,Cr)N and (Al,Cr,Si)N coatings for cutting tools deposited by HPPMS. *Thin Solid Films*, 517(3):1251–1256, December 2008.

[108] K. Sarakinos, J. Alami, and M. Wuttig. Process characteristics and film properties upon growth of TiOx films by high power pulsed magnetron sputtering. *Journal of Physics D: Applied Physics*, 40(7):2108–2114, April 2007.

[109] G. West, P. Kelly, P. Barker, A. Mishra, and J. Bradley. Measurements of Deposition Rate and Substrate Heating in a HiPIMS Discharge. *Plasma Processes and Polymers*, 6(S1):S543–S547, June 2009.

[110] K. Sarakinos, J. Alami, C. Klever, and M. Wuttig. Process stabilization and enhancement of deposition rate during reactive high power pulsed magnetron sputtering of zirconium oxide. *Surface and Coatings Technology*, 202(20):5033–5035, July 2008.

[111] J. Emmerlich, S. Mraz, R. Snyders, K. Jiang, and J. Schneider. The physical reason for the apparently low deposition rate during high-power pulsed magnetron sputtering. *Vacuum*, 82(8):867–870, April 2008.

[112] J. Alami, K. Sarakinos, G. Mark, and M. Wuttig. On the deposition rate in a high power pulsed magnetron sputtering discharge. *Applied Physics Letters*, 89(15):154104+, 2006.

[113] A. Anders. Deposition rates of high power impulse magnetron sputtering: Physics and economics. *Journal of Vacuum Science & Technology A: Vacuum, Surfaces, and Films*, 28(4):783+, 2010.

[114] N. Hosokawa, T. Tsukada, and H. Kitahara. Untitled. *Proceedings of the Eighth International Vacuum Congress*, pages 11–14, 1980.

[115] S. Konstantinidis, J. P. Dauchot, M. Ganciu, A. Ricard, and M. Hecq. Influence of pulse duration on the plasma characteristics in high-power pulsed magnetron discharges. *Journal of Applied Physics*, 99(1):013307+, 2006.

[116] S. Konstantinidis, J. P. Dauchot, M. Ganciu, and M. Hecq. Transport of ionized metal atoms in high-power pulsed magnetron discharges assisted by inductively coupled plasma. *Applied Physics Letters*, 88(2):021501+, 2006.

[117] J. Bohlmark, M. Östbye, M. Lattemann, H. Ljungcrantz, T. Rosell, and U. Helmersson. Guiding the deposition flux in an ionized magnetron discharge. *Thin Solid Films*, 515(4):1928–1931, December 2006.

[118] D. J. Christie. Target material pathways model for high power pulsed magnetron sputtering. *Journal of Vacuum Science & Technology A: Vacuum, Surfaces, and Films*, 23(2):330+, 2005.

[119] J. Vlček and K. Burcalová. A phenomenological equilibrium model applicable to high-power pulsed magnetron sputtering. *Plasma Sources Science and Technology*, 19(6):065010+, November 2010.

[120] MKS Instruments Inc., Andover, USA. *MKS Type 1179A and 2179A Mass-Flo® Controller and Type 179A Mass-Flo Meter*, 1998.

[121] MKS Instruments Inc., Andover, USA. *MKS Baratron® Type 627B Absolute Pressure Transducer*, 1998.

[122] Tektronix Inc., Wilsonville, USA. *User manual Tektronix TDS3000 series Digital Phosphor Oscilloscope*.

[123] Tektronix Inc., Beaverton, USA. *Instruction manual Tektronix TCP202 15 Ampere AC/DC Current Probe*.

[124] Tektronix Inc., Beaverton, USA. *Instruction manual Tektronix CT4 high current transformer*.

[125] Tektronix Inc., Beaverton, USA. *Instruction manual Tektronix P5100 high voltage probe*.

[126] Stanford Research Systems, Sunnyvale, USA. *User manual DG645 Digital Delay Generator*, 2008.

[127] Hirst Magnetic Instruments Ltd., Falmouth, UK. *GM04 & GM05 Gaussmeters*.

[128] S. Powell. Finite element modelling of magnetostatics for magnetron sputter sources. *CAD for Electromagnetic devices*, 2006.

[129] J^2Technology Consulting, Linköping, Sweden. *Sinex 3.0, Pulsed power supply for HIPIMS applications, Technical Manual*, 2007.

[130] B. Liebig. *Power supply for High Power Impulse Magnetron Sputtering (HIPIMS)*. University of Liverpool, Liverpool, UK, 2011.

[131] J. W. Bradley, G. C. B. Clarke, Braithwaite, P. M. Bryant, and P. J. Kelly. Time resolved 2-D optical imaging of a pulsed unbalanced magnetron plasma. *Plasma Sources Science and Technology*, 15(2):S44–S50, 2006.

[132] B. Liebig, Braithwaite, P. J. Kelly, and J. W. Bradley. Spatial and temporal investigation of high power pulsed magnetron discharges by optical 2D-imaging. *Thin Solid Films*, 519(5):1699–1704, December 2010.

[133] A. Hecimovic, T. de los Arcos, V. Schulz-von der Gathen, M. Böke, and J. Winter. Temporal evolution of the radial plasma emissivity profile in HIPIMS plasma discharges. *Plasma Sources Science and Technology*, 21(3):035017+, May 2012.

[134] U. Fantz. Basics of plasma spectroscopy. *Plasma Sources Science and Technology*, 15(4):S137+, November 2006.

[135] R. H. Huddlestone and S. L. Leonard. *Plasma Diagnostic Techniques*. Academic Press, New York, 1965.

[136] J. W. Coburn and M. Chen. Optical emission spectroscopy of reactive plasmas: A method for correlating emission intensities to reactive particle density. *Journal of Applied Physics*, 51(6):3134–3136, 1980.

[137] B. J. Curtis and Brunner. End Point Determination of Aluminum CCl[sub 4] Plasma Etching by Optical Emission Spectroscopy. *Journal of The Electrochemical Society*, 125(5):829–830, 1978.

[138] J. Strümpfel. *Prozeßstabilisierung beim reaktiven Hochratezerstäuben mittels optischer Emissionsspektroskopie zur industriellen Herstellung von Indium-Zinn-Oxidschichten und Titandioxidschichten*. PhD dissertation, Technische Universität Chemnitz, 1990.

[139] U. Fantz, H. Falter, P. Franzen, D. Wünderlich, M. Berger, A. Lorenz, W. Kraus, P. McNeely, R. Riedl, and E. Speth. Spectroscopy - a powerful diagnostic tool in source development. *Nuclear Fusion*, 46(6):S297+, May 2006.

[140] H. M. Katsch, A. Tewes, E. Quandt, A. Goehlich, T. Kawetzki, and H. F. Döbele. Detection of atomic oxygen: Improvement of actinometry and comparison with laser spectroscopy. *Journal of Applied Physics*, 88(11):6232+, 2000.

[141] A. Ricard, J. Henriques, S. Cousty, S. Villeger, and J. Amorim. Determination of N-, H- and O-Atom Densities in N2-H2 and in N2-O2 Gas Mixtures by Optical Actinometry in Flowing Microwave Discharges and by NO Titration in Post-Discharges. *Plasma Processes and Polymers*, 4(S1):S965–S968, April 2007.

[142] N. K. Podder, J. A. Johnson, C. T. Raynor, S. D. Loch, C. P. Ballance, and M. S. Pindzola. Helium line intensity ratio in microwave-generated plasmas. *Physics of Plasmas*, 11(12):5436+, 2004.

[143] R. F. Boivin, S. D. Loch, C. P. Ballance, D. Branscomb, and M. S. Pindzola. Line ratio diagnostics in helium and helium seeded argon plasmas. *Plasma Sources Science and Technology*, 16(3):470–479, May 2007.

[144] R. Gorenflo and S. Vessella. *Abel Integral Equations. Analysis and Applications*, volume 1461 of *Lecture Notes in Mathematics*. Springer-Verlag, Berlin, 1991.

[145] S. Gueron and M. Deutsch. A fast Abel inversion algorithm. *Journal of Applied Physics*, 75(9):4313–4318, 1994.

[146] G. C. B. Clarke. *Diagnostic study of the pulsed magnetron*. PhD dissertation, Manchester Metropolitan University, 2007.

[147] Andor Technology, Belfast. *User's Guide to the Andor iStar*, 1999.

[148] Andor Technology Ltd., Belfast, UK. *ICCD Performance*, 1999.

[149] I. D. Swindell. *Plasma Diagnostics and Characterisation of Magnetron Sputtering Discharges*. PhD thesis, University of Liverpool, 2007.

[150] L.O.T. Oriel Ltd., Leatherhead, UK. *MS 260i Imaging 1/4m Spectrograph Models 74050 and 74055*, 1991.

[151] L.O.T. Oriel. *Calibration data optical filter 436FS05-50, serial no. Q191-02*, 2009.

[152] Melles Griot. *Calibration data optical filter 03FIV006 serial no. M168-10*.

[153] L.O.T. Oriel. *Calibration data optical filter 590FS10-50, serial no. Q191-01*, 2009.

[154] L.O.T. Oriel. *Calibration data optical filter 636FS10-50, serial no. Q191-02*, 2009.

[155] Melles Griot. *Calibration data optical filter 03FII002*, 2002.

[156] L.O.T. Oriel. *Calibration data optical filter 810FS10-50, serial no. M178-03*, 2005.

[157] L. D. Schearer and W. C. Holton. Magnetic Resonance of Some Optically Oriented Excited Ions of Zn and Cd. *Physical Review Letters*, 24:1214–1217, June 1970.

[158] E. B. Saloman. Energy Levels and Observed Spectral Lines of Ionized Argon, Ar-II through Ar-XVIII. *Journal of Physical and Chemical Reference Data*, 39(3):033101+, 2010.

[159] W. R. Bennett Jr., P. J. Kindlmann, and G. N. Mercer. Measurement of excited state relaxation rates. In J N Howard, editor, *Chemical Lasers: Applied Optics Supplement 2*. Opt. Soc. America, Easton, Pa., 1965.

[160] G. Norlén. Wavelengths and Energy Levels of Ar I and Ar II based on New Interferometric Measurements in the Region 3 400-9 800 Å. *Physica Scripta*, 8(6):249+, January 2007.

[161] B. Wende. Optische übergangswahrscheinlichkeiten der Konfigurationen 3p5 4s - 3p5 5p des Argon I. *Zeitschrift für Physik A Hadrons and Nuclei*, 213(4):341–351, August 1968.

[162] J. B. Shumaker and C. H. Popenoe. Experimental Transition Probabilities for the Ar I 4s-4p Array. *Journal of the Optical Society of America*, 57(1):8+, January 1967.

[163] P. Forsberg. The spectrum and term system of neutral titanium, Ti I. *Physica Scripta*, 44(5):446+, September 2006.

[164] D. E. Nitz, M. E. Wickliffe, and J. E. Lawler. Atomic Transition Probabilities in Ti I. *The Astrophysical Journal Supplement Series*, pages 313+, January 2009.

[165] D. E. Blackwell, S. L. R. Menon, A. D. Petford, and M. J. Shallis. Precision measurement of relative oscillator strengths for Ti I - II. Transitions from levels a 5F1-4 (0.81 - 0.84 eV), a 1D2 (0.90 eV) and a 3P0-2 (1.05 - 1.07 eV),. *Mon. Not. R. Astron. Soc.*, 201:611–617, 1982.

[166] D. E. Blackwell, A. J. Booth, S. L. R. Menon, and A. D. Petford. Measurement of relative oscillator strengths for Ti I-IV. Transitions from levels of excitation energy between 1.42 and 2.31 eV. *Mon. Not. R. Astron. Soc.*, 220:289–302, 1986.

[167] R. J. Blackwell-Whitehead, H. Lundberg, G. Nave, J. C. Pickering, H. R. A. Jones, Y. Lyubchik, Y. V. Pavlenko, and S. Viti. Experimental Tiï¿½i oscillator strengths and their application to cool star analysis. *Monthly Notices of the Royal Astronomical Society*, 373(4):1603–1609, December 2006.

[168] W. Whaling, J. M. Scalo, and L. Testerman. Transition probabilities in TI I and the solar titanium abundance. *The Astrophysical Journal*, 212:581+, March 1977.

[169] D. C. Morton. Atomic Data for Resonance Absorption Lines. III. Wavelengths Longward of the Lyman Limit for the Elements Hydrogen to Gallium. *The Astrophysical Journal Supplement Series*, 149(1):205–238, December 2008.

[170] R. I. Kostyk. Oscillator-strengths for lines of neutral titanium. *Astronomicheskiĭ zhurnal*, 59(4):693–698, 1982.

[171] I. Johansson and R. H. Contreras. New Measurements in the Arc Spectrum of Zinc. *Ark. Fys.*, 37:513–520, 1968.

[172] J. Sugar and A. Musgrove. Energy Levels of Zinc, Zn I through Zn XXX. *Journal of Physical and Chemical Reference Data*, 24(6):1803–1872, 1995.

[173] J. R. Fuhr and W. L. Wiese. Nist atomic transition probabilities. In D R Lide, editor, *CRC Handbook of Chemistry and Physics*. CRC Press, Boca Raton, FL, 86th edition, 2005.

[174] A. M. Crooker and K. A. Dick. Extensions to the spark spectra of zinc. I. Zinc II and zinc IV. *Canadian Journal of Physics*, 46(10):1241–1251, 1968.

[175] H. F. Winters and J. W. Coburn. Surface science aspects of etching reactions. *Surface Science Reports*, 14(4-6):162–269, January 1992.

[176] I. Velchev, W. Hogervorst, and W. Ubachs. Precision VUV spectroscopy of Ar I at 105 nm. *Journal of Physics B: Atomic, Molecular and Optical Physics*, 32(17):L511–L516, September 1999.

[177] L. Matsuoka and S. Hasegawa. Two-color resonance ionization spectroscopy of highly excited titanium atoms. *Journal of the Optical Society of America B*, 24(10):2562+, 2007.

[178] S. M. Rossnagel and K. L. Saenger. Optical emission in magnetrons: Nonlinear aspects. *Journal of Vacuum Science & Technology A: Vacuum, Surfaces, and Films*, 7(3):968–971, 1989.

[179] O. Tukhlibaev and U. Z. Alimov. Laser photoionization spectroscopy of the zinc atom and the study of zinc sulfide evaporation. *Optics and Spectroscopy*, 88(4):506–509, April 2000.

[180] J. Sugar and C. Corliss. Atomic Energy Levels of the Iron-Period Elements: Potassium through Nickel. *J. Phys. Chem. Ref. Data*, 14(Suppl. 2):1–664, 1985.

[181] T. Dunger, T. Welzel, S. Welzel, and F. Richter. Time-resolved investigation of an asymmetric bipolar pulsed magnetron discharge: Influence of pressure. *Surface and Coatings Technology*, 200(5-6):1676–1682, November 2005.

[182] J. B. Boffard, G. A. Piech, M. F. Gehrke, L. W. Anderson, and C. C. Lin. Measurement of electron-impact excitation cross sections out of metastable levels of argon and comparison with ground-state excitation. *Physical Review A*, 59(4):2749–2763, 1999.

[183] T. Welzel, T. Dunger, and F. Richter. Two-Dimensional Double Probe Study of the Temporal Evolution of the Charge Carrier Density in a Pulsed Magnetron. *Plasma Processes and Polymers*, 4(S1):S931–S936, April 2007.

[184] L. Gu and M. A. Lieberman. Axial distribution of optical emission in a planar magnetron discharge. *Journal of Vacuum Science & Technology A: Vacuum, Surfaces, and Films*, 6(5):2960+, September 1988.

[185] M. Hayashi. Bibliography of electron and photon cross sections with atoms and molecules published in the 20th century: Argon. National Institute for Fusion Science, 2003.

[186] G. Clarke, A. Mishra, P. J. Kelly, and J. W. Bradley. Cathode Current Density Distributions in High Power Impulse and Direct Current Magnetron Sputtering Modes. *Plasma Processes Polym.*, 6(S1):S548–S553, 2009.

[187] A. E. Wendt and M. A. Lieberman. Spatial structure of a planar magnetron discharge. *Journal of Vacuum Science & Technology A: Vacuum, Surfaces, and Films*, 8(2):902+, March 1990.

[188] J. Lopez, W. Zhu, A. Freilich, A. Belkind, and K. Becker. Time-resolved optical emission spectroscopy of pulsed DC magnetron sputtering plasmas. 38(11):1769–1780, 2005.

[189] F. Kannari, M. Obara, and T. Fujioka. An advanced kinetic model of electron-beam-excited KrF lasers including the vibrational relaxation in KrF*(B) and collisional mixing of KrF*(B,C). *Journal of Applied Physics*, 57(9):4309–4322, 1985.

[190] A. Vetushka, S. K. Karkari, and J. W. Bradley. Two-dimensional spatial survey of the plasma potential and electric field in a pulsed bipolar magnetron discharge. *Journal of Vacuum Science & Technology A: Vacuum, Surfaces, and Films*, 22(6):2459+, 2004.

[191] Th Welzel, Th Dunger, B. Liebig, and F. Richter. Spatial and temporal development of the plasma potential in differently configured pulsed magnetron discharges. *New Journal of Physics*, 10(12):123008+, December 2008.

[192] T. Welzel, K. Barucki, and K. Ellmer. Observation of the Magnetic Separatrix Between a Magnetron and an Electron-Cyclotron Resonance Discharge. *Plasma Science, IEEE Transactions on*, 39(11):2464–2465, November 2011.

[193] K. Kadota and Y. Kaneko. Secondary Electron Ejection from Contaminated Metal Surface by He and Ar Atoms. *Japanese Journal of Applied Physics*, 13(10):1554–1561, October 1974.

[194] A. Holys and J. R. Fuhr. Absolute transition-probabilities of neutral titanium lines. *Astron. Astrophys.*, 90:14–17, 1980.

[195] P. Palmeri, P. Quinet, E. Biemont, J. Gurell, P. Lundin, L. O. Norlin, P. Royen, K. Blagoev, and S. Mannervik. Lifetimes of metastable levels of singly ionized titanium: theory and experiment. *Journal of Physics B: Atomic, Molecular and Optical Physics*, 41(12):125703+, 2008.

[196] G. Wenig, M. Schulze, P. Awakowicz, and Keudell. Modelling of pulsed low-pressure plasmas and electron re-heating in the late afterglow. *Plasma Sources Science and Technology*, 15(2):S35–S43, 2006.

[197] C. A. DeJoseph, V. I. Demidov, J. Blessington, and M. E. Koepke. Investigation of a radio-frequency inductive- coupled-plasma discharge afterglow in noble gases. *Journal of Physics B: Atomic, Molecular and Optical Physics*, 40(19):3823–3833, 2007.

[198] D. Ohebsian, N. Sadeghi, C. Trassy, and J. Mermet. Kinetic reactions involving the titanium atoms in an argon-titanium hollow cathode afterglow. *Optics Communications*, 32(1):81–86, January 1980.

[199] N. Nafarizal, N. Takada, and K. Sasaki. Production of Ar metastable atoms in the late afterglow of pulse-modulated rf magnetron sputtering plasmas. *Journal of Physics D: Applied Physics*, 41(3):035206+, 2008.

[200] C. A. DeJoseph and V. I. Demidov. Spectroscopic study of a pulsed argon rf ICP discharge: stepwise excitation in the afterglow and its application in optical spectroscopy. *Journal of Physics B: Atomic, Molecular and Optical Physics*, 38(21):3805–3814, November 2005.

[201] A. Bogaerts, R. Gijbels, and G. P. Jackson. Modeling of a millisecond pulsed glow discharge: Investigation of the afterpeak. *J. Anal. At. Spectrom.*, 18(6):533–548, 2003.

[202] H. S. W. Massey, E. H. S. Burhop, and H. B. Gilbody. *Electronic and ionic impact phenomena*. Clarendon Press, Oxford, UK, second edition, 1969.

[203] Y. J. Shiu and M. A. Biondi. Dissociative recombination in argon: Dependence of the total rate coefficient and excited-state production on electron temperature. *Physical Review A*, 17(3):868–872, March 1978.

[204] A. Bogaerts. The afterglow mystery of pulsed glow discharges and the role of dissociative electron-ion recombination. *J. Anal. At. Spectrom.*, 22(5):502–512, 2007.

[205] B. M. Smirnov. Tables for Cross Sections of the Resonant Charge Exchange Process. *Physica Scripta*, pages 595+, May 2000.

[206] K. Sarakinos, J. Alami, J. Dukwen, J. Woerdenweber, and M. Wuttig. A semi-quantitative model for the deposition rate in non-reactive high power pulsed magnetron sputtering. *Journal of Physics D: Applied Physics*, 41(21):215301+, November 2008.

[207] N. Brenning, C. Huo, D. Lundin, M. A. Raadu, C. Vitelaru, G. D. Stancu, T. Minea, and U. Helmersson. Understanding deposition rate loss in high power impulse magnetron sputtering: I. Ionization-driven electric fields. *Plasma Sources Science and Technology*, 21(2):025005+, March 2012.

[208] D. Meschede. *Gerthsen Physik*. Springer, Heidelberg, 23. auflage edition, 2006.

[209] I. Langmuir and K. T. Compton. Electrical Discharges in Gases Part II. Fundamental Phenomena in Electrical Discharges. *Review of Modern Physics*, 3:191+, 1931.

[210] I. Langmuir. The pressure effect and other phenomena in gaseous discharges. *Journal of the Franklin Institute*, 196(6):751–762, December 1923.

[211] J. P. Sheehan, Y. Raitses, N. Hershkowitz, I. Kaganovich, and N. J. Fisch. A comparison of emissive probe techniques for electric potential measurements in a complex plasma. *Physics of Plasmas*, 18(7):073501+, 2011.

[212] R. F. Kemp and J. M. Sellen. Plasma Potential Measurements by Electron Emissive Probes. *Review of Scientific Instruments*, 37(4):455–461, 1966.

[213] J. R. Smith, N. Hershkowitz, and P. Coakley. Inflection-point method of interpreting emissive probe characteristics. *Review of Scientific Instruments*, 50(2):210–218, 1979.

[214] M. Y. Ye and S. Takamura. Effect of space-charge limited emission on measurements of plasma potential using emissive probes. *Physics of Plasmas*, 7(8):3457–3463, 2000.

[215] L. A. Schwager. Effects of secondary and thermionic electron emission on the collector and source sheaths of a finite ion temperature plasma using kinetic theory and numerical simulation. *Physics of Fluids B: Plasma Physics*, 5(2):631–645, 1993.

[216] G. D. Hobbs and J. A. Wesson. Heat flow through a Langmuir sheath in the presence of electron emission. *Plasma Physics*, 9(1):85+, December 2002.

[217] S. Iizuka, P. Michelsen, Juul J. Rasmussen, R. Schrittwieser, R. Hatakeyama, K. Saeki, and N. Sato. A method for measuring fast time evolutions of the plasma potential by means of a simple emissive probe. *Journal of Physics E: Scientific Instruments*, 14(11):1291+, November 1981.

[218] A. Siebenförcher and R. Schrittwieser. A new simple emissive probe. *Review of Scientific Instruments*, 67(3):849–850, 1996.

[219] M. A. Fink, M. Endler, and T. Klinger. New Developments of Self-emitting Electrostatic Probes for use in High Temperature Plasmas. *Contributions to Plasma Physics*, 44(7-8):668–676, November 2004.

[220] N. Hershkowitz, B. Nelson, J. Pew, and D. Gates. Self-emissive probes. *Review of Scientific Instruments*, 54(1):29+, 1983.

[221] S. Ono and S. Teii. Laser-heated emission of electrons from a carbon-coated metal surface and its application to the emissive probe measurements. *Review of Scientific Instruments*, 50(10):1264+, 1979.

[222] R. Schrittwieser, C. Ionita, P. Balan, R. Gstrein, O. Grulke, T. Windisch, C. Brandt, T. Klinger, R. Madani, G. Amarandei, and A. K. Sarma. Laser-heated emissive plasma probe. *Review of Scientific Instruments*, 79(8):083508+, 2008.

[223] E. Y. Wang, N. Hershkowitz, D. Diebold, T. Intrator, R. Majeski, H. Persing, G. Severn, B. Nelson, and Y. J. Wen. Secondary electron emission-capacitive probes for plasma potential measurements in plasmas with hot electrons. *Journal of Applied Physics*, 61(10):4786+, 1987.

[224] J. P. Sheehan and N. Hershkowitz. Emissive probes. *Plasma Sources Science and Technology*, 20(6):063001+, December 2011.

[225] J. M. Sanders, A. Rauch, R. J. Mendelsberg, and A. Anders. A synchronized emissive probe for time-resolved plasma potential measurements of pulsed discharges. *Review of Scientific Instruments*, 82(9):093505+, 2011.

[226] H. Fujita, S. Nowak, B. A. Hoegger, and H. Schneider. Potential measurements by an emissive probe in a magnetized plasma. *Physics Letters A*, 78(3):263–265, August 1980.

[227] S. L. Cartier and R. L. Merlino. Anode-type double layers in a nonuniform magnetic field. *Physics of Fluids*, 30(8):2549+, 1987.

[228] E. Mravlag and P. Krumm. Space potential measurements with a continuously emitting probe. *Review of Scientific Instruments*, 61(8):2164–2170, 1990.

[229] J. W. Bradley, R. A. Khamis, M. I. Sanduk, J. A. Elliott, and M. G. Rusbridge. Measurements of the sheath potential in low density plasmas. *Journal of Physics D: Applied Physics*, 25(10):1443+, April 2000.

[230] P. Balan, R. Schrittwieser, C. Ionita, J. A. Cabral, H. F. C. Figueiredo, H. Fernandes, C. Varandas, J. Adamek, M. Hron, J. Stöckel, E. Martines, and M. Tichy. Emissive probe measurements of plasma potential fluctuations in the edge plasma regions of tokamaks. *Review of Scientific Instruments*, 74(3):1583+, 2003.

[231] L. Dorf, Y. Raitses, and N. J. Fisch. Electrostatic probe apparatus for measurements in the near-anode region of Hall thrusters. *Review of Scientific Instruments*, 75(5):1255+, 2004.

[232] J. W. Bradley, S. Karkari, and A. Vetushka. Electric Probe Measurements in Pulsed Magnetron Plasmas. *Surface Engineering*, 20(3):186–188, June 2004.

[233] S. M. Borah, H. Bailung, and J. Chutia. Study of the sheath potential structure using emissive probe in a dc magnetron plasma. *Journal of Physics: Conference Series*, 208(1):012128+, March 2010.

[234] UNI-Trend Technology Ltd., Dong Guan City. *Model UT70A: Operating Manual*, 2001.

[235] Tektronix Inc., Beaverton, USA. *Instruction manual Tektronix P6015A 1000X high voltage probe*.

[236] J. W. Bradley, S. K. Karkari, and A. Vetushka. A study of the transient plasma potential in a pulsed bi-polar dc magnetron discharge. *Plasma Sources Science and Technology*, 13(2):189+, May 2004.

[237] H. Fujita and S. Yagura. Measurements of Fast Time Evolutions of Plasma Potential Using Emissive Probe. *Japanese Journal of Applied Physics*, 22(Part 1, No. 1):148–151, January 1983.

[238] D. Diebold, N. Hershkowitz, A. D. Bailey, M. H. Cho, and T. Intrator. Emissive probe current bias method of measuring dc vacuum potential. *Review of Scientific Instruments*, 59(2):270–275, 1988.

[239] A. Rauch, R. J. Mendelsberg, J. M. Sanders, and A. Anders. Plasma potential mapping of high power impulse magnetron sputtering discharges. *Journal of Applied Physics*, 111(8):083302+, 2012.

[240] A. Mishra, P. J. Kelly, and J. W. Bradley. The 2D plasma potential distribution in a HiPIMS discharge. *Journal of Physics D: Applied Physics*, 44(42):425201+, October 2011.

[241] D. Horwat and A. Anders. Compression and strong rarefaction in high power impulse magnetron sputtering discharges. *Journal of Applied Physics*, 108(12):123306+, 2010.

[242] D. Horwat and A. Anders. Ion acceleration and cooling in gasless self-sputtering. *Applied Physics Letters*, 97(22):221501+, 2010.

[243] S. K. Karkari, A. Vetushka, and J. W. Bradley. Measurement of the plasma potential adjacent to the substrate in a midfrequency bipolar pulsed magnetron. *Journal of Vacuum Science & Technology A: Vacuum, Surfaces, and Films*, 21(6):L28+, 2003.

[244] J. W. Bradley. The plasma properties adjacent to the target in a magnetron sputtering source. *Plasma Sources Science and Technology*, 5(4):622+, November 1996.

[245] I. Kolev, A. Bogaerts, and R. Gijbels. Influence of electron recapture by the cathode upon the discharge characteristics in dc planar magnetrons. *Physical Review E*, 72(5):056402+, November 2005.

[246] E. Bultinck and A. Bogaerts. Particle-in-cell/Monte Carlo collisions treatment of an Ar/O2 magnetron discharge used for the reactive sputter deposition of TiOx films. *New Journal of Physics*, 11(10):103010+, October 2009.

[247] D. Lundin, S. A. Sahab, N. Brenning, C. Huo, and U. Helmersson. Internal current measurements in high power impulse magnetron sputtering. *Plasma Sources Science and Technology*, 20(4):045003+, August 2011.

[248] A. Vetushka and J. W. Bradley. The current-density distribution in a pulsed dc magnetron deposition discharge. *Journal of Physics D: Applied Physics*, 40(7):2037–2044, April 2007.

[249] R. E. Kiel. Electrostatic probe theory for free molecular cylinders. *AIAA Journal*, 6(4):708–712, 1968.

[250] M. J. Druyvesteyn. Der Niedervoltbogen. *Zeitschrift für Physik A Hadrons and Nuclei*, 64(11):781–798, September 1930.

[251] V. A. Godyak and V. I. Demidov. Probe measurements of electron-energy distributions in plasmas: what can we measure and how can we achieve reliable results? *Journal of Physics D: Applied Physics*, 44(23):233001+, May 2011.

[252] H. M. Mott-Smith and I. Langmuir. The Theory of Collectors in Gaseous Discharges. *Physical Review Online Archive (Prola)*, 28(4):727–763, October 1926.

[253] J. E. Allen, R. L. F. Boyd, and P. Reynolds. The Collection of Positive Ions by a Probe Immersed in a Plasma. *Proceedings of the Physical Society. Section B*, 70(3):297+, March 1957.

[254] I. B. Bernstein and I. N. Rabinowitz. Theory of Electrostatic Probes in a Low-Density Plasma. *Physics of Fluids*, 2(2):112+, 1959.

[255] J. G. Laframboix. University of toronto institute of aerospace studies report 100, 1966.

[256] Y. S. Chou, L. Talbot, and D. R. Willis. Kinetic Theory of a Spherical Electrostatic Probe in a Stationary Plasma. *Physics of Fluids*, 9(11):2150+, 1966.

[257] Z. Zakrzewski and T. Kopiczynski. Effect of collisions on positive ion collection by a cylindrical Langmuir probe. *Plasma Physics*, 16(12):1195+, October 2002.

[258] M. Tichý, M. Šícha, P. David, and T. David. A Collisional Model of the Positive Ion Collection by a Cylindrical Langmuir Probe. *Contributions to Plasma Physics*, 34(1):59–68, 1994.

[259] D. Trunec, P. Španěl, and D. Smith. The Influence of Ion - Neutral Collisions in the Plasma Sheath on the Ion Current to an Electrostatic Probe: Monte Carlo Simulation. *Contributions to Plasma Physics*, 35(3):203–212, 1995.

[260] Z. Sternovsky, S. Robertson, and M. Lampe. The contribution of charge exchange ions to cylindrical Langmuir probe current. *Physics of Plasmas*, 10(1):300+, 2003.

[261] Z. Sternovsky, S. Robertson, and M. Lampe. Ion collection by cylindrical probes in weakly collisional plasmas: Theory and experiment. *Journal of Applied Physics*, 94(3):1374–1381, 2003.

[262] F. Iza and J. K. Lee. Particle-in-cell simulations of planar and cylindrical Langmuir probes: Floating potential and ion saturation current. *Journal of Vacuum Science & Technology A: Vacuum, Surfaces, and Films*, 24(4):1366+, 2006.

[263] J. E. Allen, B. M. Annaratone, and U. de Angelis. On the orbital motion limited theory for a small body at floating potential in a Maxwellian plasma. *Journal of Plasma Physics*, 63(04):299–309, 2000.

[264] J. E. Allen. Probe theory - the orbital motion approach. *Physica Scripta*, 45(5):497–503, May 1992.

[265] J. E. Allen. Probe theories and applications: modern aspects. *Plasma Sources Science and Technology*, 4(2):234+, May 1995.

[266] F. F. Chen. Langmuir probe analysis for high density plasmas. *Physics of Plasmas*, 8(6):3029–3041, 2001.

[267] F. F. Chen. Langmuir probes in RF plasma: surprising validity of OML theory. *Plasma Sources Science and Technology*, 18(3):035012+, August 2009.

[268] B. M. Annaratone, M. W. Allen, and J. E. Allen. Ion currents to cylindrical Langmuir probes in RF plasmas. *Journal of Physics D: Applied Physics*, 25(3):417+, March 1992.

[269] A. A. Sonin. Free-molecule Langmuir probe and its use in flow-field studies. *AIAA Journal*, 4(9):1588–1596, September 1966.

[270] G. J. H. Brussaard, M. van der Steen, M. Carrère, M. C. M. van de Sanden, and D. C. Schram. Langmuir probe measurements in an expanding magnetized plasma. *Physical Review E*, 54:1906–1911, August 1996.

[271] P. C. Stangeby. Effect of bias on trapping probes and bolometers for Tokamak edge diagnosis. *Journal of Physics D: Applied Physics*, 15(6):1007+, November 2000.

[272] V. I. Demidov, S. V. Ratynskaia, and K. Rypdal. Electric probes for plasmas: The link between theory and instrument. *Review of Scientific Instruments*, 73(10):3409+, 2002.

[273] W. Lotz. Electron-impact ionization cross-sections and ionization rate coefficients for atoms and ions from scandium to zinc. *Zeitschrift fÃ¼r Physik A Hadrons and Nuclei*, 220(5):466–472–472, October 1969.

[274] E. O. Johnson and L. Malter. A Floating Double Probe Method for Measurements in Gas Discharges. *Physical Review Online Archive (Prola)*, 80(1):58–68, October 1950.

[275] S. L. Chen and T. Sekiguchi. Instantaneous Direct-Display System of Plasma Parameters by Means of Triple Probe. *Journal of Applied Physics*, 36(8):2363–2375, 1965.

[276] S. G. Ingram and N. S. J. Braithwaite. Ion and electron energy analysis at a surface in an RF discharge. *Journal of Physics D: Applied Physics*, 21(10):1496+, November 2000.

[277] Private communication with dr. p. poolcharuansin.

[278] Scientific Systems, Dublin, Ireland. *Smartprobe Automatic Langmuir Probe - User Manual*, 2003.

[279] S. Huldt, S. Johansson, U. Litzén, and J. F. Wyart. The Spectrum and Term System of Singly Ionized Titanium, Ti II. *Physica Scripta*, 25(2):401+, December 2006.

[280] J. E. Sansonetti and W. C. Martin. Handbook of Basic Atomic Spectroscopic Data. *Journal of Physical and Chemical Reference Data*, 34(4):1559–2259, 2005.

[281] S. M. Thompson and J. W. Bradley. The Effect of Rotating Cylindrical Langmuir Probes in Magnetron Plasmas. *Contributions to Plasma Physics*, 41(5):481–487, September 2001.

[282] J. Vlcek, P. Kudlacek, K. Burcalova, and J. Musil. High-power pulsed sputtering using a magnetron with enhanced plasma confinement. *Journal of Vacuum Science & Technology A: Vacuum, Surfaces, and Films*, 25(1):42+, 2007.

[283] E. Bultinck, S. Mahieu, D. Depla, and A. Bogaerts. Reactive sputter deposition of TiNx films, simulated with a particle-in-cell/Monte Carlo collisions model. *New Journal of Physics*, 11(2):023039+, February 2009.

[284] M. Holik, J. Bradley, V. Bellido-Gonzalez, and D. Monaghan. Monte Carlo Simulation of Electrons' and Ions' Trajectories in Magnetron Sputtering Systems. *Plasma Processes and Polymers*, 6(S1):S789–S791.

[285] I. Kolev and A. Bogaerts. Numerical study of the sputtering in a dc magnetron. *Journal of Vacuum Science & Technology A: Vacuum, Surfaces, and Films*, 27(1):20+, 2009.

[286] J. van Dijk, G. M. W. Kroesen, and A. Bogaerts. Plasma modelling and numerical simulation. *Journal of Physics D: Applied Physics*, 42(19):190301+, 2009.

[287] S. M. Rossnagel. Deposition and redeposition in magnetrons. *Journal of Vacuum Science & Technology A: Vacuum, Surfaces, and Films*, 6(6):3049–3054, 1988.

[288] S. M. Rossnagel. Magnetron plasma diagnostics and processing implications. *Journal of Vacuum Science & Technology A: Vacuum, Surfaces, and Films*, 6(3):1821–1826, 1988.

[289] T. Motohiro and Y. Taga. Monte Carlo simulation of the particle transport process in sputter deposition. *Thin Solid Films*, 112(2):161–173, February 1984.

[290] A. P. Ehiasarian, J. Andersson, and A. Anders. Distance-dependent plasma composition and ion energy in high power impulse magnetron sputtering. *Journal of Physics D: Applied Physics*, 43(27):275204+, July 2010.

[291] W. H. Press. *Numerical Recipes in C: the art of scientific computing*. Cambridge University Press, Cambridge, UK, 1992.

[292] T. Hurtig, N. Brenning, and M. A. Raadu. Three-dimensional electrostatic particle-in-cell simulation with open boundaries applied to a plasma beam entering a curved magnetic field. *Physics of Plasmas*, 10(11):4291+, 2003.

[293] T. Hurtig, N. Brenning, and M. A. Raadu. The role of high frequency oscillations in the penetration of plasma clouds across magnetic boundaries. *Physics of Plasmas*, 12(1):012308+, 2005.

[294] K. Okazawa, E. Shidoji, and T. Makabe. Prediction of the evolution of the erosion profile in a direct current magnetron discharge. *Journal of Applied Physics*, 86(6):2984+, 1999.

[295] Y. Kudriavtsev, A. Villegas, A. Godines, and R. Asomoza. Calculation of the surface binding energy for ion sputtered particles. *Applied Surface Science*, 239(3-4):273–278, January 2005.

[296] P. Poolcharuansin, M. Bowes, T. J. Petty, and J. W. Bradley. Ionized metal flux fraction measurements in HiPIMS discharges. *Journal of Physics D: Applied Physics*, 45(32):322001+, July 2012.